Emission, scattering and localization of light in complex structures: From nanoantennas to disordered media

Thèse présentée pour l'obtention du grade de

DOCTEUR DE L'UNIVERSITÉ PIERRE ET MARIE CURIE

Spécialité : Physique

(ED389 : "La Physique, de la particule à la matière condensée")

préparée à l'Institut Langevin "Ondes et Images"

par

Alexandre Cazé

Soutenue le 15 Novembre 2013 devant le jury composé de

Rapporteurs :	**Didier Felbacq**	Professeur, UM2, Montpellier, France
	Lukas Novotny	Professeur, ETHZ, Zurich, Suisse
Examinateurs :	**Joël Bellessa**	Professeur, UCBL, Lyon, France
	Agnès Maitre	Professeur, UPMC, Paris, France
	Anne Sentenac	Directeur de Recherche, CNRS, France
Directeur :	**Rémi Carminati**	Professeur, ESPCI, Paris, France
Invité :	**Romain Pierrat**	Chargé de Recherche, CNRS, France

Remerciements

Le travail présenté ici est le fruit d'un peu moins de quatre années passées à l'Institut Langevin, à Paris. Il a été influencé par de nombreuses personnes avec qui j'ai eu le plaisir et la chance d'interagir. Je vais tâcher ici de les remercier.

Je doute trouver les mots pour exprimer ma reconnaissance à Rémi Carminati pour ces quatre années à apprendre à ses côtés. Heureusement, les mots sont bien peu de chose, et tenter de retranscrire ici tout ce qu'il m'a apporté me paraît bien futile et nécessairement réducteur. Je tiens simplement à le remercier pour l'infinie bienveillance qu'il a eue pour moi. Rémi est de ces personnes qui ont l'élégance rare de donner sans attendre de retour, ce qui est trop stylé.

Un grand merci à Romain Pierrat pour sa grande disponibilité et son infinie patience. Il m'a tout appris en simulation numérique, et a souvent payé de sa personne pour me sortir d'impasses. La richesse de cette thèse lui doit énormément.

Collaborer avec Yannick De Wilde et Valentina Krachmalnicoff a été une grande chance et un grand plaisir. Tous deux à leur manière ont une ouverture d'esprit, un professionnalisme et un réel enthousiasme pour tout ce qui touche à la physique qui en font des personnes avec qui il fait bon travailler. J'ai beaucoup appris à leur contact, et je les en remercie.

Je tiens à remercier Lukas Novotny, Didier Felbacq, Joël Bellessa, Anne Sentenac et Agnès Maitre d'avoir accepté de participer à mon jury. Je suis fier et honoré d'avoir réuni un jury si prestigieux.

Je remercie Etienne Castanié, qui a pleinement joué son rôle de grand-frère de thèse, ce qui a beaucoup compté pour moi. Profiter de sa curiosité et de sa bonne humeur (toutes deux éternelles semble-t'il) fût un réel bonheur.

Un grand merci à Kévin Vynck pour sa bienveillance et ses conseils toujours avisés. Ce manuscrit a bénéficié de ses lumières, et – j'en suis sûr – présage de belles collaborations futures.

Je souhaite bonne chance à mes cothésards Da Cao et Olivier Leseur pour la fin de leurs thèses respectives.

Merci à la direction de l'Institut Langevin d'oeuvrer à en faire un endroit aussi dynamique et enrichissant pour les thésards. Un immense merci à Jérôme Gaumet pour s'être occupé pour

moi de tonnes de considérations administratives horribles mais nécessaires. Merci à Patricia Daenens, Lorraine Monod, Delphine Charbonneau, Christelle Jacquet et Marie Do pour leur professionnalisme et leur bonne humeur.

Merci à tous les gens avec qui j'ai pû échanger au labo, en vrac Pierre Bondareff, Emilie Benoit, Daria Andreoli, Baptiste Jayet, Mickaël Busson, Hugo Defienne, David Martina, Mariana Varna, Miguel Bernal, Gilles Tessier, Sylvain Gigan et Sébastien Bideau. Une mention spéciale à Marc et Nico, qui sont devenus plus que de simples collègues de bureau.

Un merci tout particulier à Madame Vinot, ma professeur de physique de première année de classe prépa. C'est dans sa salle de cours, grâce à son sens de la pédagogie et sa bienveillance que m'est venu le goût de la physique. Il ne m'a jamais plus quitté, et c'est une des plus belles choses qui me soit arrivées.

Je tiens à remercier mes proches d'avoir été là pour moi d'une manière ou d'une autre au long de ces quatre années. Mes amis Kad, Ped, Alice, Futé, Nico, Clémiche, Ricky, Max, Luc, Karim, Totor et Yvo. Mon cousin Charles. Mes cousins Albert et Carole (j'en profite pour souhaiter la bienvenue à leur fille, qui naîtra peu après l'impression de cette thèse). Ma marraine Virginie, son mari David, et ma filleule prérérée Mila. Ma grand-mère Yvette et son mari Gérard. Mon beau-frère Yannig. Mes soeurs Agathe et Margaux.

Enfin, merci du fond du coeur à mes parents Frédéric et Bénédicte, qui ont toujours un peu de mal à croire qu'ils sont pour quelque chose dans tout ça (et bah si).

Résumé

Utiliser des milieux nanostructurés pour confiner la lumière permet d'augmenter l'interaction entre un émetteur et le rayonnement électromagnétique. Dans cette thèse, nous utilisons un formalisme classique (présenté au Chap. 1) pour décrire cette interaction dans différents contextes, qui peuvent être regroupés en deux parties (respectivement Parties II et III).

Dans un premier temps, nous étudions l'apparition de modes localisés en champ proche de structures complexes. Nous nous intéressons à deux différents types de structures: des nanoantennes d'or et des films d'or désordonnés. Nos résultats nous permettent de discerner les modes radiatifs et non-radiatifs. Nous introduisons le concept de Cross Density Of States (CDOS) pour décrire quantitativement la cohérence spatiale intrinsèque associée à la structure modale d'un milieu complexe. Nous démontrons ainsi une réduction de l'extention spatiale des modes au voisinage de la percolation électrique des films d'or désordonnés.

Nous nous intéressons ensuite à des milieux fortement diffusants. En éclairant de telles structures par une source cohérente, on obtient une figure d'intensité complexe appelée speckle. Nous utilisons une méthode diagrammatique pour démontrer une corrélation négative entre les figures de speckle réfléchie et transmise à travers une tranche dans le régime mésoscopique. Nous nous intéressons ensuite à la corrélation C_0, qui apparait lorsque la source est enfouie dans le milieu. Nous proposons une démonstration générale de l'égalité entre la corrélation C_0 et les fluctuations normalisées de la LDOS, et soulignons le rôle fondamental des interactions de champ proche. Finalement, nous observons numériquement le régime de couplage fort entre un diffuseur résonnant et un mode localisé d'Anderson au sein d'un milieu désordonné 2D.

Mots-clés

Nanooptique, Densité locale d'états électromagnétique, Cross Density Of States, Films métalliques désordonnés, Corrélations de speckle; Couplage fort, Localisation d'Anderson

Summary

Using nanostructures to confine light allows to increase the interaction between an emitter and electromagnetic radiation. In this thesis, we use a classical formalism (presented in Chap. 1) to describe this interaction in various contexts, that can be gathered in two parts (respectively Parts II and III).

First, we study the apparition of localized modes in the near field of complex metallic structures. We study numerically the spatial distribution of the local density of states (LDOS) in the vicinity of two different structures: gold nanoantennas and disordered metallic films. Our results allow us to discriminate between radiative and non-radiative modes. We introduce the concept of cross density of states (CDOS) to quantitatively study the intrinsic spatial coherence associated with the modal structure of a complex medium. We use the CDOS to demonstrate an overall spatial squeezing of the modes near the electric percolation of disordered metallic films.

Then, we focus on strongly scattering media. By illuminating such structures by a coherent source, one obtains a chaotic intensity pattern called speckle. First, we use a diagramatic method to demonstrate an anticorrelation between the reflected and transmitted speckle patterns in the case of a diffusive slab in the mesoscopic regime. Then, we study the C_0 correlation, that appears the source is embedded inside the medium. We propose a general derivation of the equality between the C_0 correlation and the normalized fluctuations of the LDOS, and emphasize the fundamental role of near-field interactions. Finally, we study two-dimensional disordered media in the Anderson localized regime. We observe the strong coupling regime between such a mode and a resonant scatterer, in excellent agreement with theoretical predictions.

Keywords

Nanooptics, Local Density Of States, Cross Density Of States, Disordered metallic films, Speckle correlations, Weak coupling, Strong coupling, Anderson localization

Contents

I Introduction and basic concepts **1**

General introduction **3**

1 Light-matter interaction: a classical formalism **11**
1.1 Electromagnetic radiation: the dyadic Green function 12
1.1.1 Green formalism 12
1.1.2 Eigenmode expansion of the dyadic Green function 13
1.2 Small particle in vacuum: the dynamic polarizability 15
1.2.1 Polarizability of a small spherical particle 15
1.2.2 Resonant scatterer polarizability 18
1.3 Light-matter interaction: weak and strong coupling regimes 19
1.3.1 Dressed polarizability in the presence of an environment 20
1.3.2 Coupling to one eigenmode: Weak and strong coupling regimes 21
1.3.3 General formulas in the weak-coupling regime 25
1.4 Conclusion 26

II Light localization in complex metallic nanostructures **27**

2 Characterization of a nanoantenna **29**
2.1 Experimental setup and results 31
2.1.1 Fluorescent beads probe the LDOS 31
2.1.2 Experimental setup 33
2.1.3 Experimental results 35
2.2 Numerical model of the experiment 36
2.2.1 The Volume Integral Method 36
2.2.2 Model for the LDOS 37
2.2.3 Model for the fluorescence intensity 38
2.3 Numerical results 43
2.3.1 Numerical maps of the LDOS and fluorescence intensity 43

2.3.2 Resolution of the LDOS maps . . . 44
2.4 Conclusion . . . 46

3 Spatial distribution of the LDOS on disordered films 49
3.1 Simulation of the growth of the films . . . 51
3.1.1 Numerical generation of disordered metallic films . . . 51
3.1.2 Percolation threshold . . . 52
3.1.3 Apparition of fractal clusters near the percolation threshold . . . 53
3.2 Spatial distribution of the LDOS on disordered films . . . 57
3.2.1 Statistical distribution of the LDOS . . . 57
3.2.2 Distance dependence of the LDOS statistical distribution . . . 59
3.2.3 LDOS maps and film topography . . . 61
3.3 Radiative and non-radiative LDOS . . . 62
3.3.1 Definition . . . 62
3.3.2 Statistical distributions of the radiative and non-radiative LDOS . . . 63
3.3.3 Distance dependence of the radiative and non-radiative LDOS distributions 63
3.4 Conclusion . . . 64

4 The Cross Density Of States 67
4.1 The Cross Density Of States (CDOS) . . . 68
4.1.1 Definition . . . 69
4.1.2 CDOS and spatial coherence in systems at thermal equilibrium . . . 69
4.1.3 Interpretation based on a mode expansion . . . 69
4.2 Squeezing of optical modes on disordered metallic films . . . 72
4.2.1 Numerical maps of the CDOS on disordered metallic films . . . 73
4.2.2 Intrinsic coherence length . . . 74
4.2.3 Finite-size effects . . . 76
4.3 Conclusion . . . 77

III Speckle, weak and strong coupling in scattering media 79

5 R-T intensity correlation in speckle patterns 81
5.1 Intensity correlations in the mesoscopic regime . . . 82
5.1.1 The mesoscopic regime . . . 82
5.1.2 Dyson equation for the average field . . . 83
5.1.3 Bethe-Salpether equation for the average intensity . . . 84
5.1.4 Long range nature of the reflection-transmission intensity correlation . . . 86
5.2 Reflection-Transmission intensity correlations . . . 89

5.2.1 Geometry of the system and assumptions . . . 90
5.2.2 Ladder propagator for a slab in the diffusion approximation . . . 90
5.2.3 Diffuse intensity inside the slab . . . 91
5.2.4 Intensity correlation between reflection and transmission . . . 92
5.2.5 Discussion . . . 93
5.3 Conclusion . . . 95

6 Nonuniversality of the C_0 correlation 97
6.1 C_0 equals the normalized fluctuations of the LDOS . . . 98
6.1.1 The C_0 correlation equals the fluctuations of the normalized LDOS . . . 99
6.1.2 Physical origin of the C_0 correlation . . . 100
6.2 Long-tail behavior of the LDOS distribution . . . 101
6.2.1 The "one-scatterer" model . . . 101
6.2.2 Asymmetric shape of the LDOS distribution: Numerical results . . . 104
6.3 C_0 is sensitive to disorder correlations . . . 106
6.3.1 The effective volume fraction: a "correlation parameter" . . . 107
6.3.2 LDOS distribution and correlation parameter . . . 107
6.3.3 C_0 and correlation parameter . . . 108
6.4 Conclusion and perspectives . . . 109

7 Strong coupling to 2D Anderson localized modes 111
7.1 An optical cavity made of disorder: Anderson localization . . . 112
7.1.1 LDOS spectrum of a weakly lossy cavity mode . . . 112
7.1.2 Numerical characterization of a 2D Anderson localized mode . . . 113
7.2 Strong coupling to a 2D Anderson localized mode . . . 116
7.2.1 Strong coupling condition for a TE mode in 2D . . . 116
7.2.2 Numerical observation of the strong coupling regime . . . 117
7.3 Alternative formulation of the strong coupling criterion . . . 118
7.4 Conclusion . . . 119

General conclusion and perspectives 121

Appendices 123

A Lippmann-Schwinger equation 127

B Regularized Green function and eigenmode expansion 129
B.1 Regularized Green function . . . 129
B.1.1 General case of an arbitrary volume δV . . . 129

B.1.2 Case of a spherical volume δV . . . 130
B.2 Eigenmode expansion of the regularized Green function . . . 131
B.2.1 Case of a closed non-absorbing medium . . . 131
B.2.2 Phenomenological approach of lossy environments . . . 133

C Coupled Dipoles method **135**

D Simulation of the growth of disordered films **137**
D.1 Description of the algorithm . . . 137
D.1.1 Vocabulary and notations . . . 137
D.1.2 Interaction potential . . . 138
D.1.3 Energy barrier for particle diffusion . . . 139
D.1.4 Choice of a process . . . 139

E Volume Integral method **143**
E.1 Weyl expansion of the Green function . . . 143
E.1.1 Spatial Fourier transform . . . 143
E.1.2 Weyl expansion . . . 144
E.2 The Volume Integral method . . . 145
E.2.1 The Lippmann-Schwinger equation . . . 145
E.2.2 Analytical integration of the Green function over the unit cells . . . 145
E.3 Energy balance . . . 147
E.3.1 Power transferred to the environment . . . 147
E.3.2 Absorption by the medium (non-radiative channels) . . . 147
E.3.3 Radiation to the far field (radiative channels) . . . 148

F T-T speckle intensity correlations in the diffusive regime **149**
F.1 Leading term for the long-range correlation . . . 149
F.2 Useful integrals . . . 150

Bibliography **159**

Part I

Introduction and basic concepts

General introduction

The interaction of light with matter requires deeply different descriptions, depending on the scales of the object under observation. The propagation of light in macroscopic homogeneous media is described by the laws of geometrical optics. Our reflection in a mirror, or the distortion of an object embedded in water, can be explained by the laws of refraction. However, when one looks at a painted wall, a cloud or a glass of milk, one sees a diffuse white uniform color, that geometrical optics fails to describe. Those are called *complex media*, because they exhibit a microscopic structure that can "scramble" light and cause this homogeneous appearance. The propagation of optical waves in complex media is described by the multiple scattering theory. In this framework, light follows a random walk, where collisions are due to scattering by the heterogeneities. On large distances, this description leads to a diffusion equation for the transport of light intensity, that explains, e.g., the blurry appearance of a car headlamp in foggy weather.



Figure 1: Illustration of three different regimes of light-matter interaction: a mirror, a cloud and a compact disk.

In complex media exhibiting heterogeneities at the scale of one optical wavelength ($400 - 800$ nm), interferences can also lead to new interesting optical effects. When the heterogeneities are ordered in a periodic structure, the laws of diffraction predict that the reflection of light will occur on discrete directions, that depend on the wavelength. As an example, the holes printed on a compact disk are of the order of one micron, and are responsible for the colored rays reflected on CDs. In this thesis, we study the interaction of light with complex structures, either ordered of disordered. To illustrate the new physical phenomena that can be observed in such media, let us take four examples that were the subject of recent publications. In Ref. [1],

A. G. Curto and coworkers designed a Yagi-Uda nanoantenna [see Fig. 2(a)], optical equivalent of the Yagi-Uda antenna that is used for radio and television broadcast. Using nanoantennas, they were able to force quantum dots to emit in a chosen direction. In Ref. [2], R. Sapienza and coworkers embedded fluorescent nanosources in a strongly scattering media composed of ZnO particle [see Fig. 2(b)]. They demonstrated that in such a disordered medium, the spontaneous emission of some emitters was fastened by a factor up to 8.8 compared to average. Those two works illustrate the ability of complex media to influence the emission of light sources.

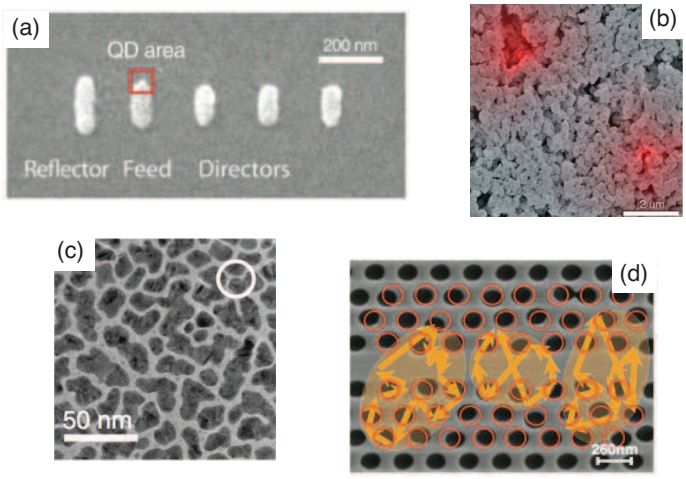


Figure 2: (a) Yagi-Uda nanoantenna, reproduced from Ref. [1]; (b) Fluorescent nano sources embedded in a scattering media made of ZnO powder, reproduced from Ref. [2]; (c) Disordered metallic film exhibiting fractal geometry, reproduced from Ref. [3]; (d) One-dimensional photonic crystal waveguide exhibiting disorder, reproduced from Ref. [4].

In Ref. [3], V. Krachmalnicoff and coworkers have evaporated thin layers of gold on glass substrates, giving rise to disordered metallic films [see Fig. 2(c)]. Those surfaces are known to exhibit high values of the electric field confined in deeply subwavelength areas, called "hot-spots". Using fluorescent lifetime measurement and nanosources in the near field of these structures, they observed high fluctuations of the fluorescence lifetime in the regime where the "hot-spots" are expected to dominate. In Ref. [4], L. Sapienza and coworkers fabricated 1D photonic crystal waveguides, where confined modes appear by the mechanism of Anderson localization, due to inherent fabrication disorder [see Fig. 2(d)]. They observed that the interaction with Anderson localized modes could significantly enhance the spontaneous emission of quantum dots. More recently, it was demonstrated on the same kind of sample that the regime of strong coupling between an emitter and a localized mode could be reached [5]. Those last two works illustrate the ability of localized optical modes to influence light emission. In this thesis, we address both the emission and the localization of light in complex media. The manuscript is organized in three parts and seven chapters, that we will briefly describe.

Part I - Introduction and basic concepts

In the process of light emission, atoms or molecules often behave as electric dipoles [6, 7]. Many aspects of light-matter interaction can be understood from the behavior of classical electric dipoles. Let us introduce the two following characteristic time scales:

- τ_p is the lifetime of the electric dipole (its decay being caused by radiation).
- τ_E is the typical time that the energy radiated by the dipole remains in its vicinity once it is emitted.

Depending on the respective values of τ_p and τ_E, two regimes can be identified in the interaction of an emitter with the electromagnetic field.

- The regime where $\tau_E \ll \tau_p$ is known as the *weak coupling regime*. Physically, this means that the energy leaks to the far field or is absorbed as soon as it is emitted by the dipole. In this limit, the structure of the electromagnetic field remains unaffected by the presence of the emitter. Its influence on the dipole emission is a fastening of its exponential decay, with a decay rate Γ_p proportional to the Local Density Of States (LDOS) $\rho(\mathbf{r}, \omega_0)$ [8]

$$\Gamma_p = \frac{1}{\tau_p} \propto \rho(\mathbf{r}, \omega_0), \tag{1}$$

  where $\mathbf{r}$ is the position of the emitter and ω_0 the frequency of its radiation.

- Confining light in the vicinity of the emitter, e.g. using a two-mirror cavity [9], one can reach $\tau_E \approx \tau_p$, and enter the *strong coupling regime*. In this regime, the emitter strongly interacts with one eigenmode of the electromagnetic field, which central frequency equals ω_0. Contrary to the case of the weak coupling regime, the presence of the emitter affects the eigenmode structure. Spectrally, both the electric field and the emitter are described by two new hybrid eigenmodes, with "splitted" eigenfrequencies $\omega_0 - \Delta\omega$ and $\omega_0 + \Delta\omega$ [10, 11]. Temporally, the energy flows back and forth between the two hybrid eigenmodes, a phenomenon known as Rabi oscillations [12].

The weak and strong coupling regimes are described in many textbooks in the framework of Cavity Quantum Electrodynamics [13, 14]. This theory is well adapted to describe experiments involving single atoms and optical cavities [9, 15]. However, recent works have shown that significant enhancement of light-matter interaction could be obtained in materials such as strongly scattering media [2], where the full quantization of the electromagnetic field is deeply involved.

In Chap. 1, we present a classical formalism to describe the interaction of resonant scatterers and electromagnetic radiation. The electromagnetic field is described by the Green function, and resonant scatterers are described by their electric polarizability.

This formalism is well suited to describe light propagation in complex structures, including strongly scattering media. We recover the weak ($\tau_E \ll \tau_p$) and the strong ($\tau_E \approx \tau_p$) coupling regimes, and derive a theoretical condition to reach the latter.

Part II - Light localization in complex metallic nanostructures

In order to enhance light-matter interaction, one needs to confine radiation in the vicinity of emitters. From another point of view, an enhancement of light-matter interaction can be understood as a signature of light localization. The LDOS is the central quantity that drives light-matter interaction, as illustrated by Eq. (1) in the weak coupling regime. One interest of the LDOS is that it can be measured by a fluorescence lifetime experiment [8]. In such an experiment, the LDOS is deduced from the temporal behavior of the fluorescence emission, and is therefore not sensitive to any calibration. At Institut Langevin, a setup allowing to measure simultaneously the LDOS and the fluorescence intensity using a nanosource in the near field of nanostructures has been developed [16]. Experimental maps in the near field of a metallic nanoantenna composed of three gold cylinders were performed by Valentina Krachmalnicoff and coworkers.

In Chap. 2, we present a numerical algorithm based on the moment method [17] to solve the Maxwell equations and compute the LDOS in the near field of this metallic nanoantenna. Our calculations take into account retardation, polarization and near-field effects. Using this numerical tool, we model the experimental setup and compute LDOS and fluorescence intensity maps in good agreement with measurements. Numerically, we are able to discuss the influence of the finite extent of the nanosources used in the experiment on the resolution of LDOS maps.

In disordered media, the LDOS is a random quantity and needs to be studied statistically. It was theoretically predicted that the fluctuations of the LDOS could be related to the apparition of localized eigenmodes of the electric field [18]. Intuitively, an intensity pattern with highly localized modes suits the picture of high fluctuations of the LDOS. Based on this prediction, enhanced LDOS fluctuations at the surface of disordered metallic films were reported in Ref. [3]. Due to a mechanism that is still debatable, these peculiar systems are known to exhibit high intensities of the electric field on subwavelength areas, called "hot-spots" [19, 20].

In Chap. 3, we study numerically the spatial distribution of the LDOS in the vicinity of disordered metallic films. First, we present a numerical algorithm – initially proposed in Ref. [21] – to simulate the growth of the films. Using the numerical method presented in Chap. 2, we solve the Maxwell equations on the simulated structures and study the spatial distribution of the LDOS. We recover the trends that were observed in experimental LDOS distributions, and analyze them by computing the

corresponding LDOS maps. Numerically, we are able to distinguish between the radiative LDOS, associated to modes that couple to the far field, and the non-radiative LDOS, associated to modes that stay confined in the near field of the structure. We analyze the spatial distributions of both contributions, and study quantitatively the trade-off as a function of the distance to the films.

Although LDOS maps give a direct information on the eigenmode spatial structure, it does not contain any quantitative information on the spatial extent of the eigenmodes. As a matter of fact, two "hot-spots" of a LDOS map can belong to one and the same eigenmode, as well as one hot-spot can involve several eigenmodes. The spatial extent of eigenmodes is a fundamental quantity that drives, e.g., the coherence length of surface plasmons, the range of non-radiative energy transfer [22], or the lower limit for spatial focusing by time reversal or phase conjugation [23].

In Chap. 4, we introduce the Cross Density Of States (CDOS) as a new tool to describe quantitatively the average spatial extent of the eigenmodes at any position. This gives a rigorous framework to the study of light localization and spatial coherence in complex structures. We compute the CDOS numerically on disordered metallic films, using the same numerical method as in Chap. 3. We demonstrate an overall spatial squeezing of the eigenmodes near the percolation threshold.

Part III - Speckle, weak and strong coupling in strongly scattering media

When coherent light propagates in a strongly scattering medium, a chaotic intensity pattern appears, known as a *speckle* [24]. Light propagation in such media can be modeled as a random walk, where collisions are scattering events by the heterogeneities, as sketched in Fig. 3. The scattering mean free path ℓ is defined as the average distance between two scattering events. In

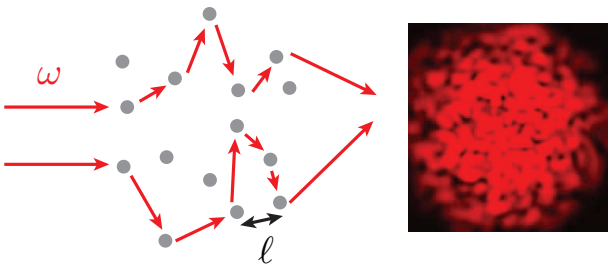


Figure 3: Illustration of wave propagation in strongly scattering media. Grey points represent scattering events by the heterogeneities of the medium.

this picture, the electric field at point $\mathbf{r}$ can be pictured as a sum of random complex variables

associated to scattering paths [25]

$$\mathrm{E}(\mathbf{r}) = \sum_{\text{path}} A_{\text{path}}(\mathbf{r}) \exp\left[i\phi_{\text{path}}(\mathbf{r})\right]. \tag{2}$$

The speckle pattern is usually studied statistically via its spatial intensity correlation function[1]

$$C(\mathbf{r}, \mathbf{r}') = \langle \mathrm{E}(\mathbf{r})\mathrm{E}^*(\mathbf{r})\mathrm{E}(\mathbf{r}')\mathrm{E}^*(\mathbf{r}')\rangle, \tag{3}$$

where $\langle . \rangle$ denotes the average over disorder. This correlation involves the product of four fields, that can all be considered as the result of all possible scattering paths as described by Eq. (2). Averaging this product over disorder is deeply involved, and cannot be done analytically in most regimes. However, in the limit where $\ell \gg \lambda$, some leading contributions to the correlation can be computed theoretically [26, 27].

In Chap. 5, we study the intensity spatial correlations between reflexion and transmission. In a first part, we introduce the ladder approximation, that is valid when $\ell \gg \lambda$, and give the leading terms of the spatial intensity correlation function. Although these correlations are now textbook for the reflected or the transmitted speckle [26, 27], poor attention has been paid to the correlation between the reflected and transmitted intensity patterns. However, such a correlation does exist and exhibits a long range behavior. We compute the leading contribution to this correlation in a slab geometry, assuming the ladder approximation valid. We make the diffusion approximation to obtain analytical expressions, and discuss the results.

When a speckle is generated by a point source embedded *inside* the disordered medium, an infinite range term appears in the correlation function defined by Eq. (3) [28]. This contribution has been called C_0, by analogy with the previously known correlations C_1, C_2 and C_3 [29]. Interestingly, C_0 has been proved to be nonuniversal, in the sense that it varies dramatically with the local environment of the source [30]. For an infinite nonabsorbing medium in the ladder approximation, it has been shown that C_0 equals the normalized fluctuations of the LDOS at the source position [31]. This last result shows a fundamental connection between light-matter interaction and speckle correlations.

In Chap. 6, we study the C_0 correlation using arguments of energy conservation that hold in any scattering medium, including regimes where the ladder approximation is not valid. We demonstrate that the connection between C_0 and the fluctuations of the LDOS – first demonstrated in Ref. [31] – remains valid in a statistically isotropic finite medium with any strength of disorder. Using numerical simulations based on

[1] The intensity correlation defined here is not normalized for the sake of simplicity. A normalized correlation function will be considered in Chaps. 5 and 6.

the coupled dipole method, we demonstrate that the variance of the LDOS is driven by rare configurations of the disorder associated to high values of the LDOS. These high values are the signature of the interaction between the source and its near-field environment. Interestingly, measuring the C_0 correlation is a way to obtain information on the deep local properties of a strongly scattering medium by a far-field measurement.

In a strongly scattering medium where the ladder approximation breaks down ($k\ell \approx 1$, with $k = 2\pi/\lambda$), spatially localized modes can arise from the phenomenon of Anderson localization [32]. Although the localization of electromagnetic waves by a 3D system is still a very discussed topic, Anderson localized modes have been reported in 1D [33] and 2D [34] systems. Localized eigenmodes are the substrate of a strong light-matter interaction, since the radiated energy remains longer in the vicinity of the source. Observations of strong enhancement of the interaction between a 1D disordered photonic crystal exhibiting Anderson localized modes have been reported both in the weak [4] and strong [5] coupling regimes.

In Chap. 7, we demonstrate theoretically the ability of a 2D scattering medium in the Anderson localized regime to reach the strong coupling with an emitter. Using numerical simulations based on the coupled dipole method, we first characterize an Anderson localized mode by computing a LDOS spectrum. Then, we demonstrate the spectral splitting between this mode and a resonant scatterer, described by its electric polarizability. The results are in great agreement with predictions by the theory developed in Chap. 1. We propose a new formulation of the strong coupling criterion, using the Thouless conductance and the Purcell factor.

Chapter 1

Light-matter interaction: a classical scattering formalism

Contents

1.1 Electromagnetic radiation: the dyadic Green function 12
1.1.1 Green formalism 12
1.1.2 Eigenmode expansion of the dyadic Green function 13
1.2 Small particle in vacuum: the dynamic polarizability 15
1.2.1 Polarizability of a small spherical particle 15
1.2.2 Resonant scatterer polarizability 18
1.3 Light-matter interaction: weak and strong coupling regimes 19
1.3.1 Dressed polarizability in the presence of an environment 20
1.3.2 Coupling to one eigenmode: Weak and strong coupling regimes 21
1.3.3 General formulas in the weak-coupling regime 25
1.4 Conclusion 26

The most complete description of light-matter interaction is provided by quantum electrodynamics, where both radiation and matter are quantized. However, many phenomenon can be understood by the semi-classical theory, where a quantized emitter interacts with the classical electric field. The fundamental reason for this success is that the Maxwell equations in the classical and quantum formalisms are identical.

In this first chapter, we present a fully classical description of light-matter interaction. The eigenmode structure is implicitly computed using a Green function formalism. The interaction with matter is described by the volume integral equation. Small particles are described by their electric polarizability. Introducing resonances in the polarizability makes the theory relevant for the study of two-level systems. We recover the well-known weak and strong coupling regimes in the case of the interaction with one single eigenmode, like in the Cavity Quantum Electrodynamics (CQED) theory [13, 14].

1.1 Electromagnetic radiation: the dyadic Green function

The aim of this section is to introduce the Green formalism in the case of the electromagnetic wave equation. We define all the technical concepts and tools that will be necessary to the theory, and refer to other sections of this thesis for detailed derivations of the main results.

1.1.1 Green formalism

To introduce the dyadic Green function, let us consider a medium described by its dielectric constant $\epsilon(\mathbf{r},\omega)$, and sources described by their current density $\mathbf{j}_s(\mathbf{r},\omega)$. The medium is supposed non-magnetic ($\mu = 1$).

Dyadic Green function

It follows from the Maxwell equation that the electric field in the harmonic regime is solution of the Helmoltz equation

$$\boldsymbol{\nabla} \times \boldsymbol{\nabla} \times \mathbf{E}(\mathbf{r},\omega) - \epsilon(\mathbf{r},\omega) k^2 \mathbf{E}(\mathbf{r},\omega) = i\omega\mu_0 \, \mathbf{j}_s(\mathbf{r},\omega), \tag{1.1}$$

where $k = \omega/c$. The electric[1] dyadic Green function $\mathbf{G}$ of the medium is defined as the solution of Eq. (1.1) with a delta source

$$\boldsymbol{\nabla} \times \boldsymbol{\nabla} \times \mathbf{G}(\mathbf{r},\mathbf{r}',\omega) - \epsilon(\mathbf{r},\omega) k^2 \mathbf{G}(\mathbf{r},\mathbf{r}',\omega) = \delta(\mathbf{r}-\mathbf{r}'). \tag{1.2}$$

Two solutions of Eq. (1.2) exist, behaving respectively like an outgoing and an incoming wave at infinite distance[2]. We impose the outgoing wave boundary condition to fully characterize $\mathbf{G}(\mathbf{r},\mathbf{r}',\omega)$. Since Eq. (1.1) is linear, the electric field at any point $\mathbf{r}$ can be expressed using the Green function as

$$\mathbf{E}(\mathbf{r},\omega) = i\omega\mu_0 \int \mathbf{G}(\mathbf{r},\mathbf{r}',\omega) \, \mathbf{j}_s(\mathbf{r}',\omega) \, \mathrm{d}\mathbf{r}'. \tag{1.3}$$

To give a physical picture of the Green function, let us consider an electric dipole source located at $\mathbf{r}'$, with a dipole moment $\mathbf{p}_s$. The current density associated to such a source reads $\mathbf{j}_s(\mathbf{r},\omega) = -i\omega\mathbf{p}_s\delta(\mathbf{r}-\mathbf{r}')$. Eq. (1.3) transforms into

$$\mathbf{E}(\mathbf{r},\omega) = \mu_0\omega^2 \mathbf{G}(\mathbf{r},\mathbf{r}',\omega) \, \mathbf{p}_s. \tag{1.4}$$

The Green function $\mathbf{G}(\mathbf{r},\mathbf{r}',\omega)$ connects the dipole moment of a source located at $\mathbf{r}'$ to the electric field it radiates at $\mathbf{r}$ at frequency ω.

[1] In this whole thesis, we refer to the electric Green function as the Green function for the sake of brevity.

[2] Rigorously, this assertion is true if the medium is non-homogeneous only on a finite region (i.e. if the dielectric constant is uniform at infinite) from $\mathbf{r}'$.

Regularized Green function

The Green function defined by Eq. (1.2) is a distribution. It only gets a physical meaning when integrated over a volume. Let us consider the integral

$$I = \int_{\delta V} \mathbf{G}(\mathbf{r}, \mathbf{r}', \omega)\, \mathrm{d}\mathbf{r}, \tag{1.5}$$

where δV is a small volume surrounding $\mathbf{r}'$. When δV tends to zero, the integral I is indefinite, in the sense that it depends on the shape of the vanishing volume δV [35, 36]. One can separate this integral into a singular and a regular part

$$I = -\frac{\mathbf{L}}{k^2} + \delta V \mathbf{G}^{\mathrm{reg}}(\mathbf{r}, \mathbf{r}, \omega), \tag{1.6}$$

where $\mathbf{L}$ is a real dyadic describing the non-integrable singularity, and $\mathbf{G}^{\mathrm{reg}}$ is the *regularized Green function*. The dyadic $\mathbf{L}$ depends on the shape of the volume δV (see Appendix B for details). The regularized Green function is the quantity that enters the description of the coupling of small particles to radiation, as we shall see in sections 1.2 and 1.3.

1.1.2 Eigenmode expansion of the dyadic Green function

We present an expansion of the dyadic Green function on a normal set of eigenmodes, using a standard approach, initially developed in Ref. [37] to quantify the electromagnetic field. We consider a non-absorbing system described by a real and non dispersive[3] dielectric constant $\epsilon(\mathbf{r})$, embedded in a closed cavity so that the set of eigenmodes is well-defined and discrete.

Eigenmode expansion of the regularized Green function

The eigenmodes $\mathbf{e}_n(\mathbf{r})$ of the propagation equation (1.1) are solutions of

$$\nabla \times \nabla \times \mathbf{e}_n(\mathbf{r}) + \epsilon(\mathbf{r}) \frac{\omega_n^2}{c^2} \mathbf{e}_n(\mathbf{r}) = 0, \tag{1.7}$$

where ω_n are the associated eigenfrequencies. In a lossless cavity, the eigenmodes have no linewidth and are spectrally represented by delta-functions (see Appendix B for details). In an open or absorbing system, the eigenmodes are not discrete anymore. Though, in the limit of weak losses, one can consider that the set of eigenmodes remains discrete. Attenuation can be accounted for using a phenomenological approach [12]. An eigenmode is given a Lorentzian spectral lineshape with a linewith Γ_n. In this approach, the regularized Green function defined in Eq. (1.6) reads

$$\mathbf{G}^{\mathrm{reg}}(\mathbf{r}, \mathbf{r}', \omega) = \frac{c^2}{2\omega_n} \sum_n \frac{\mathbf{e}_n^*(\mathbf{r}') \mathbf{e}_n(\mathbf{r})}{\omega_n - \omega - i\Gamma_n/2}, \tag{1.8}$$

where ω_n and Γ_n are respectively the resonant frequency and the linewidth of the eigenmodes [see Appendix B for the derivation of Eq. (1.8)].

[3] This condition is necessary to recover a classical eigenvalue problem.

Local Density Of States (LDOS)

The Local Density Of States (LDOS) is the fundamental quantity that drives light-matter interaction. It is defined from the imaginary part of the Green function as[4]

$$\rho(\mathbf{r},\omega) = \frac{2\omega}{\pi c^2}\,\mathrm{Im}\,\left[\mathrm{Tr}\,\mathbf{G}(\mathbf{r},\mathbf{r},\omega)\right]. \tag{1.9}$$

It follows from Eqs. (1.8) and (1.9) that the LDOS can be expanded over the set of eigenmodes

$$\rho(\mathbf{r},\omega) = \sum_n \rho_n(\mathbf{r},\omega) = \sum_n \frac{A_n}{\pi}\frac{\Gamma_n/2}{(\omega_n-\omega)^2+(\Gamma_n/2)^2}, \tag{1.10}$$

where the intensity $A_n = |\mathbf{e}_n(\mathbf{r})|^2$ of the eigenmode has been introduced. Note that the definition given by Eq. (1.9) is independent on the set of eigenmodes. The LDOS can be measured via a fluorescence lifetime experiment in the weak-coupling regime (described in section 1.3). It is connected to the spontaneous decay rate of a fluorescent emitter averaged over its dipole orientation $\mathbf{u}$ via

$$\langle\Gamma\rangle_{\mathbf{u}} = \frac{\omega\pi}{3\epsilon_0\hbar}|\mathbf{p}|^2\rho(\mathbf{r},\omega), \tag{1.11}$$

where $\langle . \rangle_{\mathbf{u}}$ is the average over dipole orientation, $\mathbf{p}$ is the transition dipole of the emitter and $\hbar$ is the reduced Planck constant. A derivation of Eq. (1.11) as well as a detailed description of the principle of LDOS measurements are presented in Chap. 2.

Characterization of one eigenmode

In a system where the electric response at point $\mathbf{r}$ is dominated by one eigenmode (e.g. an optical cavity [39]), it follows from Eq. (1.10) that the LDOS can be fitted by a Lorentzian shape

$$\rho(\mathbf{r},\omega) \approx \rho_M(\mathbf{r},\omega) = \frac{A_M}{\pi}\frac{\Gamma_M/2}{(\omega_M-\omega)^2+(\Gamma_M/2)^2}, \tag{1.12}$$

where ω_M is the resonant frequency, Γ_M the linewidth and A_M the intensity of the eigenmode that contributes at point $\mathbf{r}$. To describe the ability of the eigenmode to couple with an emitter, one can introduce the Purcell factor, defined as

$$\mathrm{F_P} = \frac{\rho(\mathbf{r},\omega_M)}{\rho_0} = 2\pi\frac{c^3 A_M}{\omega_M^3\Gamma_M}, \tag{1.13}$$

where $\rho_0 = \omega^2/(\pi^2c^3)$ is the LDOS in vacuum. Note that the Purcell factor defined in Eq. (1.13) is averaged over the emitter transition dipole [as in Eq. (1.11)] and only depends on the eigenmode parameters (resonant frequency, linewidth, intensity). To take into account the dipole orientation in the enhancement of its spontaneous decay rate, one can define a partial LDOS [8].

[4]Note that since the singularity in Eq. (1.6) is real (observation point in vacuum [38]), the imaginary part of the Green function is equal to the imaginary part of the regularized Green function, which makes Eq. (1.8) relevant for the expansion of the LDOS on the set of eigenmodes.

1.2 Small particle in vacuum: the dynamic polarizability

As light propagates in a non-homogeneous medium, it induces electric dipoles in the heterogeneities, that become secondary sources for the electric field. The heretogeneities behave as scatterers. Their ability to get polarized under illumination by an incident field is described by their polarizability. Here, we derive the expression of the electric polarizability of a small spherical particle in vacuum and show that it is constrained by energy conservation. We also establish the general expression of the polarizability of a scatterer exhibiting a resonance. This provides a description also valid for point emitters such as two-level atoms (far from saturation). The polarizability will be a central concept in the description of the coupling of a resonant scatterer (or equivalently a point emitter) to its environment in section 1.3.

1.2.1 Polarizability of a small spherical particle

Let a small spherical particle with volume δV be located at $\mathbf{r}_s$ in free space, and described by a dielectric constant $\epsilon_s(\omega)$. In the presence of an exciting field $\mathbf{E}^{\text{exc}}(\mathbf{r}_s, \omega)$, a dipole moment $\mathbf{p}_s(\omega)$ is induced in the particle. By definition of the polarizability $\alpha_s(\omega)$, one has[5]

$$\mathbf{p}_s(\omega) = \epsilon_0 \alpha_s(\omega) \mathbf{E}^{\text{exc}}(\mathbf{r}_s, \omega). \tag{1.14}$$

Dipole moment and polarization density

If the particle is small enough compared to the wavelength of the incident radiation, one can assume that the electric field is uniform in its volume. In this limit, the polarization density $\mathbf{P}(\mathbf{r}, \omega)$ inside the particle is also homogeneous, and is connected to the electric field inside the particle via

$$\mathbf{P}(\mathbf{r}_s, \omega) = \epsilon_0 \left[\epsilon_s(\omega) - 1\right] \mathbf{E}(\mathbf{r}_s, \omega). \tag{1.15}$$

Hence, the induced dipole $\mathbf{p}_s(\omega)$ in the particle reads

$$\mathbf{p}_s(\omega) = \delta V \mathbf{P}(\mathbf{r}_s, \omega) = \delta V \epsilon_0 \left[\epsilon_s(\omega) - 1\right] \mathbf{E}(\mathbf{r}_s, \omega). \tag{1.16}$$

To get an expression of the polarizability, one needs to express the electric field inside the particle in terms of the exciting field. To do so, we will use the Lippmann-Schwinger equation, that is based on the Green formalism described in section 1.1.

Lippmann-Schwinger equation

The exciting field is the field that would exist in the absence of the particle. Since the environment is vacuum here, it satisfies the free-space propagation equation

$$\nabla \times \nabla \times \mathbf{E}^{\text{exc}}(\mathbf{r}, \omega) - k^2 \mathbf{E}^{\text{exc}}(\mathbf{r}, \omega) = 0. \tag{1.17}$$

[5]Note that in the general case, $\boldsymbol{\alpha}_s(\omega)$ is a dyadic, and the induced dipole is not parallel to the exciting field. For the sake of simplicity, we focus on the case of a spherical particle, which polarizability in vacuum is scalar. A general approach for arbitrary shapes can be derived easily based on this section and Appendix B.

It is convenient to decompose the total field inside the particle as the sum of the exciting and scattered fields

$$\mathbf{E}(\mathbf{r},\omega) = \mathbf{E}^{\text{exc}}(\mathbf{r},\omega) + \mathbf{E}_s(\mathbf{r},\omega). \tag{1.18}$$

The dielectric constant of the environment in the presence of the particle can be expressed as $\epsilon(\mathbf{r},\omega) = 1 + \theta(\mathbf{r})\,(\epsilon_s(\omega) - 1)$, where $\theta(\mathbf{r})$ equals 1 when $\mathbf{r}$ is inside the particle and 0 elsewhere. Hence, the total electric field satisfies the propagation equation

$$\nabla \times \nabla \times \mathbf{E}(\mathbf{r},\omega) - k^2\left[1 + \theta(\mathbf{r})\,(\epsilon_s(\omega) - 1)\right]\mathbf{E}(\mathbf{r},\omega) = 0. \tag{1.19}$$

Substracting Eq. (1.17) to Eq. (1.19), one obtains the equation satisfied by the scattered field

$$\nabla \times \nabla \times \mathbf{E}_s(\mathbf{r},\omega) - k^2\mathbf{E}_s(\mathbf{r},\omega) = \theta(\mathbf{r})k^2\,(\epsilon_s(\omega) - 1)\,\mathbf{E}(\mathbf{r},\omega). \tag{1.20}$$

Eq. (1.20) is a propagation equation in vacuum, with a source term proportional to the total electric field. Its solution can be written using the free-space Green function $\mathbf{G}_0$, associated to the propagation equation (1.17)

$$\mathbf{E}_s(\mathbf{r},\omega) = k^2\left[\epsilon_s(\omega) - 1\right]\int_{\delta V} \mathbf{G}_0(\mathbf{r},\mathbf{r}',\omega)\mathbf{E}(\mathbf{r}',\omega)\,\mathrm{d}\mathbf{r}'. \tag{1.21}$$

Using Eq. (1.18), the total field at point $\mathbf{r}$ reads

$$\mathbf{E}(\mathbf{r},\omega) = \mathbf{E}^{\text{exc}}(\mathbf{r},\omega) + k^2\left[\epsilon_s(\omega) - 1\right]\int_{\delta V} \mathbf{G}_0(\mathbf{r},\mathbf{r}',\omega)\mathbf{E}(\mathbf{r}',\omega)\,\mathrm{d}\mathbf{r}'. \tag{1.22}$$

In this thesis, we refer to Eq. (1.22) as the Lippmann-Schwinger equation. In Chap. 2, we present the volume integral method, that allows to solve numerically this equation in the near-field of metallic structures.

Dynamic and quasistatic polarizabilities

Since the electric field is assumed uniform inside the particle, Eq. (1.22) for $\mathbf{r} = \mathbf{r}_s$ transforms into

$$\left[\mathbf{I} - k^2\left[\epsilon_s(\omega) - 1\right]\int_{\delta V} \mathbf{G}_0(\mathbf{r}_s,\mathbf{r}',\omega)\,\mathrm{d}\mathbf{r}'\right]\mathbf{E}(\mathbf{r}_s,\omega) = \mathbf{E}^{\text{exc}}(\mathbf{r}_s,\omega) \tag{1.23}$$

The integration of the Green function needs to be performed with care, since the Green function exhibits a non-integrable singularity when $\mathbf{r} = \mathbf{r}'$ (as discussed in section 1.1). Using Eq. (1.6), one can introduce the regularized Green function of vacuum

$$\int_{\delta V} \mathbf{G}_0(\mathbf{r}_s,\mathbf{r}',\omega)\,\mathrm{d}\mathbf{r}' = -\frac{\mathbf{L}}{k^2} + \delta V\,\mathbf{G}_0^{\text{reg}}(\mathbf{r}_s,\mathbf{r}_s,\omega). \tag{1.24}$$

For a spherical volume δV in vacuum, one has $\mathbf{L} = \mathbf{I}/3$ and $\mathbf{G}_0^{\text{reg}}(\mathbf{r}_s,\mathbf{r}_s,\omega) = ik/(6\pi)\,\mathbf{I}$ (see Appendix B). From Eqs. (1.14), (1.16) and (1.23), one can deduce the expression of the polarizability [40]

$$\alpha_s(\omega) = \frac{\alpha_s^0(\omega)}{1 - (ik^3/6\pi)\alpha_s^0(\omega)}, \tag{1.25}$$

where $\alpha_s^0(\omega)$ is the *quasistatic polarizability*, defined as[6]

$$\alpha_s^0(\omega) = 3\delta V \frac{\epsilon_s(\omega) - 1}{\epsilon_s(\omega) + 2}. \tag{1.26}$$

Eq. (1.25) defines the *dynamic polarizability*, valid in the optical regime. In the limit where the volume δV of the particle tends to zero, both expressions are equivalent. However, in the optical regime, the quasistatic expression is an approximation. Although it might be convenient to obtain orders of magnitudes of the scattering properties of a particle, it is not consistent with energy conservation, as we shall demonstrate now.

Energy conservation and dynamic polarizability

When light hits a scatterer, the latter removes energy from the incident field. This phenomenon is known as extinction, and is the result of both scattering and absorption. Hence, energy conservation for a scatterer can be expressed in the form [42, 43]

$$\text{Extinction} = \text{Scattering} + \text{Absorption}. \tag{1.27}$$

The power P_{ext} extracted by an oscillating dipole $\mathbf{p}_s(\omega)$ from an incident field $\mathbf{E}^{\text{exc}}(\mathbf{r}_s, \omega)$ reads[7]

$$P_{\text{ext}} = \frac{\omega}{2} \text{Im}\left[\mathbf{p}_s(\omega) \cdot \mathbf{E}^{\text{exc}}(\mathbf{r}_s, \omega)^*\right]. \tag{1.28}$$

In the case of a scatterer described by a polarizability $\alpha_s(\omega)$, Eq. (1.28) transforms into

$$P_{\text{ext}} = \frac{\omega\epsilon_0}{2} |\mathbf{E}^{\text{exc}}(\mathbf{r}_s, \omega)|^2 \, \text{Im}\left[\alpha_s(\omega)\right]. \tag{1.29}$$

From Eqs. (1.26) and (1.29), one can see that a non-absorbing particle ($\text{Im}\,\epsilon(\omega) = 0$) has a real quasistatic polarizability, corresponding to a vanishing extinction. Hence, the quasistatic polarizability cannot describe accurately a non-absorbing radiating scatterer. Let us be more specific on the constraint imposed on the polarizability. The power scattered by an oscillating dipole $\mathbf{p}_s(\omega)$ in vacuum reads

$$P_s = \frac{\mu_0\omega^4}{12\pi c} |\mathbf{p}_s(\omega)|^2. \tag{1.30}$$

In the case of a scatterer described by a polarizability $\alpha_s(\omega)$, this power transforms into

$$P_s = \frac{\omega\epsilon_0}{2} |\mathbf{E}^{\text{exc}}(\mathbf{r}_s, \omega)|^2 \frac{k^3}{6\pi} |\alpha_s(\omega)|^2. \tag{1.31}$$

[6] The electrostatic polarizability of a spherical particle, whatever its size, reads $\alpha_0 = 3\delta V(\epsilon_s - 1)/(\epsilon_s + 2)$ [41], where ϵ_s is the static dielectric constant.

[7] The instantaneous power density exchanged between an electric field $\mathbf{E}^{\text{exc}}(\mathbf{r})$ and charges generating a current density $\mathbf{j}_s(\mathbf{r})$ reads $P_{\text{ext}} = \mathbf{j}_s(\mathbf{r}) \cdot \mathbf{E}^{\text{exc}}(\mathbf{r})$. In the harmonic regime, this power density can be averaged over the optical oscillations and reads $P_{\text{ext}} = (1/2)\text{Re}\,[\mathbf{j}_s(\mathbf{r}, \omega) \cdot \mathbf{E}^{\text{exc}}(\mathbf{r}, \omega)^*]$. In the case of an oscillating dipole located at $\mathbf{r}_s$, $\mathbf{j}_s(\mathbf{r}, \omega) = -i\omega\mathbf{p}_s(\omega)\delta(\mathbf{r} - \mathbf{r}_s)$.

The polarizability of a non-absorbing particle needs to satisfy $P_{\text{ext}} = P_s$, i.e.

$$\operatorname{Im} \alpha_s(\omega) = \frac{k^3}{6\pi} |\alpha_s(\omega)|^2. \tag{1.32}$$

This condition is satisfied by the dynamic polarizability as defined by Eq. (1.25), whatever the expression of $\alpha_s^0(\omega)$ (as long as it remains real).

1.2.2 Resonant scatterer polarizability

In the semi-classical theory, two-level emitters are described by an electric polarizability, that exhibits a resonance at their emission frequency [44]. Here, we derive the general expression of the polarizability of a resonant scatterer, consistently with energy conservation as discussed in section 1.2.1. This encompasses the case of a two-level emitter far from saturation. This will allow us to address the coupling of an emitter to radiation using a fully classical formalism in section 1.3.

Polarizability of a metallic nanoparticle

To introduce the general expression of the polarizability of a resonant scatterer, let us consider first the particular case of a spherical metallic nanoparticle. To introduce a resonance, let us describe the metal dielectric constant by a Drude model

$$\epsilon(\omega) = 1 - \frac{\omega_p^2}{\omega^2 + i\gamma\omega}, \tag{1.33}$$

where ω_p is the plasma frequency and γ accounts for absorption losses inside the particle. Inserting Eq. (1.33) into Eqs. (1.25) and (1.26) the polarizability of this particle reads

$$\alpha_s(\omega) = \frac{3\pi}{k^3} \frac{(k^3/2\pi)\delta V \omega_s}{\omega_s - \omega - (i/2)\left[\gamma + (k^3/2\pi)\delta V \omega_s\right]} \tag{1.34}$$

where $\omega_s = \omega_p/\sqrt{3}$ is the resonant frequency. The total linewidth of the scatterer can be decomposed into a non-radiative linewidth $\Gamma_s^{\text{NR}} = \gamma$ and a radiative linewidth $\Gamma_s^{\text{R}} = (k^3/2\pi)\delta V \omega_s$. The non-radiative linewidth describes absorption inside the metallic particle. The radiative linewidth describes radiation losses, and appears both at the numerator and the denominator of the polarizability because of the constraint defined by Eq. (1.32).

General expression for a resonant scatterer

The dynamic polarizability of an isotropic resonant scatterer with resonant frequency ω_s, radiative linewidth Γ_s^{R} and non-radiative linewidth Γ_s^{NR} can be written as[8]

$$\alpha_s(\omega) = \frac{3\pi}{k^3} \frac{\Gamma_s^R}{\omega_s - \omega - (i/2)\left[\Gamma_s^{\text{NR}} + \Gamma_s^{\text{R}}\right]}. \tag{1.35}$$

[8]Note that this expression is an approximation, known as the known as the "rotating-wave approximation", that is valid when $|\omega - \omega_s| \ll \omega_s$. An exact form can be found in Ref. [45].

The radiative linewidth Γ_s^{R} takes into account radiation losses. The non-radiative linewidth Γ_s^{NR} takes into account all internal non-radiative energy losses by the scatterer (absorption in the case of the metal particle). In the following, we will denote by Γ_s the total linewidth defined as

$$\Gamma_s = \Gamma_s^{\mathrm{NR}} + \Gamma_s^{\mathrm{R}}. \tag{1.36}$$

This form of polarizability is very general. It describes the scattering of light by small particles, but also includes the case of a quantum two-level systems far from saturation [44]. Hence, it is relevant to study the coupling between dipole emitters like atoms or molecules to radiation. The radiative linewidth of the scatterer is the equivalent of the spontaneous decay rate of the emitter. Note that the spontaneous decay rate can describe the coupling to radiative channels (emission of a photon to the far field) or non-radiative channels (the energy is eventually absorbed in the local environment). This is discussed in Chapters 2 and 3.

Radiative and non-radiative linewidth

To justify the introduction of the radiative and non-radiative linewidth in Eq. (1.35), let us express explicitly the extinction, scattered and absorbed powers by a particle described by a resonant polarizability. Let us consider an exciting field at the position of the particle $\mathbf{E}^{\mathrm{exc}}(\mathbf{r}_s, \omega)$, and introduce the constant $\kappa = (\epsilon_0 c/2)|\mathbf{E}^{\mathrm{exc}}(\mathbf{r}_s, \omega)|^2$, homogeneous to a power flux per unit surface. It follows from Eq. (1.29) that the extinct power reads

$$P_{\mathrm{ext}} = \left(\kappa \frac{3\pi}{2k^2} \frac{\Gamma_s^{\mathrm{R}}}{(\omega_s - \omega)^2 + \Gamma_s^2/4} \right) \Gamma_s. \tag{1.37}$$

It is proportional to the total linewidth Γ_s. From Eq. (1.31), one can deduce the scattered power

$$P_s = \left(\kappa \frac{3\pi}{2k^2} \frac{\Gamma_s^{\mathrm{R}}}{(\omega_s - \omega)^2 + \Gamma_s^2/4} \right) \Gamma_s^{\mathrm{R}}, \tag{1.38}$$

that is proportional to the radiative linewidth Γ_s^{R} with the same prefactor. Finally, the absorbed power can be deduced from Eqs. (1.37) and (1.38) thanks to energy conservation as stated in Eq. (1.27)

$$P_{\mathrm{abs}} = P_{\mathrm{ext}} - P_s = \left(\kappa \frac{3\pi}{2k^2} \frac{\Gamma_s^{\mathrm{R}}}{(\omega_s - \omega)^2 + \Gamma_s^2/4} \right) \Gamma_s^{\mathrm{NR}}, \tag{1.39}$$

and is proportional to the non-radiative linewidth Γ_s^{NR}, once again with the same prefactor. This justifies the physical interpretation of Γ_s^{R} (scattering), Γ_s^{NR} (internal absorption) and Γ_s (total extinction).

1.3 Light-matter interaction: weak and strong coupling regimes

We now study the coupling between resonant scatterers and their electromagnetic environment described in the two first sections. Our formalism encompasses both the weak-coupling regime,

where the interaction with the environment results in an enhancement of the radiative linewidth of the scatterer, and the strong-coupling regime, where new eigenstates of the coupled scatterer-field system appear.

1.3.1 Dressed polarizability in the presence of an environment

Let us consider a small spherical particle described by its dynamic polarizability in vacuum $\alpha_s(\omega)$ given by Eq. (1.25). We consider that the scatterer is lying in a small volume of vacuum around position $\mathbf{r}_s$. The Lippmann-Schwinger equation [Eq. (1.21)] transforms into

$$\mathbf{E}(\mathbf{r},\omega) = \mathbf{E}^{\text{exc}}(\mathbf{r},\omega) + k^2\left[\epsilon_s(\omega)-1\right]\int_{\delta V}\mathbf{G}(\mathbf{r},\mathbf{r}',\omega)\mathbf{E}(\mathbf{r}',\omega)\,\mathrm{d}\mathbf{r}', \tag{1.40}$$

where $\epsilon_s(\omega)$ is the dielectric constant describing the particle, δV its small volume and $\mathbf{G}(\mathbf{r},\mathbf{r}',\omega)$ is the Green function describing the electromagnetic response of the environment[9]. Importantly, because the scatterer is lying in vacuum, the singularity dyadic $\mathbf{L}$ associated to the environment Green function $\mathbf{G}(\mathbf{r}_s,\mathbf{r}_s,\omega)$ at the position of the scatterer is the same that of the vacuum Green function [38]. Hence, one can introduce the regularized Green function

$$\int_{\delta V\to 0}\mathbf{G}(\mathbf{r}_s,\mathbf{r}',\omega)\,\mathrm{d}\mathbf{r}' \approx \delta V\mathbf{G}^{\text{reg}}(\mathbf{r}_s,\mathbf{r}_s,\omega) - \frac{\mathbf{I}}{3k^2}. \tag{1.41}$$

Inserting Eq. (1.41) into Eq. (1.40), and using the dynamic polarizability in vacuum defined by Eq. (1.25) as a reference, one can show that the *dressed polarizability* $\boldsymbol{\alpha}(\omega)$, defined as the polarizability of the particle in the environment reads [46]

$$\boldsymbol{\alpha}(\omega) = \alpha_s(\omega)\left\{\mathbf{I} - k^2\alpha_s(\omega)\left[\mathbf{G}^{\text{reg}}(\mathbf{r}_s,\mathbf{r}_s,\omega) - \mathbf{G}_0^{\text{reg}}(\mathbf{r}_s,\mathbf{r}_s,\omega)\right]\right\}^{-1}. \tag{1.42}$$

All information on the coupling between the scatterer and its environment is included in Eq. (1.42), as we shall see in this section. Note that even if the vacuum polarizability of the scatterer is scalar, the dressed polarizability is a dyadic[10]. An analog expression of the dressed polarizability was derived in Ref. [47]. An equivalent expression, using the quasistatic polarizability $\alpha_0(\omega)$ as a reference instead of the dynamic polarizability, was derived in Ref. [46]. Note that because the scatterer is surrounded by vacuum, the singularities of $\mathbf{G}$ and $\mathbf{G}_0$ cancel out in Eq. (1.42), and the dressed polarizability expression is rigorously defined. As commented at the end of section 1.2.1, the singularity dyadic $\mathbf{L}$ only appears in the vacuum polarization $\alpha_s(\omega)$ and does not play any role in the coupling between the scatterer and the field. It is convenient to introduce the regularized scattered Green function $\mathbf{S}^{\text{reg}}(\mathbf{r},\mathbf{r}',\omega) = \mathbf{G}^{\text{reg}}(\mathbf{r},\mathbf{r}',\omega) - \mathbf{G}_0^{\text{reg}}(\mathbf{r},\mathbf{r}',\omega)$ to transform Eq. (1.43) into

$$\boldsymbol{\alpha}(\omega) = \alpha_s(\omega)\left\{\mathbf{I} - k^2\alpha_s(\omega)\mathbf{S}^{\text{reg}}(\mathbf{r}_s,\mathbf{r}_s,\omega)\right\}^{-1}. \tag{1.43}$$

[9] Note that changing the Green function in the Lippmann-Schwinger equation implies a change of the exciting field definition. See Appendix A for details.

[10] Note that the form of Eq. (1.42) does not change in the case of a non-isotropic scatterer [dyadic vacuum polarizability $\boldsymbol{\alpha}_s(\omega)$]). This case is not presented here for the sake of simplicity.

This notation will be used in the following.

1.3.2 Coupling to one eigenmode: Weak and strong coupling regimes

In this section, we describe the coupling between a resonant scatterer and the environment in the case where the electromagnetic response at point $\mathbf{r}_s$ is dominated by one eigenmode of the electromagnetic field. This encompasses the case of engineered optical cavities [48, 15] or multiple scattering systems in the localized regime [4, 33].

Hybrid eigenmodes

In a weakly lossy system, the regularized Green function around eigenfrequency ω_M corresponding to an eigenmode $\mathbf{e}_M$ reads (see Appendix B)

$$\mathbf{G}^{\mathrm{reg}}(\mathbf{r},\mathbf{r}',\omega) = \frac{c^2}{2\omega_M}\frac{\mathbf{e}_M^*(\mathbf{r}')\,\mathbf{e}_M(\mathbf{r})}{\omega_M-\omega-i\Gamma_M/2}. \tag{1.44}$$

As derived in Appendix B, this expression is non-singular and corresponds to the regularized Green function. Denoting by $\mathbf{u}$ the direction of the electric field $\mathbf{e}_M(\mathbf{r}_s)$ at the position of the scatterer, one can use Eq. (1.44) to express the scattered regularized Green function as

$$\mathbf{S}^{\mathrm{reg}}(\mathbf{r}_s,\mathbf{r}_s,\omega) = \frac{c^2}{2\omega_M}\frac{\rho_M\,\mathbf{uu}}{\omega_M-\omega-i\Gamma_M/2} - \frac{ik}{6\pi}\mathbf{I}, \tag{1.45}$$

where $\rho_M = |\mathbf{e}_M(\mathbf{r}_s)|^2$. Let us consider an isotropic resonant scatterer, with polarizability $\alpha_s(\omega)$ in vacuum, given by Eq. (1.35). An eigenmode of the coupled system {scatterer+electromagnetic field} is characterized by a pole in the dressed polarizability given by Eq. (1.43). Since the dressed polarizability is a dyadic, the equation satisfied by the coupled eigenfrequencies depends on the direction. The coupled eigenmodes corresponding to a resonance of the scatterer in direction $\mathbf{u}$ are associated to poles of the coefficient $\mathbf{u}\cdot\boldsymbol{\alpha}(\omega)\mathbf{u}$. These eigenfrequencies thus satisfy the coupling equation

$$1 = k^2\alpha_s(\omega)\mathbf{u}\cdot\mathbf{S}^{\mathrm{reg}}(\mathbf{r}_s,\mathbf{r}_s,\omega)\mathbf{u}. \tag{1.46}$$

Let us introduce the classical coupling constant, defined as

$$g_c^2 = \frac{3}{4}\Gamma_s^R\Gamma_M \mathrm{F_P}. \tag{1.47}$$

g_c is the classical analog of the coupling constant introduced in cavity QED to describe the interaction between a quantum emitter and an optical cavity [13, 14, 49]. Using the Purcell factor introduced in section 1.1.2, and introducing the variable $\Delta\omega = \omega - \omega_M$, Eq. (1.46) transforms into

$$\Delta\omega^2 + i\frac{\Delta\omega}{2}\left(\Gamma_M+\Gamma_s^{\mathrm{NR}}\right) - \left(\frac{\Gamma_M\Gamma_s^{\mathrm{NR}}}{4}+g_c^2\right) = 0. \tag{1.48}$$

As the result of the coupling between the scatterer and the field, two hybrid eigenmodes, with complex eigenfrequencies $\omega_M + \Delta\omega^+$ and $\omega_M + \Delta\omega^-$ appear [where $\Delta\omega^+$ and $\Delta\omega^-$ are the two solutions of Eq. (1.48)]. Depending on the parameters of both the scatterer and the eigenmode, the solutions of this equation are imaginary or real, giving rise respectively to the weak and strong coupling regimes.

Weak coupling regime

When the eigenfrequencies $\omega_M + \Delta\omega^\pm$ are imaginary, the coupling between the eigenmode and the scatterer only results in a change of the linewidth of both systems. In the weak-coupling regime, the losses out of the environment are considered much higher than those of the scatterer

$$\Gamma_M \gg \Gamma_s. \tag{1.49}$$

The picture in this case is the following: as soon as a photon is emitted by the scatterer to its environment, the latter is immediately lost (i.e. radiated to the far field or absorbed in the environment). Hence, an emitted photon will never come back from the environment to the scatterer. Solving Eq. (1.48), one can show that, to the first order of Γ_s/Γ_M,

$$\Delta\omega^+ = -\frac{i}{2}\left(\Gamma_s^{\mathrm{NR}} + 3\mathrm{F_P}\Gamma_s^{\mathrm{R}}\right) \tag{1.50}$$

$$\Delta\omega^- \approx -i\frac{\Gamma_M}{2}. \tag{1.51}$$

The eigenfrequency $\Delta\omega^-$ corresponds to the non-perturbed mode of the electric field, that keeps its resonant frequency ω_M and linewidth Γ_M. The eigenfrequency $\Delta\omega^+$ corresponds to the perturbed scatterer, which resonant frequency remains $\omega_s = \omega_M$, but which radiative linewidth has become

$$\frac{\Gamma^{\mathrm{R}}}{\Gamma_s^{\mathrm{R}}} = 3\,\mathrm{F_P} = 3\,\frac{\rho(\mathbf{r}_s,\omega)}{\rho_0}. \tag{1.52}$$

We recover the well-known expression of the enhancement of the spontaneous decay rate driven by the Purcell factor. The factor 3 is due to the average over transition dipole orientation in our definition of the Purcell factor[11]. Note that the internal non-radiative linewidth is not affected by the coupling to the environment.

Strong coupling regime

The strong coupling regime occurs when the eigenfrequencies $\omega_M + \Delta\omega^\pm$ are real, meaning that the two eigenmodes of the coupled system are no longer degenerate. The condition to reach this

[11] Let $\mathbf{u}$ be the orientation of the electric field at $\mathbf{r}_s$. Let $\mathbf{v}$ and $\mathbf{w}$ be two unit vectors that form an orthonormal basis joint with $\mathbf{u}$, the orientation averaged decay rate reads $\langle\Gamma\rangle = \left(\Gamma_{\mathbf{u}} + \Gamma_{\mathbf{v}} + \Gamma_{\mathbf{w}}\right)/3 = \Gamma_{\mathbf{u}}/3$ since $\Gamma_{\mathbf{v}} = \Gamma_{\mathbf{w}} = 0$ (dipole orientation orthogonal to the electric field).

regime reads[12]

$$g_c^2 \geq \frac{\left(\Gamma_s^{\mathrm{NR}} - \Gamma_M\right)^2}{16}. \tag{1.53}$$

For a quantum two-level system, $\Gamma_s^{\mathrm{NR}} = 0$ and the condition is simply $g_c \geq \Gamma_M/4$, which is consistent with the usual criterion in cavity-QED [15]. In the usual formulation, the explicit use of the transition dipole of the two-level system makes the criterion slightly different (but equivalent). In our formalism the transition dipole is implicitly in the coupling constant g_c through the radiative linewidth Γ_s^{R} (because of energy conservation, as commented in section 1.2). The eigenfrequencies of the hybrid eigenmodes of the coupled system {electromagnetic field + scatterer} then read

$$\Delta\omega^{\pm} = \pm\left[g_c^2 - \frac{\left(\Gamma_s^{\mathrm{NR}} - \Gamma_M\right)^2}{16}\right]^{1/2} - i\,\frac{\Gamma_M + \Gamma_s^{\mathrm{NR}}}{4}. \tag{1.54}$$

The resonant frequencies are splitted symmetrically around ω_M and are separated by the *Rabi frequency*, defined as

$$\Omega_R = \frac{1}{2}\left[g_c^2 - \frac{\left(\Gamma_s^{\mathrm{NR}} - \Gamma_M\right)^2}{16}\right]^{1/2} \tag{1.55}$$

The linewidth of the hybrid eigenmodes read

$$\Gamma = \frac{\Gamma_M + \Gamma_s^{\mathrm{NR}}}{2}. \tag{1.56}$$

Note that Γ_s^R is not implied in this linewidth, since this term corresponds to the radiation of the scatterer towards the eigenmode, and hence does not correspond to losses out of the coupled system. Finally, let us stress that satisfying Eq. (1.53) is not sufficient to observe the splitting in the coupled system spectrum or to observe temporal Rabi oscillations. For such an observation, the Rabi frequency has to overcome the linewidth of the hybrid eigenmodes, i.e.

$$2\Omega_R \geq \Gamma. \tag{1.57}$$

This condition reads

$$g_c^2 \geq \frac{\left(\Gamma_s^{\mathrm{NR}} + \Gamma_M\right)^2}{8}. \tag{1.58}$$

To reach the strong coupling regime, the coupling constant needs to overcome the intrinsic losses of each uncoupled system.

Graphical criterion

The graphical interpretation of the coupling condition presented here results from a very inspiring conversation with Juan-José Sáenz (Universidad Autónoma de Madrid, Spain). The coupling

[12] The discriminant of Eq. (1.48) reads $\Delta = \left[16g_c^2 - \left(\Gamma_M - \Gamma_s^{\mathrm{NR}}\right)^2\right]/4$.

condition Eq. (1.46) can be written

$$\frac{1}{\alpha_s(\omega)} = k^2 \mathbf{u}.\mathbf{S}^{\mathrm{reg}}(\mathbf{r}_s, \mathbf{r}_s, \omega)\mathbf{u}. \tag{1.59}$$

The real part of this equation drives the eigenfrequencies of the hybrid eigenmodes, while its imaginary part drives their linewidth. Here, we focus on the eigenfrequencies, independently on the linewidths. Let us consider a resonant scatterer with a resonant frequency ω_s, described by Eq. (1.35). The real part of the left term of Eq. (1.59) reads

$$\mathrm{Re}\left[\frac{1}{\alpha_s(\omega)}\right] = \frac{k^3}{3\pi\Gamma_s^{\mathrm{R}}}\left(\omega_s - \omega\right). \tag{1.60}$$

Let us consider an eigenmode with eigenfrequency ω_M. The regularized scattered Green function is given by Eq. (1.45), and the real part of the right term of Eq. (1.59) reads

$$\mathrm{Re}\left[k^2 \mathbf{u}.\mathbf{S}^{\mathrm{reg}}(\mathbf{r}_s, \mathbf{r}_s, \omega)\mathbf{u}\right] = \frac{\omega_M \rho_M}{2} \frac{\omega_M - \omega}{\left(\omega_M - \omega\right)^2 + \Gamma_M^2/4}. \tag{1.61}$$

The eigenfrequencies of the coupled system are found when Eq. (1.60) equals Eq. (1.61). We represent both expressions versus $\Delta\omega = \omega - \omega_M$ in Fig. 1.1, for two different sets of parameters corresponding respectively to the weak and the strong coupling regime. The crossing between the

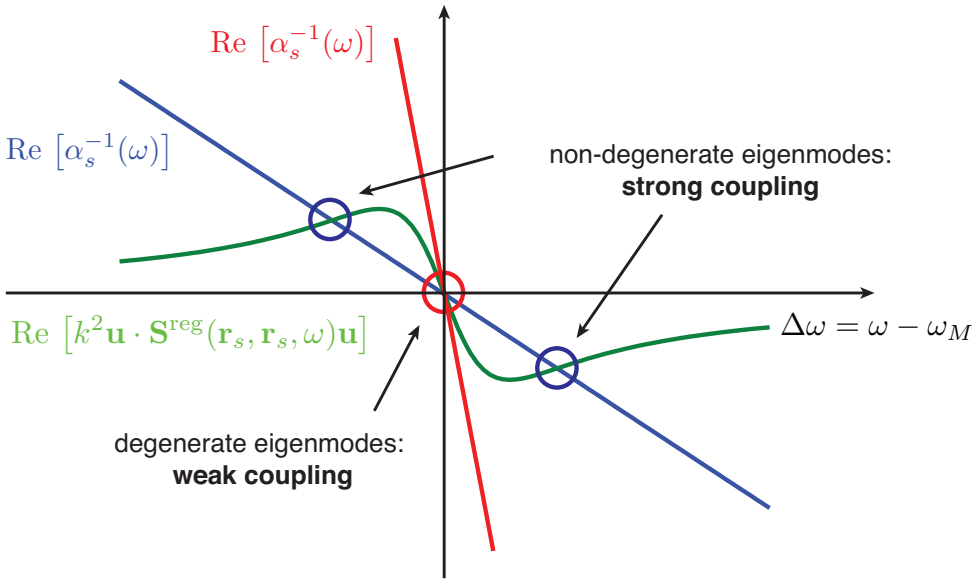


Figure 1.1: Graphical representation of the weak and strong coupling regimes. (Green) Eq. (1.61) plotted as a function of $\Delta\omega$ (Red and blue) Eq. (1.60) plotted as a function of $\Delta\omega$ for two different set of parameters corresponding respectively to the weak and strong-coupling regimes.

red and the blue curve corresponds to the two degenerate eigenmodes with eigenfrequency ω_M

obtained in the weak-coupling regime. Varying the slope of the red curve to reach the blue curve, two new intersections appear with the green curve. They correspond to the two eigenmodes with eigenfrequencies $\omega_M \pm \Delta\omega$ obtained in the strong-coupling regime. This graphical representation is very helpful for a qualitative understanding of the coupled system {scatterer+electromagnetic field}. For example, when one increases Γ_s^{R}, the slope of Eq. (1.60) decreases in absolute value, and one tends to the strong coupling regime. This could have been intuited, since Γ_s^{R} is the spontaneous decay rate of the emitter in free space. However, it can be directly deduced from this method[13]. Last but not least, this graphical representation could be useful to get insight on regimes where the analytical calculations become heavy, e.g. when the resonant frequencies of the scatterer and the eigenmode are shifted. This last idea is an open question that we have not addressed in the present thesis.

1.3.3 General formulas in the weak-coupling regime

In the case where the electric response of the environment cannot be reduced to one eigenmode, the explicit derivation of a coupling condition from Eq. (1.43) is non-trivial because of the dyadic nature of the dressed polarizability[14]. Here, we show that the formalism is consistent with known results for a point dipole emitter (atom, molecule, ...) in the weak-coupling regime (see e.g. Ref. [50]). We consider a resonant scatterer with a fixed polarization direction $\mathbf{u}$, that reads

$$\boldsymbol{\alpha}_s(\omega) = \alpha_s(\omega)\, \mathbf{u}\mathbf{u}, \tag{1.62}$$

where

$$\alpha_s(\omega) = \frac{3\pi}{k^3} \frac{\Gamma_s^{\mathrm{R}}}{\omega_s - \omega - i\Gamma_s/2}. \tag{1.63}$$

Forcing the scatterer to polarize in direction $\mathbf{u}$ is consistent with the fluorescence lifetime measurement procedure, where emitters are excited with a fixed orientation of the transition dipole. Using Eqs. (1.43) and (1.63), one can show that the projection of the dressed polarizability of the particle on direction $\mathbf{u}$ reads[15]

$$\mathbf{u} \cdot \boldsymbol{\alpha}(\omega)\mathbf{u} = \alpha_s(\omega) \left[1 - k^2 \alpha_s(\omega) \mathbf{u} \cdot \mathbf{S}^{\mathrm{reg}}(\mathbf{r}_s, \mathbf{r}_s, \omega)\mathbf{u}\right]^{-1}. \tag{1.64}$$

A resonance of $\mathbf{u}.\boldsymbol{\alpha}(\omega)\mathbf{u}$ is a resonance of $\mathbf{p}_s(\omega)$ without illumination, i.e. an eigenmode of the system. Hence, the eigenfrequencies satisfy

$$1 = k^2 \alpha_s(\omega)\, \mathbf{u} \cdot \mathbf{S}^{\mathrm{reg}}(\mathbf{r}_s, \mathbf{r}_s, \omega)\mathbf{u} \tag{1.65}$$

[13] The influence of Γ_s^{R} on the coupling between a resonant scatterer and an eigenmode of the electromagnetic field in the case of a disordered medium is studied numerically in Chap. 7 (Fig. 7.5)

[14] Only the case where the regularized Green function is diagonal is easily described in the case of a scatterer with scalar polarizability.

[15] Here, we admit that the expression of the dressed polarizability given by Eq. (1.43) remains valid in the case of a dyadic vacuum polarizability $\boldsymbol{\alpha}_s(\omega)$. This derivation can be done with our formalism, but is not presented here for the sake of simplicity.

In the weak coupling regime, the intrinsic losses out of the environment are large compared to that of the resonant scatterer. Mathematically, this approximation can be translated to the frequency domain by assuming that the environment Green function spectrum is large compared to the one of the scatterer. In Eq. (1.65), one makes the approximation

$$\mathbf{S}^{\mathrm{reg}}(\mathbf{r}_s, \mathbf{r}_s, \omega) \approx \mathbf{S}^{\mathrm{reg}}(\mathbf{r}_s, \mathbf{r}_s, \omega_s). \tag{1.66}$$

Denoting by $\omega = \omega_s + \Delta\omega - i\Gamma/2$ the complex eigenfrequencies of the coupled system, Eq. (1.65) transforms into

$$\Delta\omega = -\frac{3\pi}{k}\Gamma_s^R \,\mathrm{Re}\,\mathbf{u}\cdot\mathbf{S}^{\mathrm{reg}}(\mathbf{r}_s, \mathbf{r}_s, \omega_s)\mathbf{u} \tag{1.67}$$

and

$$\Gamma = \Gamma_s^{\mathrm{NR}} + \Gamma_s^{\mathrm{R}}\left(1 + \frac{6\pi}{k}\,\mathrm{Im}\,\mathbf{u}\cdot\mathbf{S}^{\mathrm{reg}}(\mathbf{r}_s, \mathbf{r}_s, \omega_s)\mathbf{u}\right). \tag{1.68}$$

The real and imaginary parts of the complex eigenfrequency of the scatterer are modified from their value in free space due to the (weak) coupling to the electromagnetic environment. From Eq. (1.67), one sees that the resonant frequency – that corresponds to the frequency of the radiated light – is shifted from its value in free space. This shift is known as the Lamb shift. In practice, it is very weak compared to the resonant frequency ω_M and can be neglected (see e.g. numerical simulations in the case of the coupling to a metallic nanoparticle in Ref. [51]). From Eq. (1.68), one sees that the internal non-radiative linewidth is not affected by the environment. Averaging Eq. (1.68) over dipole orientation and using Eq. (1.9), one can show that the modification of the radiative linewidth averaged over transition dipole orientation is equal to the modification of the LDOS

$$\frac{\langle\Gamma - \Gamma_s^{\mathrm{NR}}\rangle_{\mathbf{u}}}{\Gamma_s^{\mathrm{R}}} = \frac{\rho(\mathbf{r}_s, \omega)}{\rho_0}, \tag{1.69}$$

where ρ_0 is the LDOS in vacuum. This result is well known for the spontaneous decay rate of an emitter [8], that is the equivalent of the radiative linewidth of a resonant scatterer. Finally, let us stress that the results of section 1.3.2 in the case of the coupling to one eigenmode are recovered when the scattered regularized Green function is replaced by Eq. (1.45).

1.4 Conclusion

To sum up, we have introduced a classical formalism that describes the interaction of a resonant scatterer to the electric field. Our description is relevant to describe the canonical situation encountered in cavity QED of a two-level system far from saturation coupled to an optical cavity [13, 14]. We have shown that the interaction of such a scatterer with one eigenmode of the electric field gives rise to the well-known weak and strong coupling regimes. For the sake of completeness, we show that our formalism allows to recover the general formulas in the case of the weak coupling between an emitter and the electromagnetic field.

Part II

Light localization in complex metallic nanostructures

Chapter 2

Characterization of the near-field optical properties of a metallic nanoantenna

Contents

2.1 Experimental setup and results 31
2.1.1 Fluorescent beads probe the LDOS 31
2.1.2 Experimental setup 33
2.1.3 Experimental results 35
2.2 Numerical model of the experiment 36
2.2.1 The Volume Integral Method 36
2.2.2 Model for the LDOS 37
2.2.3 Model for the fluorescence intensity 38
2.3 Numerical results 43
2.3.1 Numerical maps of the LDOS and fluorescence intensity 43
2.3.2 Resolution of the LDOS maps 44
2.4 Conclusion 46

Metallic nanostructures have a strong interaction with electric dipoles such as fluorescent molecules and quantum dots. This encompasses different mechanisms which are often hard to disentangle.

- *Light absorption* can be enhanced, leading to an increased effective absorption cross section [46]. This can be advantageously used in photodetection and photovoltaics [52]. Disorder can even help to design efficiently nanostructures in thin film solar cells [53].
- The *spontaneous emission* can be fastened by the Purcell effect. Experimental observation of large Purcell factors have been reported in the vicinity of gold nanoparticles [54, 55, 56]. At Institut Langevin, Valentina Krachmalnicoff and coworkers have demonstrated strong

enhancement of the spontaneous decay rate of fluorescent beads at the surface of disordered metallic films [3, 57] (see Chap. 3).

- Changes of the *fluorescence intensity* were mapped in pioneering experiments using single-emitters for optical microscopy [58, 59]. As we shall explain in this chapter, local field enhancement and non-radiative processes are the two phenomena in competition to drive this signal.

The Local Density Of States (LDOS) is the basic quantity which governs these three mechanisms. Experimentally, several methods have been proposed to map the spatial variations of the LDOS on photonic nanostructures, among which measuring the thermal emission in the near field [60, 61], measuring the "forbidden light" signals from the aperture of a near-field scanning optical microscope [62], or using a scanning electron beam as a point dipole source [63]. The LDOS can be directly inferred from measurements of the spontaneous fluorescence decay rate of a single nanoemitter in its local environment, $\Gamma = 1/\tau$, where τ is the fluorescence lifetime. Recently, a decrease of the fluorescence lifetime was measured by scanning a fluorescent bead across a 250 nm diameter silver rod, pointing to an increased LDOS due to the existence of plasmonic modes on the rod [64].

While a detailed knowledge of the LDOS is clearly required, it is not enough to provide a full characterization of a system involving dipoles coupled with plasmonic nanostructures. Local changes of fluorescence intensity depend on other parameters such as the radiative and non-radiative part of the LDOS and the local field enhancement factor [65]. To characterize a plasmonic antenna, one needs at least to measure both the LDOS and the fluorescence enhancement factor at the nanometer scale in the near field of the antenna.

In this chapter, we present a collaboration with Etienne Castanié, Da Cao, Valentina Krachmalnicoff and Yannick De Wilde at Institut Langevin on the characterization of the near-field properties of a metallic nanoantenna. They have created an experimental setup able to record simultaneously two-dimensional maps of both the fluorescence signal and the LDOS in the near-field of nanostructures. The experiments presented here were led using fluorescent beads attached to an AFM tip approaching a nanoantenna composed of three aligned gold cylinders (see artist view in Fig. 2.1). During my thesis, we have developed a numerical algorithm based on the moment method to solve the Maxwell equations in the near field of 3D resonant nanostructures. Together with the experimentalists, we have designed a model of their experiment based on this method in order to analyze their results. First, we briefly describe the concept of the experimental setup, and present the LDOS and intensity maps that were measured on the metallic nanoantenna. Then, we describe in details our numerical model and emphasize the robustness of the LDOS compared to the fluorescence intensity to obtain intrinsic quantitative information. Finally, we present our numerical results, that are in excellent agreement with the experimental data, and discuss the resolution of the experimental maps by modeling the

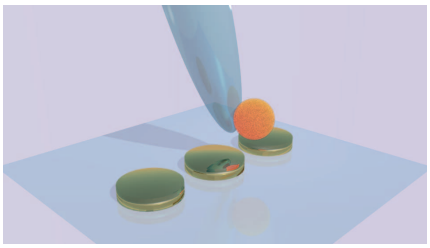


Figure 2.1: Artist view of the gold nanoantenna and the experimental probe.

influence of the spatial extent of the fluorescent sources.

This work has been published in Optics Express [16].

2.1 Experimental setup and results

Here, we describe the experimental setup that was realized by Etienne Castanié, Da Cao, Valentina Krachmalnicoff and Yannick De Wilde at Institut Langevin. Our aim is not to enter the details, but to understand the important phenomena to take into account in the numerical model presented in section 2.2. Details of the setup are given in Etienne Castanié's PhD thesis [66], or in Refs. [3, 57, 16]. First, we explain the principle of the LDOS measurement using a fluorescent bead. Then, we present the experimental setup. Finally, we comment on the LDOS and fluorescence intensity maps measured on the metallic nanoantenna.

2.1.1 Fluorescent beads probe the LDOS

In the experiment, beads containing a few thousand of identical fluorescent molecules (dyes) are used as probes of the LDOS. These beads are composed of a polystyrene matrix inside which the emitters are embedded. Importantly, each fluorescent molecule is randomly oriented. Here, we explain why such sources are good candidates to perform a direct measurement of the LDOS.

Spontaneous decay rate of an emitter

A fluorescent emitter can be modeled by a three-level system (see Fig. 2.2). $|g\rangle$ is the ground state and $|e_1\rangle$ and $|e_2\rangle$ are two vibrational levels of an excited electronic state. We denote by ω_{exc} the frequency of the transition $|g\rangle \rightarrow |e_1\rangle$, and ω_{fluo} the frequency of the transition $|e_2\rangle \rightarrow |g\rangle$. ω_{exc} corresponds to the frequency of the incident laser used to excite the emitters. ω_{fluo} is the frequency of the fluorescence emission. We denote by K and Γ respectively the rates of the transitions $|e_1\rangle \rightarrow |e_2\rangle$ and $|e_2\rangle \rightarrow |g\rangle$. We make the assumption that the transition rate K is very large compared to Γ. In these conditions, if the emitter is excited – i.e. put in the state $|e_1\rangle$ – at time $t = 0$, it immediately decays to the lower vibrational state $|e_2\rangle$. Then, the system behaves like a two-level system [10]. Let us introduce the following notations:

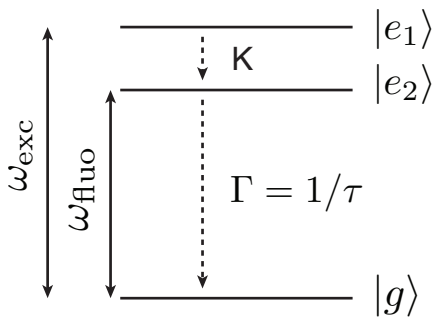


Figure 2.2: Three-level system.

- $P(t)$ is the probability, for the emitter initially in the excited state $|e_2\rangle$, to still be excited at time t.

- $h(t)\,\mathrm{d}t$ is the probability, for the emitter initially in the excited state $|e_2\rangle$, to emit a photon between times t and $t + \mathrm{d}t$.

- $\Gamma\,\mathrm{d}t$ is the probability, knowing that the emitter is still in its excited state at time t, that it will emit a photon between t and $t + \mathrm{d}t$. Note that Γ does not depend on time, which is a fundamental hypothesis for the process of spontaneous emission [44].

Using these notations, one can express $P(t + \mathrm{d}t)$ using the definition of Γ

$$P(t + \mathrm{d}t) = P(t)\,(1 - \Gamma \mathrm{d}t)\,, \tag{2.1}$$

meaning that the probability to still be excited at time $t+\mathrm{d}t$ is the probability to still be excited at time t *and* not to emit a photon between t and $t+\mathrm{d}t$. Solving this differential equation yields

$$P(t) = \exp\left(-\Gamma t\right). \tag{2.2}$$

Γ is called the *spontaneous decay rate*. Experimentally, one measures $h(t)$, the probability to emit between t and $t + \mathrm{d}t$ knowing that the emitter was excited at $t = 0$. One can express $P(t)$ as a function of $h(t)$

$$P(t) = 1 - \int_0^t h(t')\,\mathrm{d}t', \tag{2.3}$$

meaning that the probability to still be excited at time t is the probability not to have emitted a photon between 0 and t. Differentiating Eq. (2.3) yields

$$h(t) = \Gamma \exp\left(-\Gamma t\right). \tag{2.4}$$

Spontaneous decay rate and LDOS

If the emitter is placed at point $\mathbf{r}$ in an environment described by a Green function $\mathbf{G}$, the decay rate reads[1] [8]

$$\Gamma = \frac{2}{\hbar}\mu_0\omega_{\text{fluo}}^2|\mathbf{p}|^2 \,\text{Im}\,\left[\mathbf{u}.\mathbf{G}(\mathbf{r},\mathbf{r},\omega_{\text{fluo}})\mathbf{u}\right], \tag{2.5}$$

where $\mathbf{p}$ is the dipole of the transition $|e_2\rangle \rightarrow |g\rangle$, $\mathbf{u}$ the unit vector defining its orientation and $\hbar = h/2\pi$, where h is the Planck constant. Eq. (2.5) can be averaged over the dipole orientation $\mathbf{u}$, using the identity

$$\langle \mathbf{u}\cdot\mathbf{G}\mathbf{u}\rangle_{\mathbf{u}} = \frac{1}{4\pi}\int_{4\pi}\mathbf{u}\cdot\mathbf{G}\mathbf{u}\,\mathrm{d}\Omega = \frac{1}{3}\,\text{Tr}\,\mathbf{G}, \tag{2.6}$$

that is valid for any dyadic $\mathbf{G}$. One obtains

$$\langle\Gamma\rangle_{\mathbf{u}} = \frac{2}{3\hbar}\mu_0\omega_{\text{fluo}}^2|\mathbf{p}|^2 \,\text{Im}\,\left[\text{Tr}\,\mathbf{G}(\mathbf{r},\mathbf{r},\omega_{\text{fluo}})\right]. \tag{2.7}$$

The LDOS at point $\mathbf{r}$ and frequency ω_{fluo} can be expressed from the dyadic Green function $\mathbf{G}$

$$\rho(\mathbf{r},\omega_{\text{fluo}}) = \frac{2\omega_{\text{fluo}}}{\pi c^2}\text{Im}\,\left[\text{Tr}\,\mathbf{G}(\mathbf{r},\mathbf{r},\omega_{\text{fluo}})\right]. \tag{2.8}$$

One can see from Eqs. (2.7) and (2.8) that the decay rate averaged over the orientation dipole reads

$$\langle\Gamma\rangle_{\mathbf{u}} = \frac{\omega_{\text{fluo}}\pi}{3\epsilon_0\hbar}|\mathbf{p}|^2\rho(\mathbf{r},\omega_{\text{fluo}}) \tag{2.9}$$

Hence, providing that the amount of emitters is sufficiently large to make a statistical average over dipole orientation, a lifetime measurement of the fluorescent beads is a direct measurement of the LDOS. One can notice that the measured LDOS is actually averaged over the spatial extent of the bead. The role of the spatial averaging on the resolution of the experimental maps is discussed in section 2.3.2.

2.1.2 Experimental setup

The principle of the experiment is summed up in Fig. 2.3. The fluorescent bead is attached to a sharp tip and approached in the near field of a nanostructure standing on a glass substrate. The tip is attached to an Atomic Force Microscope (AFM) cantilever that controls its position with a nanometer precision. The AFM records a map of the topography of the substrate while the measurement is performed. The beads are excited by a pulsed laser at frequency ω_{exc} through an inverted microscope located below the glass substrate. This same microscope gathers the fluorescence emission at frequency $\omega_{\text{fluo}} \leq \omega_{\text{exc}}$ of the molecules. An avalanche photodiode is placed behind a filter that selects only the fluorescence photons. The photodetection signal is processed to record the delay between the excitation pulse and the photodetection events.

[1] In the following, we will omit the dependance of Γ on the emitter position $\mathbf{r}$ and the frequency ω. All values will be computed for $\omega = \omega_{\text{fluo}}$, the emission frequency of the experimental molecules.

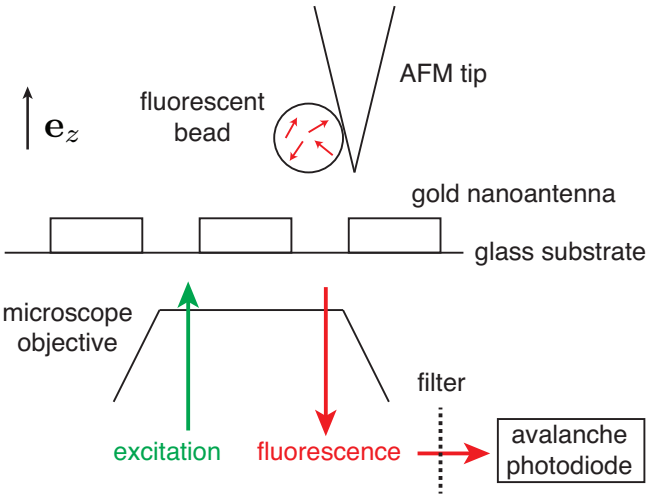


Figure 2.3: Sketch of the experimental concept. The vertical direction is denoted by $\mathbf{e}_z$.

Plotting the arrival times in a histogram $h(t)$ and repeating the experiment many times (thanks to the repetition rate of the pulsed laser), one obtains the typical histogram shown in Fig. 2.4. The fluorescence intensity is the total number of photons actually detected by the avalanche

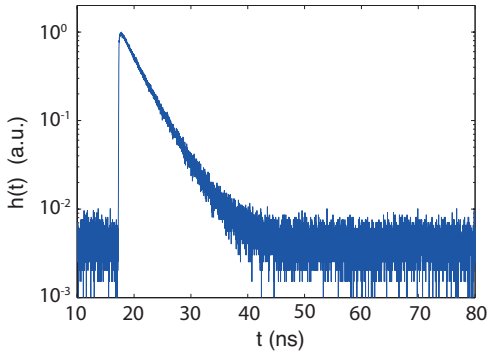


Figure 2.4: Histogram of the photons arrival times $h(t)$ for one fluorescent bead at one position. This figure is taken from Ref. [66].

photodiode after one excitation. Hence, *it is simply equal to the integral of the arrival time histogram*.

Provided that a sufficiently high number of arrival times are measured, the histogram $h(t)$ must converge towards an exponential decaying function of t, which slope is the fluorescent decay rate, as shown in Eq. (2.4). Since this decay rate is intrinsically averaged over dipole orientation, *the slope of this curve is directly proportional to the LDOS at the position of the nanosource*.

2.1.3 Experimental results

The nanoantenna we study is composed of a linear chain of three 150 nm-diameter gold nanodisks separated by 50 nm gaps on a glass substrate. These structures were manufactured by Stéphane Collin and Nathalie Bardou at Laboratoire de Photonique des Nanostructures (LPN) using electron beam lithography on a glass microscope coverslip. Each disk is made of a 2 nm thick wetting layer of chromium and a 30 nm thick layer of gold. In Fig. 2.5, we show an AFM image of the topography. One can remark that the disks appear elliptical instead of circular. We

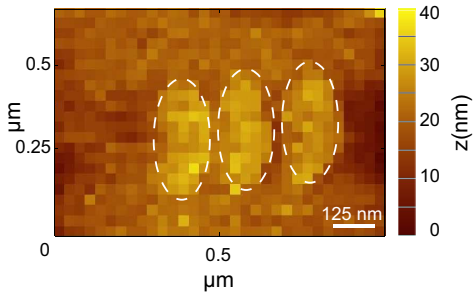


Figure 2.5: AFM image of the topography of the sample.

show in Fig. 2.6 the maps of the LDOS and fluorescence intensity that were measured using the method described previously. The contour of the measured topography (Fig. 2.5) is reported on the maps to guide the eye (dashed lines).

The intensity map gives more insight on the apparent asymmetric shape of the disks on the AFM image. This is due to the fact that the bead is attached on the size of the tip, and not perfectly at the center, breaking the symmetry of the AFM tip (as illustrated in Fig. 2.3). This can be seen in the intensity signal. The latter only decreases in three circularly shaped regions located on the upper half of the elliptical contour. Since the fluorescence signal only comes from the bead, this confirms that the three gold disks are scanned twice, once by the bead and then by the tip, which results in this elliptical topography. The trends of these maps will be discussed in section 2.2 together with the numerical results. Roughly, one can notice that the fluorescence intensity is significantly reduced when the fluorescent bead passes on the top of each disk (approximately by a factor 3). The LDOS exhibits two hot-spots in the two gaps between the disks, and one minor hot-spot on the side. As will be discussed later, this asymmetry is most likely due to a defect of the sample. Interestingly, the hot-spots of the LDOS maps have a spatial extent of the order of 50 nm, which is lower than the diameter of the fluorescent beads. This phenomenon was already observed in Ref. [64], and is discussed in details based on numerical simulations in section 2.3.2.

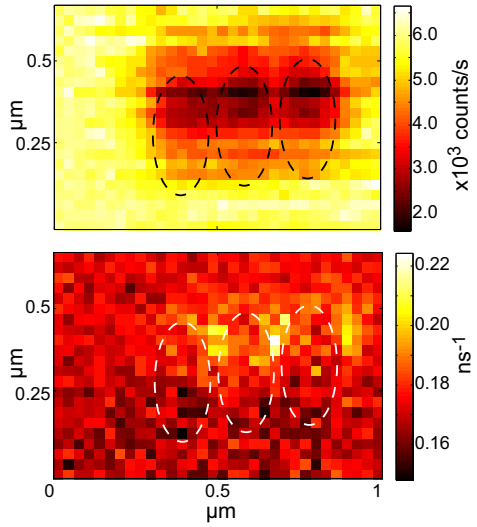


Figure 2.6: (Top) Fluorescence intensity map. (Bottom) Decay rate (LDOS) map. The contour of the topographic relief (dashed line), as measured by the active AFM asymmetric probe [see Fig. (2.5)], is reported on the two maps to guide the eye.

2.2 Numerical model of the experiment

In order to analyze the experimental results, we have developed an exact 3D numerical method to solve the Maxwell equations. We present this algorithm in details here, and identify the important phenomena to take into account. In particular, we study the influence of the finite size of the bead and the finite aperture of the detection setup.

2.2.1 Solving the Maxwell equations on 3D nanostructures: the Volume Integral Method

The Volume Integral Method we have developed is based on the Lippmann-Schwinger equation

$$\mathbf{E}(\mathbf{r},\omega) = \mathbf{E}_0(\mathbf{r},\omega) + k^2 \int_V [\epsilon(\omega) - 1]\, \mathbf{G}_0(\mathbf{r},\mathbf{r}',\omega)\mathbf{E}(\mathbf{r}',\omega)\mathrm{d}\mathbf{r}', \tag{2.10}$$

where V is the volume occupied by gold, $\mathbf{E}_0$ is the incident field, $\mathbf{G}_0$ is the dyadic Green function of the host medium (vacuum in our simulations) and $\epsilon(\omega)$ is the dielectric constant of gold, tabulated in Ref. [67]. Eq. (2.10) is derived in Appendix A. The numerical computation is done by discretizing the volume of integration V into cubic cells with lateral size $\Delta = 5\,\mathrm{nm}$. On each cell, the field is considered constant, but the Green function $\mathbf{G}_0$ is integrated analytically to improve convergence (moment method [17]). This integration is the difference between our

method and the Discrete Dipole Approximation (DDA), and is necessary to deal with near-field modes of resonant metals. Our simulations are exact, given that the discretization of the volume is sufficient to get convergence. In particular, they take into account the vectorial nature of the field, near-field interactions and retardation.

2.2.2 Model for the LDOS

An ideal measurement of the LDOS requires a point-like emitter averaged over orientations. However, to understand the resolution of the experimental maps, one needs to take into account the influence of the finite size of the bead.

Calculation using a point-like source dipole

The numerical method to compute the LDOS is actually very intuitive if one understand the concept of the experiment. As in the experiment, a point source dipole is located at $\mathbf{r}_s$ to probe the LDOS. Numerically, this is done by using an illuminating field in the Lippmann-Schwinger equation that corresponds to the radiation of a source dipole $\mathbf{p}$ located at $\mathbf{r}_s$

$$\mathbf{E}(\mathbf{r},\omega) = \mu_0\omega^2\mathbf{G}_0(\mathbf{r},\mathbf{r}_s,\omega)\mathbf{p} + k^2\int_V [\epsilon(\omega)-1]\,\mathbf{G}_0(\mathbf{r},\mathbf{r}',\omega)\mathbf{E}(\mathbf{r}',\omega)\mathrm{d}\mathbf{r}'. \tag{2.11}$$

Solving this equation for three orthogonal orientations[2] of the source dipole $\mathbf{p}$ gives access to the complete dyadic Green function $\mathbf{G}$ of the system. From the Green function, one can retrieve the decay rate of the emitter for one dipole orientation from Eq. (2.8), or the LDOS by averaging the decay rate over three dipole orientations (see section 2.1.1). In our calculations, we compute the LDOS for the emission frequency ω_{fluo} of the experimental molecules.

Finite size of the fluorescent beads

To address the issue of the resolution of the experimental maps, one needs to take into account that the illumination is not point-like[3]. To do this numerically, we randomly choose N_{em} relative emitter positions inside a sphere of radius $R = 50$ nm that models the bead. As in the experiment, we perform a constant-height scan of this sphere over the structure and solve Eq. (2.11) for 3 orthogonal orientations and N_{em} positions of the source dipole. The LDOS is deduced by averaging the $3N_{em}$ values of the decay rate. Note that the relative positions of the emitters inside the bead are considered fixed during the scan.

In first approximation, we consider a uniform distribution of emitters inside the bead. In these conditions, the probability densities $P(x)$ [respectively $P(y)$, $P(z)$] for an emitter to have

[2]Note that averaging over the three dipole orientations in the simulations is equivalent to averaging over dipole orientations in the real fluorescent beads.

[3]Experiments have been performed using single molecules [58, 59], but knowing the dipole orientation remains a challenging issue.

a coordinate x (resp. y, z) inside the bead reads

$$P(x) = \frac{3}{4R^3}\left[R^2 - (R-x)^2\right]. \tag{2.12}$$

In all calculations presented here, $N_{em} = 100$, which is lower than the experimental value (few thousands emitters) for computation time considerations. To check that this value is sound, we show in Fig. 2.7 a comparison between the numerical and theoretical probability densities. Although the statistical distributions of x, y and z coordinates are not perfectly uniform, they

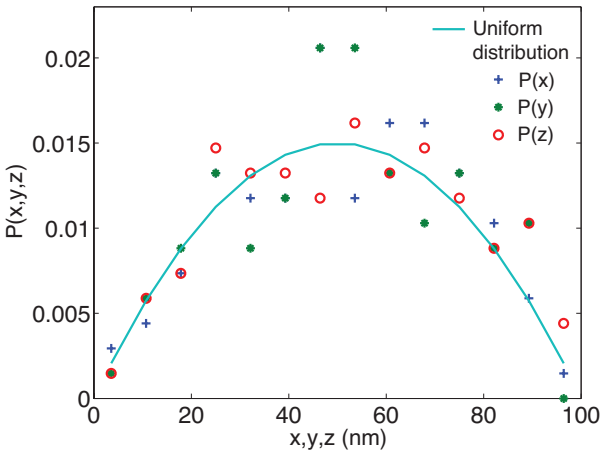


Figure 2.7: (Full green line) Analytic expression [Eq. (2.12)] of the probability density $P(z)$ for an emitter to be located at relative vertical coordinate z inside the bead; (Blue circles) Numerical estimation for $N_{em} = 100$ (corresponding to the numerical model of the bead used in all calculations presented here).

are good enough to get a rough idea of the influence of the size of the bead.

Fig. 2.8 shows two maps of the LDOS $\rho(\mathbf{r}, \omega)$ – normalized by its value in vacuum $\rho_0 = \omega^2/(\pi^2 c^3)$ – computed respectively with one pointlike emitter at a point $\mathbf{r}$ and using 100 emitters inside a bead of radius $R = 50$ nm centered at the same point $\mathbf{r}$. Counterintuitively, the averaging over a 100 nm diameter bead does not dramatically decrease the resolution of the map. It even seems that the random assembly of emitters probes smaller details than the single emitter centered in the bead. This will be discussed in details in section 2.3.2.

2.2.3 Model for the fluorescence intensity

The fluorescence intensity maps are driven both by the exciting intensity and the trade-off between radiative and non-radiative channels. We define precisely the relevant quantities for a computation of the fluorescence intensity, and expose our numerical method to compute the fluorescence enhancement. We emphasize the strong influence of the detection scheme on the

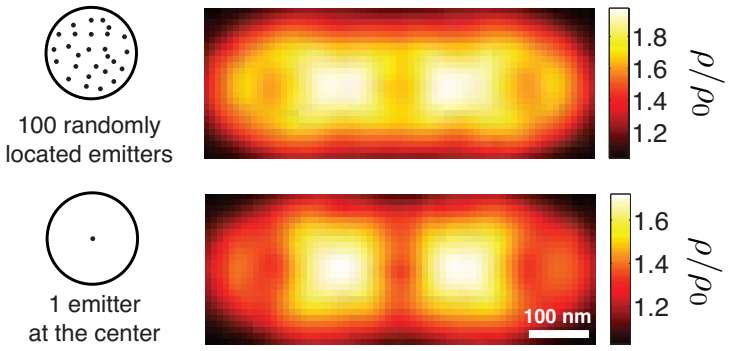


Figure 2.8: (Top) Normalized LDOS map averaged over 100 randomly located emitters; (Bottom) Normalized LDOS map computed using a pointlike emitter located at the center of the fluorescent bead. ρ_0 denotes the LDOS in vacuum.

measured signal. This illustrates the limits of the fluorescence signal for a quantitative characterization of a nanostructure.

Local intensity enhancement

Let a nanostructure be illuminated by an incident field $\mathbf{E}_0(\mathbf{r}, \omega_{\text{exc}})$. Let us denote by $\mathbf{E}(\mathbf{r}, \omega_{\text{exc}})$ the total field at point $\mathbf{r}$ in the presence of the nanostructure. The modification of the intensity due to this nanostructure is measured by the local intensity enhancement, that we define as

$$K^2(\mathbf{r}, \omega_{\text{exc}}) = \frac{|\mathbf{E}(\mathbf{r}, \omega_{\text{exc}})|^2}{|\mathbf{E}_0(\mathbf{r}, \omega_{\text{exc}})|^2}. \tag{2.13}$$

This quantity is highly sensitive to the illumination conditions. To model the laser light used in the experiment, we consider a plane-wave illumination $\mathbf{E}_0(\mathbf{r}, \omega_{\text{exc}}) = \mathbf{E}_0 \exp(-i\mathbf{k}_0.\mathbf{r})$ in the Lippmann-Schwinger equation, where $\mathbf{k}_0 = (\omega_{\text{exc}}/c)\mathbf{e}_z$ is the incident wave-vector. The propagation direction $\mathbf{e}_z$ (defined in Fig. 2.3) accounts for the illumination from below the structure. The local intensity enhancement at each position is averaged over two orthogonal polarizations $\mathbf{E}_0$ of the plane-wave, to take into account the non-polarized nature of the laser light. Finally, we take into account the finite size of the bead by computing the values of $K^2(\mathbf{r}, \omega_{\text{exc}})$ over N_{em} positions inside a 100 nm diameter sphere, exactly as in the LDOS calculations. Importantly, we do not average these values until the final calculation of the fluorescence signal.

Apparent quantum yield

For a fluorescent emitter, the emitted energy can either be radiated in the far field, or transferred non-radiatively to its local environment to be eventually absorbed. In other words, its decay rate can be decomposed into a radiative and a non-radiative part

$$\Gamma = \Gamma_R + \Gamma_{NR}. \tag{2.14}$$

The apparent quantum yield is the ratio between radiative and non-radiative channels available at the position of one emitter. It is defined as

$$\eta(\mathbf{r}, \omega_{\text{fluo}}) = \frac{\Gamma_R}{\Gamma_R + \Gamma_{NR}}. \tag{2.15}$$

It is the probability for an emitter in its excited state to eventually emit a photon in the far field. Numerically, we have explained in section 2.2.2 that the decay rate Γ of an emitter was computed by solving Eq. (2.10) under the illumination of a source dipole. From this calculation, we can deduce the electric field at any position inside the metal. The non-radiative decay rate of an emitter is proportional to the power absorbed inside the medium, and reads[4]

$$\frac{\Gamma_{NR}}{\Gamma_0} = \frac{6\pi\epsilon_0^2}{k^3|\mathbf{p}|^2}\,\text{Im}[\epsilon(\omega_{\text{fluo}})]\int_V |\mathbf{E}(\mathbf{r}', \omega_{\text{fluo}})|^2\,\text{d}^3\mathbf{r}'. \tag{2.16}$$

where Γ_0 is the decay rate of a point emitter located in the host medium. The radiative decay rate Γ_R is deduced from Γ and Γ_{NR} from Eq. (2.14).

We take into account the finite size of the fluorescent bead exactly as in the LDOS calculation. The apparent quantum yield is computed for 3 dipole orientations for each of $N_{em} = 100$ random positions of the source dipole inside a 100 nm diameter sphere. Here also, we do not average these values before the final computation of the fluorescence signal.

In the experiment, the collection is not performed over 4π steradian, but is limited to a finite solid angle Ω. To model this effect, we denote by $\Gamma_R(\mathbf{u})$ the radiative contribution to the decay rate that corresponds to photons collected in a unit solid angle around direction $\mathbf{u}$. This quantity is proportional to the power radiated in a unit solid angle in this direction (this will be important for the numerical calculation). $\Gamma_R(\mathbf{u})$ and Γ_R are connected via

$$\Gamma_R = \int_{4\pi} \Gamma_R(\mathbf{u})\text{d}\Omega. \tag{2.17}$$

We define the directional apparent quantum yield as

$$\eta(\mathbf{r}, \omega_{\text{fluo}}, \mathbf{u}) = \frac{\Gamma_R(\mathbf{u})}{\Gamma_R + \Gamma_{NR}}. \tag{2.18}$$

Integrating $\eta(\mathbf{r}, \omega_{\text{fluo}}, \mathbf{u})$ over the solid angle Ω covered by the detector yields the probability, once an emitter is excited, to detect a photon on the avalanche photodiode.

Numerically, from the resolution of the Lippmann-Schwinger equation (under dipole illumination), we know the electric field at any point in space. One can compute rigorously the power radiated by the source dipole in the far-field in a unit solid angle using the far-field expression of the Green function of vacuum (see Appendix A). We can deduce the change in $\Gamma_R(\mathbf{u})$ due to

[4]See Appendix A. The host medium is vacuum here, which explains why $k = k_h$.

the environment by

$$\frac{\Gamma_R(\mathbf{u})}{\Gamma_0} = \frac{3}{8\pi}\,\frac{\epsilon_0^2}{\omega_{\text{fluo}}k^3|\mathbf{p}|^2}\,\Big|\Big\{\mu_0\omega_{\text{fluo}}^2\,[\mathbf{I}-\mathbf{u}\otimes\mathbf{u}]\,\mathbf{p} + k^2\int_V \{\epsilon(\omega_{\text{fluo}})-1\}\,e^{-ik\mathbf{u}.\mathbf{r}'}\,[\mathbf{I}-\mathbf{u}\otimes\mathbf{u}]\,\mathbf{E}(\mathbf{r}',\omega_{\text{fluo}})\,\mathrm{d}^3\mathbf{r}'\Big\}\Big|^2, \tag{2.19}$$

where $\mathbf{I}$ is the unit dyadic, and $k = \omega_{\text{fluo}}/c$.

Note that integrating $\Gamma_R(\mathbf{u})$ over 4π steradians, one can retrieve the value of Γ_R. We have used this second way of computing Γ_R as a probe of numerical errors. In all presented calculations, the two methods are in excellent agreement for at least one position of the source dipole illumination. The details of this computation can be found in Appendix E.

Fluorescence intensity

The fluorescence intensity is the number of photons per second detected in the experimental setup. For emitters far from saturation, the fluorescence intensity signal reads [68]

$$S = C\left[\int_\Omega \eta\,(\mathbf{r},\omega_{\text{fluo}},\mathbf{u})\,\mathrm{d}\Omega\right]\sigma(\omega_{\text{exc}})K^2(\mathbf{r},\omega_{\text{exc}})I_{inc}. \tag{2.20}$$

In this equation, $\eta(\mathbf{r},\omega_{\text{fluo}},\mathbf{u})$ is the directional apparent quantum yield for a detection in direction $\mathbf{u}$, and Ω is the solid angle of the detection objective. The constant C is a calibration parameter of the detection (that accounts for transmissivity of filters, detector efficiency, ...), $\sigma(\omega_{\text{exc}})$ is the absorption cross-section of the bare fluorescent beads, I_{inc} is the incident laser intensity and $K^2(\mathbf{r},\omega_{\text{exc}})$ is the local-intensity enhancement factor.

The quantity that drives the contrast of fluorescence intensity maps is the *fluorescence enhancement factor*, defined as

$$F(\mathbf{r},\omega_{\text{fluo}},\omega_{\text{exc}}) = \left[\int_\Omega \eta\,(\mathbf{r},\omega_{\text{fluo}},\mathbf{u})\,\mathrm{d}\Omega\right]K^2(\mathbf{r},\omega_{\text{exc}}). \tag{2.21}$$

This is the quantity that we will compute to understand the fluorescence intensity maps. Let us sum up the numerical procedure.

- We randomly choose $N_{em} = 100$ positions inside a 100 nm diameter sphere.
- For one point of the fluorescence map, we solve the Lippmann-Schwinger equation under plane-wave illumination (exciting laser beam) to compute $2 \times N_{em}$ values of the local intensity enhancement $K^2(\mathbf{r},\omega_{\text{exc}})$ corresponding to N_{em} emitter positions and 2 orthogonal polarizations of the incident field. Then, we solve the Lippmann-Schwinger equation under a source dipole illumination to compute $3\times N_{em}$ values of the directional apparent quantum yield $\eta(\mathbf{r},\omega_{\text{fluo}},\mathbf{u})$ corresponding to N_{em} emitter positions and 3 orthogonal orientations of the source dipole.

- We obtain $3 \times 2 \times N_{em} = 600$ values of the fluorescence enhancement factor $F(\mathbf{r}, \omega_{\text{fluo}}, \omega_{\text{exc}})$ corresponding to N_{em} emitter positions, 3 orthogonal orientations of the source dipoe and 2 orthogonal polarizations of the incident field. We average all these values to deduce $F(\mathbf{r}, \omega_{\text{fluo}}, \omega_{\text{exc}})$.

- We repeat the procedure for each point of the map[5].

Influence of the detection setup on the fluorescence intensity measurement

The microscope objective does not detect all photons emitted by the fluorescent bead, but only those emitted in a finite solid angle Ω. To observe the influence of this limitation on the fluorescence signal, we show in Fig. 2.9 two different computations of the fluorescence enhancement factor F. The first one corresponds to an ideal experiment where all photons emitted in the far

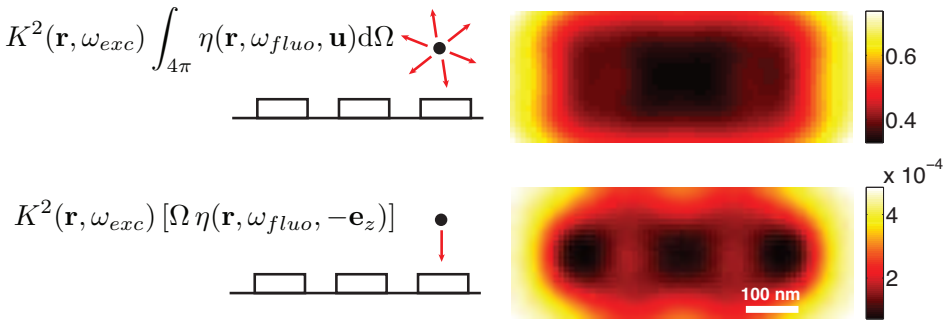


Figure 2.9: (Top) Fluorescence signal integrated over 4π steradians; (Bottom) Fluorescence signal in a small solid angle $\Omega = 10^{-2}$ steradian around direction $-\mathbf{e}_z$ pointing towards the detector.

field would be detected. It is obtained by performing the integration in Eq. (2.21) over $\Omega = 4\pi$ steradians. In the second one, the directional quantum yield in direction $\mathbf{u} = -\mathbf{e}_z$ is considered constant over a small solid angle $\Omega = 10^{-2}$ steradians. The direction $-\mathbf{e}_z$ corresponding to a detection from below the sample, like in experiments. Integrating over a solid angle corresponding to the real setup is perfectly possible numerically. Though, as we will see in section 2.3.1, this crude model gives a very satisfying agreement with experiments. Since our purpose is to find the simplest model to understand the measurements, we have limited ourself to this approach in all calculations presented here.

Strikingly, the two maps have a very different structure. The influence of the detection scheme on the fluorescence intensity was already emphasized in Ref. [69]. It is due to the non-isotropical radiation pattern of the nanosource placed in the vicinity of the nanostructure. A precise description of the influence of nanoantennas on fluorescence emission directivity can be

[5]Note that the relative positions of the emitters inside the bead are the same for every point in the map.

found in Ref [68]. In particular, enhanced directivity in the radiation pattern of quantum dots was reported using a Yagi-Uda shaped nanoantenna [1]. This effect is a strong limitation for the quantitative characterization of nanostructures using fluorescence intensity. The LDOS is a more robust quantity to measure, since a lifetime measurement is independent on the detection scheme. It only depends on the absolute value of the LDOS at the fluorescent source position.

2.3 Numerical results

We present here the numerical maps that were computed using the model described previously to understand the experimental ones. These maps are in very good agreement with experimental data. Our method allows us to go further and model the fluorescent beads to try to understand the experimental resolution in the LDOS maps, that looks better than the size of the sources.

2.3.1 Numerical maps of the LDOS and fluorescence intensity

We show in Fig. 2.10 the numerical maps of the fluorescence enhancement factor and the normalized LDOS computed according to the model presented in section 2.2. The experimental

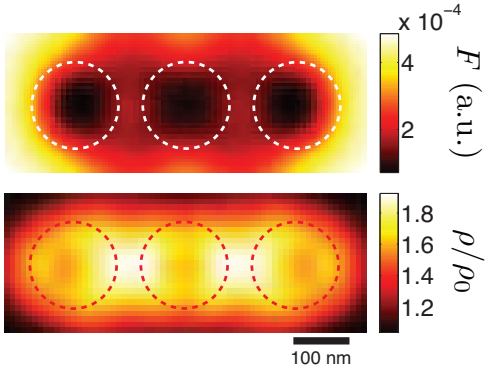


Figure 2.10: (Top) Fluorescence enhancement factor $F(\mathbf{r}, \omega_{\text{fluo}}, \omega_{\text{exc}}) = \eta(\mathbf{r}, \omega_{\text{fluo}}, -\mathbf{e}_z)K^2(\mathbf{r}, \omega_{\text{exc}})$ expressed in arbitrary units; (Bottom) LDOS $\rho(\mathbf{r}, \omega_{\text{fluo}})$ normalized by its value in vacuum ρ_0. The dashed lines represent the contours of the nanoantenna. As in experiments, $\lambda_{fluo} = 575\,\text{nm}$ and $\lambda_{exc} = 605\,\text{nm}$. The distance between the bottom of the bead and the top of the nanoantenna is set to $d = 20\,\text{nm}$ and the bead diameter equals 100 nm.

fluorescence intensity map (Fig. 2.6) is well recovered by the computed directional fluorescence enhancement factor $F(\mathbf{r}, \omega_{\text{fluo}}, \omega_{\text{exc}})$. The fluorescence intensity is reduced by a factor of the order of 3 on top of the disks. The agreement is almost quantitative.

In the experimental map, the LDOS increases by about 30% in three regions presenting an extension of about 60 nm each and separated by 100 nm. The two regions located between the gold disks are predicted by the numerical simulations. As in the case of the fluorescence

intensity map, numerical and experimental data are in almost quantitative agreement regarding the expected change of the decay rate in the region between the disks with respect to a region far away from the nanoantenna. The presence of the third lateral region of enhanced LDOS in the experimental map is more speculative. The numerical simulations predict the presence of two such regions of enhanced LDOS, on the external sides of the nanoantenna. A possible explanation for this is an asymmetry of the gold structure, caused for example by a defect of the lift-off process, that would translate in an asymmetry of the structured the electromagnetic file on the surface of the nanoantenna. Numerical calculations with asymmetric shaped nanoantennas have been done and produce similar asymmetries in the LDOS images. However, since the exact shape of the nanoantenna is not accessible at the required level of resolution, having an exact matching between theory and experiment is a very speculative task and the discussion is therefore limited here to a comparison between the experimental results with numerical simulations made on an ideal antenna formed by three regularly spaced circular disks.

2.3.2 Resolution of the LDOS maps

One interesting feature of both the experimental and numerical LDOS maps is that both seem to exhibit variations on scales well below 100 nm, the size of the fluorescent bead. To explain this phenomenon, already observed in [64], we compare the contribution to the decay rate of the emitters located in the lower and upper half of the bead. Figure 2.11 shows the LDOS maps averaged respectively over 100 emitters located at random positions inside a 100 nm diameter bead, over the emitters located in the lower half of the bead and over the emitters located in its upper half. Each map is normalized by the value of the LDOS in vacuum to allow for the comparison between the maps. Every map is computed for a distance $d = 20\,\text{nm}$ between the bottom of the bead and the top of the trimer. A detailed observation allows us to assert that the resolution of the LDOS map is not limited by the size of the bead. Indeed, the similarity between the top and bottom maps clearly shows that the measured LDOS is driven by the emitters situated on the lower half of the bead. The two hot spots which are visible on the right and on the left side of the nanoantenna are smeared out when considering only the contribution of the emitters populating the upper part of the sphere. More insight can be given by plotting the section of the LDOS maps along the lines drawn in every map. The obtained profiles are shown in Fig. 2.12. Each curve is normalized by the maximum value of the corresponding map ρ_{max}, in order to quantify the contrast of each hotspot. The lateral hot-spot is clearly resolved when the LDOS signal is averaged on the emitters located on the bottom of the sphere or over all the sphere, while it is washed out when the signal is averaged over the top of the sphere. Therefore the resolution of this detail is clearly due to the bottom emitters. Consequently, the effective resolution is not limited by the size of the bead but is smaller and in the case presented in this thesis is of the order of 50 nm.

It is very instructive to consider the influence of the distance between the bead and the

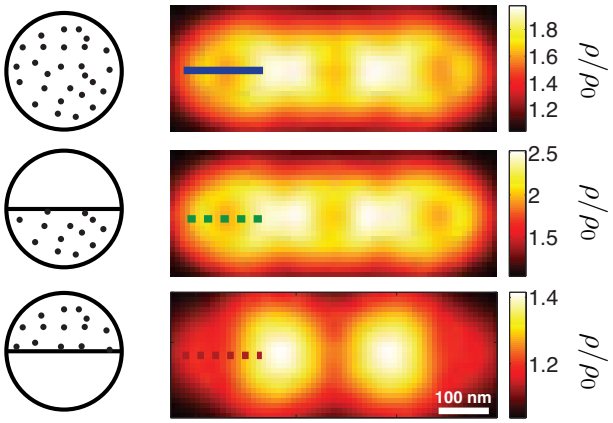


Figure 2.11: Computed normalized LDOS maps a distance $d = 20\,\text{nm}$ between the bottom of the bead and the top of the trimer. (Top) Average over 100 emitters randomly located in the bead; (Middle) Contribution of the 48 emitters located in the lower half of the bead; (Bottom) Contribution of the 52 emitters located in the upper half of the bead. $\lambda_{exc} = 560\,\text{nm}$; $\lambda_{fluo} = 605\,\text{nm}$. Diameter of the bead: 100 nm.

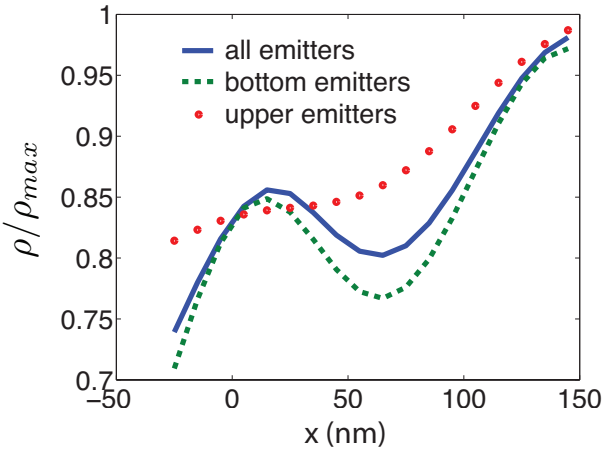


Figure 2.12: Section view of the maps shown in Fig. 2.11 along the lines shown on the maps. Note that in this case the LDOS has been normalized by the maximum value of each map ρ_{max} to quantify the contrast of the image.

nanostructure on the resolution. Subwavelength details are exponentially decaying with the distance to the sample [8]. Hence, the closer the emitter, the better the resolution is expected to be. We show in Fig. 2.13 the maps and profiles of the LDOS computed exactly as in Figs. 2.11 and 2.12 but for a distance $d = 50\,\text{nm}$ between the bottom of the bead and the top of the

nanoantenna. A comparison between Figs. 2.11 and 2.13 confirms that the smallest details

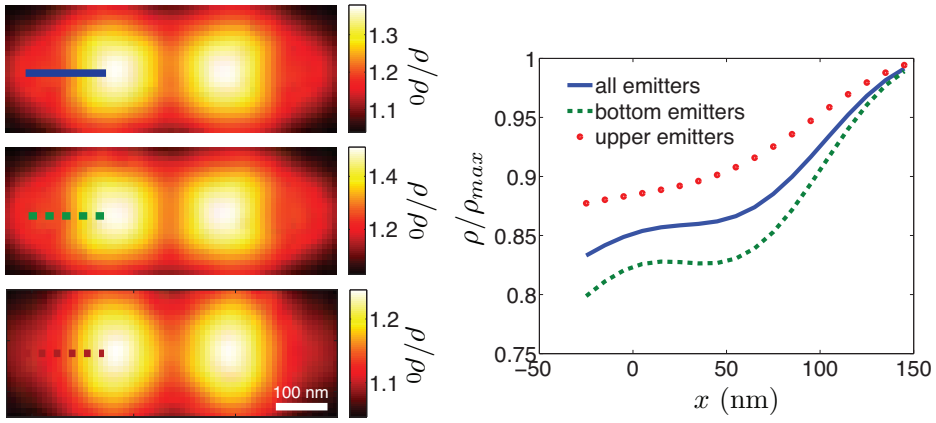


Figure 2.13: Map and profile of the LDOS computed exactly as the ones of Figs. 2.11 and 2.12, for a distance between the bottom of the bead and the top of the sample equal to $d = 50\,\text{nm}$.

(such as for example the two LDOS hot spots visible on the right-hand and left-hand sides of the nanoantenna) are washed out when the distance of the bead to the sample surface increases. Since these details are visible on the experimental map, this study confirms that the real distance between the bottom of the probe and the sample surface is of the order of 20 nm. Interestingly, at $d = 50\,\text{nm}$, even if a non-monotonic behavior is observed in the profiles, the bottom emitters are too far away from the sample surface and the smallest details are washed out. The high resolution compared to the size of the bead is fundamentally a near-field effect and can only be obtained at very subwavelength distances to the sample.

2.4 Conclusion

To sum up, we have developed a numerical model based on the Lippmann-Schwinger equation to identify the important phenomena and understand the maps that were measured in the real experiment at Institut Langevin. Our numerical results are in great agreement with experimental data. In particular, we have shown that the finite size of the bead has a positive influence on the resolution of the maps, clarifying a phenomenon that was first observed in [64]. We have also emphasized the sensitivity of the fluorescence signal to the angular aperture of the detection setup. The LDOS, as opposed to the fluorescence intensity, is robust and contains intrinsic quantitative informations about the optical near-field properties of the nanoantenna.

As a perspective, an ingredient is missing in our numerical model and would be very interesting to take into account: the influence of the substrate. In all our calculations, the metallic nanoantenna (as well as the disordered metallic films in the next chapter) are lying in vacuum.

Even if we do not believe this will fundamentally change the trends of our results, it would help being even more quantitative. In the volume integral method, taking this effect into account is possible, by replacing the Green function of vacuum in the Lippmann-Schwinger equation by the Green function of the semi-infinite space described by the dielectric constant of glass.

Another perspective is the experimental measurement of the radiative and non-radiative decay rate of a dipolar emitter near a nanoantenna. This is a very challenging issue, that should be the subject of future work at Institut Langevin. Our numerical tool is already able to compute these quantities, and can be used to save some time by predicting the interesting measurements.

Chapter 3

Spatial distribution of the LDOS on disordered metallic films

Contents

3.1 Simulation of the growth of the films 51
3.1.1 Numerical generation of disordered metallic films 51
3.1.2 Percolation threshold 52
3.1.3 Apparition of fractal clusters near the percolation threshold 53
3.2 Spatial distribution of the LDOS on disordered films 57
3.2.1 Statistical distribution of the LDOS 57
3.2.2 Distance dependence of the LDOS statistical distribution 59
3.2.3 LDOS maps and film topography 61
3.3 Radiative and non-radiative LDOS 62
3.3.1 Definition 62
3.3.2 Statistical distributions of the radiative and non-radiative LDOS 63
3.3.3 Distance dependence of the radiative and non-radiative LDOS distributions 63
3.4 Conclusion 64

By evaporating thin layers of noble metal on a glass substrate, one obtains structures with very peculiar optical properties. These structures are called *disordered metallic films*. Depending on the surface filling fraction, three regimes can be identified, as illustrated in Fig. 3.1.

- For low filling fraction, the films look pink to the eye. The local structure shows that these films are mainly composed of isolated gold particles. The color is well explained by the plasmon resonances of individual particles.

- For high filling fraction, the films look green to the eye. This color is that of a thin continuous layer of gold (transmitted light is responsible for the green color). It is well explained by the spectral dependence of the Fresnel transmission factors.

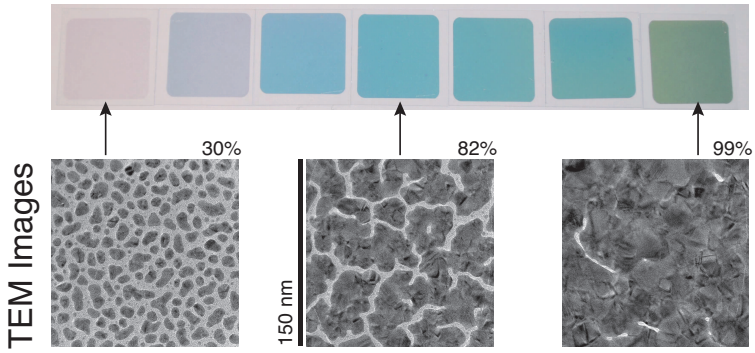


Figure 3.1: (Top) Naked eye pictures of disordered gold films deposited on a white substrate. From left to right, the gold filling fraction is increasing from 30% to 99%; (Bottom) Transmission Electron Microscope (TEM) image of the films for three different gold filling fractions.

- In between these two extreme regimes, the films look blue to the eye. This regime is found close to the electric percolation, which occurs when a continuous metallic path appears between two sides of the sample. In this regime, the films are known to exhibit fractal geometry, and to support deep subwavelength areas with high intensity of the electric field, called *hot spots* [19, 70, 71]. These hot spots are responsible for an absorption plateau in the red and near infrared [72], and have an influence on the macroscopic optical properties of the films [73], as illustrated by the blue color in Fig. 3.1.

In the fractal regime (near the percolation threshold), these systems are resonant on a broadband spectrum. Many potential applications can benefit from this property, e.g. in photodetection or photovoltaics. Moreover, basic experiments in nanophotonics can be though of using the disordered films as platforms. As we have seen in Chap. 2, the LDOS and its radiative and non-radiative contributions are the fundamental quantities that drive photon absorption of the radiation of emitters in the vicinity of a nanostructure. A characterization as complete as possible of disordered films based on the LDOS is a promising path both towards applications and fundamental experiments. Recently, at Institut Langevin, V. Krachmalnicoff and coworkers have measured LDOS distributions in the near field of disordered films, and have shown that enhanced spatial LDOS fluctuations occur in the regime dominated by fractal clusters compared to the "isolated particle" regime (low filling fractions) [3]. These experiments were the motivation at the start of my PhD to develop a numerical method to compute the LDOS in the near field of disordered films. Although an exact numerical study has been reported recently using a FDTD (finite-difference time-domain) scheme [74], all theoretical and numerical results until then were based on approximations, such as mean-field theories [75] or quasi-static calculations [76, 77].

Here, we present a method to simulate the growth of disordered films numerically, with realistic fractal properties near the percolation threshold. The volume integral method we

have presented in Chap. 2 offers an exact 3D resolution of the Maxwell equations in order to compute the field scattered by the films generated numerically. In particular, it takes into account retardation, polarization and near-field interactions. We recover the enhanced LDOS fluctuations observed experimentally in the fractal regime. A study of the distance dependence of the LDOS statistical distribution shows a nearly quantitative agreement between experiments and numerics. By analyzing this data qualitatively, we deduce an order of magnitude of the typical spatial extent of a hot spot, in good agreement with near-field intensity observations [19, 70]. We use numerical simulations to go further in the characterization of the films. In particular, we compare LDOS maps to the films topography and show that the appearance of hot-spots in the fractal regime comes from a complex collective interaction. Finally, we study the spatial distributions of the radiative and non-radiative LDOS. We show that the hot spots observed in the fractal regime are dominated by non-radiative channels, and study quantitatively the distance dependence of the trade-off between radiative and non-radiative LDOS.

The results presented here have been published in Photonics and Nanostructures: From Fundamental to Applications [78] and Optics Letters [57].

3.1 Simulation of the growth of the films

Our first goal is to generate numerically disordered metallic films that have the same properties as the real ones. Here, we describe the algorithm we have implemented. It was first proposed in Ref. [21], and is based on a Kinetic Monte-Carlo algorithm (KMC). We show that fractal properties of experimental films are recovered in the numerical results, which is an evidence of the reliability of the approach.

3.1.1 Numerical generation of disordered metallic films

A detailed description of the algorithm is given in Appendix D. The idea is to randomly deposit 5 nm gold particles on a square grid via an iterative algorithm, and let the particles diffuse under the influence of an interaction potential until a stable geometry is reached. At every iteration of the algorithm, we randomly choose either to deposit a new particle (probability p_0) or to make a particle on the grid jump to a more stable neighbour site (probability p_{ij} to diffuse from site i to site j). Using the normalization $p_0 + \sum_{i,j} p_{ij} = 1$, we only need to pick a random number out of $[0, 1]$ to determine the relative weight of each process. More precisely, the probability to deposit a particle reads[1] $p_0 = aN_{dep}F$, where N_{dep} is the number of particles that remains to be deposited in order to reach the prescribed filling fraction, and F is a constant (with dimension s^{-1}) modeling the experimental deposition rate. The probability for a particle located on site i to jump to the neighbor site j reads (see footnote 1)

$$p_{ij} = b \exp[-\Delta E_{ij}/(k_B T)], \tag{3.1}$$

[1] a and b are two constants determined by the normalization.

where k_B is the Boltzmann constant, T the temperature of the surface and ΔE_{ij} the activation energy barrier. Computing ΔE_{ij} is a complex issue for atoms [79, 80], and is not possible from first principles for nanometer size particles. In the present approach, we have chosen to deal with a rescaled atomic potential that renormalizes the energy barrier in order to apply to a nanoparticle. This potential is given by the following expression, based on a tight-binding second moment method [81]

$$E_i = A \sum_{j \neq i} e^{-p(r_{ij}/r_0 - 1)} - B \left[\sum_{j \neq i} e^{-2q(r_{ij}/r_0 - 1)} \right]^{1/2} . \tag{3.2}$$

In this expression, r_0 is the size of one particle (that defines the scaling), r_{ij} the distance between two sites i and j and A, B, p and q are constants that were tabulated for atoms [81]. E_i is the rescaled "atomic" potential of a particle located on site i, which is allowed to jump to the neighbor site j if $E_i > E_j$. We assume that the activation energy barrier reads

$$\Delta E_{ij} = \alpha (E_i - E_j), \tag{3.3}$$

where α is a positive dimensionless adjustable parameter taking into account the influence of the substrate and the scaling. The iterative deposition process is stopped when all particles have been deposited (so that the prescribed filling fraction has been reached) and no particle can move to a more stable site.

Three examples of films are shown in Fig. 3.2, with a lateral size of 375 nm and three different surface filling fractions f.



Figure 3.2: Numerically generated gold films for three different filling fractions f (gold is represented in dark). The parameters for the computation are: $T = 300\,\mathrm{K}$, $\alpha = 2 \times 58.10^2$, $F = 1014\,\mathrm{s}^{-1}$, $A = 0.2061\,\mathrm{eV}$, $B = 1.79\,\mathrm{eV}$, $p = 10.229$, $q = 4.036$.

3.1.2 Percolation threshold

When the filling fraction is high enough, a continuous metallic path appears between two sides of the sample. This is the *percolation phenomenon*, and the filling fraction corresponding to

the transition is called the percolation threshold. To determine roughly this filling fraction in the numerical films, we have implemented the Hoshen-Kopelman algorithm to label the clusters of the films [82]. In Figure 3.3, we show four films generated for different filling fractions, in which each cluster has been identified by one color. We observe that percolation occurs between $f = 50\%$ and $f = 60\%$.

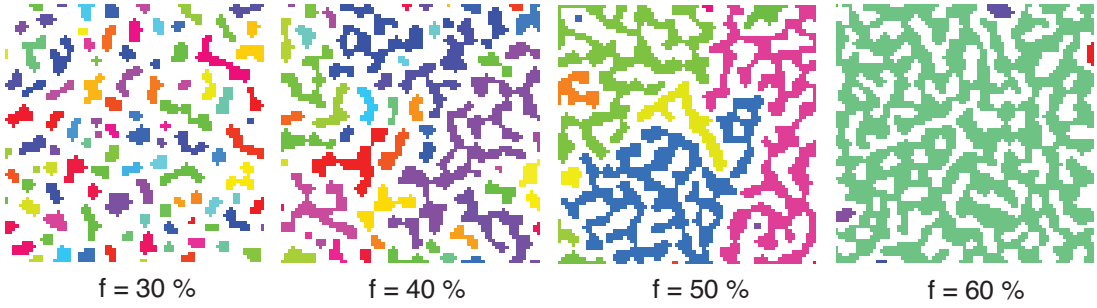


Figure 3.3: Disordered films generated numerically for four filling fractions between $f = 30\%$ and $f = 60\%$. Clusters have been labelled using the Hoshen-Kopelman algorithm, one color identifies one cluster. The films with filling fractions $f = 50\%$ and $f = 60\%$ are percolated.

3.1.3 Apparition of fractal clusters near the percolation threshold

One can see in Fig. 3.3 that for a filling fraction $f = 50\%$, clusters with complex shapes appear. Disordered metallic films are known to support fractal clusters near the percolation threshold [83]. This fractality has been correlated to the apparition of localized modes [3]. Here, we give the basic mathematical definitions to understand fractality and self-similarity. Based on the von Koch flake example, we show that the percolation clusters have fractal contours, characterized by a specific relation between their perimeter and surface. The numerically generated films exhibit exactly the same fractal features as the real ones.

Fractality and self-similarity

The definitions given in this section are freely inspired from B. Mandelbrot's book on fractals [84], and should not be understood as general definitions. Our aim is not to make a general description of the fractal geometry, but to give an intuitive picture of the connection between self-similarity and fractality in the case of disordered films.

Let $r \in \mathbb{R}_+^*$ and $P \in \mathbb{N}^*$. Let $[x_1, x_2]$ a segment of $\mathbb{R}$ and f a real function defined on $[x_1, x_2]$. f is *self-similar* on $[x_1, x_2]$ if it satisfies

$$\forall x \in [x_1, x_2], f(x) = Pf(rx). \tag{3.4}$$

We denote by r the *homothety coefficient* and P the *number of parts*. We admit the following equivalence

$$\forall x \in [x_1, x_2], f(x) = Pf(rx) \Leftrightarrow \exists \lambda, \forall x \in [x_1, x_2], f(x) = \lambda x^D \tag{3.5}$$

where D is the *homothety dimension*, defined as

$$D = \frac{\log P}{\log (1/r)}. \tag{3.6}$$

Hence, the self-similar functions are the power-law functions. We call *fractal* on an interval $[x_1, x_2]$ any self-similar function which homothety dimension is *non-integer*. We call *fractal dimension* (or Haussdorf dimension) the homothety dimension of a fractal function[2].

Fractality of the von Koch curve

The von Koch curve is defined as the limit when n tends to infinity of the serie defined in Fig. 3.4. Let us denote by a, and call linear extent of the von Koch curve, the length of its first iteration.

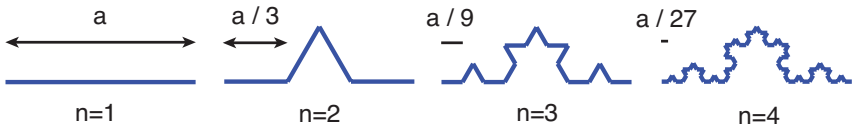


Figure 3.4: First four iterations of the von Koch curve.

Let us denote by G the length of the unit segment that is used to draw it. Let $M(a, G)$ the mass of the von Koch curve, defined as the number of unit segments that compose it. The mass of the von Koch curve is a self-similar function, since its satisfies the relation

$$M(a, G) = 4M(a/3, G). \tag{3.7}$$

This self-similarity is illustrated in Fig. 3.5. The von Koch curve of linear extent a (blue curve) is composed of four von Koch curves of linear extent $a/3$ (red curve) arranged in the same configuration. In a self-similar curve, "the ensemble resembles the unit bricks". Hence, the von Koch curve is a fractal ensemble with dimension

$$D = \frac{\log 4}{\log 3} \approx 1.262. \tag{3.8}$$

Using Eq. (3.5), for a fixed size G of the unit segment, M can be expressed as

$$M(a, G) = \lambda a^D. \tag{3.9}$$

[2]A self-similar function is fractal when its number of parts P is a non-integer power of the inverse of its homothety coefficient $1/r$.

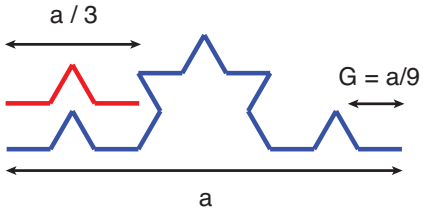


Figure 3.5: Illustration of the self-similarity of the von Koch curve.

Let us stress the physical signification of the unit segment size G. It is related to the scale used to observe a physical phenomenon. Depending on the observation scale G, a same object can have different dimensions, integer or not. In his book [84], B. Mandelbrot takes the example of a base-ball ball. If we observe it at the scale of a whole stadium, it is basically a zero-dimensional object, i.e. a point. When we get closer to the size of the ball, it becomes a three-dimensional object, since its more or less spherical shape appears. Now if we get even closer, we will at some point reach the scale of the strings that compose the ball, and we will now consider it as a one-dimensional object.

In this section, we consider self-similarity properties for a fixed unit segment length G. This means that we do not change the observation scale. As we shall see, the fractality of the percolation clusters of disordered films is observed for an observation scale of the order of a few nanometers.

Surface and perimeter - The von Koch flake

The von Koch flake with linear extent a is composed of three von Koch curves of linear extent a as shown in Fig. 3.6. The perimeter of the von Koch curve $P(a, G)$ is defined from the mass of the von Koch curve as

$$P(a, G) = 3G\, M(a, G). \tag{3.10}$$

For a given length of the unit segment G, the perimeter of the von Koch flake satisfies the same self-similarity relation Eq. (3.7) as the mass of the von Koch curve. Hence, it has a fractal shape with dimension $D = \log 4/\log 3$. Using Eq. (3.5), one can show that $P(a, G)$ satisfy

$$P(a, G) \propto a^D. \tag{3.11}$$

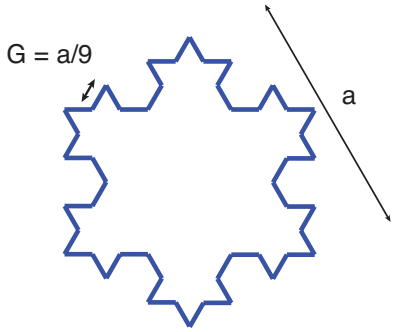


Figure 3.6: von Koch flake of linear extent a drawn using unit segments of length $G = a/9$.

Let us denote by $S(a, G)$ the area inside the von Koch flake of linear extent a drawn with unit segments of length G. Summing a geometric series under the assumption $G \ll a$ yields[3]

$$S(a, G) \propto a^2. \tag{3.12}$$

The surface of the von Koch flake is not fractal. Though, for a sufficiently small length G of the unit segment, the perimeter fractality can be observed by comparing the surface and perimeter of flakes for various linear extent

$$P \propto S^{D/2}. \tag{3.13}$$

Apparition of fractal clusters near the percolation threshold

The fractality of the clusters appearing near the percolation threshold on disordered metallic films is analog to that of the von Koch curve. To check this feature, we have generated 100 films with filling fractions $f = 20\%$ and $f = 50\%$. We have extracted the perimeter and surface of all clusters, using the Hoshen-Kopelman algorithm. The surface was defined as the number of pixels, and the surface as the number of empty neighbor pixels[4]. We show in Fig. 3.7 the location of each cluster in a perimeter/surface diagram, in a log-log scale (each blue cross corresponds to one cluster), for both filling fractions. One clearly sees on Fig. 3.7 that for the low-filling fraction ($f = 20\%$), the perimeters and surfaces of the clusters scale as

$$P \propto S^{1/2}, \tag{3.14}$$

[3] According to the interpretation of G exposed before, this means that the observation scale is small enough to observe the details of the structure.

[4] Note that in these images, the observation scale G is the lateral size of one pixel, i.e. 5 nm.

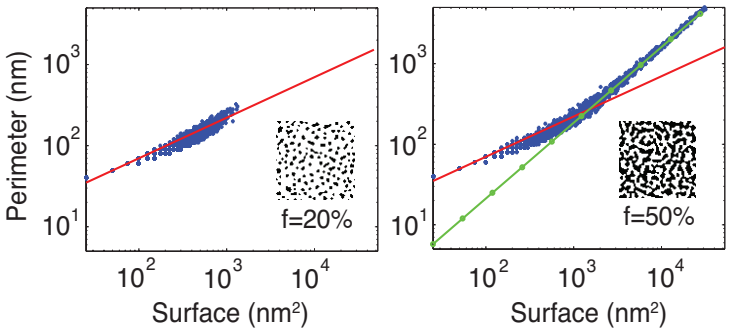


Figure 3.7: Distribution in a perimeter/surface diagram of the clusters taken out from 100 numerically generated films. Left: filling fraction $f = 20\%$. Right: filling fraction $f = 50\%$. The red solid line and green dotted line are guides for the eye, corresponding to $P = 7 \times S^{1/2}$ and $P = 0.28 \times S^{1.88/2}$, respectively.

which is the expected behavior for a euclidian cluster (perimeter dimension $D = 1$). For $f = 50\%$, a new collection of clusters appear, which perimeters and surfaces satisfy

$$P \propto S^{1.88/2}, \tag{3.15}$$

corresponding to a fractal dimension $D = 1.88$. This value is consistent with experimental observations [83, 66]. This result, already shown in Ref. [21], is a strong evidence that the geometrical features of real films are well described by the numerical generation method.

The contour fractal dimension satisfies $1 \leq D \leq 2$ because of the fundamentally two-dimensional approach used for its characterization. Experimental studies of the surface/volume relation taking into account the three-dimensional roughness of the films exist. A fractal dimension $D = 2.26$, satisfying $2 \leq D \leq 3$, has been reported [85]. Although this approach is more complete, it does not contradict the method used here. The very good results we obtain seem to indicate that the most important physical phenomenon are comprised in the 2D geometrical properties of the films.

3.2 Spatial distribution of the LDOS in the near field of disordered films

3.2.1 Statistical distribution of the LDOS

Measurements of the LDOS statistical distribution on top of disordered metallic films were performed at Institut Langevin by Valentina Krachmalnicoff and coworkers [3, 57]. The principle of this experiment is to deposit a thin silica layer (a few tens of nanometers) on top of a disordered film and to spin-coat fluorescent beads at random positions on the surface of this layer (that we will call *spacer*). Addressing each bead with a confocal microscope and recording

the arrival-time histogram as described in chapter 2, one can retrieve the statistical distribution of the LDOS at a given distance from the film. Fig. 3.8(a) is taken from Ref [3] and shows the experimental statistical distribution of the orientation-averaged decay rate[5] measured on two disordered films, respectively in the low-filling fraction and in the fractal regimes. For both distributions, the spacer thickness was 40 nm, and the measurement was performed using 25 nm-diameter beads. To get more insight on the experimental results, we have developed the following

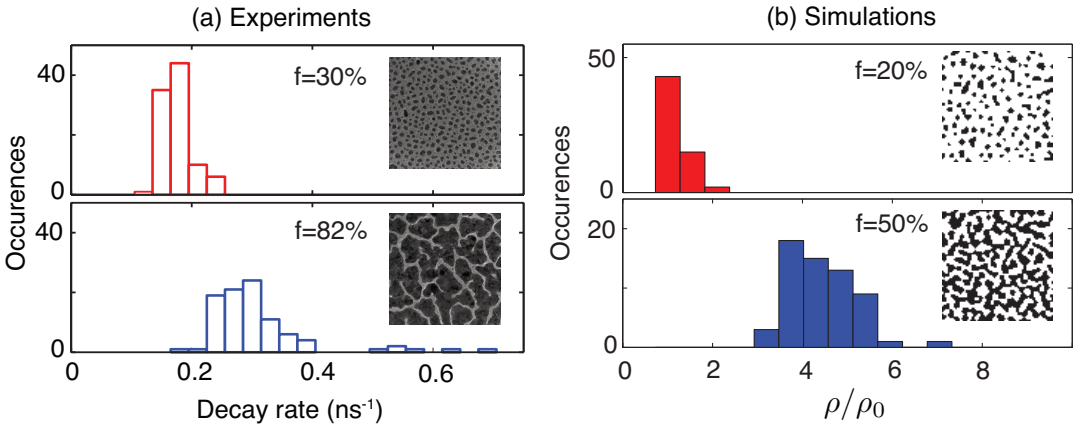


Figure 3.8: (a) Experimental spatial distribution of the orientation-averaged decay rate on top of two real films with respective filling fractions $f = 30\%$ and $f = 82\%$. The beads have a 25 nm diameter, and an emission wavelength $\lambda_{\text{fluo}} = 607$ nm. The spacer thickness is 40 nm; (b) Spatial distribution of the normalized LDOS at 40 nm distance of two numerically generated films with respective filling fractions $f = 20\%$ and $f = 50\%$. The wavelength is $\lambda_{\text{fluo}} = 780$ nm. The films size is set to 375 nm. The volume is discretized into unit cells of size $\Delta = 2.5$ nm.

numerical method. We consider that the films generated following the procedure described in section 3.1 are 5 nm thick. We solve the Maxwell equations in 3D using the volume integral method described in Chap 2. The whole structure is discretized into cubic unit cells of lateral size Δ[6]. Using this method, we are able to compute the LDOS at any point in space. For two filling fractions corresponding to the regimes studied experimentally, we have generated 60 films. We have computed the LDOS at 40 nm from the center of each film and gathered the results in a histogram. Note that our purpose here is not to describe quantitavely the experiment but to observe the same qualitative trends, which explains the different filling fractions and emission wavelengths chosen in numerics. Fig. 3.8(b) shows the corresponding LDOS distributions.

The qualitative agreement between experiments and simulation is very good. Two major differences are observed as one goes from the low-filling fraction regime to the fractal regime.

[5]The decay rate of an emitter, averaged over its dipole orientation, is proportional to the LDOS, see Chap. 2, section 2.1.1.

[6]Note that the smaller the distance to the film, the faster the electric field spatial variations and the smaller the unit cell size Δ necessary to obtain a satisfying numerical convergence.

- The mean value of the LDOS increases.
- The fluctuations of the LDOS are enhanced. In particular, very high values of the LDOS (up to three times the average value) are observed.

The enhanced fluctuations of the LDOS in the fractal regime are connected to the apparition of spatially localized modes, as will be discussed later. Let us comment on the difference between the experimental and numeric parameters in Figure 3.8. First, the wavelength $\lambda_{\text{fluo}} = 780\,\text{nm}$ in the simulations was chosen because the fluctuations are known to be stronger in this regime [72, 20]. This is confirmed in our simulations (see Fig. 3.12). Then, the correspondence between the appearance of fractal clusters on disordered films and the filling fraction is highly dependent on the experimental conditions (substrate, temperature, ...). In the numerical model, we have chosen the filling fractions $f = 20\%$ and $f = 50\%$. We have checked in section 3.1 that they correspond respectively to a regime where fractal clusters do not exist and to another where they clearly appear, thus defining regimes that are similar to the regimes $f = 30\%$ and $f = 82\%$ used experimentally. A detailed study of the dependence of the discussed optical properties on the filling fraction would require a more sophisticated algorithm to simulate the growth of the films, which is beyond the scope of the present work.

Finally, let us stress that for the sake of simplicity, the calculations of the LDOS are performed with a point-like source dipole (we do not take into account the finite size of the bead). Moreover, we consider that the system lies in vacuum. In Ref [57], we have performed calculations taking into account the size of the bead and considered a system embedded in glass instead of vacuum. The trends of the calculations are not modified by these sophistications.

3.2.2 Distance dependence of the LDOS statistical distribution

Using the same experimental setup and numerical scheme, we have studied the distance dependence of the LDOS statistical distribution in the fractal regime. Experimentally, a control of the distance was achieved by varying the spacer thickness. In Fig. 3.9(a), we show measurements of the orientation-averaged decay rate distribution measured for three different thicknesses of the silica spacer. A reference measurement is presented for fluorescent beads deposited on a bare glass substrate. The diameter of the beads used here is 25 nm. The distribution were obtained from lifetime measurements on 30 beads. To get more insight on the experimental data, we have used the volume integral method to compute the LDOS distribution as a function of the distance to a numerically generated film. Figure 3.9(b) displays the spatial distribution of the normalized LDOS (ρ_0 is the LDOS in vacuum) computed at three distances corresponding to that used in the experiment.

The experimental and numerical data exhibit the same trends. One clearly sees that both the mean value and the width of the distribution are affected by the proximity of the disordered gold film. The behavior of the averaged value can be qualitatively understood replacing the film

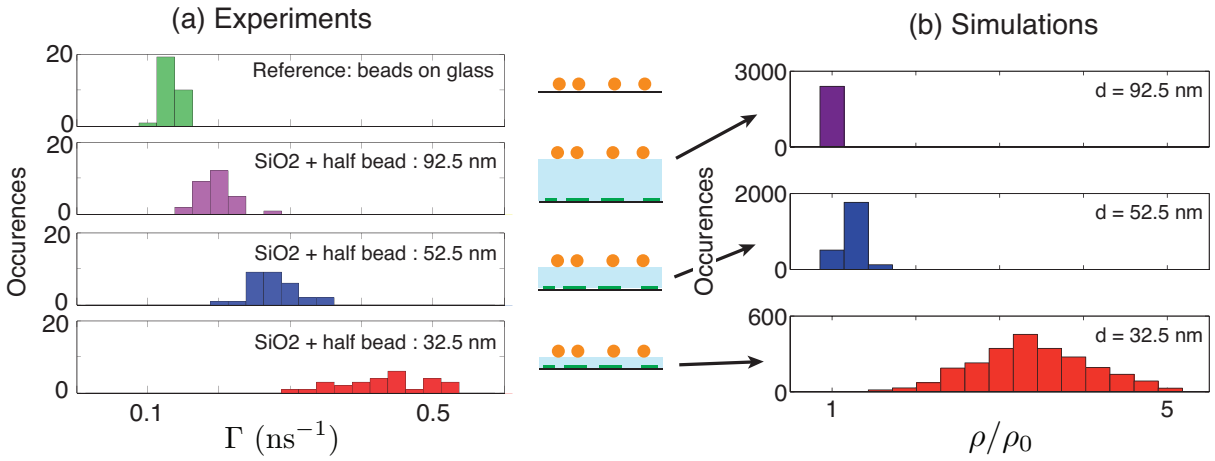


Figure 3.9: Experimental distributions of the orientation-averaged decay rate (normalized by its averaged value on a glass substrate) for different distances d between the center of the fluorescent nanosources and the film (i.e. spacer thickness + 12.5 nm).

by an effective homogeneous film. The averaged LDOS close to this absorbing homogeneous film is expected to be larger than that on the glass cover slide (the reference) due to an increase of the non-radiative LDOS at short distance [86, 40]. This will be discussed in details in section 3.3.

The broadening of the decay rate distribution when the distance to the film decreases is more interesting. Close to the film, as shown in section 3.2.1, high fluctuations of the LDOS are induced by the disordered surface. An important feature in the data is the substantial change in the shape and width of the statistical distribution with the distance to the film, in the range $d \approx 30 - 90\,\text{nm}$. This is due to spatial filtering of optical modes laterally confined on scales below the wavelength. Indeed, the field distribution in a plane at a distance d is exponentially filtered in Fourier space by a factor $\exp(-Kd)$ compared to the distribution at $d = 0\,\text{nm}$, with K the spatial frequency in the transverse direction (parallel to the film plane) [8]. We show in Fig. 3.10 numerical maps of the LDOS corresponding to the three distances considered in Fig. 3.9(b). In these maps, the spatial filtering of subwavelength details is striking. From this simple observation, an order of magnitude of the lateral confinement ξ of the field can be extracted. Since field variations giving rise to substantial fluctuations of the LDOS strongly attenuate between $d = 32.5\,\text{nm}$ and $d = 52.5\,\text{nm}$, the attenuation length can be estimated to be $1/K \approx 10\,\text{nm}$. One can deduce $\xi \sim 2\pi/K \approx 60\,\text{nm}$ as a typical size of hot spots at the surface of the films. This is in agreement with orders of magnitude found by near-field optical microscopy [19, 70, 87].

Note that ξ is an estimation of the typical scale of the electric field variations, but cannot be linked to the spatial extent of the modes, since a mode can be composed of several hot spots. In Chap 4, we introduce the Cross Density Of States (CDOS) to study quantitatively the spatial

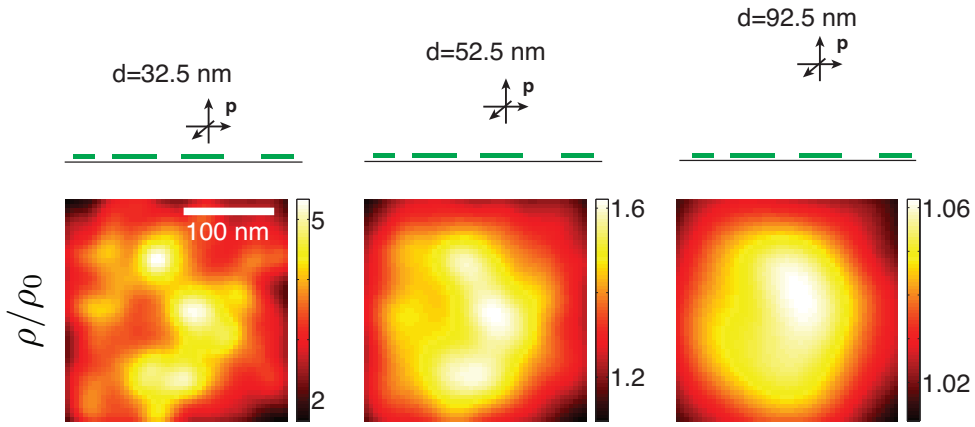


Figure 3.10: Maps of the normalized LDOS at three distance from the top of a 245 nm size film with filling fraction $f = 53\%$. Parameters are those of Fig. 3.9(b).

extent of the modes, and hence address the problem of coherence on these structures.

3.2.3 LDOS maps and film topography

One advantage of the numerical tool is to give access to LDOS maps, while obtaining them experimentally is a difficult task. In Fig. 3.11, we show LDOS maps in the low filing fraction and the fractal regime for a wavelength $\lambda_{\text{fluo}} = 780\,\text{nm}$ and a distance 40 nm to the films. In

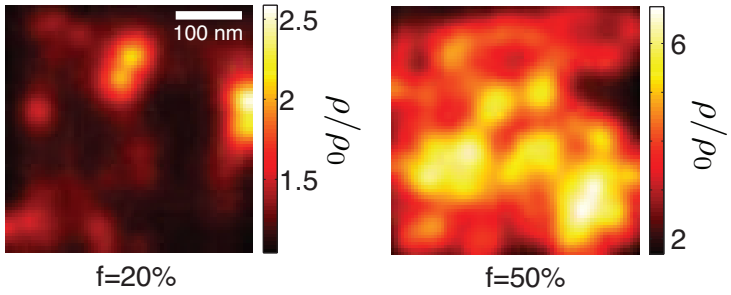


Figure 3.11: LDOS maps computed at 40 nm of two disordered films, with respective filling fractions $f = 20\%$ and $f = 50\%$. The wavelength is $\lambda_{\text{fluo}} = 780\,\text{nm}$. The films size is set to 375 nm, and the discretization is set to $\Delta = 2.5\,\text{nm}$.

both maps, we observe very subwavelength areas of high LDOS, but with very different physical origin. At $f = 20\%$, two significative "hot spots" are observed, very separated from each other, where the maximum LDOS is twice its value in vacuum. At $f = 50\%$, a higher number of "hot spots" are observed, all of them being more intense (up to six times the vacuum LDOS) than in the low filling fraction regime. To get more insight on the underlying phenomena, we show in

Fig. 3.12 the topography of the films superimposed on several LDOS maps (gold is represented in black). For each filling fraction, we present calculations for four different wavelengths. In the low

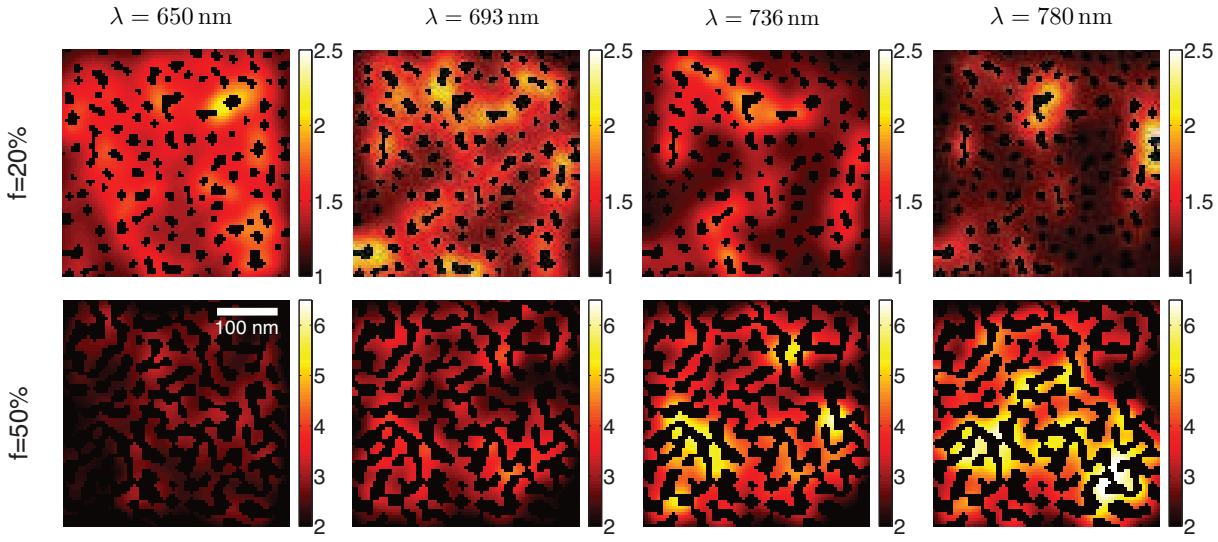


Figure 3.12: Maps of the normalized LDOS ρ/ρ_0 at $d = 40\,\text{nm}$ of two disordered films with filling fractions $f = 20\%$ and $f = 50\%$. The discretization is set to $\Delta = 2.5\,\text{nm}$. The topography of the films are superimposed on the LDOS maps (black=gold). The maps are shown for four different wavelengths.

filling fraction film, one can observe that the hot spots are always correlated to a single particle. The hot spots are actually due to the plasmon resonances of the individual particles. Since they have different geometries and sizes, one can observe that these resonances are switched on and off when the wavelength is modified.

In the fractal regime, connecting the topography and the LDOS maps is much more involved. It was observed in experiments that the hot spots in this regime can appear either in gaps or on metal [20]. In Fig. 3.12, we observe that their positions and shapes cannot be trivially explained from the topography, but seems to be the result of a complex collective interaction. In Chap. 4, we propose a new approach to quantify the trade-off between localized and delocalized modes in complex media, which allows us to describe quantitatively this regime, independently on the underlying phenomenon.

3.3 Radiative and non-radiative LDOS

3.3.1 Definition

In Chap 2, we have introduced the radiative and non-radiative decay rates and explained their calculation in the frame of the volume integral method. The total decay rate Γ of an emitter

can be expanded into these two contributions Γ^{R} and Γ^{NR} and reads

$$\Gamma = \Gamma^{\mathrm{R}} + \Gamma^{\mathrm{NR}}. \tag{3.16}$$

By analogy with the LDOS, one can define the radiative and the non-radiative LDOS as the quantities that drive respectively the orientation-averaged radiative and non-radiative decay rates.

$$\begin{aligned} \frac{\rho_{\mathrm{R}}}{\rho_0} &= \frac{\langle \Gamma^{\mathrm{R}} \rangle_{\mathbf{u}}}{\Gamma_0} \\ \frac{\rho_{\mathrm{NR}}}{\rho_0} &= \frac{\langle \Gamma^{\mathrm{NR}} \rangle_{\mathbf{u}}}{\Gamma_0}, \end{aligned} \tag{3.17}$$

where $\langle . \rangle_{\mathbf{u}}$ denotes the average over dipole orientation $\mathbf{u}$, ρ_0 the LDOS in vacuum and Γ_0 the decay rate of an emitter in vacuum. ρ_{R} and ρ_{NR} are intrinsic quantities that characterize the nanostructure. They quantify the trade-off between radiative and non-radiative decay channels available for a fluorescent emitter depending on its position in the vicinity of a nanostructure.

3.3.2 Statistical distributions of the radiative and non-radiative LDOS

We have shown in section 3.2 that one feature of the disordered films in the fractal regime is the apparition of hot-spots due to collective interactions in the disordered fractal structure. One signature of these hot-spots is the existence of enhanced fluctuations of the LDOS, compared to that observed on a low-filling fraction film. In order to use this property in future basic experiments or applications, it is fundamental to determine whether high localized excitations are radiative or non-radiative. Radiative modes can be used e.g. for Surface Enhanced Fluorescence [88]. Non-radiative modes can enhance the interaction between emitters, as discussed in the conclusion of the present chapter.

In Fig. 3.13, we show the spatial distribution of the total, radiative and non-radiative LDOS at 40 nm distance from disordered films of filling fractions $f = 20\%$ and $f = 50\%$. Parameters are those of Fig. 3.8(b). One can clearly see that at 40 nm from the films, the enhanced fluctuations of the LDOS are mainly due to non-radiative channels. This means that the hot-spot structure observed in Fig. 3.11 is mostly associated to non-radiative modes.

3.3.3 Distance dependence of the radiative and non-radiative LDOS distributions

In this last section, we use numerical simulations to study quantitatively the distance dependence of both the radiative and non-radiative LDOS distribution. We plot in Fig. 3.14 the total, radiative and non-radiative LDOS distributions for three different distances to the films. Parameters are those of Fig. 3.9(b). As expected, the increase of ρ at short distance is mainly due to the increase of ρ_{NR}. Interestingly, at $d = 92.5$ nm, the non-radiative LDOS ρ_{NR} is small

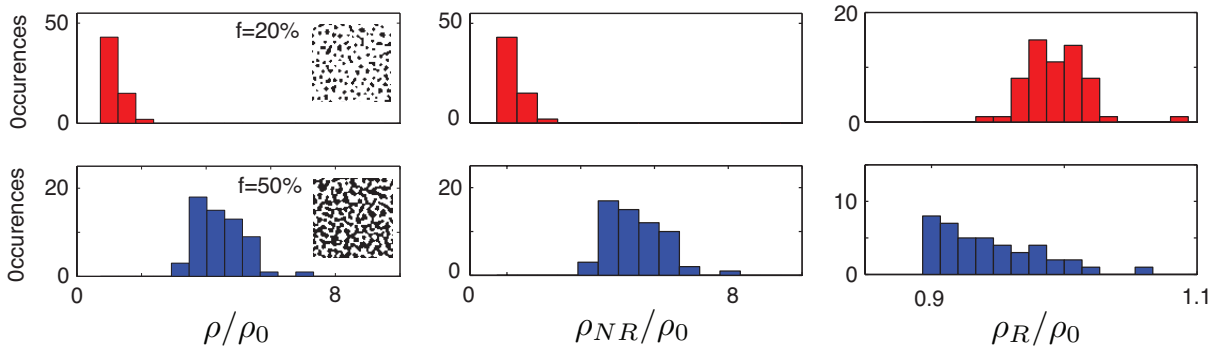


Figure 3.13: Spatial distribution of the total, radiative and non-radiative LDOS computed at 40 nm distance from 60 disordered films for each filling fraction $f = 20\%$ and $f = 50\%$. The discretization is set to $\Delta = 2.5$ nm.

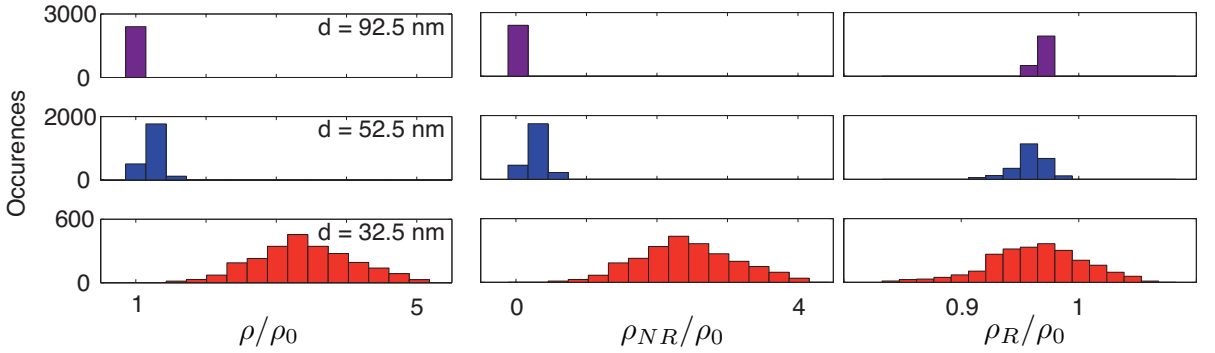


Figure 3.14: Distributions of the normalized total, radiative and non-radiative LDOS, normalized by ρ_0, the LDOS in vacuum. Three different distances d are considered, as in Fig. 3.9(b).

compared to ρ_{R}, that is approximately equal to the vacuum LDOS ρ_0. Beyond the average value, one needs to be careful about the fluctuations of the LDOS. At $d = 92.5$ nm, even though the LDOS is dominated by radiative modes, its fluctuations are still dominated by the non-radiative LDOS fluctuations. To illustrate this result, we show in Fig. 3.15 the maps of ρ, ρ_{NR} and ρ_{R} normalized by the vacuum LDOS ρ_0. As a result of the high fluctuations of the non-radiative LDOS – compared to those of the radiative LDOS – the contrast of the LDOS maps are very similar to the one of the non-radiative LDOS map.

3.4 Conclusion

To sum up, we have presented exact numerical calculations of the spatial distribution of the LDOS in the near field of disordered metallic films. The calculations are in very good agreement with experimental data. In particular, we have recovered the well-known existence of localized

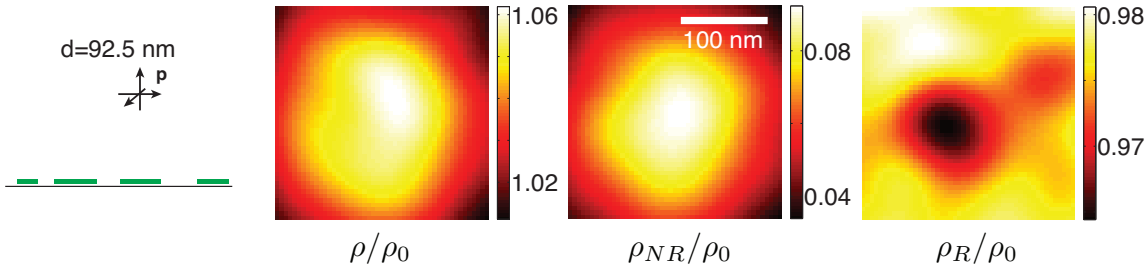


Figure 3.15: Maps of the total, radiative and non-radiative LDOS computed at $d = 92.5\,\text{nm}$ distance from a disordered film of filling fraction $f = 50\%$. The discretization is set to $\Delta = 2.5\,\text{nm}$.

enhancements of the near-field intensity and the LDOS on subwavelength areas (hot-spots) in the fractal regime. Based on the distance dependence of the LDOS distributions, we have estimated the extent of a hot-spot at the surface of a fractal film to roughly 60 nm, in good agreement with previous experimental observations. Comparing numerical LDOS maps to the film topography, we have shown that LDOS maps in the low-filling fraction and the fractal regime are explained by fundamentally different phenomena. Finally, we have studied numerically the radiative and non-radiative LDOS. We have shown that at a distance 40 nm above the film, the LDOS is chiefly driven by non-radiative modes. The fluctuations of the LDOS are driven by the fluctuations of the non-radiative LDOS for distances up to 90 nm. As a consequence, below these distances, the LDOS maps and the non-radiative LDOS maps are very similar. Though, above $d = 90\,\text{nm}$, the average value of the non-radiative LDOS is very low compared to the radiative LDOS. This means that for such distances, an emitter will hardly couple to non-radiative modes.

Our work gives a better characterization of the near-field optical properties of disordered metallic films, and paves the way to future potential applications. In particular, the non-radiative nature of the hot-spot structure in the fractal regime is very promising to enhance the interaction between emitters. Two examples of applications are exposed below.

Non-radiative modes such as ideal plasmons can be used to enhance Förster Resonant Energy Transfer (FRET) between two emitters (a donor and an acceptor). In this particular situation, emission to the far field is considered as losses. In Ref. [89], a donor and an acceptor molecules were located on two opposite sides of a 120 nm thick metallic layer. Energy transfer was possible because of the coupling between the surface plasmon polaritons of the two interfaces of the layer. In Ref. [90], the surface plasmon of a gold nanoparticle was used to enhance the photoluminescence intensity of an acceptor quantum dot. A FRET experiment in the near field of disordered metallic films would be interesting both to enhance the interaction range between emitters, but also to probe the spatial extent of excitations on these structures.

Recently, cooperative emission between emitters coupled by plasmon modes of an individual gold nanoparticle was predicted theoretically [91]. This effect is the analog – using non-radiative

coupling – of the Dicke superradiance, where an ensemble of dipoles coupled radiatively emit in a non-individual way. The observation of coherent emission by a disordered set of molecular emitters (J-aggregated dyes) strongly coupled to a surface plasmon was experimentally reported in Ref. [92]. Here again, disordered metallic films are potentially good substrates for future basic experiments in nanophotonics.

Chapter 4

Spatial coherence in complex systems: the Cross Density Of States

Contents

4.1 The Cross Density Of States (CDOS) 68
4.1.1 Definition 69
4.1.2 CDOS and spatial coherence in systems at thermal equilibrium 69
4.1.3 Interpretation based on a mode expansion 69
4.2 Squeezing of optical modes on disordered metallic films 72
4.2.1 Numerical maps of the CDOS on disordered metallic films 73
4.2.2 Intrinsic coherence length 74
4.2.3 Finite-size effects 76
4.3 Conclusion 77

The ability of nanostructures to concentrate and transport light at subwavelength scales make them promising candidates for the design of efficient sources and absorbers of visible and near-infrared radiation, or for optical storage and information processing with ultrahigh spatial density. Metallic nanostructures benefit from the excitation of surface plasmons that permit concentration at ultra-small length scales and ultra-fast time scales [93]. Disordered media also offer the possibility to build up spatially localized modes (e.g. by the process of Anderson localization) [26]. Optical modes with subwavelength structure are the substrate for many interesting phenomena.

- Localized optical modes can *enhance light-matter interaction.* In the weak coupling regime, enhanced Purcell factors have been observed in disordered 1D photonic crystals [4], ZnO powders [94, 2] or in the nanoscale gap of a gold particle dimer [56]. Strong coupling can be reached between plasmons modes and single emitters [95] or disordered set of molecules [92]. Experimental observation of strong coupling between scatterers and An-

derson localized modes has been reported recently in 1D photonic crystals [5]. This phenomenon is discussed theoretically in Chaps. 1 and 7.

- The coupling between emitters can be enhanced, leading to *superradiance* or *non-radiative energy transfer*. Super and sub-radiant states have been observed coupling two emitters by a graphene surface plasmon mode [96]. Förster Resonant Energy Transfer (FRET) between emitters can be achieved beyond the usual Förster radius using surface plasmon modes [90].

- Subwavelength mode structures can allow *light focusing beyond the diffraction limit*. Microwave antennas separated by $\lambda/30$ (λ being the wavelength) have been addressed individually in the near field of a disordered subwavelength environment using a time-reversal cavity [97]. Using plasmonic nanosystems to realize an equivalent experiment in the optical regime has been proposed theoretically [98]. A nanoscale mode structure can also be provided by periodically patterned substrates, that have been shown in simulations to allow focalization on spots as small as one-sixth of a wavelength [99].

In all these phenomena, the spatial extent of eigenmodes is of central importance, since it characterizes the ability of the system to support concentrated or delocalized excitations. It drives, e.g., the coherence length of surface plasmons, the range of non-radiative energy transfer, or the lower limit for spatial focusing by time reversal or phase conjugation. On disordered metallic films, as discussed in Chap. 3, quantifying the trade-off between localzed and delocalized excitations is a central issue.

In this chapter, we introduce the Cross Density Of States (CDOS) as a quantity that characterizes the overall spatial extent of eigenmodes on any complex photonic or plasmonic system. We use this quantity to address the spatial localization of light on disordered metallic films. We demonstrate unambiguously the spatial squeezing of eigenmodes in the fractal regime. This illustrates the relevance of the CDOS to characterize the intrinsic spatial coherence in photonic and plasmonic systems.

This work was published in Physical Review Letters [100].

4.1 The Cross Density Of States (CDOS)

Here, we introduce the Cross Density Of States (CDOS) as the imaginary part of the Green function of the propagation equation of electromagnetic waves. This quantity has two spatial dependences, and characterizes the intrinsic spatial coherence of a photonic or plasmonic system.

We propose an interpretation based on an eigenmode expansion, and show that it quantifies the connection between two points $\mathbf{r}$ and $\mathbf{r}'$ provided by the set of eigenmodes.

4.1.1 Definition

In order to characterize the intrinsic spatial coherence of complex photonic or plasmonic systems at a given frequency ω, we introduce a two-point quantity $\rho(\mathbf{r}, \mathbf{r}', \omega)$ that we will refer to as CDOS, defined as

$$\rho(\mathbf{r}, \mathbf{r}', \omega) = \frac{2\omega}{\pi c^2} \mathrm{Im} \left[\mathrm{Tr}\, \mathbf{G}(\mathbf{r}, \mathbf{r}', \omega) \right] . \tag{4.1}$$

In this expression, c is the speed of light in vacuum, $\mathbf{G}(\mathbf{r}, \mathbf{r}', \omega)$ is the electric dyadic Green function, and Tr denotes the trace of a tensor. This definition has been chosen so that one recovers the LDOS when $\mathbf{r} = \mathbf{r}'$.

4.1.2 CDOS and spatial coherence in systems at thermal equilibrium

The choice of this quantity as a measure of the intrinsic spatial coherence results from the observation that the imaginary part of the Green function at two different points appears in a number of situations where the spatial coherence of random fields (produced by random sources and/or a disordered medium) needs to be characterized. In a system at thermal equilibrium, the spatial correlation tensor of the electric field at a given frequency $\mathcal{E}_{kl}(\mathbf{r}, \mathbf{r}', \omega)$, defined as

$$\langle E_k(\mathbf{r}, \omega) E_l^*(\mathbf{r}', \omega') \rangle = 2\pi\delta(\omega - \omega')\mathcal{E}_{kl}(\mathbf{r}, \mathbf{r}', \omega), \tag{4.2}$$

has been known for long to be proportional to the imaginary part of the dyadic Green function, a consequence of the fluctuation-dissipation theorem [61]

$$\mathcal{E}_{kl}(\mathbf{r}, \mathbf{r}', \omega) \propto \mathrm{Im}\, G_{kl}(\mathbf{r}, \mathbf{r}', \omega). \tag{4.3}$$

The same relation connects the spatial correlation function of acoustic or seismic wavefields under white-noise excitation [101, 102]. More generally, any field generated by a statistically homogeneous and isotropic distribution of sources produces a spatial correlation function characterized by the imaginary part of the Green function [103]. Fully developed speckle patterns belong to the same class of systems [26]. The imaginary part of the Green function also describes the process of focusing by time reversal. Indeed, under perfect time reversal conditions (ideally using a time-reversal cavity enclosing the medium), the field distribution around the focal spot at a given frequency is given by the imaginary part of the Green function [104, 23]. The spatial correlation under uncorrelated excitation (thermal sources, white noise) or the ultimate spot size that can be created in a medium under perfect time reversal eventually depend on the spatial extent of the underlying eigenmodes at the observation frequency. As we shall see, this spatial extent can be rigorously defined using the CDOS.

4.1.3 Interpretation based on a mode expansion

The physical picture behind the CDOS is a counting of optical eigenmodes that connect two different points at a given frequency. In a network picture, the LDOS measures the number

of channels crossing at a given point, whereas the CDOS measures the number of channels connecting two points. In order to give a more rigorous basis to this picture, we first consider the canonical situation of a non-absorbing system placed in a closed cavity. In this situation, we derive the expansion of the Cross Density Of States (CDOS) on the well-defined set of normal modes. Then, we generalize this result to the case of a system with low losses, using a phenomenological approach.

Non-absorbing system embedded in a close cavity

Let us first consider the canonical situation of a non-absorbing system (e.g., a nanostructured material) placed in a closed cavity. In this case an orthonormal discrete basis of eigenmodes can be defined, with eigenfrequencies ω_n and eigenvectors $\mathbf{e}_n(\mathbf{r})$. The expansion of the dyadic Green function reads [105]

$$\mathbf{G}(\mathbf{r},\mathbf{r}',\omega) = \sum_n c^2 \frac{\mathbf{e}_n^*(\mathbf{r}')\mathbf{e}_n(\mathbf{r})}{\omega_n^2 - \omega^2} \tag{4.4}$$

where the superscript * stands for complex conjugate. This expression contains a singularity (see Appendix B for details). It can be rewritten in the more explicit form

$$\mathbf{G}(\mathbf{r},\mathbf{r}',\omega) = \sum_n c^2 \left\{ \mathrm{PV}\left[\frac{1}{\omega_n^2 - \omega^2}\right] + \frac{i\pi}{2\omega_n}\delta(\omega-\omega_n)\right\} \mathbf{e}_n^*(\mathbf{r}')\mathbf{e}_n(\mathbf{r}), \tag{4.5}$$

where PV stands for principal value. Introducing Eq. (4.5) into Eq. (4.1) yields

$$\rho(\mathbf{r},\mathbf{r}',\omega) = \sum_n \delta(\omega-\omega_n)\mathrm{Re}\left[\mathbf{e}_n^*(\mathbf{r}')\cdot\mathbf{e}_n(\mathbf{r})\right] + \frac{2\omega}{\pi}\sum_n \mathrm{PV}\left[\frac{1}{\omega_n^2-\omega^2}\right]\mathrm{Im}\left[\mathbf{e}_n^*(\mathbf{r}')\cdot\mathbf{e}_n(\mathbf{r},\omega)\right] \tag{4.6}$$

One can simplify Eq. (4.6) using the reciprocity theorem

$$\mathbf{G}(\mathbf{r},\mathbf{r}',\omega) = {}^t\mathbf{G}(\mathbf{r}',\mathbf{r},\omega), \tag{4.7}$$

which, using Eq. (4.5), transforms into

$$\sum_n c^2 \left\{ \mathrm{PV}\left[\frac{1}{\omega_n^2-\omega^2}\right] + \frac{i\pi}{2\omega_n}\delta(\omega-\omega_n)\right\}\left[\mathbf{e}_n^*(\mathbf{r}')\mathbf{e}_n(\mathbf{r}) - \mathbf{e}_n(\mathbf{r}')\mathbf{e}_n^*(\mathbf{r})\right] = 0. \tag{4.8}$$

Since $\mathbf{e}_n^*(\mathbf{r}')\mathbf{e}_n(\mathbf{r}) - \mathbf{e}_n(\mathbf{r}')\mathbf{e}_n^*(\mathbf{r}) = 2i\,\mathrm{Im}\left[\mathbf{e}_n^*(\mathbf{r}')\mathbf{e}_n(\mathbf{r})\right]$, the imaginary part of Eq. (4.8) leads to

$$\sum_n \mathrm{PV}\left[\frac{1}{\omega_n^2-\omega^2}\right]\mathrm{Im}\left[\mathbf{e}_n^*(\mathbf{r}')\mathbf{e}_n(\mathbf{r})\right] = 0. \tag{4.9}$$

Taking the trace of Eq. (4.9) yields

$$\sum_n \mathrm{PV}\left[\frac{1}{\omega_n^2-\omega^2}\right]\mathrm{Im}\left[\mathbf{e}_n^*(\mathbf{r}')\cdot\mathbf{e}_n(\mathbf{r})\right] = 0, \tag{4.10}$$

showing that the last term in Eq. (4.6) actually vanishes. Finally, the CDOS expansion Eq. (4.6) simplifies into

$$\rho(\mathbf{r},\mathbf{r}',\omega) = \mathrm{Re}\sum_n \left[\mathbf{e}_n^*(\mathbf{r}')\cdot\mathbf{e}_n(\mathbf{r})\right]\delta(\omega-\omega_n) \tag{4.11}$$

This expression explicitly shows that the CDOS sums up all eigenmodes connecting $\mathbf{r}$ to $\mathbf{r}'$ at frequency ω, weighted by their strength at both points $\mathbf{r}$ and $\mathbf{r}'$.

Phenomenological approach for a weakly lossy system

In the case of an open and/or absorbing system, the rigorous introduction of a basis of eigenmodes is more involved. Approaches have been developed in the quasi-static limit [106], or based on statistical properties of the spectral expansion of non-Hermitian matrices [107]. A proper treatment of the normalization of quasi-normal modes in the presence of dissipation has been proposed recently [108]. Here, we restrict ourselves to a simple but very common phenomenological approach [12]. Assuming weak leakage, quasi-modes with linewidth γ_n replace the delta functions in Eq. (4.4), so that the dyadic Green function reads

$$\mathbf{G}(\mathbf{r},\mathbf{r}',\omega) = \sum_n c^2 \frac{\mathbf{e}_n^*(\mathbf{r}')\mathbf{e}_n(\mathbf{r})}{\omega_n^2-\omega^2-i\gamma_n\omega}. \tag{4.12}$$

Using reciprocity exactly as in the previous case, one can derive the following expansion of the CDOS

$$\rho(\mathbf{r},\mathbf{r}',\omega) = \mathrm{Re}\sum_n \frac{\gamma_n}{2\pi}\frac{\mathbf{e}_n^*(\mathbf{r}')\cdot\mathbf{e}_n(\mathbf{r})}{(\omega-\omega_n)^2+(\gamma_n/2)^2}. \tag{4.13}$$

Eq. (4.13) shows that our interpretation of the CDOS remains meaningful in the more realistic case of a system with weak losses, in which the spectral delta function has been replaced by a Lorentzian lineshape. Let us stress that by using the mathematical identity

$$\lim_{\gamma_n\to 0}\frac{1}{\pi}\frac{\gamma_n/2}{(\omega-\omega_n)^2+(\gamma_n/2)^2} = \delta(\omega-\omega_n), \tag{4.14}$$

Eq. (4.13) leads to Eq. (4.11), i.e. to the case of non-dissipative systems. This generalizes the physical picture to lossy systems. Nevertheless, it is important to note that all calculations presented in this chapter are performed using Eq. (4.1), in which the correct counting of modes is implicit, without referring to a basis of eigenmodes.

Spatial coherence and polarization

The trace operator in Eq. (4.1) was voluntarily added to restrict the discussion to spatial coherence and wash out the polarization degrees of freedom. Though, a CDOS dyadic can be defined as follows to take into account all cross-polarized components.

$$\boldsymbol{\rho}(\mathbf{r},\mathbf{r}',\omega) = \frac{2\omega}{\pi c^2}\,\mathrm{Im}\,\mathbf{G}(\mathbf{r},\mathbf{r}',\omega). \tag{4.15}$$

This defines a tensor that characterizes the intrinsic spatial coherence and polarization state. In the canonical situation where a discrete set of modes can be defined, the mode expansion of the CDOS given in Eq. (4.11) can be generalized to the CDOS dyadic, and reads

$$\rho_{ij}(\mathbf{r},\mathbf{r}',\omega) = \mathrm{Re}\sum_n \left[\mathbf{e}_n^*(\mathbf{r}')\cdot\mathbf{u}_i\right]\left[\mathbf{e}_n(\mathbf{r})\cdot\mathbf{u}_j\right]\delta(\omega-\omega_n), \tag{4.16}$$

where $\mathbf{u}_i$ and $\mathbf{u}_j$ are two unit vectors defining two polarization directions i and j. Eq. (4.16) shows that the co-polarized component along direction $\mathbf{u}_i$ is described by the coefficient ρ_{ii} of the CDOS dyadic, while the cross-polarized component between directions $\mathbf{u}_i$ and $\mathbf{u}_j$ is described by ρ_{ij}. This definition is in agreement with the relation between the CDOS and the spatial correlation tensor mentioned in Eq. (4.3). The CDOS used in this chapter is the sum of the co-polarized components of the CDOS dyadic

$$\rho(\mathbf{r},\mathbf{r}',\omega) = \sum_i \rho_{ii}(\mathbf{r},\mathbf{r}',\omega). \tag{4.17}$$

4.2 Overall squeezing of the optical modes on disordered metallic films

In the near field of disordered metallic films, as discussed in Chap. 3, high values of the electric field located on very subwavelength areas, called hot-spots, appear in the fractal regime. The physical origin of the apparition of these hot-spots was the subject of a controversy. Using a scaling theory in the quasi-static limit, a mechanism based on Anderson localization has been put forward [109]. Anderson localization on percolating systems for electronic (quantum) transport leads to a clear transition between the localized and delocalized regimes [110, 111]. Moreover, localized electronic states are known to be exponentially decaying in space (on average). For light scattering on percolating metallic systems, a theoretical analysis has proved the existence of localized modes characterized by algebraic rather than exponential spatial confinement [107]. Numerical simulations on planar random composites have even shown that localized and delocalized plasmonic eigenmodes could coexist [76]. This has been confirmed by computations and measurements of intensity fluctuations in the near field [112, 113], that have also indicated that localized modes should dominate around the percolation threshold.

For nanophotonics, a major issue is the description of the overall spatial extent of *the full set* of eigenmodes whatever the underlying mechanism. Spatial coherence and the concept of CDOS appear as a natural tool to address this issue. Here, we present numerical maps of the CDOS computed in the near field of disordered metallic films. We demonstrate unambiguously an overall squeezing of the optical modes near the percolation threshold of the films. To be more quantitative, we introduce the intrinsic coherence length as a measure of this overall spatial extent, and study its dependence on the metal surface filling fraction of the films.

4.2.1 Numerical maps of the CDOS on disordered metallic films

The CDOS can be calculated numerically using exact three-dimensional simulations. The procedure is fully described in Chaps. 2 and 3. Solving the Lippmann-Schwinger equation with the volume integral method allows us to compute the Green function of the system and to deduce the CDOS. We show in Fig. 4.1 the LDOS maps (center column) and CDOS maps (right column) computed in a plane at a distance $z = 40\,\text{nm}$ above two different films (shown in the left column) corresponding to two different regimes. The films were generated numerically using the procedure described in Chap. 3 (section 3.1). For $f = 20\%$ (left column), the film is composed of isolated nanoparticles whereas for $f = 50\%$ (right column) the film is near the percolation threshold, a regime in which fractal clusters dominate, as discussed in Chap. 3 (section 3.1.3). Before studying spatial coherence and the extent of eigenmodes based on the CDOS, let us

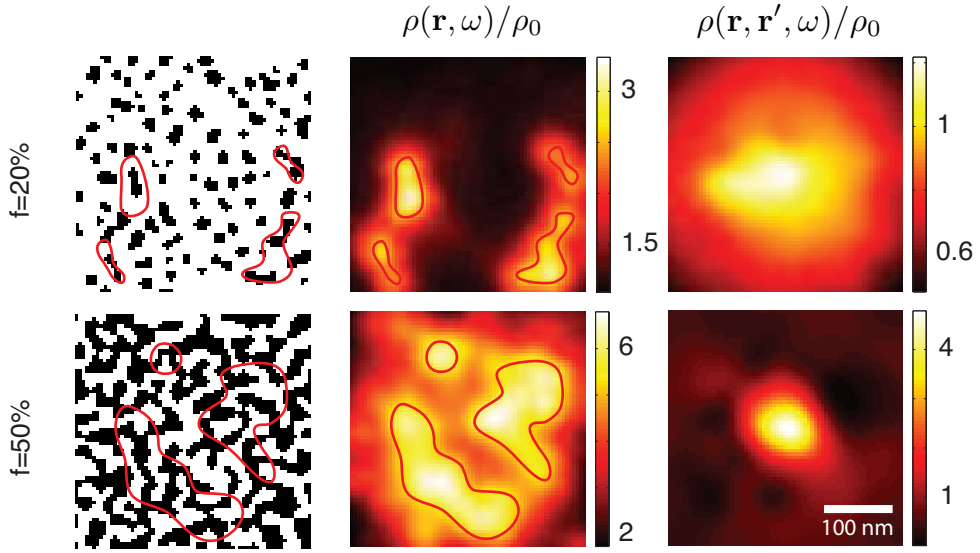


Figure 4.1: (Left column) Geometry of the disordered films generated numerically (with gold in black color). (Center column) Maps of the normalized LDOS $\rho(\mathbf{r},\omega)/\rho_0$ calculated in a plane at a distance $z = 40$ nm above the film surface. Red lines corresponding to LDOS hot-spots have been drawn both on the topography and the LDOS maps to guide the eye; (Right column) Maps of the normalized CDOS $\rho(\mathbf{r},\mathbf{r}',\omega)/\rho_0(\omega)$ with $\mathbf{r}'$ fixed at the center of the sample. $\lambda = 780$ nm.

summarize here the main features of the LDOS maps (already discussed in Chap. 3). For low surface fraction (top row), LDOS peaks are observed on top of isolated nanoparticles that are resonant at the observation wavelength. A correspondence between LDOS peaks and the position of one or several nanoparticles is easily made. For a different observation wavelength (see Fig. 3.12 in Chap. 3), particles can switch on or off resonance and the position of the LDOS peaks change, but remain attached to individual particles. The sample behaves as a collection of individual nanoparticles with well identified surface plasmon resonances. In the multiscale

resonant regime (bottom row), the LDOS structure is more complex. There is no obvious correspondence between the film topography (composed of fractal clusters in which the concept of individual nanoparticles becomes meaningless) and the localized field enhancements responsible for LDOS fluctuations.

The maps of the CDOS $\rho(\mathbf{r}, \mathbf{r}', \omega)$ are displayed versus $\mathbf{r}$ for a fixed position $\mathbf{r}'$ (chosen at the center of the sample). Their meaning can be understood as follows: They display the ability of a point $\mathbf{r}$ at a given distance from the center point $\mathbf{r}'$ to be connected to this center point by the underlying structure of the optical eigenmodes. For example, a large CDOS (larger than the vacuum CDOS) would allow two quantum emitters at $\mathbf{r}$ and $\mathbf{r}'$ to couple efficiently. It would also ensure coherent (correlated) fluctuations of the light fields at $\mathbf{r}$ and $\mathbf{r}'$ under thermal excitation. The CDOS also allows one to discriminate between hot spots that belong to the same eigenmode (or that are connected by at least one eigenmode), or that are completely independent. Last but not least, since the CDOS implicitly sums up the spatial extent of the full set of eigenmodes, it appears as a natural tool to describe the overall spatial localization in the multiscale resonant regime. It is striking to see that the extent of the CDOS in the multiscale resonant regime is reduced to a smaller range compared to the case of a film composed of isolated nanoparticles. The reduction of the extent of the CDOS clearly demonstrates an *overall spatial squeezing of the eigenmodes close to the percolation threshold*. Let us stress that the approach based on the CDOS gives a non-ambiguous description of this overall spatial squeezing, whatever the underlying mechanism. It is based on a concept implicitly related to field-field spatial correlations as in classical spatial coherence theory, that seems to carry sufficient information to describe one of the most striking features in the optics of disordered metallic films.

4.2.2 Intrinsic coherence length

In order to quantify the overall reduction of the spatial extent of eigenmodes in the multiscale resonant regime, we introduce an intrinsic coherence length ℓ_{coh}, defined from the width of the CDOS. More precisely, fixing $\mathbf{r}'$ at the center of the sample, we use polar coordinates in the plane $z = 40\,\text{nm}$ parallel to the sample mean surface to write

$$\rho(\mathbf{r}, \mathbf{r}', \omega) = \rho(R, \theta, \omega), \tag{4.18}$$

with $R = |\mathbf{r} - \mathbf{r}']$ and define an angularly-averaged CDOS

$$\bar{\rho}(R, \omega) = \frac{1}{2\pi} \int_0^{2\pi} \rho(R, \theta, \omega) \mathrm{d}\theta. \tag{4.19}$$

The intrinsic coherence length ℓ_{coh} is defined as the half width at half maximum of $\bar{\rho}(R, \omega)$ considered as a function of R. It is important to note that ℓ_{coh} is not necessarily the size of the hot spots observed on the surface, since a given eigenmode can be composed of several hot spots. Two different hot spots separated by a distance smaller than ℓ_{coh} can be intrinsically connected

(meaning that they are connected by at least one eigenmode). The ability to clarify this distinction between eigenmodes and hot spots is an essential feature of the CDOS. The averaged value of $\langle \ell_{coh} \rangle$ (solid line) and its variance $\mathrm{Var}(\ell_{coh})$ (error bars) are shown in Fig. 4.2 versus the film surface fraction for two wavelengths $\lambda = 650$ nm and $\lambda = 780$ nm. Both quantities are

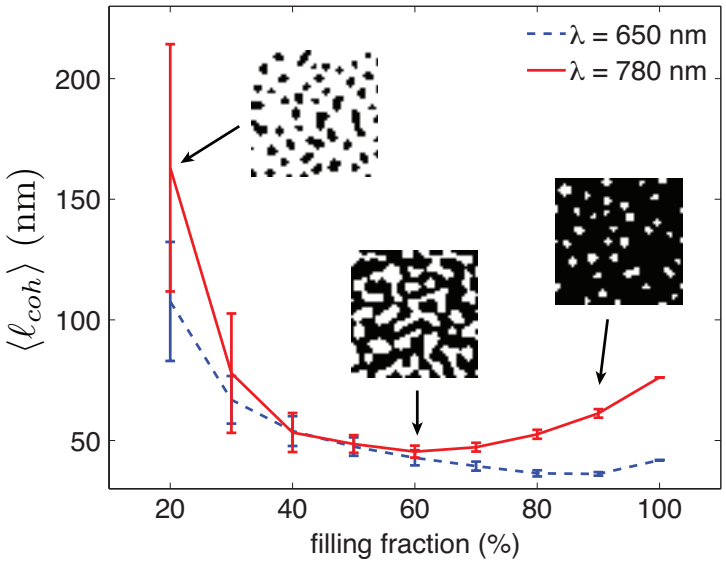


Figure 4.2: Averaged value (solid line) and variance (error bars) of the intrinsic coherence length ℓ_{coh} calculated at a distance $z = 40$ nm above a disordered film, versus the gold surface fraction f. Inset: Typical film geometries (black color corresponds to gold). Lateral sizes of the films range from 500 nm for $f = 20\%$ to 205 nm for $f = 100\%$.

calculated using a statistical ensemble of realizations of disordered films generated numerically (the error bars indicate the real variance of ℓ_{coh}, and not computations errors due to lack of numerical convergence, the latter being ensured by a sufficiently large set of realizations). For both wavelengths, the average value $\langle \ell_{coh} \rangle$ is significantly smaller near the percolation threshold than for lower filling fractions. This unambiguously demonstrates the overall spatial squeezing of eigenmodes in the regime dominated by fractal clusters, with a stronger squeezing at $\lambda = 780$ nm where more pronounced resonances occur [20]. The curve for $\lambda = 780$ nm even shows a minimum near the percolation threshold. Our approach provides a theoretical description of the experiment of Krachmalnicoff and coworkers [3] discussed in Chap. 3, although in this study, the inverse participation ratio was used to connect qualitatively the spatial extent of eigenmodes to the variance of the LDOS fluctuations. Therefore only a qualitative comparison with the curve in Fig. 4.2 is possible (the inverse participation ratio and the intrinsic coherence length cannot be compared directly).

The behavior of $\mathrm{Var}(\ell_{coh})$ is also instructive. Strong fluctuations are observed in the regime

of isolated nanoparticles. In this regime, optical modes attached to a single particle and delocalized modes are observed. This difference with the known behavior in quantum electronic transport [110, 111] is due to long-range interactions. The strong fluctuations reflect the fluctuations in the interparticle distance. Conversely, in the multiscale resonant regime, the reduction of the fluctuations reinforces the assumption of a mechanism based on collective interactions that involve the sample as a whole.

4.2.3 Finite-size effects

An important limitation of our simulations is the limited size of the numerical films, due to computation time considerations. On real films, modes with spatial extent larger than the size of the numerical films could exist, that are not taken into account in the simulations. The existence of such modes would change the exact shape of Fig. 4.2. In Fig. 4.2, the size of the films decreased from 500 nm for $f = 20\%$ to 205 nm for $f = 100\%$. To check that the trends we observe are physically sound, we have checked their robustness when the film size was reduced to 180 nm for all filling fractions. Comparison, for $\lambda = 780$ nm between the curve in Fig. 4.2 and the same curve computed for a uniform lateral size of the films equal to 180 nm is shown in Fig. 4.3. The trends observed in Fig. 4.2 for filling fractions near the percolation threshold

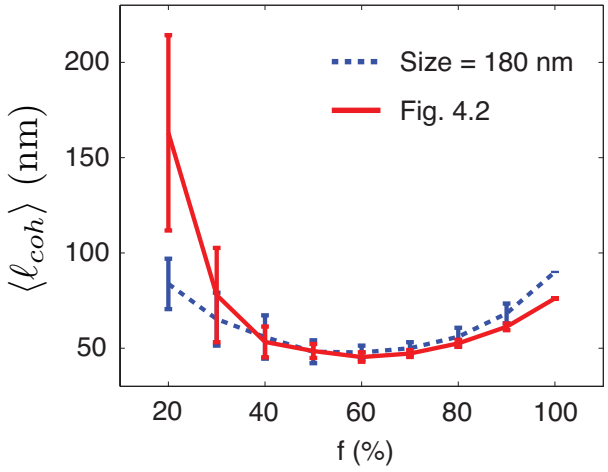


Figure 4.3: (Red full line) Intrinsic coherence length computed for $\lambda = 780$ nm (curve shown in Fig. 4.2); (Blue dashed line) Intrinsic coherence length computed for the same parameters with films of reduced lateral size 180 nm.

are robust on smaller films, showing that the results are physically sound. The discrepancy for low filling fractions is a finite-size effect, since the intrinsic coherence length calculated on these systems cannot be larger than half the size of the system ($\mathbf{r}'$ is fixed at the center of the film). This observation is actually compatible with the CDOS picture of spatial coherence. For low

filling fractions, the CDOS is broad and the center point "feels" the borders of the system. For intermediate filling fractions, the CDOS is squeezed, and the center point is no longer influenced by the topography further than ℓ_{coh}. It is consistent to observe that for very high filling fractions, the intrinsic coherence length increases again, and the discrepancy between the two calculations increases as well.

4.3 Conclusion

In summary, we have introduced the CDOS that characterizes the intrinsic spatial coherence of a photonic or plasmonic system, independently on the illumination conditions. Using this concept, we have demonstrated unambiguously the spatial squeezing of plasmonic eigenmodes on disordered metallic films close to the percolation threshold. This clarifies a basic issue in plasmonics concerning the description of the optical properties of these films, that have been discussed in Chap. 3. This also illustrates the relevance of the CDOS in the study of spatial coherence in photonics and plasmonics systems, and more generally in wave physics.

Part III

Speckle, weak and strong coupling in scattering media

Chapter 5

Reflection-transmission intensity correlation in speckle patterns

Contents

5.1 Intensity correlations in the mesoscopic regime 82
5.1.1 The mesoscopic regime 82
5.1.2 Dyson equation for the average field 83
5.1.3 Bethe-Salpether equation for the average intensity 84
5.1.4 Long range nature of the reflection-transmission intensity correlation . . 86
5.2 Reflection-Transmission intensity correlations 89
5.2.1 Geometry of the system and assumptions 90
5.2.2 Ladder propagator for a slab in the diffusion approximation 90
5.2.3 Diffuse intensity inside the slab 91
5.2.4 Intensity correlation between reflection and transmission 92
5.2.5 Discussion 93
5.3 Conclusion 95

When a slab of strongly scattering medium is illuminated by a monochromatic plane wave (e.g. a laser), two speckle patterns are generated: one in transmission and one in reflection (see Fig. 5.1). In these intensity patterns, one can identify bright spots with comparable sizes. These "speckle grains" are the signature of a short range spatial correlation, known as the C_1 correlation [114, 29]. This short range correlation vanishes for large distances, and has an exponentially small contribution to the reflection-transmission correlation in the case of a slab in the multiple scattering regime. However, a long range correlation survives at large distance, and has been denoted by C_2 [29]. Although the C_2 correlation has been computed for two points either in the reflected or in the transmitted speckle [115], little attention has been paid to the reflection-transmission correlation[1].

[1]Note that another long-range contribution to the spatial intensity correlation is denoted by C_3 and is the

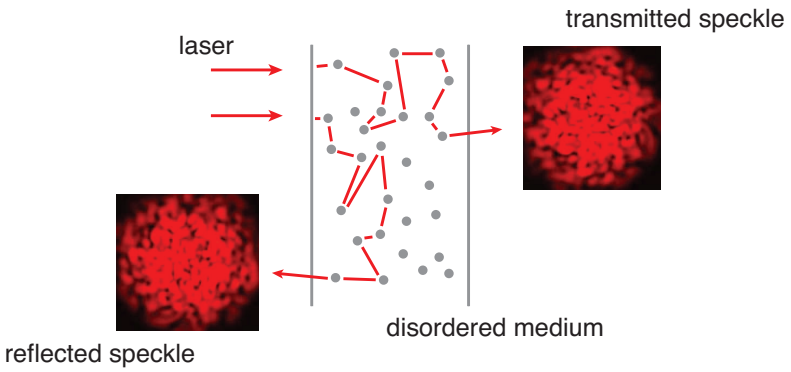


Figure 5.1: Sketch of the system.

In this chapter, we compute explicitly this correlation for a slab in the mesoscopic regime. In a first part, we make a brief review of the leading terms of the speckle intensity correlation function within the ladder approximation. We do not enter the details of the derivations, since all the results we present are detailed in textbooks [26, 27, 117]. In the second part, we compute the long range correlation C_2 in the reflection-transmission geometry. We consider a slab in the mesoscopic regime, and make the diffusion approximation to obtain analytical solutions of the transport problem. We obtain an analytical expression of the leading term of the reflection-transmission intensity correlation. Our prediction should pave the way towards an experimental observation, and should inspire future applications making use of this statistical connection between reflected and transmitted speckle patterns.

5.1 Intensity correlations in the mesoscopic regime

5.1.1 The mesoscopic regime

Let us consider a non-absorbing disordered medium described by a fluctuating dielectric constant[2]

$$\epsilon(\mathbf{r}) = 1 + \delta\epsilon(\mathbf{r}), \tag{5.1}$$

where $\langle . \rangle$ denotes the average over disorder realizations, and $\langle \delta\epsilon(\mathbf{r}) \rangle = 0$. We assume that the fluctuating part of the dielectric constant $\delta\epsilon$ satisfies white-noise statistics, i.e.

$$\langle \delta\epsilon(\mathbf{r}_1)\delta\epsilon(\mathbf{r}_2) \rangle = U\delta(\mathbf{r}_1 - \mathbf{r}_2), \tag{5.2}$$

cause of universal conductance fluctuations [29, 116]. This contribution is known as a second-order term in the perturbation theory we develop here, and is therefore not considered in this chapter.

[2] A more general approach taking into account a non-unity background dielectric constant is used e.g. in Ref. [117], but is not considered here for the sake of simplicity.

where U is a constant that can be connected to the scattering mean free path ℓ of the medium via [27]

$$U = \frac{4\pi}{k^4 \ell}, \tag{5.3}$$

with $k = 2\pi/\lambda$. Equation (5.3) is valid only if the wavelength λ inside the medium satisfies

$$\lambda \ll \ell, \tag{5.4}$$

with ℓ the scattering mean free path. We make the additional assumption that the medium is in the multiple scattering regime, i.e. that

$$\ell \ll d, \tag{5.5}$$

where d is the typical size of the system (the slab thickness in our case). The regime where Eqs. (5.3) and (5.5) are valid is often referred to as the *mesoscopic regime*.

5.1.2 Dyson equation for the average field

A complete description of light propagation requires the resolution of the vector wave equation. However, in a disordered medium, the scalar model describes accurately wave propagation upon large distances (compared to the scattering mean free path) [118, 119]. The scalar model is not sufficient to describe polarization dependent measurements, and fails when near-field interactions are not negligible (see Chap. 6 for an example). In this study, we limit ourself to the scalar wave equation satisfied by the scalar electric field $\mathrm{E}(\mathbf{r}, \omega)$

$$\nabla^2 \mathrm{E}(\mathbf{r}, \omega) + k^2 \epsilon(\mathbf{r}) \mathrm{E}(\mathbf{r}, \omega) = 0. \tag{5.6}$$

In any statistically homogeneous and isotropic disordered medium, the average field $\langle \mathrm{E}(\mathbf{r}, \omega) \rangle$ satisfies a wave equation in an homogeneous and isotropic effective medium described by an effective dielectric constant ϵ_{eff}

$$\nabla^2 \langle \mathrm{E}(\mathbf{r}, \omega) \rangle + k^2 \epsilon_{\text{eff}} \langle \mathrm{E}(\mathbf{r}, \omega) \rangle = 0. \tag{5.7}$$

The effective dielectric function ϵ_{eff} is a local quantity (independent on the wavevector) when only field variations at a scale larger than the correlation length of the disorder are considered. This result is a consequence of the Dyson equation [27, 26]. The calculation of the effective dielectric constant is deeply involved. In the mesoscopic regime, the perturbation theory described in Ref. [27] shows that it can be estimated to the first order in $(k\ell)^{-1}$ by

$$\epsilon_{\text{eff}} = 1 + \frac{i}{k\ell}. \tag{5.8}$$

Let us introduce $\langle \mathrm{G}(\mathbf{r}, \mathbf{r}', \omega) \rangle$ the Green function of Eq. (5.7), solution of

$$\nabla^2 \langle \mathrm{G}(\mathbf{r}, \mathbf{r}', \omega) \rangle + k^2 \epsilon_{\text{eff}} \langle \mathrm{G}(\mathbf{r}, \mathbf{r}', \omega) \rangle = \delta(\mathbf{r} - \mathbf{r}'), \tag{5.9}$$

that describes the propagation of the average field inside the medium. In the case of an infinite medium, imposing an outgoing wave condition, the average Green function takes the form

$$\langle \mathrm{G}(\mathbf{r},\mathbf{r}',\omega)\rangle = \frac{\exp\left(ik|\mathbf{r}-\mathbf{r}'|\right)}{4\pi|\mathbf{r}-\mathbf{r}'|}\exp\left(-\frac{|\mathbf{r}-\mathbf{r}'|}{2\ell}\right). \tag{5.10}$$

5.1.3 Bethe-Salpether equation for the average intensity

The intensity of the field is defined as[3]

$$\mathrm{I}(\mathbf{r},\omega) = \left|\langle \mathrm{E}(\mathbf{r},\omega)\rangle + \delta\mathrm{E}(\mathbf{r},\omega)\right|^2. \tag{5.11}$$

Therefore, since by definition $\langle \delta\mathrm{E}(\mathbf{r},\omega)\rangle = 0$, one can expand the average intensity into

$$\langle \mathrm{I}(\mathbf{r},\omega)\rangle = \underbrace{\left|\langle \mathrm{E}(\mathbf{r},\omega)\rangle\right|^2}_{\mathrm{I}_b(\mathbf{r},\omega)} + \underbrace{\langle\left|\delta\mathrm{E}(\mathbf{r},\omega)\right|^2\rangle}_{\mathrm{I}_d(\mathbf{r},\omega)}. \tag{5.12}$$

The first term defines the *ballistic intensity*, that corresponds to the intensity of the average field. It is denoted by $\mathrm{I}_b(\mathbf{r},\omega)$. The ballistic beam corresponds to light that has not been scattered, and is attenuated by scattering as it propagates inside the medium. The second term defines the *diffuse intensity* and is denoted by $\mathrm{I}_d(\mathbf{r},\omega)$.

Bethe-Salpether equation

The average intensity obeys the Bethe-Salpether equation [26, 27]

$$\begin{aligned}\langle \mathrm{I}(\mathbf{r},\omega)\rangle = \left|\langle \mathrm{E}(\mathbf{r},\omega)\rangle\right|^2 + \int &\langle \mathrm{G}(\mathbf{r},\mathbf{r}_1,\omega)\rangle\langle \mathrm{G}^*(\mathbf{r},\mathbf{r}_2,\omega)\rangle \\ &\times \Gamma(\mathbf{r}_1,\mathbf{r}_2,\mathbf{r}_3,\mathbf{r}_4)\langle \mathrm{E}(\mathbf{r}_3,\omega)\mathrm{E}^*(\mathbf{r}_4,\omega)\rangle\,\mathrm{d}\mathbf{r}_1\,\mathrm{d}\mathbf{r}_2\,\mathrm{d}\mathbf{r}_3\,\mathrm{d}\mathbf{r}_4,\end{aligned} \tag{5.13}$$

where, $\Gamma(\mathbf{r}_1,\mathbf{r}_2,\mathbf{r}_3,\mathbf{r}_4)$ is the irreducible vertex, that takes into account all multiple scattering events inside the medium. As the effective dielectric constant, the existence of the irreducible vertex is mathematically proven, but its calculation is deeply involved. To the lowest order of $(k\ell)^{-1}$ in the perturbation theory, and for the white-noise disorder considered here, it reads [27]

$$\Gamma(\mathbf{r}_1,\mathbf{r}_2,\mathbf{r}_3,\mathbf{r}_4) = \frac{4\pi}{\ell}\delta(\mathbf{r}_1-\mathbf{r}_2)\delta(\mathbf{r}_3-\mathbf{r}_4)\delta(\mathbf{r}_1-\mathbf{r}_3). \tag{5.14}$$

This approximation of the vertex is known as the *ladder approximation*, and is commented later in this chapter. Using Eq. (5.14), Eq. (5.13) transforms into

$$\langle \mathrm{I}(\mathbf{r},\omega)\rangle = \left|\langle \mathrm{E}(\mathbf{r},\omega)\rangle\right|^2 + \frac{4\pi}{\ell}\int \left|\langle \mathrm{G}(\mathbf{r},\mathbf{r}_1,\omega)\rangle\right|^2 \langle \mathrm{I}(\mathbf{r}_1,\omega)\rangle\,\mathrm{d}\mathbf{r}_1. \tag{5.15}$$

The expression of the diffuse intensity can be deduced directly from Eqs (5.12) and (5.15). It reads

$$\mathrm{I}_d(\mathbf{r},\omega) = \frac{4\pi}{\ell}\int \left|\langle \mathrm{G}(\mathbf{r},\mathbf{r}_1,\omega)\rangle\right|^2 \langle \mathrm{I}(\mathbf{r}_1,\omega)\rangle\,\mathrm{d}\mathbf{r}_1. \tag{5.16}$$

[3] We consider a dimensionless intensity with no restriction, since the correlation functions we consider are normalized.

Ladder propagator and diffuse intensity

Let us introduce the ladder propagator $\mathrm{L}(\mathbf{r}_2,\mathbf{r}_1)$, solution of

$$\mathrm{L}(\mathbf{r}_2,\mathbf{r}_1)=\frac{4\pi}{\ell}\delta(\mathbf{r}_2-\mathbf{r}_1)+\frac{4\pi}{\ell}\int \mathrm{d}\mathbf{r}_3|\langle \mathrm{G}(\mathbf{r}_2,\mathbf{r}_3)\rangle|^2\mathrm{L}(\mathbf{r}_3,\mathbf{r}_1). \tag{5.17}$$

Using the ladder propagator L, one can extract from Eq. (5.15) the following expression of the diffuse intensity

$$\mathrm{I}_d(\mathbf{r},\omega)=\int \mathrm{d}\mathbf{r}_1\mathrm{d}\mathbf{r}_2|\langle \mathrm{G}(\mathbf{r},\mathbf{r}_2,\omega)\rangle|^2\,\mathrm{L}(\mathbf{r}_2,\mathbf{r}_1)|\langle \mathrm{E}(\mathbf{r}_1,\omega)\rangle|^2. \tag{5.18}$$

To give an intuitive picture of the ladder approximation, let us expand Eq. (5.18) using Eq. (5.17).

$$\begin{aligned}\mathrm{I}_d(\mathbf{r},\omega)=&\int \mathrm{d}\mathbf{r}_1|\langle \mathrm{G}(\mathbf{r},\mathbf{r}_1,\omega)\rangle|^2\left(\frac{4\pi}{\ell}\right)|\langle \mathrm{E}(\mathbf{r}_1,\omega)\rangle|^2\\&+\int \mathrm{d}\mathbf{r}_1\mathrm{d}\mathbf{r}_2|\langle \mathrm{G}(\mathbf{r},\mathbf{r}_2,\omega)\rangle|^2\left(\frac{4\pi}{\ell}\right)|\langle \mathrm{G}(\mathbf{r}_2,\mathbf{r}_1,\omega)\rangle|^2\left(\frac{4\pi}{\ell}\right)|\langle \mathrm{E}(\mathbf{r}_1,\omega)\rangle|^2+\ldots\end{aligned} \tag{5.19}$$

We have seen in the general introduction of this thesis that wave propagation in scattering media could be described as a random walk, where collisions are scattering events by pointlike heterogeneities (white-noise model). Equation (5.19) gives a rigorous basis to this picture. In this equation, each scattering event is represented by a factor $(4\pi/\ell)$. The propagation between two scattering events is described by the square modulus of the average Green function $|\langle \mathrm{G}(\mathbf{r}_2,\mathbf{r}_1,\omega)\rangle|^2$. Finally, each scattering sequence starts with the ballistic intensity $|\langle \mathrm{E}(\mathbf{r}_1,\omega)\rangle|^2$ at the position of the first scattering event. This representation is sketched in Fig. 5.2. Grey points correspond to scattering events, full lines represent the average Green function, and dashed line its complex conjugate. In the ladder approximation, only the contributions where

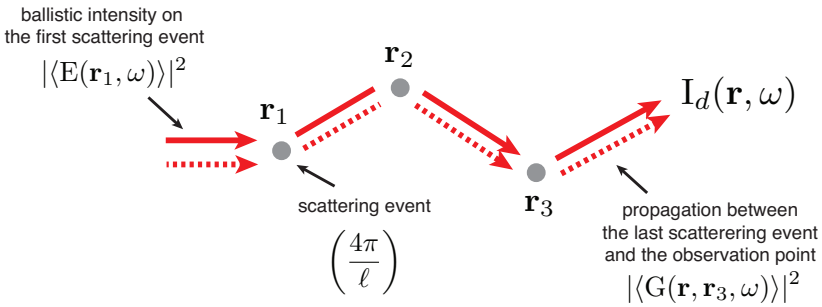


Figure 5.2: Illustration the ladder approximation for the diffuse intensity.

the electric field and its complex conjugate follow one same scattering sequence are taken into account. This approximation is valid to the lowest order in $(k\ell)^{-1}$, i.e. when $\ell \gg \lambda$. This can be understood by considering the contribution to the diffusive intensity of the product $\langle \mathrm{E}_1(\mathbf{r},\omega)\mathrm{E}_2^*(\mathbf{r},\omega)\rangle$ where E_1 and E_2^* are obtained by two scattering paths that differ by one

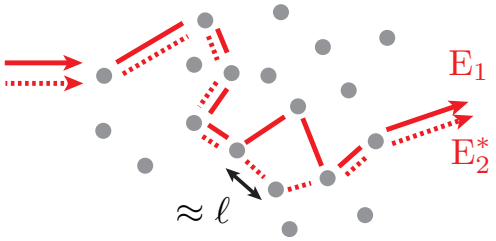


Figure 5.3: Contribution to the diffuse intensity not included in the ladder approximation.

scattering event only (see Fig. 5.3). In the limit where $\ell \gg \lambda$, the phase difference between these two scattering paths can take very large values. Therefore, the average over disorder cancels out the contribution of $\langle \mathrm{E}_1(\mathbf{r},\omega)\mathrm{E}_2^*(\mathbf{r},\omega)\rangle$ to the diffuse intensity.

5.1.4 Long range nature of the reflection-transmission intensity correlation

Let $\mathbf{r}$ and $\mathbf{r}'$ be two observation points. The normalized spatial intensity correlations function is defined as

$$C(\mathbf{r},\mathbf{r}') = \frac{\langle \mathrm{I}(\mathbf{r},\omega)\mathrm{I}(\mathbf{r}',\omega)\rangle}{\langle \mathrm{I}(\mathbf{r},\omega)\rangle\langle \mathrm{I}(\mathbf{r}',\omega)\rangle} - 1. \tag{5.20}$$

Following the picture sketched in Fig. 5.2, the intensity correlation function involves four scattering paths (two for each observation point). Here, we present (without derivation) the leading terms of $C(\mathbf{r},\mathbf{r}')$ for short and long distances between $\mathbf{r}$ and $\mathbf{r}'$. The expressions presented here can be found in textbooks [26, 27]. Discussing the spatial range of the respective contributions, we show that reflection-transmission correlation does not exhibit any short range contribution.

Leading term of the short range correlation

The main contribution to the intensity correlation is called C_1, according to the classification introduced in Ref. [29], and was first computed in Ref. [114]. In its integral form, it is given by

$$\begin{aligned}\langle \mathrm{I}(\mathbf{r})\mathrm{I}(\mathbf{r}')\rangle_1 = \int \mathrm{d}\mathbf{r}_1\,\mathrm{d}\mathbf{r}_2\,\mathrm{d}\mathbf{r}_3\,\mathrm{d}\mathbf{r}_4\,|\langle \mathrm{E}(\mathbf{r}_1)\rangle|^2|\langle \mathrm{E}(\mathbf{r}_3)\rangle|^2\mathrm{L}(\mathbf{r}_2,\mathbf{r}_1)\mathrm{L}(\mathbf{r}_4,\mathbf{r}_3)\\ \times \langle \mathrm{G}(\mathbf{r}_2,\mathbf{r})\rangle\langle \mathrm{G}^*(\mathbf{r}_2,\mathbf{r}')\rangle\langle \mathrm{G}(\mathbf{r}_4,\mathbf{r})\rangle\langle \mathrm{G}^*(\mathbf{r}_4,\mathbf{r}')\rangle.\end{aligned} \tag{5.21}$$

It is convenient to use diagrams to visualize the meaning of Eq. (5.21). The analogy between the integral and diagrammatic representations is described in Table 5.1. The diagram associated to the C_1 correlation is displayed in Fig. 5.4. For the intensities at $\mathbf{r}$ and $\mathbf{r}'$ to be correlated, the scattering paths leading to $\mathbf{r}$ and $\mathbf{r}'$ need to share scattering events, i.e. to cross. In the C_1 correlation, this crossing appears at the position of the last scattering event, and is followed by a straight propagation to the observation points. Therefore, no further propagation inside the medium is possible after the apparition of the correlation, which gives an intuitive picture of its short range character. Interestingly, as a consequence of this short range character, Eq. (5.21)

Diagram	Integral form	Description
Arrows	$\lvert\langle \mathrm{E}(\mathbf{r}_1,\omega)\rangle\rvert^2$	Ballistic intensity
Full horizontal lines	$\langle \mathrm{G}(\mathbf{r}_2,\mathbf{r}_1,\omega)\rangle$	Average Green function
Dashed horizontal lines	$\langle \mathrm{G}^*(\mathbf{r}_2,\mathbf{r}_1,\omega)\rangle$	Conjugate of the average Green function
L-box	$\mathrm{L}(\mathbf{r}_2,\mathbf{r}_1)$	Ladder propagator
H-box	$\mathrm{H}(\boldsymbol{\rho}_1,\boldsymbol{\rho}_2,\boldsymbol{\rho}_3,\boldsymbol{\rho}_4)$	Hikami box (crossing of two ladder propagators)

Table 5.1: Analogy between the integral and diagrammatic representations.

$\langle \mathrm{I}(\mathbf{r},\omega)\mathrm{I}(\mathbf{r}',\omega)\rangle_1 =$

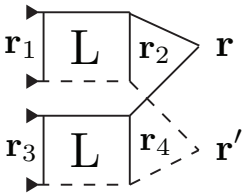


Figure 5.4: Diagrammatic representation of the C_1 correlation.

can be factorized into

$$\langle \mathrm{I}(\mathbf{r})\mathrm{I}(\mathbf{r}')\rangle_1 = \left[\int \mathrm{d}\mathbf{r}_1\,\mathrm{d}\mathbf{r}_2\,|\langle \mathrm{E}(\mathbf{r}_1)\rangle|^2 \mathrm{L}(\mathbf{r}_2,\mathbf{r}_1)\langle \mathrm{G}(\mathbf{r}_2,\mathbf{r})\rangle\langle \mathrm{G}^*(\mathbf{r}_2,\mathbf{r}')\rangle\right]^2. \tag{5.22}$$

Leading term of the long range correlation

As we shall see below, for distances larger than ℓ, the short range correlation C_1 is exponentially decaying, and one needs to consider higher order diagrams. Following the picture that we used to understand the short range character of the C_1 correlation, a crossing between scattering paths inside the medium is necessary to obtain a long range correlation. This crossing was first described to leading order of $(k\ell)^{-1}$ in Ref. [120], and is represented by a Hikami box. The long range correlation induced by such crossings was first computed in Ref. [115], and is denoted by C_2 [29]. Its diagram is displayed in Fig. 5.5. The ladder propagators between $\boldsymbol{\rho}_2$, $\boldsymbol{\rho}_4$ (associated

$\langle \mathrm{I}(\mathbf{r},\omega)\mathrm{I}(\mathbf{r}',\omega)\rangle_2 =$

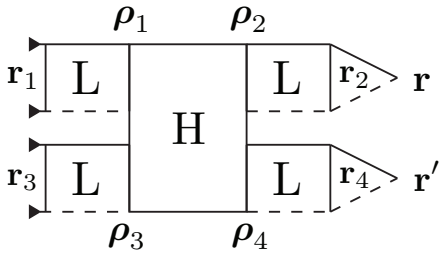


Figure 5.5: Diagrammatic representation of the C_2 correlation.

to the Hikami box) and $\mathbf{r}_2$, $\mathbf{r}_4$ (last scattering events) allow $\mathbf{r}$ and $\mathbf{r}'$ to be separated by large

distances. In its integral form, the C_2 correlation is given by

$$\langle \mathrm{I}(\mathbf{r})\mathrm{I}(\mathbf{r}')\rangle_2 = \int \mathrm{d}\mathbf{r}_1\,\mathrm{d}\mathbf{r}_2\,\mathrm{d}\mathbf{r}_3\,\mathrm{d}\mathbf{r}_4 \int \mathrm{d}\boldsymbol{\rho}_1\,\mathrm{d}\boldsymbol{\rho}_2\,\mathrm{d}\boldsymbol{\rho}_3\,\mathrm{d}\boldsymbol{\rho}_4\,|\langle \mathrm{E}(\mathbf{r}_1)\rangle|^2|\langle \mathrm{E}(\mathbf{r}_3)\rangle|^2\mathrm{L}(\boldsymbol{\rho}_1,\mathbf{r}_1)\mathrm{L}(\boldsymbol{\rho}_3,\mathbf{r}_3) \times \mathrm{H}(\boldsymbol{\rho}_1,\boldsymbol{\rho}_2,\boldsymbol{\rho}_3,\boldsymbol{\rho}_4)\mathrm{L}(\mathbf{r}_2,\boldsymbol{\rho}_2)\mathrm{L}(\mathbf{r}_4,\boldsymbol{\rho}_4)|\langle \mathrm{G}(\mathbf{r},\mathbf{r}_2)\rangle|^2|\langle \mathrm{G}(\mathbf{r}',\mathbf{r}_4)\rangle|^2, \tag{5.23}$$

where $\mathrm{H}(\boldsymbol{\rho}_1,\boldsymbol{\rho}_2,\boldsymbol{\rho}_3,\boldsymbol{\rho}_4)$ is the Hikami box, given by (see Ref. [27])

$$\mathrm{H}(\boldsymbol{\rho}_1,\boldsymbol{\rho}_2,\boldsymbol{\rho}_3,\boldsymbol{\rho}_4) = h\int \mathrm{d}\boldsymbol{\rho}\prod_{i=1}^{4}\delta(\boldsymbol{\rho}-\boldsymbol{\rho}_i)\boldsymbol{\nabla}_2\cdot\boldsymbol{\nabla}_4, \tag{5.24}$$

where $\boldsymbol{\nabla}_2$,$\boldsymbol{\nabla}_4$ are gradient operators acting on the two output ladder propagators and $h = l^5/(48\pi k^2)$. Note that an equivalent formulation exists, where the gradient operators act on the input ladder propagators [27].

Orders of magnitude

In Ref. [114], it was shown that in an infinite medium, the short range correlation reads

$$C_1(\Delta r) = \left(\frac{\sin(k\Delta r)}{k\Delta r}\right)\exp\left(-\frac{\Delta r}{\ell}\right), \tag{5.25}$$

where Δr is the distance between the two points. Note that this correlation decays exponentially with Δr, on a typical distance of one scattering mean free path (short range). In Ref. [115], it was shown that for two points located on the output plane of a slab, the long range correlation reads[4]

$$C_2(\Delta r) = \frac{1}{24(k\ell)^2}\left(\frac{\ell}{d}\right)\left[\frac{1}{2}\int_0^\infty J_0(q\Delta r/L_e)\left\{\frac{\sinh(2q)-2q}{\sinh^2(q)}-2\right\}\mathrm{d}q+\frac{d}{\Delta r}\right], \tag{5.26}$$

where J_0 is the Bessel function of first kind and zero order, defined as

$$J_0(x) = \frac{1}{\pi}\int_0^\pi \mathrm{d}\theta\,\exp(ix\cos\theta). \tag{5.27}$$

Note that this expression diverges for small distances Δr because of an approximation detailed in Appendix F. An exact expression, valid at short distance, but less convenient from a numerical point of view is given by

$$C_2(\Delta r) = \frac{3}{76(k\ell)^2}\frac{d}{\ell}\int_0^\infty J_0(q\Delta r/d)\frac{\sinh^2(q\ell_e/d)}{q^2}\frac{\sinh(2q)-2q}{\sinh^2(q)}\,\mathrm{d}q. \tag{5.28}$$

In Fig. 5.6, we display both the C_1 correlation in the case of an infinite medium and the C_2 correlation in the output plane of a slab versus the distance between the observation points Δr. For the sake of simplicity, we have not considered the slab geometry in the calculation of the C_1 correlation here, since our purpose is to qualitatively compare the orders of magnitude of each

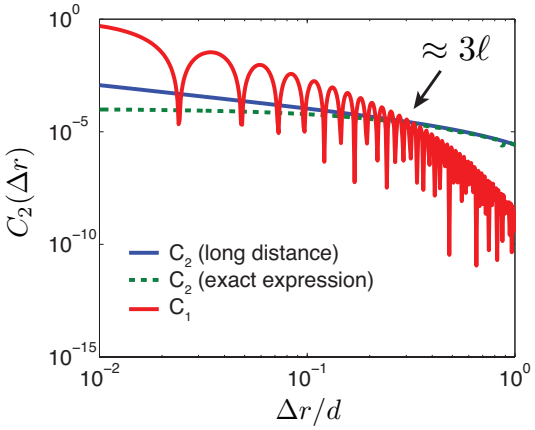


Figure 5.6: (Red full line) short range correlation C_1 for an infinite medium [Eq. (5.25)]; (Green dashed line) long range correlation C_2 for a slab of thickness d [exact expression Eq. (5.28)]; (Blue full line) long range correlation C_2 in the same slab (approached expression for long distances Eq. (5.26)). Δr is the distance between the observation points. Parameters are coherent with Ref. [116]: $d = 13\,\mu$m; $\ell = 1.35\,\mu$m; $\lambda = 628\,$nm. The long range correlation at the origin is $C_2(\Delta r = 0) \approx 10^{-4}$.

contribution. The parameters are consistent with those used in Ref. [116]. Figure 5.6 shows that the C_1 correlation is the leading term for distances $\Delta r \leq 3\ell$. The C_2 correlation is the dominant term for larger distances.

Leading diagram for the reflection-transmission intensity correlation

In the case of the reflection-transmission intensity correlation, the minimum distance between two observation points is the thickness of the slab d. For a slab in the multiple-scattering regime ($d \gg \ell$) the C_1 correlation has an exponentially small contribution. Hence, to compute the leading contribution, one needs to consider a C_2 diagram. In Fig. 5.7, we display both the corresponding diagram and the input and output planes of a slab of disordered medium. This diagram gives an intuitive picture of this correlation. After a crossing inside the medium, described by a Hikami box, two ladder propagators reach both sides of the slab and create a correlation between the two observation points.

5.2 Reflection-Transmission intensity correlation

Based on the formalism described in section 5.1, we now compute an explicit expression of the reflection-transmission intensity correlation for a slab geometry in the diffusion approximation.

[4]The prefactor given here differs from the reference, and corresponds to the calculation proposed in Appendix F. It is coherent with the computation performed in section 5.2. Different prefactors were found in other references [121, 122].

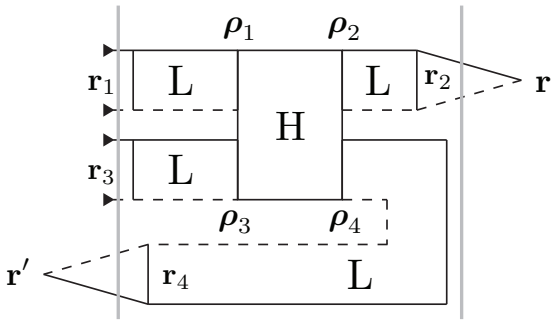


Figure 5.7: Diagrammatic representation of the reflection-transmission C_2 correlation. Grey lines represent the slab interfaces.

5.2.1 Geometry of the system and assumptions

We consider a slab of disordered media of thickness d in the z direction, infinite in both x and y directions, as sketched in Fig. 5.8. We assume that the medium is non-absorbing and satisfies $\lambda \ll \ell \ll d$ (mesoscopic regime). A plane-wave propagating along the z direction is illuminating the system. In this geometry one can solve the Dyson equation [Eq. (5.7)] and show that the

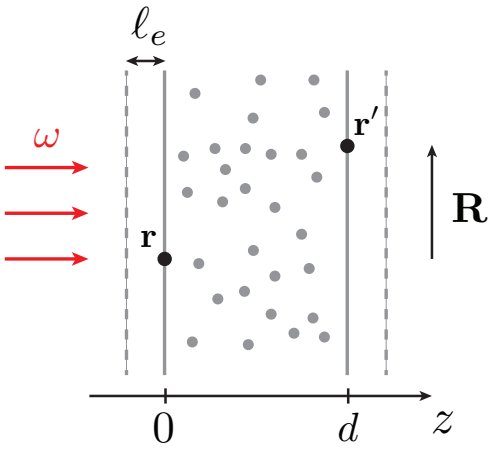


Figure 5.8: Geometry of the system.

ballistic intensity reads

$$I_b(\mathbf{r}) = \exp\left(-\frac{z}{\ell}\right), \tag{5.29}$$

for an incident plane wave of unit intensity. We consider two observation points $\mathbf{r} = \mathbf{0}$ and $\mathbf{r}' = \mathbf{R} + d\,\mathbf{e}_z$, respectively in the input plane $z = 0$ and the output plane $z = d$ of the slab.

5.2.2 Ladder propagator for a slab in the diffusion approximation

Let us consider the ladder propagator, solution of Eq. (5.17). The diffusion approximation amounts to a spatial Taylor expansion to second order of the ladder propagator $\mathrm{L}(\mathbf{r}_3, \mathbf{r}_1)$ in the

integral of Eq. (5.17)

$$\mathrm{L}(\mathbf{r}_3,\mathbf{r}_2) \approx \mathrm{L}(\mathbf{r}_2,\mathbf{r}_1) + (\mathbf{r}_3-\mathbf{r}_1)\cdot\boldsymbol{\nabla}_{\mathbf{r}_2}\mathrm{L}(\mathbf{r}_2,\mathbf{r}_1) + \frac{|\mathbf{r}_3-\mathbf{r}_2|^2}{2}\boldsymbol{\nabla}^2_{\mathbf{r}_1}\mathrm{L}(\mathbf{r}_2,\mathbf{r}_1). \tag{5.30}$$

Performing the integral in Eq. (5.17) using Eq. (5.30), only the second-order term remains, and Eq. (5.17) transforms into

$$\boldsymbol{\nabla}^2_{\mathbf{r}_2}\mathrm{L}(\mathbf{r}_2,\mathbf{r}_1) = -\frac{4\pi}{\ell^3}\delta(\mathbf{r}_2-\mathbf{r}_1), \tag{5.31}$$

which is a diffusion equation for the ladder propagator. As a consequence of translational invariance along x and y in the slab geometry, $\mathrm{L}(\mathbf{r}_2,\mathbf{r}_1)$ is a function of $\mathbf{R}_2-\mathbf{R}_1$, z_2 and z_1 only, where $\mathbf{r}_{1,2} = \mathbf{R}_{1,2} + z_{1,2}\,\mathbf{e}_z$. It is convenient to work in Fourier space with respect to $\mathbf{R}_2-\mathbf{R}_1$ to obtain an analytical expression of L. The diffusion equation satisfied by $\mathrm{L}(\mathbf{R}_2-\mathbf{R}_1,z_2,z_1)$ turns into a one-dimensional diffusion equation satisfied by $\mathrm{L}(\mathbf{K},z_2,z_1)$ in Fourier space

$$\partial^2_{z_2}\mathrm{L}(\mathbf{K},z_2,z_1) - K^2\mathrm{L}(\mathbf{K},z_2,z_1) = -\frac{4\pi}{\ell^3}\delta(z_2-z_1). \tag{5.32}$$

To solve Eq. (5.32), one needs to specify boundary conditions, which needs to be done with care. Details can be found in Ref. [25]. The most common solution to this problem is to introduce an *extrapolation length* ℓ_e (see Fig. 5.8), so that

$$\mathrm{L}(\mathbf{K},z_2=-\ell_e,z_1) = \mathrm{L}(\mathbf{K},z_2=d+\ell_e,z_1) = 0. \tag{5.33}$$

Under these conditions, the expression of the ladder propagator in Fourier space reads (see Ref. [27])

$$\mathrm{L}(K,z_2,z_1) = \frac{4\pi}{K\ell^3}\frac{\sinh\left[K\left(z_<+\ell_e\right)\right]\sinh\left[K\left(d+\ell_e-z_>\right)\right]}{\sinh\left(Kd_e\right)}, \tag{5.34}$$

where $d_e = d+2\ell_e$ is the extrapolated thickness of the slab, $z_< = \min(z_1,z_2)$ and $z_> = \max(z_1,z_2)$. The extrapolation length ℓ_e can be computed using the "P_1 approximation", that leads to [25, 123]

$$\ell_e = \frac{2\ell}{3}. \tag{5.35}$$

Let us stress that the diffusion approximation describes accurately the propagation on distances large compared to the scattering mean free paths ℓ. Therefore, the diffusion approximation fails to describe the ladder propagator for short distances. To go beyond this assumption, one needs to perform numerical simulations based on the Radiative Transport Equation (RTE) [25, 124], which is beyond the scope of the present work.

5.2.3 Diffuse intensity inside the slab

The diffuse intensity is expressed using the ladder propagator in Eq. (5.18). In the diffusion approximation, $L(\mathbf{r}_1,\mathbf{r}_2) \approx L(\mathbf{r},\mathbf{r}_2)$ and the integral over $\mathbf{r}_1$ can be performed. Equation (5.18) transforms into

$$\mathrm{I}_d(\mathbf{r},\omega) = \frac{\ell}{4\pi}\int \mathrm{d}\mathbf{r}_2\,\mathrm{L}(\mathbf{r},\mathbf{r}_2)|\langle\mathrm{E}(\mathbf{r}_2,\omega)\rangle|^2. \tag{5.36}$$

Introducing the Fourier transform of $\mathrm{L}(\mathbf{r},\mathbf{r}_2)$ along $\mathbf{R}-\mathbf{R}_2$, the integrals over $\mathbf{R}_2$ and $\mathbf{K}$ can be performed and yield

$$\mathrm{I}_d(\mathbf{r},\omega)=\frac{\ell}{4\pi}\int_0^d \mathrm{d}z_2\,\mathrm{L}(K=0,z,z_2)\exp(-z_2/\ell). \tag{5.37}$$

Using Eq. (5.34) and performing the integral over z_2, one obtains

$$\mathrm{I}_d(z,\omega)=\frac{5}{3}\frac{d-z+\ell_e}{d}. \tag{5.38}$$

5.2.4 Intensity correlation between reflection and transmission

The long range correlation displayed for the reflection-transmission geometry in Fig. 5.7 is given in its integral form by Eq. (5.23). Using the expression of the average intensity in the slab given by Eq. (5.38), its contribution to the correlation as defined in Eq. (5.20) reads

$$\begin{aligned}C_2(\mathbf{r},\mathbf{r}',\omega)=\left[\langle\mathrm{I}(\mathbf{r})\rangle\langle\mathrm{I}(\mathbf{r}')\rangle\right]^{-1}\int \mathrm{d}\mathbf{r}_1\,\mathrm{d}\mathbf{r}_2\,\mathrm{d}\mathbf{r}_3\,\mathrm{d}\mathbf{r}_4\int \mathrm{d}\boldsymbol{\rho}_1\,\mathrm{d}\boldsymbol{\rho}_2\,\mathrm{d}\boldsymbol{\rho}_3\,\mathrm{d}\boldsymbol{\rho}_4\,|\langle\mathrm{E}(\mathbf{r}_1)\rangle|^2|\langle\mathrm{E}(\mathbf{r}_3)\rangle|^2\\ \times\mathrm{L}(\boldsymbol{\rho}_1,\mathbf{r}_1)\mathrm{L}(\boldsymbol{\rho}_3,\mathbf{r}_3)\mathrm{H}(\boldsymbol{\rho}_1,\boldsymbol{\rho}_2,\boldsymbol{\rho}_3,\boldsymbol{\rho}_4)\mathrm{L}(\mathbf{r}_2,\boldsymbol{\rho}_2)\mathrm{L}(\mathbf{r}_4,\boldsymbol{\rho}_4)|\langle\mathrm{G}(\mathbf{r},\mathbf{r}_2)\rangle|^2|\langle\mathrm{G}(\mathbf{r}',\mathbf{r}_4)\rangle|^2.\end{aligned} \tag{5.39}$$

In Eq. (5.39), the integrals on $\mathbf{r}_1$ and $\mathbf{r}_3$ yield twice the diffuse intensities at $\boldsymbol{\rho}_1$ and $\boldsymbol{\rho}_3$, as can be seen from Eq. (5.36). Moreover, we make the diffusion approximation: $\mathrm{L}(\mathbf{r}_2,\boldsymbol{\rho}_2)\approx\mathrm{L}(\mathbf{r},\boldsymbol{\rho}_2)$ and $\mathrm{L}(\mathbf{r}_4,\boldsymbol{\rho}_4)\approx\mathrm{L}(\mathbf{r}',\boldsymbol{\rho}_4)$. This allows to perform the integrals on $\mathbf{r}_2$ and $\mathbf{r}_4$. Using Eq. (5.24), Eq. (5.23) transforms into

$$C_2(\mathbf{r},\mathbf{r}',\omega)=\left[\langle\mathrm{I}(\mathbf{r})\rangle\langle\mathrm{I}(\mathbf{r}')\rangle\right]^{-1}h\int \mathrm{d}\boldsymbol{\rho}\,\mathrm{I}_d(\boldsymbol{\rho},\omega)^2\,\boldsymbol{\nabla}_{\boldsymbol{\rho}}\mathrm{L}(\mathbf{r},\boldsymbol{\rho})\cdot\boldsymbol{\nabla}_{\boldsymbol{\rho}}\mathrm{L}(\mathbf{r}',\boldsymbol{\rho}). \tag{5.40}$$

Let us introduce $\boldsymbol{\rho}_\perp$ and z_1 such that $\boldsymbol{\rho}$ into $\boldsymbol{\rho}=\boldsymbol{\rho}_\perp+z_1\mathbf{e}_z$. Expanding $\mathrm{L}(\mathbf{r},\boldsymbol{\rho})$ and $\mathrm{L}(\mathbf{r}',\boldsymbol{\rho})$ in the transverse Fourier space and performing the two gradient operators, Eq. (5.40) becomes

$$\begin{aligned}C_2(\mathbf{r},\mathbf{r}',\omega)=\left[\langle\mathrm{I}(z)\rangle\langle\mathrm{I}(z')\rangle\right]^{-1}h\int \mathrm{d}z_1\,\frac{\mathrm{d}\mathbf{K}\mathrm{d}\mathbf{K}'}{(2\pi)^4}\,\mathrm{I}_d(z_1)\exp\left[i\mathbf{K}'\cdot\mathbf{R}\right]\int\exp\left[-i\boldsymbol{\rho}_\perp\cdot\left(\mathbf{K}+\mathbf{K}'\right)\right]\mathrm{d}\boldsymbol{\rho}_\perp\\ \times\left[-i\mathbf{K}\mathrm{L}(K,z,z_1)+\partial_z\mathrm{L}(K,z,z_1)\mathbf{e}_z\right]\cdot\left[-i\mathbf{K}'\mathrm{L}(K',z',z_1)+\partial_z\mathrm{L}(K,z',z_1)\mathbf{e}_z\right].\end{aligned} \tag{5.41}$$

Performing the integral upon $\boldsymbol{\rho}_\perp$ yields a function $\delta(\mathbf{K}+\mathbf{K}')$. Performing the integral upon $\mathbf{K}'$ and using the parity of $\mathrm{L}(K,z,z_1)$ upon variable K, Eq. (5.42) can be transformed into

$$C_2(\mathbf{r},\mathbf{r}',\omega)=\int\frac{\mathrm{d}\mathbf{K}}{(2\pi)^2}\,\exp\left[-i\mathbf{K}\cdot\mathbf{R}\right]F(Kd), \tag{5.42}$$

where

$$\begin{aligned}F(Kd)=\left[\langle\mathrm{I}(z)\rangle\langle\mathrm{I}(z')\rangle\right]^{-1}h\int_0^d\mathrm{d}z_1\,\mathrm{I}_s(z_1)^2\\ \times\left[\mathrm{L}(K,z,z_1)\mathrm{L}(K,z',z_1)K^2+\partial_{z_1}\mathrm{L}(K,z,z_1)\partial_{z_1}\mathrm{L}(K,z',z_1)\right].\end{aligned} \tag{5.43}$$

Eq. (5.42) is valid whatever the coordinates z and z'[5]. In the present case, $z = 0$ and $z' = d$. The average intensity at both positions can be deduced from Eqs. (5.29) and (5.38), and respectively read $\langle \mathrm{I}(z=0)\rangle = 8/3$ and $\langle \mathrm{I}(z=d)\rangle = 10\ell/(9d)$. Replacing L by its expression, and using $h = \ell^5/(48\pi k^2)$ yields

$$F(Kd) = \frac{5\pi}{16k^2 d\ell^2}\frac{\sinh^2(K\ell_e)}{\sinh^2(Kd)}\int_0^d \mathrm{d}z_1\,(d - z_1 + \ell_e)^2\cosh\left[K(d-2z_1)\right]. \tag{5.44}$$

Performing the integral (see useful integrals in Appendix F) leads to

$$F(Kd) = \frac{5\pi}{16k^2 d\ell^2}\frac{\sinh^2(K\ell_e)}{\sinh^2(Kd)}\frac{(K^2d^2+1)\sinh(Kd) - Kd\cosh(Kd)}{2K^3}. \tag{5.45}$$

Inserting Eq. (5.45) into Eq. (5.42), and introducing the Bessel function of first kind and zero order J_0, defined as

$$J_0(x) = \frac{1}{\pi}\int_0^\pi \mathrm{d}\theta\exp(ix\cos\theta), \tag{5.46}$$

one obtains, by making the change of variable $q = Kd$,

$$C_2(\mathbf{r},\mathbf{r}',\omega) = \frac{-5}{128(k\ell)^2}\int_0^\infty J_0(q\Delta r/d)\frac{\sinh^2(q\ell_e/d)}{q^2}\frac{-q\cosh q + (q^2+1)\sinh q}{\sinh^2(q)}\,\mathrm{d}q, \tag{5.47}$$

where $\Delta r = |\mathbf{R}|$ is the transverse distance between $\mathbf{r}$ and $\mathbf{r}'$ (see Fig. 5.8). The integral in Eq. (5.47) can be estimated for $q\ell_e/d \ll 1$, since the integrand behaves as $\exp(-q)$ for large values of q and $d \gg \ell_e$ (multiple-scattering). Therefore, Eq. (5.47) transforms into

$$C_2(\Delta r,\omega) = \frac{-5}{288(k\ell)^2}\left(\frac{\ell}{d}\right)^2\int_0^\infty J_0(q\Delta r/d)\frac{-q\cosh q + (q^2+1)\sinh q}{\sinh^2(q)}\,\mathrm{d}q, \tag{5.48}$$

Equation (5.48) is the main result of this chapter. It gives the leading term to the intensity correlation between one point in the input plane $z = 0$ and another in the output plane $z = d$, as a function of their transverse distance Δr. The correlation is displayed in Fig. (5.9) versus $\Delta r/d$.

5.2.5 Discussion

One can see in Fig. 5.9 that the value of the correlation for two points aligned in the transverse direction, i.e. when $\mathbf{R} = \mathbf{0}$, is of the order of -3.10^{-6}. This value can be compared to the value of the same long range correlation between two points in the output plane $z = z' = d$, that is plotted in Fig. 5.6. For a vanishing distance, this correlation tends to 10^{-4}. The two correlations have the same physical origin, and the difference between these two values have two origins. First, the normalization is different, since the average intensity in the input plane is much higher than that of the output plane. Second, for a same value of the transverse distance

[5]The calculation in the case where $z = z' = d$ is detailed in Appendix F.

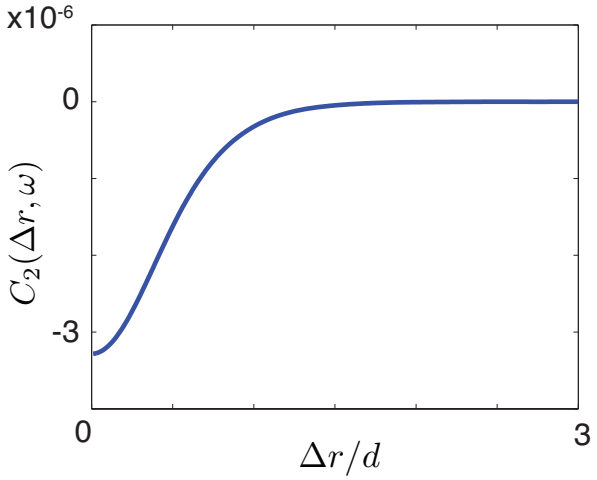


Figure 5.9: Intensity correlation between two points $\mathbf{r}$ and $\mathbf{r}'$ respectively in the input plane $z = 0$ and the output plane $z = d$ of the slab represented in Fig. 5.8. $\Delta r = |\mathbf{R}|$ is the transverse distance between $\mathbf{r}$ and $\mathbf{r}'$. Parameters are coherent with Ref. [116]: $d = 13\,\mu$m; $\ell = 1.35\,\mu$m; $\lambda = 628\,$nm.

Δr, the real distance between the observation points is higher in the reflection/transmission case. Interestingly, the reflection/transmission correlation is negative, meaning that a high intensity at point $\mathbf{r}$ will most likely lead to a lower intensity at point $\mathbf{r}' = \mathbf{r} + d\mathbf{e}_z$. This result is highly non-intuitive, and was already observed in the diffusive regime in Luis Froufe's thesis [125], using a Random Matrix Theory. Positive correlations were observed in non-diffusive regimes. Unfortunately, we cannot probe these regimes in the framework of the ladder approximation.

Let us comment on the approximations made in the calculation leading to Eq. (5.48). The use of the diffusive approximation does not describe accurately the propagation on short scattering paths. The main consequence of this approximation is that the contribution to the correlation of crossings between ladder propagators occurring within few scattering mean free paths of the entry or output planes are not correctly described by our model. This problem can be addressed numerically by computing the ladder propagator in the slab geometry using the Radiative Transfer Equation (RTE). All results presented in section 5.1 are independent on the diffusion approximation and could be the base of a future study.

However, the level of approximation used in this chapter is the same than the one used in the early calculations of speckle intensity correlations [114, 115]. The success of these calculations to predict experimental observations [121, 116] is an encouraging sign of the relevance of our approach. Before going further with the theory, we believe that an experimental study would be of tremendous interest.

5.3 Conclusion

To conclude, we have studied the reflection-transmission intensity correlation in speckle patterns in the framework of the ladder approximation. We have showed that this correlation has no short range contribution, and that its leading term needs to be described by a C_2 diagram, involving a Hikami box. We have obtained an analytical expression of this leading term for an infinite slab in the diffusion approximation. Surprisingly, the correlation is negative, meaning that two opposite points having the same transverse coordinates are anti-correlated.

A first perspective of this work is obviously to work in collaboration with experimentalists and observe this correlation. This is under progress, and should be the first step before the development of a more sophisticated theoretical model. One way to improve our model would be to go beyond the diffusion approximation, using numerical simulations based on the RTE, in order to accurately describe the contribution of short scattering paths to the correlation. While these short paths may have a negligible influence in transmission-transmission correlations, in the reflection-transmission correlation, it could be more problematic due to the influence of crossing occurring close to the input interface.

The control of the propagation of waves through complex media has been very active in the past few years [126]. One major drawback of the experimental setups involved to control the transmitted speckle is the necessity for a feedback on the transmitted side of the medium. For applications such as imaging, getting rid of this feedback would be of tremendous importance. Recently, a fluorescent object was imaged through a diffusive slab without feedback, using the memory effect (short range speckle correlations) [127]. Our work paves the way to future ideas taking advantage of the statistical connection between the transmitted and the reflected speckle to go beyond the use of this feedback.

Chapter 6

Near-field interactions and nonuniversality of the C_0 correlation

Contents

6.1 C_0 equals the normalized fluctuations of the LDOS 98
6.1.1 The C_0 correlation equals the fluctuations of the normalized LDOS . . . 99
6.1.2 Physical origin of the C_0 correlation 100
6.2 Long-tail behavior of the LDOS distribution 101
6.2.1 The "one-scatterer" model 101
6.2.2 Asymmetric shape of the LDOS distribution: Numerical results 104
6.3 C_0 is sensitive to disorder correlations 106
6.3.1 The effective volume fraction: a "correlation parameter" 107
6.3.2 LDOS distribution and correlation parameter 107
6.3.3 C_0 and correlation parameter 108
6.4 Conclusion and perspectives 109

When a disordered medium is illuminated by coherent light, the random scattering paths inside the medium interfere to create a random intensity pattern called *speckle*. The spatial structure of a speckle pattern is often characterized by the intensity spatial correlation function $\langle I(\mathbf{r})I(\mathbf{r}')\rangle$. In usual experiments the medium is illuminated by an external beam, and the speckle pattern is observed, e.g., in transmission. Short-range and long-range contributions can be identified in the intensity correlation function, which is written as a sum of three terms denoted by C_1 (short range), C_2, and C_3 (long range) [29]. These correlations have been widely studied since they are responsible for enhanced mesoscopic fluctuations [27] and their sensitivity to changes in the medium can be used for imaging in complex media [128]. More details on this approach are given in Chap 5. When a source is embedded *inside* a medium, as in Fig. 6.1, the situation is slightly different. A new contribution to the intensity correlations, fundamentally different from the previous ones, appears [28]. This contribution has been called C_0. It has

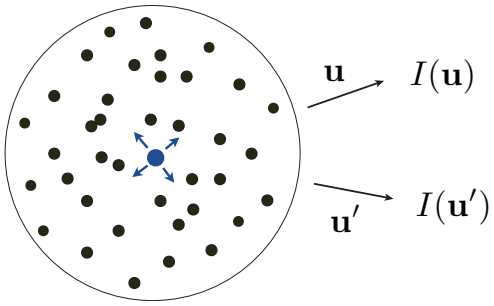


Figure 6.1: Light source embedded inside a disordered medium. We study the correlations between $I(\mathbf{u})$ and $I(\mathbf{u}')$, defined as the power per solid angle radiated by the source in the far field in directions defined by the unit vectors $\mathbf{u}$ and $\mathbf{u}'$.

infinite range, and is nonuniversal, in the sense that it does not only depend on macroscopic properties (mean free path, effective index, ...) but varies dramatically with the local environment of the source [30]. In an infinite nonabsorbing medium, it has been shown that C_0 equals the normalized fluctuations of the LDOS at the source position [31].

To our knowledge, all published works on C_0 rely on the diagrammatic approach. Though, despite of its undeniable power of prediction, the diagrammatic approach fails to give a simple physical picture of C_0. Moreover, it implies a scalar model of light that does not include near-field interactions, and requires a weakly disordered medium.

In this chapter, we present a non-diagrammatic approach of C_0, based on LDOS fluctuations and energy conservation. We generalize the equality of Ref. [31] to 3D electromagnetic waves interacting with any strength of disorder, including the Anderson localization regime, and we propose a simple and robust physical picture of C_0. Based on this picture, we present 3D exact numerical calculations of LDOS distributions, and show the sensitivity of their normalized variance C_0 to the correlations of disorder, as predicted in [30]. Analysing the numerical data with an approximate analytical model, we demonstrate the fundamental role of near-field interactions in the appearance of C_0.

This work has been published in Physical Review A [129].

6.1 C_0 equals the normalized fluctuations of the LDOS

We propose a new approach to demonstrate the equality between C_0 and the normalized variance of the LDOS, that was first derived in [31]. Our demonstration relies essentially on energy conservation, and is independent of the strength of the disorder inside the medium. It takes into account the vector nature of light. Using this new approach allows us to understand in simple terms the appearance of the C_0 correlation.

6.1.1 The C_0 correlation equals the fluctuations of the normalized LDOS

Let us consider a disordered medium embedded inside a sphere of radius R. At the center $\mathbf{r}_s$ of this sphere lies an electric-dipole source with moment $\mathbf{p}$, radiating at frequency ω.

We assume that the system is *nonabsorbing*. In this case, the power radiated outside the system P is equal to the power transferred by the emitter to its environment. Hence, averaged upon dipole orientation, it is proportional to the LDOS $\rho(\mathbf{r}_s, \omega)$ and reads [68]

$$P = \frac{\pi\omega^2}{12\epsilon_0}|\mathbf{p}|^2\rho(\mathbf{r}_s, \omega). \tag{6.1}$$

Denoting ρ_0 and P_0, respectively, the LDOS and the radiated power in vacuum, Eq. (6.1) can be normalized to give

$$\boxed{\frac{P}{P_0} = \frac{\rho(\mathbf{r}_s, \omega)}{\rho_0(\omega)}.} \tag{6.2}$$

As a characterization of the far-field speckle produced by the point source, we consider the angular intensity correlation function[1]

$$C(\mathbf{u}, \mathbf{u}') = \frac{\langle I(\mathbf{u})I(\mathbf{u}')\rangle}{\langle I(\mathbf{u})\rangle\langle I(\mathbf{u}')\rangle} - 1 \tag{6.3}$$

where $I(\mathbf{u})$ is the radiated power in the direction defined by the unit vector $\mathbf{u}$ (as illustrated in Fig. 6.1), such that

$$P = \int_{4\pi} I(\mathbf{u})\mathrm{d}\mathbf{u}. \tag{6.4}$$

From Eqs. (6.2), (6.3), and (6.4) the fluctuations of the normalized LDOS can be written

$$\begin{aligned}\left\langle \frac{\rho(\mathbf{r}_s, \omega)^2}{\rho_0(\omega)^2} \right\rangle &= \left\langle \frac{P^2}{P_0^2} \right\rangle \\ &= \frac{1}{P_0^2}\int\int \langle I(\mathbf{u})I(\mathbf{u}')\rangle \mathrm{d}\mathbf{u}\,\mathrm{d}\mathbf{u}'. \\ &= \frac{1}{P_0^2}\int\int \langle I(\mathbf{u})\rangle\langle I(\mathbf{u}')\rangle \left[C(\mathbf{u}, \mathbf{u}') + 1\right] \mathrm{d}\mathbf{u}\,\mathrm{d}\mathbf{u}'\end{aligned} \tag{6.5}$$

The second assumption we make concerning the medium is *statistical isotropy*. Under this assumption, the averaged directional radiated power $\langle I(\mathbf{u})\rangle$ is independent of the direction $\mathbf{u}$. Using Eq. (6.2), it reduces to

$$\begin{aligned}\langle I(\mathbf{u})\rangle &= \frac{1}{4\pi}\langle P\rangle \\ &= \left(\frac{P_0}{4\pi}\right)\frac{\langle\rho(\mathbf{r}_s, \omega)\rangle}{\rho_0(\omega)}.\end{aligned} \tag{6.6}$$

[1] $C(\mathbf{u}, \mathbf{u}')$ is the angular counterpart of the spatial intensity correlation $C(\mathbf{r}, \mathbf{r}') = \langle \mathrm{I}(\mathbf{r})\mathrm{I}(\mathbf{r}')\rangle$, studied in Chap. 5.

Moreover, the angular intensity correlation is a function of $x = \mathbf{u} \cdot \mathbf{u}'$. Inserting Eq. (6.6) into Eq. (6.5) yields

$$\begin{aligned} \frac{\langle \rho(\mathbf{r}_s, \omega)^2 \rangle}{\langle \rho(\mathbf{r}_s, \omega) \rangle^2} &= 1 + \frac{1}{16\pi^2} \int \int C(\mathbf{u} \cdot \mathbf{u}') \mathrm{d}\mathbf{u}\, \mathrm{d}\mathbf{u}'. \\ &= 1 + \int_{-1}^{1} C(x)\, \mathrm{d}x. \end{aligned} \tag{6.7}$$

As a continuous function defined on $[-1, 1]$, the correlation function $C(x)$ can be expanded on the basis of Legendre polynomials in the form

$$C(x) = \sum_{n=0}^{\infty} a_n L_n(x). \tag{6.8}$$

Since $L_0 = 1$, the first term is constant and corresponds to an infinite range correlation. We define the C_0 correlation as that given by the constant term, so that $a_0 = C_0$. The integral in Eq. (6.7) is performed by writing

$$C(x) = \sum_{n=0}^{\infty} a_n L_0(x) L_n(x), \tag{6.9}$$

and using the orthogonality relation of Legendre polynomials

$$\int_{-1}^{1} L_n(x) L_m(x) \mathrm{d}x = \frac{2\delta_{nm}}{2n+1}, \tag{6.10}$$

where δ_{nm} is the Kronecker delta. We finally obtain

$$\boxed{C_0 = \frac{\langle \rho(\mathbf{r}_s, \omega)^2 \rangle}{\langle \rho(\mathbf{r}_s, \omega) \rangle^2} - 1 = \frac{\mathrm{Var}\left[\rho(\mathbf{r}_s, \omega)\right]}{\langle \rho(\mathbf{r}_s, \omega) \rangle^2}.} \tag{6.11}$$

Eq. (6.11) shows that the C_0 speckle correlation and the normalized variance of the LDOS at the position of the emitter are the same, a result that was first derived in [31] based on a diagrammatic approach. Our derivation relies only on energy conservation and the assumption of a nonabsorbing and statistically isotropic medium. In particular, Eq. (6.11) holds in all wave transport regimes, from weakly scattering to strongly scattering, including Anderson localization.

6.1.2 Physical origin of the C_0 correlation

An important feature of our derivation is that it leads to a simple interpretation of the C_0 correlation. Energy conservation induces correlations between $I(\mathbf{u})$ and $I(\mathbf{u}')$, respectively the power radiated per unit solid angle in directions $\mathbf{u}$ and $\mathbf{u}'$ (see Fig 6.1). Intuitively, radiating more in direction $\mathbf{u}$ forbids to radiate too much in another direction $\mathbf{u}'$. This constraint is mediated

by the value of the radiated power P, that is driven itself by the LDOS at the position of the emitter. Fluctuations of the LDOS for various disorder configurations induce a modification of the constraint of energy conservation and hence a modification of the angular intensity correlation. This modification is a constant background correlation called the C_0 correlation, and is exactly equal to the normalized variance of the LDOS if absorption in the medium can be neglected. Recently, a direct observation of this constant background in the speckle correlation was reported in acoustic experiments using ultrasounds [130].

6.2 Near-field interactions and long-tail behavior of the LDOS distribution

We have seen that the appearance of the C_0 correlation was intimately connected to fluctuations of the LDOS inside a disordered medium. Before my PhD thesis, Luis Froufe and Rémi Carminati have studied the LDOS statistical distribution based on a numerical coupled dipoles method. In particular, they have shown that from this distribution, one could retrieve information about the trade-off between scattering and absorption in the local environment of the emitter [131]. In Ref. [132], they developed an approached analytical model – that we will refer to as the "one-scatterer" model – to understand the influence of a dipole orientation to the statistical distribution of its decay rate.

Here, we present 3D exact numerical simulations of the LDOS distribution based on the same coupled dipoles method. To analyze our data, we first present the "one-scatterer" model, where the LDOS is driven by the nearest scatterer only. Based on this model, we show that the shape of our distributions is driven by a regime where near-field interactions dominate. This paves the way for the study of the sensitivity of C_0 to the local environment of the source, which is presented in section 6.3.

6.2.1 The "one-scatterer" model

In the "one-scatterer" model, the source dipole interacts with one scatterer only. In this regime, both the Green function and the LDOS can be expressed analytically. In particular, if the scatterer is close enough to the emitter, the LDOS distribution exhibits a power-law behavior and a cut-off for a maximum value of the LDOS corresponding to the minimum distance allowed between the source and the nearest scatterer.

Green function of the system

In the configuration shown in Fig 6.2, involving a single scatterer in a spherical domain, the Green function can be expressed analytically as a function of $\alpha_p(\omega)$, the polarizability of the scatterer, and $\mathbf{G}_0$, the Green function of vacuum. Let us consider a source dipole $\mathbf{p}$ located at

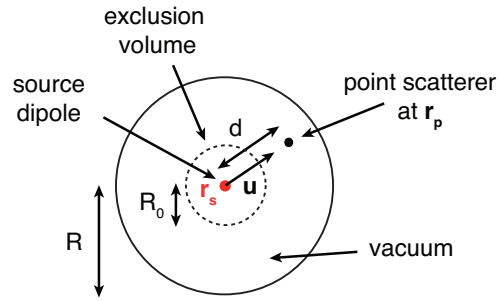


Figure 6.2: One single point scatterer in vacuum at distance d of a source dipole at $\mathbf{r}_s$.

$\mathbf{r}_s$ illuminating the system. The incident field radiated by the source dipole located at $\mathbf{r}_s$ to point $\mathbf{r}$ reads

$$\mathbf{E}_0(\mathbf{r},\omega) = \mu_0\omega^2\mathbf{G}_0(\mathbf{r},\mathbf{r}_s,\omega)\mathbf{p}. \tag{6.12}$$

Since the scatterer is lying alone in the host medium, the incident field at $\mathbf{r} = \mathbf{r}_p$ is rigorously its exciting field. Hence, the induced dipole $\mathbf{p}_p$ in the scatterer reads

$$\mathbf{p}_p = \epsilon_0\alpha_p(\omega)\mathbf{E}_0(\mathbf{r}_p,\omega) \tag{6.13}$$

The scatterered field is radiated by the induced dipole $\mathbf{p}_p$ of the scatterer. Using Eqs. (6.12) and (6.13), it reads

$$\mathbf{E}_s(\mathbf{r},\omega) = \mu_0\omega^2\mathbf{G}_0(\mathbf{r},\mathbf{r}_p,\omega)\left[\frac{\omega^2}{c^2}\alpha_p(\omega)\mathbf{G}_0(\mathbf{r}_p,\mathbf{r}_s,\omega)\mathbf{p}\right]. \tag{6.14}$$

From Eqs. (6.12) and (6.14), the Green function of the system reads

$$\boxed{\mathbf{G}(\mathbf{r},\mathbf{r}_s,\omega) = \underbrace{\mathbf{G}_0(\mathbf{r},\mathbf{r}_s,\omega)}_{\text{incident field}} + \underbrace{\frac{\omega^2}{c^2}\alpha_p(\omega)\mathbf{G}_0(\mathbf{r},\mathbf{r}_p,\omega)\mathbf{G}_0(\mathbf{r}_p,\mathbf{r}_s,\omega)}_{\text{scattered field}}} \tag{6.15}$$

LDOS at the center of the cluster

The LDOS at point $\mathbf{r}_s$ reads as a function of the Green function of the environment [8]

$$\frac{\rho(\mathbf{r}_s,\omega)}{\rho_0(\omega)} = 1 + \frac{2\pi}{k}\mathrm{Im}\left[\mathrm{Tr}\,\mathbf{S}(\mathbf{r}_s,\mathbf{r}_s,\omega)\right], \tag{6.16}$$

where $\mathbf{S} = \mathbf{G} - \mathbf{G}_0$ is the scattered Green function, $k = \omega/c$ and $\rho_0(\omega)$ is the LDOS in vacuum. Inserting Eq. (6.15) into Eq. (6.16) and using reciprocity $[\mathbf{G}_0(\mathbf{r}_s,\mathbf{r}_p) = {}^t\mathbf{G}_0(\mathbf{r}_p,\mathbf{r}_s) = \mathbf{G}_0(\mathbf{r}_p,\mathbf{r}_s)]$ yields

$$\frac{\rho(\mathbf{r}_s,\omega)}{\rho_0(\omega)} = 1 + 2\pi k\,\mathrm{Im}\left[\alpha_p(\omega)\mathrm{Tr}\,\mathbf{G}_0(\mathbf{r}_p,\mathbf{r}_s,\omega)^2\right], \tag{6.17}$$

Denoting $x = kd$, the Green function of vacuum can be written (see Appendix B)

$$\mathbf{G}_0(\mathbf{r}_p, \mathbf{r}_s, \omega) = \mathrm{PV}\left[\frac{ke^{ix}}{4\pi}\left\{\underbrace{\frac{1}{x}\left[\mathbf{I} - \mathbf{u}\otimes\mathbf{u}\right]}_{\text{far field}} + \underbrace{\left(\frac{i}{x^2} - \frac{1}{x^3}\right)\left[\mathbf{I} - 3\mathbf{u}\otimes\mathbf{u}\right]}_{\text{near field}}\right\}\right] - \frac{\mathbf{I}}{3k^2}\delta(\mathbf{r}_p - \mathbf{r}_s), \quad (6.18)$$

where $d = |\mathbf{r}_p - \mathbf{r}_s|$, $\mathbf{u} = (\mathbf{r}_p - \mathbf{r}_s)/d$, PV denotes the principal value operator and $\mathbf{I}$ is the identity matrix. The term proportional to x^{-1} is called the far field term since it is the only term that contributes to energy radiation to the far field. The terms proportional to x^{-2} and x^{-3} are called near-field terms. The term proportional to x^{-3} is the quasi-static term, that remains when $k \to 0$. The near-field terms are a feature of vector electromagnetic waves and will play a fundamental role in the behavior of C_0.

Denoting $\alpha_p(\omega) = \alpha_p'(\omega) + i\alpha_p''(\omega)$, and inserting Eq. (6.18) into Eq. (6.17), one finally obtains

$$\boxed{\frac{\rho(\mathbf{r}_s, \omega)}{\rho(\omega)} = 1 + \frac{k^3}{4\pi x^6}\left[\alpha_p'(\omega)g_1(x) + \alpha_p''(\omega)g_2(x)\right].} \quad (6.19)$$

where

$$\begin{aligned} g_1(x) &= \left(2x^3 - 6x\right)\cos(2x) + \left(x^4 - 5x^2 + 3\right)\sin(2x) \\ g_2(x) &= \left(x^4 - 5x^2 + 3\right)\cos(2x) + \left(6x - 2x^3\right)\sin(2x) \end{aligned} \quad (6.20)$$

Near-field asymptotic expression

In the limit case where $x = kd \ll 1$, the Green function of vacuum $\mathbf{G}_0$ is dominated by the quasi-static term and becomes proportional to x^{-3} [see Eq. (6.18)]. Taking the proper limit in Eq. (6.19), the LDOS becomes

$$\boxed{\frac{\rho(\mathbf{r}_s, \omega)}{\rho_0(\omega)} \approx \frac{3k^3\alpha_p''(\omega)}{4\pi x^6}.} \quad (6.21)$$

Asuming a uniform probability density for the particle inside the cluster, the probability $P(x)$ for the scatterer to be at a dimensionless distance x from the emitter is given by

$$P(x) = \frac{3x^2}{(kR)^3}. \quad (6.22)$$

Since in this case, the LDOS is a monotone (hence bijective) function of x, one can make the change of variable $|P(x)\,\mathrm{d}x| = |P(\rho/\rho_0)\,\mathrm{d}(\rho/\rho_0)|$. Using Eq. (6.21), it yields

$$\boxed{P(\rho/\rho_0) = \frac{1}{2(kR)^3}\left(\frac{3k^3\alpha_p''(\omega)}{4\pi}\right)^{1/2}\left(\frac{\rho}{\rho_0}\right)^{-3/2}} \quad (6.23)$$

This $-3/2$ power-law behavior of the statistical distribution of the LDOS is an evidence of a regime where near-field interaction dominate in the LDOS. It could not be observed, for example, for scalar waves.

Cutoff in the statistical distributions

In the one-scatterer regime, the LDOS is increasing when the distance d to the scatterer is decreasing. If a minimum distance R_0 is imposed between the emitter and the scatterer (as it will be the case in our numerical experiments), the LDOS cannot overcome a maximum value, and a cutoff is expected in its statistical distribution. In Fig. 6.3, we plot, as a function of the distance d, the analytical value of the LDOS corresponding to Eq. (6.19) and the curve $d = R_0$ to illustrate the maximum value reachable for the LDOS ($\rho/\rho_0 \approx 62$ here). The parameters are those of Fig. 6.5.

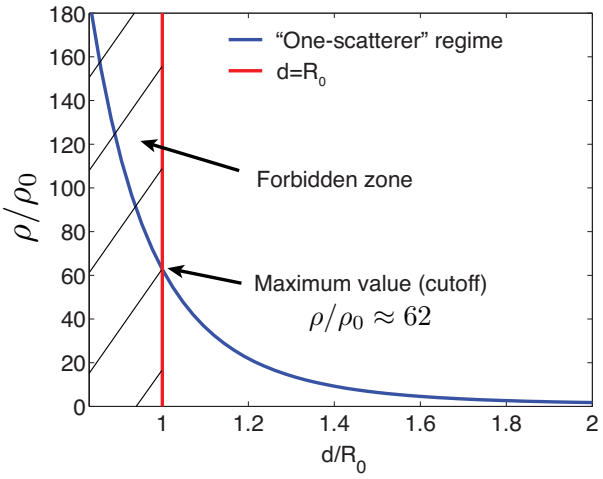


Figure 6.3: Maximum value of the LDOS inducing a cutoff in the distribution in the "one-scatterer" regime. Same parameters as in Fig. 6.5.

6.2.2 Asymmetric shape of the LDOS distribution: Numerical results

We now turn to numerical simulations of LDOS distributions. We consider a scattering medium modeled by a three-dimensional cluster of N resonant point scatterers randomly distributed inside a sphere with radius R. Each scatterer is described by the polarizability of a resonant scatterer in vacuum, that is discussed in Chap. 1.

$$\alpha_p(\omega) = \frac{3\pi}{k^3}\frac{\Gamma_p}{\omega_p - \omega - i\Gamma_p/2}, \tag{6.24}$$

where ω_p is the resonant frequency and Γ_p the linewidth of the resonance. The host medium considered in all our calculations is vacuum, described by its Green function $\mathbf{G}_0$ [Eq. (6.18)]. A dipole emitter is placed at the center of the cluster (at position $\mathbf{r}_s$) and is surrounded by a small exclusion sphere with radius R_0. A minimum distance d_0 between the scatterers is preserved for

the dipolar approximation to remain valid[2]. The geometry of the system is shown in Fig. 6.4 for one typical configuration of disorder. For a high number of configurations (i.e. random

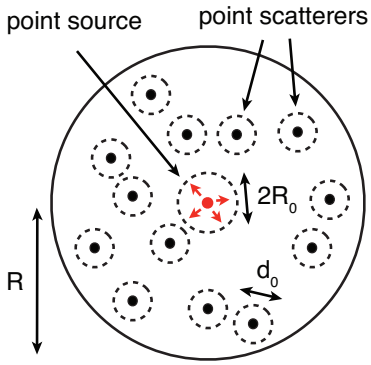


Figure 6.4: One configuration of the model 3D disordered system.

sets of positions of the scatterers), we compute the LDOS at the center $\mathbf{r}_s$. Gathering all these values in an histogram, we can plot a statistical distribution. The details of the calculation of the LDOS for one configuration of the disorder within the coupled dipoles method are given in Appendix C. It is important to note that this is an exact calculation. It takes into account the three-dimensional geometry of the system, including polarization, retardation effects, multiple scattering and near-field interactions (this is a key point in this study).

We show in Fig. 6.5 a distribution obtained for parameters corresponding to a weakly scattering sample ($R \approx 0.63\,\ell$, where ℓ is the scattering mean free path and a weak disorder ($k\ell \approx 19$). Note that, as we shall see in section 6.3, the minimum interparticle distance d_0 induces correlations between the positions of the scatterers. We focus in this section on an uncorrelated disorder, which is obtained in our case in very good approximation for a minimum interparticle $d_0 = 7.5\,\text{nm}$. The curve exhibits a broad distribution, with values of ρ/ρ_0 ranging from 0.2 to 1000. The analysis of the line shape allows us to distinguish three regimes.

First, the curve covers a zone corresponding to $\rho/\rho_0 \leq 1$, which means that some configurations lead to a reduction of the LDOS compared to that in free space. This effect has been analyzed previously and is due to collective interactions in the multiple-scattering regime [133]. Measurements of the fluorescent lifetime of emitters at the surface of a volume scattering disordered medium seem to have shown evidence of this regime [134].

Second, in the region $\rho/\rho_0 \geq 1$, a power-law decay is observed, with a statistical distribution behaving as $P(\rho) \propto \rho^{-3/2}$ (the power law is indicated by the dashed line in Fig. 6.5). This region is delimited by a cutoff (green vertical line in Fig. 6.5). As described in section 6.2.1, this

[2]Since we consider point scatterers, the dipolar approximation is always valid. Still, this minimum distance is compulsory to treat with the same formalism a real system with non-pointlike scatterers. See Appendix C for more details.

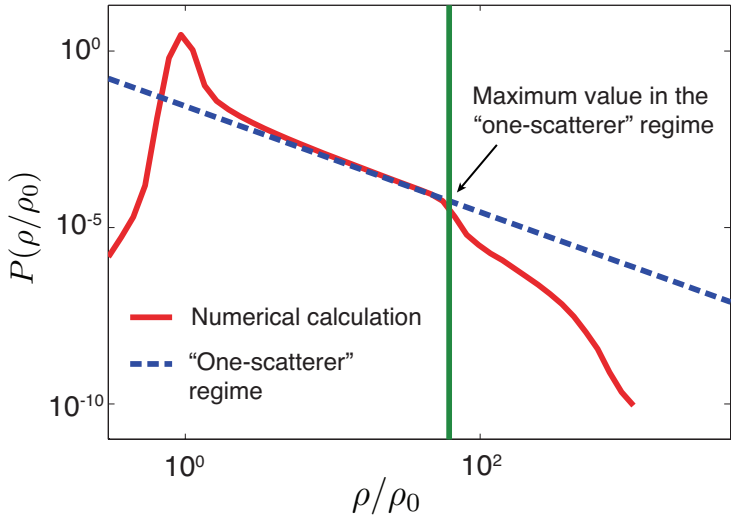


Figure 6.5: Statistical distribution of the normalized LDOS $\rho(\mathbf{r}_s,\omega)/\rho(\omega)$ for an uncorrelated system ($d_0 = 7.5\,\text{nm}$). Parameters are $N = 100$, $\omega_p = 3\times10^{15}\,\text{s}^{-1}$, $\omega-\omega_p = 10^9\,\text{s}^{-1}$ (wavelength $\lambda = 630\,\text{nm}$), $\Gamma_p = 10^9\,\text{s}^{-1}$, $R = 1.2\,\mu\text{m}$, and $R_0 = 0.05\,\mu\text{m}$. The calculations are performed using 3×10^8 configurations of disorder. This large number is necessary to correctly describe the tail of the distribution. The blue dashed line indicates a power-law behavior $P(\rho/\rho_0)\propto(\rho/\rho_0)^{-3/2}$. The vertical solid line indicates the one-scatterer cutoff.

behavior is explained by the "one-scatterer" model and corresponds to a regime where the source interacts with its nearest scatterer only. The observation of this $-3/2$ power law is an evidence of the fundamental role played by near-field interactions in the fluctuations of the LDOS, which are directly connected to C_0. It is striking to see that these interactions are fundamental even in weakly scattering materials. The LDOS distribution is non-trivially asymmetric (the distribution has a very long tail). Experimental evidences of this long-tail distribution and of its influence on the C_0 correlation, have been reported in [3] and [2].

Third, in the region $\rho/\rho_0 \gg 1$, the tail of the distribution deviates from the power law $\rho^{-3/2}$. This can be understood because the "one-scatterer" regime responsible for this power-law implies a maximum value of the LDOS ($\rho/\rho_0 = 62$ in the present case, see Fig. 6.3). The observation of a tail beyond this one-scatterer cutoff is the evidence of near-field interactions with more than one scatterer. As we shall see below, this tail contains information on the local environment of the emitter, and in particular on the degree of correlation of disorder.

6.3 C_0 is sensitive to disorder correlations

We have shown that C_0 is equal to the normalized variance of the LDOS distribution, and that the latter is driven by near-field interactions and hence contains information on the local environment of the source. It was predicted in [30], using a scalar model, that C_0 depends on

the correlation length of the disorder. Here, we artificially introduce correlations in the disorder and observe explicitly their influence on C_0.

6.3.1 The effective volume fraction: a "correlation parameter"

In the generation of the random configurations of disorder, a minimum distance d_0 is forced between the scatterers. This distance actually induces a degree of correlation of the disorder. Indeed, this amounts to simulating an effective hard-sphere potential between scatterers. One can define an effective volume fraction

$$f_{\text{eff}} = \frac{N(d_0/2)^3}{R^3 - R_0^3}, \tag{6.25}$$

that can be taken as a measure of the degree of correlation of the disorder (f_{eff} will be denoted by "correlation parameter" in the following).

For large f_{eff}, this potential is long-range (d_0 is large), so there is a weak probability of getting two closely separated scatterers. Small values of f_{eff} correspond to non overlapping point scatterers (delta-correlated disorder).

6.3.2 LDOS distribution and correlation parameter

We show in Fig. 6.6 the statistical distribution of ρ/ρ_0 for different values of the correlation parameter f_{eff}, ranging from 1% to 4.2% (i.e. d_0 ranging from 111 to 180 nm). An effective volume fraction of 4.2% already corresponds to non-negligible correlations between the positions of the scatterers. The tail of the distribution is subtantially affected by the level of correlations in the

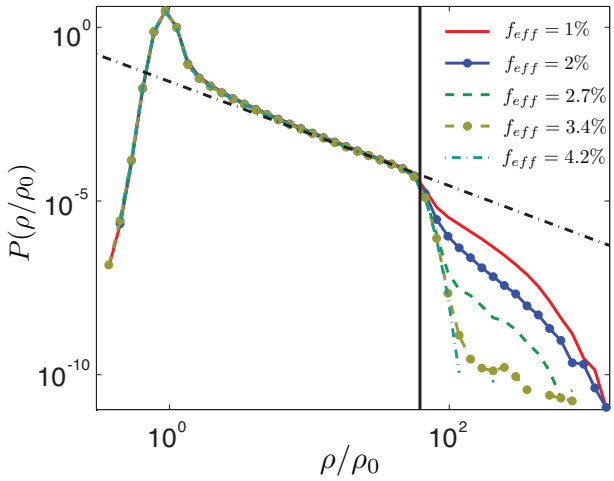


Figure 6.6: Same as Fig. 6.5, with different values of the correlation parameter f_{eff}. As a result of near-field interactions, the tail of the distribution is the signature of the local environment of the emitter

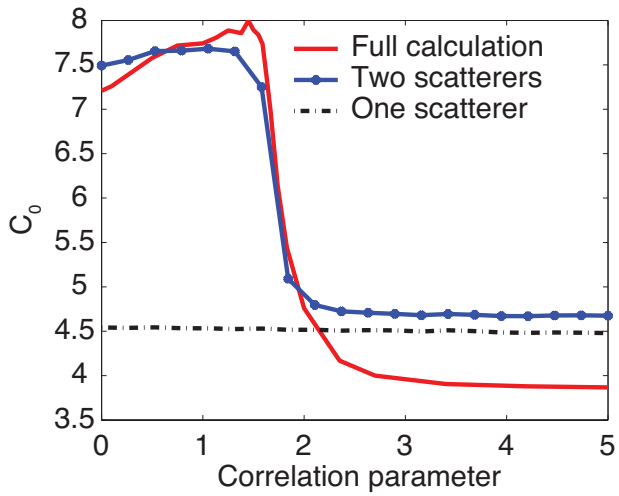


Figure 6.7: C_0 speckle correlation versus the correlation parameter f_{eff}. Red solid line: Full numerical simulation with the same parameters as in Fig. 6.5. Blue solid line with markers: Calculation considering only the two nearest scatterers. Black dashed lines: Calculation considering only the nearest scatterer.

system, while the part of the distribution corresponding to ρ/ρ_0 smaller than the "one-scatterer" cutoff remains unchanged. This means that the sensitivity of C_0 to the local environment of the emitter is driven by the near-field interactions with several surrounding scatterers, this information being encoded in the tail of the statistical distribution of the LDOS. Although this tail corresponds to events with a low probability, it is at the core of the C_0 correlation concept.

6.3.3 C_0 and correlation parameter

In order to visualize the influence of the correlation of disorder directly on C_0, we have computed numerically the variance of the LDOS distributions shown in Fig. 6.6 for more values of the correlation parameter f_{eff}. The corresponding values of C_0, deduced from Eq. (6.11), are plotted in Fig. 6.7 versus f_{eff}. A sharp transition is visible at $f_{\text{eff}} \approx 2\%$, the value of C_0 dropping by a factor of 2. In order to give a physical interpretation of this behavior, we have also plotted in Fig. 6.7 the values of C_0 computed by considering the interaction with the nearest scatterer only (black dashed curve), and with the two nearest scatterers (blue line with markers). For large f_{eff}, the emitter essentially interacts with one particle (the red solid line and the black dashed curve have a similar behavior) and the C_0 correlation can be understood in simple terms. This is the "one-scatterer" regime with its characteristic long-tail distribution. We stress here that this regime results from a near-field interaction, so the value of C_0 depends on local microscopic parameters (it cannot be described with the single scattering or transport mean free path as a single parameter). For small f_{eff}, the probability of getting more than one scatterer in the

vicinity of the emitter becomes non-negligible, and the behavior of C_0 cannot be explained (even qualitatively) with the "one-scatterer" model. One sees that by including the interaction with the two nearest scatterers (blue curve with markers), one reproduces nicely the behavior of the transition. This result demonstrates the high sensitivity of C_0 to the level of correlation of the disorder. As discussed in the previous section, this sensitivity, often referred to as the nonuniversality of C_0, is fundamentally driven by near-field interactions.

6.4 Conclusion and perspectives

In summary, we have derived the relation between the C_0 speckle correlation and the LDOS fluctuations based on energy conservation. This simple and exact derivation leads to an interpretation of C_0 based on the fluctuations of the energy delivered by a classical dipole source to a disordered environment. Using exact numerical simulations, we have shown that C_0 is essentially a correlation resulting from near-field interactions. These interactions give C_0 its nonuniversal character, which is reflected in its high sensitivity to the level of correlation of disorder. This nonuniversality confers to C_0 a potential for sensing and imaging at the submicron scale in complex media.

Several experimental measurements of the LDOS statistical distribution in complex media have been reported recently [94]. The long-tail behavior due to near-field interactions, and its influence on C_0 have been reported in [2]. These enhanced fluctuations have been correlated to the apparition of fractal clusters on disordered metallic films near the percolation threshold in [3], and used as a probe of plasmons localization on these systems (see Chaps 3 and 4). More recently, the direct observation of C_0 as a constant background in the spatial intensity speckle correlation have been observed in acoustics using ultrasounds [130]. In the future, it could be very interesting to combine both approaches and measure simultaneously LDOS fluctuations and C_0 directly from the intensity correlations. Such an experiment could, for example, probe the robustness of Eq. (6.11) in the presence of absorption.

One potential direct application of our work is the discrimination between two materials exhibiting very similar macroscopic optical properties, but different microscopic structures. One force of C_0 in such practical applications is the robustness of the measurement of the LDOS using a fluorescence lifetime measurement. This measurement is independent on any experimental calibration, since it is deduced from a temporal signal (see Chap. 2).

Another perspective is to probe the sensitivity of C_0 (or the LDOS fluctuations) to the Anderson localization transition. It was shown experimentally in acoustics that C_0 was highly correlated to the anomalous multifractal exponent [130], that is a signature of the Anderson transition [135, 136]. The issue of Anderson localization for electromagnetic waves in 3D is a very active topic at the moment. It was suggested that near-field interactions – that do not exist in the initial Anderson model for electron transport – could have a dramatic incidence

on localization [137]. Our numerical tool is very suitable to address these issues in the light of LDOS distributions.

Chapter 7

Strong coupling to 2D Anderson localized modes

Contents

7.1 An optical cavity made of disorder: Anderson localization 112

7.1.1 LDOS spectrum of a weakly lossy cavity mode 112

7.1.2 Numerical characterization of a 2D Anderson localized mode 113

7.2 Strong coupling to a 2D Anderson localized mode 116

7.2.1 Strong coupling condition for a TE mode in 2D 116

7.2.2 Numerical observation of the strong coupling regime 117

7.3 Alternative formulation of the strong coupling criterion 118

7.4 Conclusion 119

We have presented in Chap. 1 a scattering formalism that describes the coupling between a resonant scatterer or emitter and its electromagnetic environment. In particular, we have explained that two different regimes could be distinguished: the weak and the strong coupling regimes.

- In the *weak coupling regime*, the linewidth of a resonant scatterer, or equivalently the spontaneous decay rate of an emitter, depend on the environment through the LDOS. This is known as the Purcell effect [138], and was observed in optics by Drexhage [139].

- In the *strong coupling regime*, the resonant emitter and one mode of the electric field – both sharing the same resonant frequency ω_M – cannot be distinguished anymore. Two hybrid eigenmodes appear, with eigenfrequencies $\omega_M - \Omega_R$ and $\omega_M + \Omega_R$, where Ω_R is called the Rabi frequency. In the time domain, the energy flows back and forth between these two hybrid eigenmodes, a phenomenon called Rabi oscillations. Spectrally, the signature of the strong coupling regime is a splitting in the frequency spectrum [14, 13].

We focus in this chapter on the strong coupling regime. This regime has been demonstrated with single atoms in engineered vacuum cavities [140, 48], and in condensed matter using quantum-well or quantum-dot excitons in microcavities or photonic crystals [141, 15, 142]. In nanophotonics, surface-plasmon modes on metallic nanoparticles or substrates provide subwavelength light confinement without a physical cavity, and strong coupling has been reported with quantum dots or molecules [143, 95, 92, 51, 144]. Multiple scattering in disordered media provides an alternative route since confined modes can be produced by the mechanism of Anderson localization [145, 146]. Substantial modifications of the spontaneous decay rate (Purcell effect) have been demonstrated using quantum dots and localized modes in disordered photonics crystal waveguides [4]. In these one-dimensional structures, even fabrication imperfections in otherwise perfect waveguides generate efficient localization on the micrometer scale [147, 148], and the strong coupling regime was recently demonstrated experimentally [5], following its theoretical prediction [149]. In addition to multiple scattering, near-field interactions also contribute to an enhancement of light-matter interaction with large Purcell factors in the weak-coupling regime, as discussed in Chap. 6.

In this chapter, we compute numerically LDOS spectra in two-dimensional disordered coupled dipoles systems. From these spectra, we characterize an Anderson localized mode. Based on the formalism described in Chap. 1, we describe the interaction between this mode and a resonant scatterer. Using exact numerical simulations, we demonstrate the strong coupling regime by observing a splitting in the scatterer response spectrum. This splitting is in perfect agreement with a theoretical formalism based on a coupled mode approach. Using this theory, we examine the strong coupling criterion, and show that it can be expressed in terms of the Thouless conductance and the Purcell factor.

This work was published in Physical Review Letters [150].

7.1 An optical cavity made of disorder: Anderson localization

7.1.1 LDOS spectrum of a weakly lossy cavity mode

We consider a two-dimensional disordered medium and Transverse Electric (TE) waves (electric field perpendicular to the plane containing the 2D scatterers), so that we are left with a scalar problem. In the canonical situation of a non-absorbing environment placed in a closed cavity, one can define an orthonormal discrete basis of eigenmodes with eigenfrequencies ω_n and eigenvectors $\mathrm{e}_n(\mathbf{r})$. The electromagnetic response of the medium can be expanded over the set of eigenmodes (see Appendix B for details)

$$\mathrm{G}(\mathbf{r},\mathbf{r}',\omega) = \sum_n c^2 \frac{\mathrm{e}_n^*(\mathbf{r}')\mathrm{e}_n(\mathbf{r})}{\omega_n^2 - \omega^2}\,, \tag{7.1}$$

where c is the speed of light in vacuum, ω the frequency and $\mathrm{G}(\mathbf{r},\mathbf{r}',\omega)$ the outgoing 2D scalar Green function. In the general case of a leaky system, the weak losses out of each eigen mode

can be taken into account phenomenologically using a linewidth γ_n [Eq. (B.31) in Appendix B]

$$\mathrm{G}(\mathbf{r},\mathbf{r}',\omega) = \sum_n \frac{c^2}{2\omega_n} \frac{\mathrm{e}_n^*(\mathbf{r}')\mathrm{e}_n(\mathbf{r})}{\omega_n - \omega - i\gamma_n/2}. \tag{7.2}$$

The LDOS is defined as (see Chap 1)

$$\rho(\mathbf{r},\omega) = \frac{2\omega}{\pi c^2} \operatorname{Im} \mathrm{G}(\mathbf{r},\mathbf{r},\omega). \tag{7.3}$$

Therefore the LDOS spectrum in a weakly lossy environment is given by

$$\rho(\mathbf{r},\omega) = \sum_n \rho_n(\mathbf{r},\omega) = \sum_n \frac{A_n}{\pi} \frac{\gamma_n/2}{(\omega_n-\omega)^2 + (\gamma_n/2)^2}\,, \tag{7.4}$$

where $A_n = |\mathrm{e}_n(\mathbf{r})|^2$. The LDOS spectrum contains all the relevant parameters of a given eigenmode (central frequency, linewidth and local intensity), independently of an explicit knowledge of the full set of eigenmodes. A major interest is that it can in principle be determined experimentally from fluorescent lifetime measurements, even at the nanoscale in complex geometries [64, 16] (see Chap. 2). For convenience, we also define the Purcell factor associated to a given eigenmode n at position $\mathbf{r}$, as

$$\mathrm{F_P} = \rho_n(\mathbf{r},\omega_n)/\rho_0, \tag{7.5}$$

where $\rho_0 = \omega/(2\pi c^2)$ is the vacuum LDOS in 2D. The Purcell factor is the LDOS enhancement. It describes the enhancement of the spontaneous decay rate of a fluorescent emitter due to its interaction with a given electromagnetic eigenmode.

7.1.2 Numerical characterization of a 2D Anderson localized mode

In order to investigate Anderson localization numerically, we consider an assembly of 2D point scatterers randomly distributed in a cylinder of radius R. In order to compute the LDOS at the central point $\mathbf{r}_s$, we illuminate the system by a source dipole p located at $\mathbf{r}_s$. The system is illustrated in Fig. 7.1. The scatterers are described by their electric polarizability

$$\alpha_{\mathrm{sca}}(\omega) = \frac{2}{k^2} \frac{\Gamma_{\mathrm{sca}}}{\omega_{\mathrm{sca}} - \omega - i\Gamma_{\mathrm{sca}}/2}, \tag{7.6}$$

where $k = \omega/c$, ω_{sca} is the resonance frequency and Γ_{sca} the linewidth. As discussed in Chap. 1 in 3D, this form of the polarizability describes non-absorbing scatterers and satisfies energy conservation for 2D scatterers under TE illumination. We have fixed $\omega_{\mathrm{sca}} = 3\times10^{15}\,\mathrm{s}^{-1}$ (visible optical radiation) and $\Gamma_{\mathrm{sca}} = 5\times10^{16}\,\mathrm{s}^{-1} \gg \omega_{\mathrm{sca}}$. With such a wide resonance, the scattering cross-section of the scatterers is constant over the spectral range considered in the numerical simulations below.

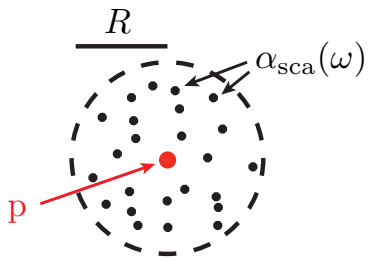


Figure 7.1: Sketch of the system. (Black) Disordered coupled dipoles system; (Red) Illumination by a source dipole p located at $\mathbf{r}_s$.

As explained in Appendix C (coupled dipoles method), the exciting field on scatterer number i is given by the self-consistent equation

$$\mathrm{E}_i = \mu_0\omega^2\mathrm{G}_0(\mathbf{r}_i,\mathbf{r}_s,\omega)\mathrm{p} + \frac{\omega^2}{c^2}\alpha_{\mathrm{sca}}(\omega)\sum_{j\neq i}\mathrm{G}_0(\mathbf{r}_i,\mathbf{r}_j,\omega)\mathrm{E}_j, \tag{7.7}$$

where $\mathbf{r}_i$ is the position of scatterer number i. The 2D vacuum Green function for TE waves reads

$$\mathrm{G}_0(\mathbf{r},\mathbf{r}',\omega) = \frac{i}{4}\,\mathrm{H}_0^{(1)}(k|\mathbf{r}-\mathbf{r}'|), \tag{7.8}$$

where $\mathrm{H}_0^{(1)}$ is the zero-order Hankel function of the first kind. For a system with N scatterers, the linear system of N self-consistent equations can be solved numerically. Once the exciting field on each scatterer is known, it is possible to compute the scattered field at $\mathbf{r}_s$ and to deduce the Green function of the system. The LDOS $\rho(\mathbf{r}_s,\omega)$ is then obtained from Eq. (7.3).

Let us consider one configuration of the random system, with $N = 5000$ scatterers in a cylinder of radius $R = 20\,\mu$m. Two computed LDOS spectra, with the same bandwidth but centered on two different central frequencies $\omega_c^d = 2.7\times10^{15}\,\mathrm{s}^{-1}$ (diffusive regime) and $\omega_c^l = 1.5\times10^{15}\,\mathrm{s}^{-1}$ (localized regime), are shown in Fig. 7.2(a) and 7.2(b), respectively. To choose these two frequencies, we have estimated the localization length by

$$\xi = \ell_s\exp[\pi\mathrm{Re}\,(k_{\mathrm{eff}})\ell_s/2], \tag{7.9}$$

with ℓ_s the scattering mean free path and k_{eff} the effective wavenumber in the medium [151, 34]. For a rough estimate, we have made the approximation $k_{\mathrm{eff}} \approx k_0 + i/(2\ell_s)$, valid in the weak scattering limit. In the spectrum shown in Fig. 7.2(a), one has $\xi \simeq 84R$ and the sample is in the diffusive regime. We observe a smooth profile corresponding to the intuitive picture of a continuum of modes. Conversely, in Fig. 7.2(b), the localization length is $\xi \simeq R/5$ and the sample is in the localized regime. We observe very sharp and well-separated peaks, each of them being a signature of a localized mode. A peaked spectrum, characteristic of localized modes, is found numerically on any configuration of the disorder, provided that $\xi \ll R$. A zoom on one of

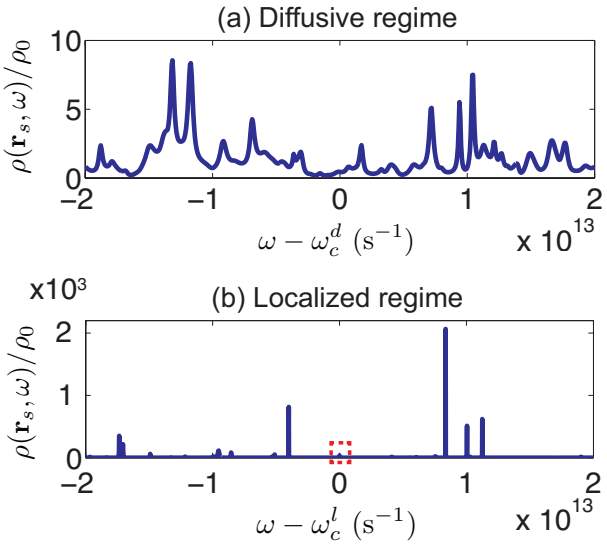


Figure 7.2: (a) LDOS spectrum centered at $\omega_c^d = 2.7 \times 10^{15}\,\mathrm{s}^{-1}$ (diffusive regime). (b) LDOS spectrum centered at $\omega_c^l = 1.5 \times 10^{15}\,\mathrm{s}^{-1}$ (localized regime). A zoom on the area indicated by red dashed lines is shown in Fig. 7.3.

the LDOS peaks, as displayed in Fig. 7.3, shows that it can be perfectly fitted by a Lorentzian lineshape as in Eq. (7.4), demonstrating the relevance of this description. Importantly, every peak we have found in this regime was perfectly fitted by Eq. (7.4), in agreement with the picture of Anderson localization. Such a Lorentzian lineshape for localized modes is consistent with measurements performed in disordered waveguides [4, 33]. The isolated Anderson localized mode shown in Fig. 7.3 will be denoted by mode M in the following. It will be used to demonstrate numerically the strong coupling regime. It is characterized by an eigenfrequency $\omega_M \simeq 1.5 \times 10^{15}\,\mathrm{s}^{-1}$, a linewidth $\Gamma_M \simeq 8 \times 10^9\,\mathrm{s}^{-1}$ (the quality factor $Q_M \simeq 1.8 \times 10^5$) and a Purcell factor $\mathrm{F_P} \simeq 36$.

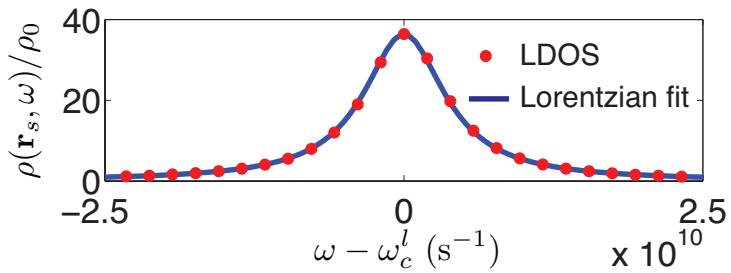


Figure 7.3: Zoom on one peak in Fig. 7.2(b). Circles correspond to a fit by Eq. (7.4).

7.2 Strong coupling to a 2D Anderson localized mode

7.2.1 Strong coupling condition for a TE mode in 2D

Let us consider a resonant scatterer, assumed on resonance with mode M (resonance frequency $\omega_s = \omega_M$, described by its scalar polarizability

$$\alpha_S(\omega) = \frac{2c^2}{\omega^2} \frac{\Gamma_s^{\mathrm{R}}}{\omega_M - \omega - i(\Gamma_s^{\mathrm{R}} + \Gamma_s^{\mathrm{NR}})/2}, \tag{7.10}$$

where Γ_s^{R} and Γ_s^{NR} are, respectively, the radiative and intrinsic non-radiative linewidth. As discussed in Chap. 1, this polarizability describes either a classical resonant scatterer (the non-radiative linewidth corresponding to dissipation in the material), or a quantum two-level system far from saturation (in this case $\Gamma_s^{\mathrm{NR}} = 0$). Note that Γ_s^{R} also appears in the numerator. This is an important feature of the scattering formalism. Radiation losses contribute to the linewidth (denominator), but the oscillator strength is also proportional to Γ_s^{R} (numerator) due to energy conservation. The theoretical formalism described in Chap. 1 allows to derive the following expression of the Rabi frequency

$$\Omega_R = \left[g_c^2 - \frac{\{\Gamma_s^{\mathrm{NR}} - \Gamma_M\}^2}{16} \right]^{1/2}, \tag{7.11}$$

where g_c is the coupling constant, defined as[1]

$$g_c = (\Gamma_s^{\mathrm{R}} \Gamma_M \mathrm{F_P}/4)^{1/2}. \tag{7.12}$$

In this expression, $\mathrm{F_P}$ is the Purcell factor of mode M, Γ_M its linewidth and Γ_s^{R} the linewidth of the emitter in vacuum. As discussed in Chap. 1, the strong coupling regime is reached when the two new eigenmodes of the coupled system are no longer degenerated. This regime is reached if the Rabi frequency is real, which requires

$$g_c^2 \geq \frac{(\Gamma_s^{\mathrm{NR}} - \Gamma_M)^2}{16}. \tag{7.13}$$

The spectral width Γ of the new eigenmodes reads

$$\Gamma = \frac{\Gamma_M + \Gamma_s^{\mathrm{NR}}}{2}. \tag{7.14}$$

Γ is the average of the intrinsic linewidths of the uncoupled systems. Let us remind that Eq. (7.13) is not sufficient to ensure that the Rabi splitting is larger than the linewidth (which is a necessary condition to observe Rabi oscillations in the time domain). One needs to satisfy the more restrictive condition $2\Omega_R \geq \Gamma$, that reads

$$g_c^2 \geq \frac{(\Gamma_s^{\mathrm{NR}})^2 + \Gamma_M^2}{8}. \tag{7.15}$$

[1] In 3D, the coupling constant differs by a factor $\sqrt{3}$, $g_c = (3\Gamma_s^{\mathrm{R}} \Gamma_M \mathrm{F_P}/4)^{1/2}$.

7.2.2 Numerical observation of the strong coupling regime

To check the expected strong coupling, we use numerical simulations based on the coupled dipole method. We consider the same system as in Fig. 7.2(a), and add at position $\mathbf{r}_s$ a resonant dipole scatterer (scatterer S), tuned to the resonance frequency ω_M of the localized mode M identified in Fig. 7.3. The polarizability of scatterer S is given by Eq. (7.10), with $\Gamma_s^{\mathrm{NR}} = 0$ (no intrinsic non-radiative losses). A sketch of the system is represented in Fig 7.4. The system

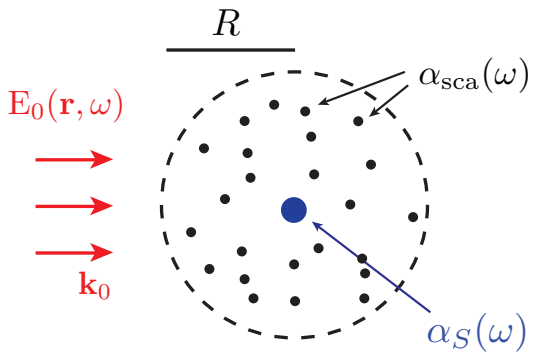


Figure 7.4: Sketch of the system. (Black) Disordered coupled dipole cavity giving rise to mode M; (Blue) Resonant scatterer S placed at the center $\mathbf{r}_s$ of the cavity; (Red) External illumination by a plane-wave $\mathrm{E}_0(\mathbf{r},\omega)$.

is illuminated by an external plane-wave $\mathrm{E}_0(\mathbf{r},\omega) = \mathrm{E}_0 \exp(i\mathbf{k}_0.\mathbf{r})$, where $\mathbf{k}_0 = (\omega/c)\mathbf{u}_0$ is the incident wavevector, directed by $\mathbf{u}_0$, a unit vector oriented in the plane transverse to the electric field. A system of N self-consistent equations similar to (7.7) can be written

$$\begin{aligned}\mathrm{E}_i = \mathrm{E}_0(\mathbf{r}_i,\omega) + \frac{\omega^2}{c^2}\alpha(\omega)\sum_{j\neq i}\mathrm{G}_0(\mathbf{r}_i,\mathbf{r}_j,\omega)\mathrm{E}_j \\ + \frac{\omega^2}{c^2}\alpha_S(\omega)\mathrm{G}_0(\mathbf{r}_i,\mathbf{r}_s,\omega)\mathrm{E}_s,\end{aligned} \tag{7.16}$$

where the exciting field E_s on scatterer S is given by the additional equation

$$\mathrm{E}_s = \mathrm{E}_0(\mathbf{r}_s,\omega) + \frac{\omega^2}{c^2}\alpha(\omega)\sum_{j=1}^{N}\mathrm{G}_0(\mathbf{r}_s,\mathbf{r}_j,\omega)\mathrm{E}_j. \tag{7.17}$$

Solving this linear systems with $N+1$ equations allows us to compute the induced dipole moment of scatterer S

$$\mathrm{p}_S(\omega) = \epsilon_0\alpha_S(\omega)\mathrm{E}_s(\mathbf{r}_s,\omega). \tag{7.18}$$

We show in Fig. 7.5(a) the resulting spectrum for five different values of the radiative linewidth Γ_s^{R} (increasing from top to bottom). The Rabi splitting $2\Omega_R$ increases with Γ_s^{R}, as expected from theory since the coupling strength g_c scales as $(\Gamma_s^{\mathrm{R}})^{1/2}$. The dependence of the Rabi splitting

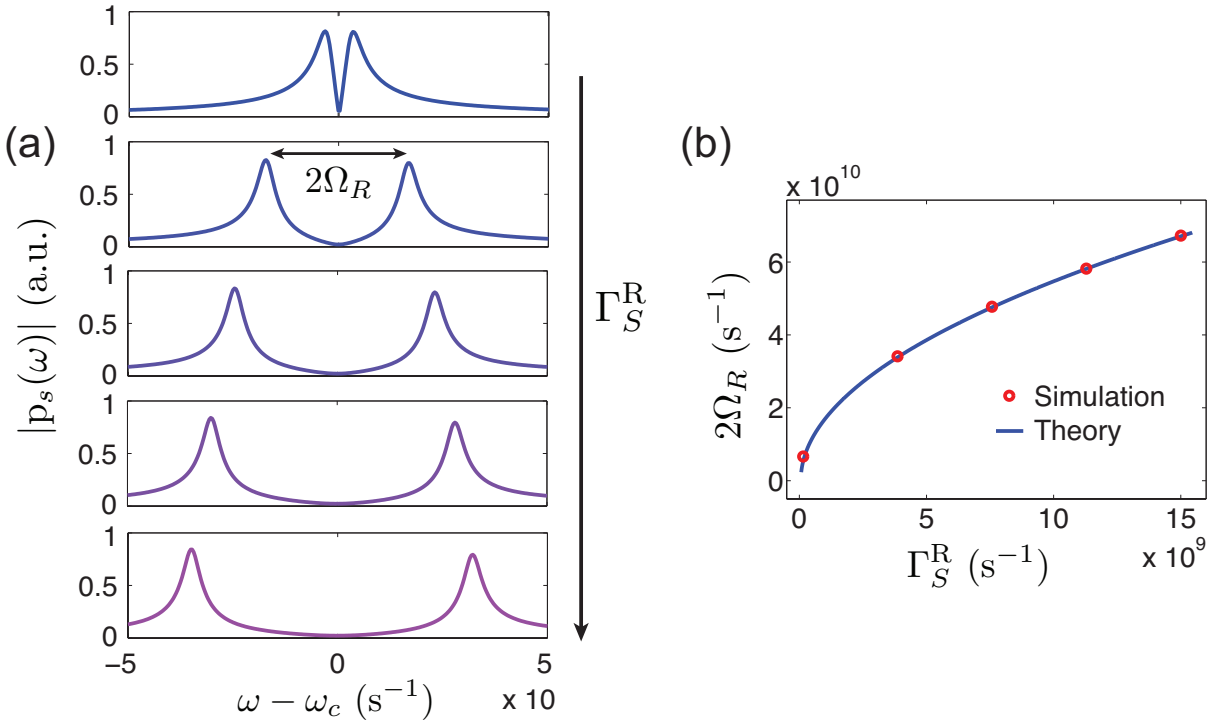


Figure 7.5: (a) Spectra of the dipole moment $|p_S(\omega)|$ of scatterer S for different values of the radiative linewidth Γ_s^R (from top to bottom $\Gamma_s^R = 1.5 \times 10^8\,s^{-1}$; $3.9 \times 10^9\,s^{-1}$; $7.5 \times 10^9\,s^{-1}$; $11 \times 10^9\,s^{-1}$; $15 \times 10^9\,s^{-1}$); (b) Frequency splitting in the spectrum of the dipole moment versus Γ_s^R. Solid line: Theoretical prediction by Eq. (7.11). Circles: Numerical simulations shown in Fig. 7.5(a).

on Γ_s^R extracted from the numerical simulations is shown in Fig. 7.5(b). Excellent agreement is found with the theoretical prediction by Eq. (7.11).

7.3 Alternative formulation of the strong coupling criterion

We shall show that an alternative formulation of the strong coupling criterion can be given, that is particularly relevant in the case of Anderson localization. Let us introduce the average linewidth of the electromagnetic modes $\delta\omega$ and the average mode spacing $\Delta\omega$. Normalized linewidths $\hat{\Gamma}_S^R = \Gamma_s^R/\Delta\omega$ and $\hat{\Gamma}_M = \Gamma_M/\delta\omega$ can be introduced, respectively for scatterer S and mode M. $\hat{\Gamma}_S^R = 1$ means that the bandwidth of the scatterer covers on average only one mode of the disordered medium (the linewidth of the resonant scatterer can be chosen or tuned to satisfy this condition). When scatterer S is resonant with the localized mode M, the strong coupling

criterion given by Eq. (7.15) becomes

$$\mathrm{F_P} \geq \frac{1}{2} \frac{\hat{\Gamma}_M}{\hat{\Gamma}_S^{\mathrm{R}}} g \,, \tag{7.19}$$

where $g = \delta\omega/\Delta\omega$ is the normalized Thouless conductance, a key concept in the theory of Anderson localization [152, 32]. The localized regime corresponds to $g < 1$ [this condition describes statistically a spectrum as that in Fig. 7.2(b)]. The inequality shows that the smaller the conductance, the smaller the critical Purcell factor permitting to enter the strong coupling regime. This confirms the idea that deeply localized modes in 2D or quasi-1D [147, 148, 149] are particularly suitable to achieve strong coupling in the optical regime in condensed matter. For $\hat{\Gamma}_S^{\mathrm{R}} \simeq 1$ and $\hat{\Gamma}_M \simeq 1$ (this condition is satisfied on average for the localized modes), the strong coupling criterion takes the remarkable simple form

$$\mathrm{F_P} \geq g/2. \tag{7.20}$$

This simple relation directly connects the Purcell factor (a central quantity in cavity QED) and the Thouless conductance (a statistical concept in transport theory). Let us remark that the inverse of the Thouless conductance is statistically the analogue of the finesse of a standard Fabry-Pérot cavity that enters standard cavity QED analyses [14, 13]. Once localization is reached, an Anderson localized mode does not behave differently from any cavity mode. Hence, the real challenge to reach strong coupling to Anderson localized modes is to reach the Anderson localized regime.

7.4 Conclusion

In conclusion, we have demonstrated numerically the strong coupling regime between a resonant scatterer and an Anderson localized mode for electromagnetic waves in two dimensions. The numerical results are in perfect agreement with the coupled-mode theory presented in chapter 1. The strong coupling threshold has been expressed in terms of the Thouless conductance and the Purcell factor. From the fundamental point of view, Eq. (7.19) establishes an interesting connection between concepts in transport theory and cavity QED. On the practical side, it shows that once localization is reached ($g < 1$), the strong coupling criterion is not restrictive. For a resonant scatterer with a linewidth on the order of the averaged mode spacing (i.e. that on average is in coincidence with only one mode), the criterion is equivalent to having a Purcell factor $\mathrm{F_P} > 1$. Although this criterion is rigorous only statistically, it provides a simple rule that could be useful in practice for the design and/or the analysis of future experiments aiming at demonstrating or using (classical or quantum) strong coupling with Anderson localized electromagnetic waves.

An important message of our work is that a LDOS spectrum fully characterizes the localization regime of a disordered sample, as proposed initially in Ref. [149]. Eq. (7.19) gives a rule

of the thumb to design an experiment using the same principle as the numerical procedure presented in section 7.3. Two-dimensional localization of electromagnetic waves have been reported or predicted in several systems. In Ref. [34], two thin copper layers, one of them containing randomly located dielectric scatterers, were shown to exhibit localized modes in the microwave regime. A theoretical study predicted that high-quality factor modes could be designed in disordered photonic crystals [153]. Recently, it was predicted that short-range correlated disorder in 2D photonic structures could help to design localized modes [154]. Our work paves the way towards an experimental observation of the strong coupling regime on such systems.

Finally, one major interest of our theoretical formalism is to be easily generalizable to other kinds of waves, such as acoustic waves. At Institut Langevin, Fabrice Lemoult and coworkers have demonstrated subdiffraction localization of acoustic waves in a Helmoltz resonator crystal. [155]. Isolating one eigenmode of the acoustic field in such a system could lead to the observation of weak and strong coupling with one resonator, as described here.

General conclusion and perspectives

In this thesis, we have studied different aspects of light emission and scattering in complex media. Theoretical and numerical approaches have been developed in close proximity to experiments. Many of our results are at the crossing between nanophotonics and light transport in strongly scattering media. Here, we summarize the main results, and present some perspectives.

- In Chap. 2, we have computed numerical maps of the LDOS and fluorescence signal in the near field of a metallic nanoantenna, in good agreement with experiments performed at Institut Langevin. Using our numerical model of the experiment, we have explained the spatial resolution observed in the LDOS maps, below the size of the fluorescent nanosources (this was also observed in Ref. [64]). These results pave the way towards a full experimental characterization of nanoantennas for the control of fluorescent emitters. Following this path, the next step is to access experimentally the radiative and non-radiative LDOS, that are the two missing parameters to fully describe the emission of an electric dipole on these structures. Work in this direction is already in progress at Institut Langevin.

- In Chap. 3, we have computed numerically the spatial structure of the LDOS in the near field of disordered metallic films. We have recovered the enhanced LDOS fluctuations, that were observed experimentally, and interpreted as a signature of the apparition of localized modes in Ref. [3]. We have showed numerically that the "hot-spot" structure observed experimentally [19] is chiefly associated to non-radiative modes. This work allows a better characterization of disordered metallic films. In particular, the non-radiative nature of the hot-spot structure makes these structures great platforms for future basic experiments in nano-optics. As an example, one idea is to use the non-radiative modes supported by the films to perform Förster Resonant Energy Transfer (FRET) at distances larger than the Förster radius.

- In Chap. 4, we have introduced the Cross Density Of States (CDOS) as a new tool to describe quantitatively the average spatial extent of eigenmodes in a complex photonic or plasmonic structure. In other words, the CDOS characterizes the intrinsic spatial coherence of a given system. Using the CDOS, we have demonstrated an overall spatial squeezing of the eigenmodes near the percolation threshold of disordered metallic films.

The concept of CDOS is a new pragmatic approach of light localization, that does not need any description of the underlying localization mechanism. It quantifies the ability of a nanostructure to connect two points coherently, i.e. via at least one eigenmode. Therefore, following the idea mentioned earlier, it should be useful, e.g., to design and understand FRET experiments taking advantage of non-radiative eigenmodes in complex media.

- In Chap. 5, we have shown the existence of a long-range correlation between the reflected and transmitted speckles generated by illuminating a slab of strongly scattering media with a plane wave. Interestingly, the explicit calculation of this correlation within the ladder approximation leads to a negative correlation (assuming diffusive transport). This implies that a bright speckle spot in the reflected speckle will be more likely associated with a dark spot in the transmitted speckle at the same transverse position. A collaboration with experimentalists has started in order to observe this new correlation. Possible sophistications of the theoretical model could involve taking into account the finite size of the incident beam [121], or numerical simulations going beyond the diffusion approximation. As a speculative but stimulating perspective, experiments of imaging and focusing through complex media often involve a CCD camera on the output size of the medium (e.g. to run optimization algorithms [156]). Finding a way to use the statistical connection between reflected and transmitted speckle to replace this feedback would be a real breakthrough, leading to noninvasive imaging setup, as proposed recently [127].

- In Chap. 6, we have derived the equality between the normalized fluctuations of the LDOS and the C_0 correlation – first derived in Ref. [31] – using energy conservation arguments. This approach generalizes this equality to finite statistically isotropic media, in any regime of transport (including Anderson localization). We have computed numerically LDOS distributions in weakly scattering media, and showed that the long-tail behavior is caused by the interaction of the source with its near-field environment. An experimental observation of this long tail behavior of the LDOS distribution in a strongly scattering media has been reported since this work was published [2, 129]. As a perspective, it could be interesting to study the sensitivity of C_0 (or the LDOS fluctuations) to the Anderson localization transition. It was shown experimentally in acoustic that C_0 was correlated to the anomalous multifractal exponent [130], that is a signature of the transition [135, 136]. Anderson localization of light in three-dimension is a very ill-understood phenomenon, and is even still a controversial issue [137]. We believe that LDOS statistics can be a very sound tool to probe Anderson localization. Numerical studies, using the same method as in this work, are in progress.

- In Chap. 7, we have derived numerically the ability of a 2D scattering medium in the Anderson localized regime to reach strong coupling with an emitter. Using the theory

presented in Chap. 1, we have expressed the strong coupling condition in terms of the Thouless conductance and the Purcell factor, showing an interesting connection between concepts in transport theory and cavity QED. One important message is that, as far as a strong coupling experiment is concerned, an Anderson localized mode behaves exactly as a cavity mode, and that the parameters entering the strong coupling criterion can all be deduced from a spectrum of the LDOS. This work should pave the way towards an experimental observation of strong coupling between a 2D disordered system in the localized regime and an emitter.

Appendices

Appendix A

Lippmann-Schwinger equation

The Lippmann-Schwinger equation is an integral formulation of the electric field in a scattering medium as a function of the Green function of a reference medium $\mathbf{G}_{\text{ref}}$. It is introduced in two different situations in this thesis:

- In Chap. 1, it describes the interaction between a small particle and its environment. The reference medium in this case is the environment in the absence of the particle.
- In Part II, it is the fundamental equation of the volume integral method (described in Appendix E), used to solve the Maxwell equations in 3D metallic nanostructures. In this case, the reference medium is a homogeneous medium (vacuum in all calculations presented in this thesis), where lies a metallic volume, described by a dielectric constant obtained from Ref. [67].

Let a reference medium described by the dielectric constant $\epsilon_{\text{ref}}(\mathbf{r},\omega)$ and its Green function $\mathbf{G}_{\text{ref}}(\mathbf{r},\mathbf{r}',\omega)$, solution of

$$\nabla\times\nabla\times\mathbf{G}_{\text{ref}}(\mathbf{r},\mathbf{r}',\omega)-k^2\epsilon_{\text{ref}}(\mathbf{r},\omega)\mathbf{E}_{\text{ref}}(\mathbf{r},\mathbf{r}',\omega)=\delta(\mathbf{r}-\mathbf{r}')\mathbf{I}. \tag{A.1}$$

In a region with no source[1], the electric field in the reference medium (reference field) satisfies the propagation equation

$$\nabla\times\nabla\times\mathbf{E}_{\text{ref}}(\mathbf{r},\omega)-k^2\epsilon_{\text{ref}}(\mathbf{r},\omega)\mathbf{E}_{\text{ref}}(\mathbf{r},\omega)=0, \tag{A.2}$$

while the electric field in the medium of interest (total field) satisfies

$$\nabla\times\nabla\times\mathbf{E}(\mathbf{r},\omega)-k^2\epsilon(\mathbf{r},\omega)\mathbf{E}(\mathbf{r},\omega)=0. \tag{A.3}$$

It is convenient to decompose the field into the reference field and a term that we define as the scattered field

$$\mathbf{E}(\mathbf{r},\omega)=\mathbf{E}_{\text{ref}}(\mathbf{r},\omega)+\mathbf{E}_s(\mathbf{r},\omega). \tag{A.4}$$

[1] We do not consider a region with sources here for the sake of simplicity, but the exact same equation can be derived in a region with sources.

One can transform Eq. (A.3) into

$$\nabla \times \nabla \times \mathbf{E}(\mathbf{r},\omega) - k^2 \epsilon_{\text{ref}}(\mathbf{r},\omega)\mathbf{E}(\mathbf{r},\omega) = k^2 \left[\epsilon(\mathbf{r},\omega) - \epsilon_{\text{ref}}(\mathbf{r},\omega)\right] \mathbf{E}(\mathbf{r},\omega). \tag{A.5}$$

Substracting Eq. (A.2) to Eq. (A.5), one sees that the scattered field satisfies

$$\nabla \times \nabla \times \mathbf{E}_s(\mathbf{r},\omega) - k^2 \epsilon_{\text{ref}}(\mathbf{r},\omega)\mathbf{E}_s(\mathbf{r},\omega) = k^2 \left[\epsilon(\mathbf{r},\omega) - \epsilon_{\text{ref}}(\mathbf{r},\omega)\right] \mathbf{E}(\mathbf{r},\omega). \tag{A.6}$$

The scattered field satisfies Eq. (A.6), a propagation equation in the reference medium, with a source term proportional to the total field. It can be expressed using the Green function of the reference medium $\mathbf{G}_{\text{ref}}(\mathbf{r},\mathbf{r}',\omega)$

$$\mathbf{E}_s(\mathbf{r},\omega) = k^2 \int \left[\epsilon(\mathbf{r}',\omega) - \epsilon_{\text{ref}}(\mathbf{r}',\omega)\right] \mathbf{G}_{\text{ref}}(\mathbf{r},\mathbf{r}',\omega)\mathbf{E}(\mathbf{r}',\omega)\,\mathrm{d}\mathbf{r}'. \tag{A.7}$$

Using Eq. (A.4), the total field at point $\mathbf{r}$ reads

$$\mathbf{E}(\mathbf{r},\omega) = \mathbf{E}_{\text{ref}}(\mathbf{r},\omega) + k^2 \int \left[\epsilon(\mathbf{r}',\omega) - \epsilon_{\text{ref}}(\mathbf{r}',\omega)\right] \mathbf{G}_{\text{ref}}(\mathbf{r},\mathbf{r}',\omega)\mathbf{E}(\mathbf{r}',\omega)\,\mathrm{d}\mathbf{r}'. \tag{A.8}$$

Eq. (1.22) is called the Lippmann-Schwinger equation.

Appendix B

Regularized Green function and eigenmode expansion in weakly lossy systems

Here, we first introduce the regularized Green function, and derive its expression in the case of vacuum. Then, we derive the expansion of the regularized Green function on the set of eigenmodes of a weakly lossy system. Those results are used to describe the coupling of a resonant scatterer to an eigenmode based on the LDOS in Chaps. 1 and 7.

B.1 Regularized Green function

The aim of this section is to introduce the regularized Green function. To do so, we concentrate on the integral

$$\int_{\delta V} \mathbf{G}_0(\mathbf{r}, \mathbf{r}', \omega)\, \mathrm{d}\mathbf{r}, \tag{B.1}$$

where $\mathbf{G}_0(\mathbf{r}, \mathbf{r}', \omega)$ is the dyadic Green function of the propagation equation of electromagnetic waves in free space and δV is a small volume surrounding $\mathbf{r}'$. In Chap. 1, this integral is used for the derivation of the polarizability of a scatterer in free space. This physical example will guide us in this appendix.

B.1.1 General case of an arbitrary volume δV

For two points $\mathbf{r} \neq \mathbf{r}'$, $\mathbf{G}_0(\mathbf{r}, \mathbf{r}', \omega)$ is given by

$$\mathbf{G}_0(\mathbf{r}, \mathbf{r}', \omega) = \frac{\exp(ikr)}{4\pi r} \left[(\mathbf{I} - \mathbf{uu}) + \frac{ikr - 1}{(kr)^2} (\mathbf{I} - 3\mathbf{uu}) \right], \tag{B.2}$$

where $r = |\mathbf{r} - \mathbf{r}'|$, $\mathbf{u} = (\mathbf{r} - \mathbf{r}')/r$, $\mathbf{I}$ is the unit dyadic, $\mathbf{uu}$ is the tensorial product of $\mathbf{u}$ with itself and $k = \omega/c$. This expression exhibits a non-integrable singularity when $\mathbf{r} = \mathbf{r}'$. Though,

for certain shapes of δV tending to zero, it is well-defined. Mathematically, the dyadic Green function needs to be written

$$\mathbf{G}_0(\mathbf{r},\mathbf{r}',\omega) = \mathrm{PV}\left\{\frac{\exp(ikr)}{4\pi r}\left[(\mathbf{I}-\mathbf{uu}) + \frac{ikr-1}{(kr)^2}(\mathbf{I}-3\mathbf{uu})\right]\right\} - \frac{\mathbf{L}}{k^2}\delta(\mathbf{r}-\mathbf{r}'), \tag{B.3}$$

where PV denotes the principal value operator, and $\mathbf{L}$ is a dyadic that depends on the shape of δV (expressions of $\mathbf{L}$ for various shapes of δV are listed in Ref. [36]). Eq. (B.3) can be integrated over δV

$$\int_{\delta V} \mathbf{G}_0(\mathbf{r},\mathbf{r}',\omega)\mathrm{d}\mathbf{r} = \mathbf{G}_0^{\mathrm{reg}}(\mathbf{r},\mathbf{r},\omega)\delta V - \frac{\mathbf{L}}{k^2}, \tag{B.4}$$

where $\mathbf{G}_0^{\mathrm{reg}}(\mathbf{r},\mathbf{r},\omega)$ is the regularized Green function (by definition). Rigorously, the limit of the integral defined by Eq. (B.1) reads

$$\int_{\delta V\to 0} \mathbf{G}_0(\mathbf{r},\mathbf{r}',\omega)\,\mathrm{d}\mathbf{r} = -\frac{\mathbf{L}}{k^2}. \tag{B.5}$$

Using this result to derive the polarizability of a scatterer in vacuum, one obtains the approached expression in the quasistatic limit Eq. (1.26). As commented in Chap. 1, this expression does not satisfy energy conservation. This is due to the fact that physically, a scatterer cannot be pointlike but must have a finite spatial extent. To correct this approximation, one needs to compute the regularized Green function $\mathbf{G}^{\mathrm{reg}}(\mathbf{r},\mathbf{r},\omega)$.

B.1.2 Case of a spherical volume δV

Let us consider a spherical volume δV, and denote by R its radius. To compute the regularized Green function, let us consider two points $\mathbf{r} \neq \mathbf{r}'$. In this case, the dyadic Green function of vacuum is non-singular and reads

$$\mathbf{G}_0(\mathbf{r},\mathbf{r}',\omega) = \frac{e^{ikr}}{4\pi r}\left[(\mathbf{I}-\mathbf{uu}) + \frac{ikr-1}{(kr)^2}(\mathbf{I}-3\mathbf{uu})\right] \tag{B.6}$$

$$= \frac{k}{4\pi}\frac{\cos(kr)+i\sin(kr)}{(kr)^3}\left[(kr)^2(\mathbf{I}-\mathbf{uu}) + (ikr-1)(\mathbf{I}-3\mathbf{uu})\right]. \tag{B.7}$$

Separating real and imaginary part yields

$$\mathrm{Re}\,\mathbf{G}_0(\mathbf{r},\mathbf{r}',\omega) = \frac{k}{4\pi(kr)^3}\left\{\cos(kr)\left[(kr)^2(\mathbf{I}-\mathbf{uu}) - (\mathbf{I}-3\mathbf{uu})\right] - \sin(kr)(kr)(I-3\mathbf{uu})\right\}, \tag{B.8}$$

$$\mathrm{Im}\,\mathbf{G}_0(\mathbf{r},\mathbf{r}',\omega) = \frac{k}{4\pi(kr)^3}\left\{\sin(kr)\left[(kr)^2(\mathbf{I}-\mathbf{uu}) - (\mathbf{I}-3\mathbf{uu})\right] + \cos(kr)(kr)(I-3\mathbf{uu})\right\}. \tag{B.9}$$

In the limit where $r \to 0$,

$$\mathrm{Re}\,\mathbf{G}_0(\mathbf{r},\mathbf{r}',\omega) \approx \left[\frac{3\mathbf{uu}-\mathbf{I}}{4\pi k^2}\right]\frac{1}{r^3} \tag{B.10}$$

and

$$\mathrm{Im}\,\mathbf{G}_0(\mathbf{r},\mathbf{r}',\omega) \approx \frac{k}{6\pi}\mathbf{I}. \tag{B.11}$$

Integrating the real part of the Green function on an infinitely small spherical volume is complicated and performed carefully in Refs. [157] and [35]. It yields[1]

$$\mathrm{Re}\int_{\delta V\to 0}\mathbf{G}_0(\mathbf{r},\mathbf{r}',\omega)\,\mathrm{d}\mathbf{r} = \frac{-\mathbf{I}}{3k^2}. \tag{B.12}$$

Integrating the imaginary part of $\mathbf{G}_0$ yields

$$\mathrm{Im}\int_{\delta V\to 0}\mathbf{G}_0(\mathbf{r},\mathbf{r}',\omega)\,\mathrm{d}\mathbf{r} = \frac{k\delta V}{6\pi}\mathbf{I}. \tag{B.13}$$

From Eqs. (B.4), (B.12) and (B.13), the regularized Green function of vacuum can be deduced

$$\mathbf{G}_0^{\mathrm{reg}}(\mathbf{r},\mathbf{r},\omega) = i\frac{k}{6\pi}\mathbf{I}. \tag{B.14}$$

Therefore, in the case of a spherical particle, Eq. (B.5) transforms into

$$\int_{\delta V\to 0}\mathbf{G}_0(\mathbf{r},\mathbf{r}',\omega)\,\mathrm{d}\mathbf{r} = \left(-\frac{1}{k^2}+i\frac{k}{6\pi}\right)\mathbf{I}. \tag{B.15}$$

Using the corrected integral Eq. (B.15), one obtains the expression of the dynamic polarizability of a particle in vacuum Eq. (1.25), that satisfies energy conservation.

B.2 Eigenmode expansion of the regularized Green function

In this section, we use the normal set of eigenmodes of the propagation equation of the electric field for a non-lossy system embedded in a closed cavity to expand the Green function of this equation. We generalize this expansion to the case of weakly lossy environment based on a phenomenological approach. In this thesis, we use this expansion to fit the LDOS of a weakly lossy system in Chap. 1, and to give a physical picture to the Cross Density Of States (CDOS) introduced in Chap. 4.

B.2.1 Case of a closed non-absorbing medium

The following derivation was first proposed in Ref. [37]. Let us consider a closed system with no absorption (the dielectric function $\epsilon(\mathbf{r})$ is real) and no dispersion ($\epsilon(\mathbf{r})$ does not depend on ω). In such a system, one can introduce a discrete set of eigenmodes $\{\mathbf{e}_n\}$ of the vector wave equation that obey

$$\boldsymbol{\nabla}\times\boldsymbol{\nabla}\times\mathbf{e}_n(\mathbf{r}) - \epsilon(\mathbf{r})\frac{\omega_n^2}{c^2}\mathbf{e}_n(\mathbf{r}) = 0, \tag{B.16}$$

[1] NB: Using the identity $\int_{4\pi}\mathbf{uu}\,\mathrm{d}\Omega = (4\pi)/3\,\mathbf{I}$ here might be tempting, since the term $\mathbf{I}-3\mathbf{uu}$ in Eq. (B.10) seems to vanish with the angular integration. Though, one needs to be extremely careful about inverting integrals and limits here, and this reasoning is thus incorrect.

where ω_n is the resonant frequency of eigenmode n. This equation can be rewritten in the form

$$\left[\frac{1}{\sqrt{\epsilon(\mathbf{r})}}\boldsymbol{\nabla}\times\boldsymbol{\nabla}\times\frac{1}{\sqrt{\epsilon(\mathbf{r})}}\right]\mathbf{u}_n(\mathbf{r})=\frac{\omega_n^2}{c^2}\mathbf{u}_n(\mathbf{r}) \tag{B.17}$$

with $\mathbf{u}_n(\mathbf{r})=\sqrt{\epsilon(\mathbf{r})}\mathbf{e}_n(\mathbf{r})$. Eq. (B.17) is an eigenvalue equation with an Hermitian operator, that admits a set of orthogonal solutions (eigenmodes) satisfying the orthogonality relationship

$$\int \mathbf{u}_m(\mathbf{r}).\mathbf{u}_n^*(\mathbf{r})\mathrm{d}^3\mathbf{r}=\delta_{mn}. \tag{B.18}$$

As a result, the orthogonality condition for the eigenmodes solution of Eq. (B.16) reads

$$\int |\epsilon(\mathbf{r})|\mathbf{e}_m(\mathbf{r}).\mathbf{e}_n^*(\mathbf{r})\mathrm{d}^3\mathbf{r}=\delta_{mn}. \tag{B.19}$$

Our goal is to expand the Green function on the basis of eigenmodes of Eq. (B.16), in the form

$$\mathbf{G}(\mathbf{r},\mathbf{r}',\omega)=\sum_n \mathbf{A}_n(\mathbf{r}',\omega)\mathbf{e}_n(\mathbf{r},\omega). \tag{B.20}$$

The Green function satisfies

$$\boldsymbol{\nabla}\times\boldsymbol{\nabla}\times\mathbf{G}(\mathbf{r},\mathbf{r}',\omega)-\epsilon(\mathbf{r})\frac{\omega^2}{c^2}\mathbf{G}(\mathbf{r},\mathbf{r}',\omega)=\delta(\mathbf{r}-\mathbf{r}')\mathbf{I} \tag{B.21}$$

Inserting Eq. (B.20) into Eq. (B.21) yields

$$\sum_n \mathbf{A}_n(\mathbf{r}',\omega)\left[\boldsymbol{\nabla}\times\boldsymbol{\nabla}\times\mathbf{e}_n(\mathbf{r})-\epsilon(\mathbf{r})\frac{\omega^2}{c^2}\mathbf{e}_n(\mathbf{r})\right]=\delta(\mathbf{r}-\mathbf{r}')\mathbf{I} \tag{B.22}$$

which, using Eq. (B.16), leads to

$$\sum_n \mathbf{A}_n(\mathbf{r}',\omega)\left(\omega_n^2-\omega^2\right)\epsilon(\mathbf{r})\mathbf{e}_n(\mathbf{r})=c^2\delta(\mathbf{r}-\mathbf{r}')\mathbf{I} \tag{B.23}$$

Multiplying both sides by $\mathbf{e}_m^*(\mathbf{r}')$, integrating over $\mathbf{r}$ and using the orthogonality condition leads to

$$(\omega_n^2-\omega^2)\mathbf{A}_n(\mathbf{r}',\omega)=c^2\mathbf{e}_n^*(\mathbf{r}') \tag{B.24}$$

This equation only defines the distribution $\mathbf{A}_n(\mathbf{r}',\omega)$ modulo two complex constants ϖ and ϖ'.

$$\mathbf{A}_n(\mathbf{r}',\omega)=c^2\mathbf{e}_n^*(\mathbf{r}')\left\{\mathrm{PV}\left[\frac{1}{\omega_n^2-\omega^2}\right]+\varpi\delta(\omega-\omega_n)+\varpi'\delta(\omega+\omega_n)\right\} \tag{B.25}$$

Not all distributions described by Eq. (B.25) have a physical meaning. One way to set ϖ and ϖ' is to consider the case of a very slowly damped harmonic oscillator. Taking the limit when the damping tends to zero should give the exact physical result of the ideal case of a non-damped oscillator. Mathematically speaking, we use the identity

$$\lim_{\Gamma\to 0}\frac{1}{\omega_n^2-\omega^2-i\Gamma\omega}=\mathrm{PV}\left[\frac{1}{\omega_n^2-\omega^2}\right]+\frac{i\pi}{2\omega_n}\delta(\omega-\omega_n)-\frac{i\pi}{2\omega_n}\delta(\omega+\omega_n) \tag{B.26}$$

which allows us to set $\varpi = i\pi/(2\omega_n)$ and $\varpi' = -i\pi/(2\omega_n)$. Finally, we obtain the expression of the physical distribution solution of Eq. (B.24)

$$\mathbf{A}_n(\mathbf{r}',\omega) = c^2\mathbf{e}_n^*(\mathbf{r}')\left\{\mathrm{PV}\left[\frac{1}{\omega_n^2-\omega^2}\right] + \frac{i\pi}{2\omega_n}\delta(\omega-\omega_n) - \frac{i\pi}{2\omega_n}\delta(\omega+\omega_n)\right\}. \tag{B.27}$$

Thus, dropping the term proportionnal to $\delta(\omega+\omega_n)$ corresponding to non-physical negative frequencies, the Green function reads

$$\mathbf{G}(\mathbf{r},\mathbf{r}',\omega) = \sum_n c^2\mathbf{e}_n^*(\mathbf{r}')\mathbf{e}_n(\mathbf{r})\left\{\mathrm{PV}\left[\frac{1}{\omega_n^2-\omega^2}\right] + \frac{i\pi}{2\omega_n}\delta(\omega-\omega_n)\right\} \tag{B.28}$$

For sake of brevity, this expression is usually written

$$\mathbf{G}(\mathbf{r},\mathbf{r}',\omega) = \sum_n \frac{c^2\mathbf{e}_n^*(\mathbf{r}')\mathbf{e}_n(\mathbf{r})}{\omega_n^2-\omega^2}, \tag{B.29}$$

where the expansion into the principal value and the delta distribution is implicit. Note that this decomposition is non-singular when $\mathbf{r}=\mathbf{r}'$. Eq. (B.30) actually gives the expression of the regularized Green function, where the non-integrable singularity at the origin has been removed. This was shown in Ref. [158]. Here, we admit that the expansion obtained here is valid for the regularized Green function, so that

$$\mathbf{G}^{\mathrm{reg}}(\mathbf{r},\mathbf{r}',\omega) = \sum_n c^2\mathbf{e}_n^*(\mathbf{r}')\mathbf{e}_n(\mathbf{r})\left\{\mathrm{PV}\left[\frac{1}{\omega_n^2-\omega^2}\right] + \frac{i\pi}{2\omega_n}\delta(\omega-\omega_n)\right\} \tag{B.30}$$

B.2.2 Phenomenological approach of lossy environments

In many cases, losses have to be taken into account. Dealing with the definition of eigenmodes in open or lossy media is a very complex issue since the operator considered in Eq. (B.17) is not hermitian anymore [37]. Nevertheless, eigenmode attenuation can be accounted for using a phenomenological approach [12]. One introduces a eigenmode damping rate γ_n and modifies Eq. (B.30) in the following way

$$\mathbf{G}^{\mathrm{reg}}(\mathbf{r},\mathbf{r}',\omega) = \sum_n c^2\frac{\mathbf{e}_n^*(\mathbf{r}')\mathbf{e}_n(\mathbf{r})}{\omega_n^2-\omega^2-i\gamma_n\omega}. \tag{B.31}$$

One can remark, using Eq. (B.26), that the limit when all γ_n tend to zero of this phenomenological approach is the expansion of Eq. (B.30). This expansion being valid for weak losses, the linewidth γ_n introduced in Eq. (B.31) is very small compared to the resonant frequency ω_n. Hence, a very good approximation of Eq. (B.31) is given by

$$\mathbf{G}^{\mathrm{reg}}(\mathbf{r},\mathbf{r}',\omega) = \frac{c^2}{2\omega_n}\sum_n \frac{\mathbf{e}_n^*(\mathbf{r}')\mathbf{e}_n(\mathbf{r})}{\omega_n-\omega-i\gamma_n/2}. \tag{B.32}$$

Appendix C

Coupled Dipoles method

We give here a detailed presentation of the coupled dipoles method, that is used to compute the Green function of a disordered system in Chaps. 7 (in 2D with transverse electric polarization) and 6 (in 3D). In the coupled dipoles method, a disordered system is modeled by an assembly of point scatterers randomly located inside a geometrical contour. The scatterers are supposed to be lying in a host medium described by its Green function $\mathbf{G}_0$, that connects the field radiated at point $\mathbf{r}$ by a dipole located at $\mathbf{r}'$ by

$$\mathbf{E}(\mathbf{r},\omega) = \mu_0\omega^2\mathbf{G}_0(\mathbf{r},\mathbf{r}',\omega)\mathbf{p}. \tag{C.1}$$

A typical system obtained for a spherical geometry is shown in Fig. (C.1). Each scatterer is

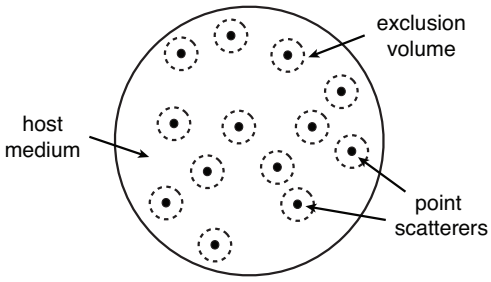


Figure C.1: Coupled dipoles system. Note that an exclusion volume needs to be imposed around the source for the dipolar approximation to remain valid.

described by its polarizability $\alpha(\omega)$, that connects the exciting field $\mathbf{E}^{exc}$ at its position to its induced dipolar momentum $\mathbf{p}$ by

$$\mathbf{p} = \epsilon_0\alpha(\omega)\mathbf{E}^{exc}. \tag{C.2}$$

Considering an external illumination $\mathbf{E}_0$, the exciting field $\mathbf{E}_j^{exc}$ at the position $\mathbf{r}_j$ of scatterer number j reads

$$\mathbf{E}_j^{exc} = \mathbf{E}_0(\mathbf{r}_j) + \frac{\omega^2}{c^2}\alpha(\omega)\sum_{i\neq j}\mathbf{G}_0(\mathbf{r}_j,\mathbf{r}_i,\omega)\mathbf{E}_i^{exc}. \tag{C.3}$$

Eq. (C.3) actually is a set of N coupled linear equations which N unknown are the exciting fields $\mathbf{E}_j^{exc}$ at the position of all scatterers. Inverting this system, one has access to these exciting fields, and thus to the field at any point $\mathbf{r}$ of space, via Eq. (C.4)

$$\mathbf{E}(\mathbf{r},\omega) = \mathbf{E}_0(\mathbf{r},\omega) + \frac{\omega^2}{c^2}\alpha(\omega)\sum_{j=1}^{N}\mathbf{G}_0(\mathbf{r},\mathbf{r}_j,\omega)\mathbf{E}_j^{exc}. \tag{C.4}$$

Illuminating the system by a source dipole $\mathbf{p}$ located at $\mathbf{r}_s$ corresponds to takes an illuminating field $\mathbf{E}_0(\mathbf{r},\omega) = \mu_0\omega^2\mathbf{G}_0(\mathbf{r},\mathbf{r}_s,\omega)$. In this configuration, illustrated in Fig. C.2, one can compute the Green function, and hence the LDOS at the source position $\mathbf{r}_s$. Eqs. (C.3) and (C.4) remain

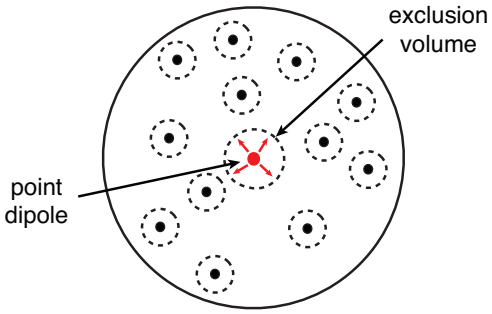


Figure C.2: Coupled dipoles system illuminated by a point dipole. Note that an exclusion volume needs to be imposed around the source for the dipolar approximation to remain valid.

valid if each scatterer is treated within the dipolar approximation. In this thesis, we only consider toy models with rigorously pointlike dipolar scatterers, so that no approximation is done. However, the coupled dipoles method holds for non pointlike scatterers, as long as they remain distant enough from each other, as well as from any source of illumination. In this case, one needs to be careful to only compute the field far away enough from every scatterer. In practice, a minimum distance between the scatterers corresponding to twice their spatial extent is sufficient to satisfy the dipolar approximation, which is hence not a very severe constraint.

Apart from this restriction, the coupled dipoles method allows one to solve the Maxwell equations with no approximation. In particular, it takes into account multiple scattering, polarization, retardation and near-field interactions, which is a crucial point for our work.

Appendix D

Simulation of the growth of disordered metallic films: the KMC 2D algorithm

In this appendix, we describe the algorithm that we implemented to simulate the growth of disordered metallic films. This algorithm was first described in the PhD thesis of Jérémie Aubineau [21]. Figure D.6 sums up the general idea of the algorithm.

D.1 Description of the algorithm

D.1.1 Vocabulary and notations

Our vocabulary and notations are summarized in figure D.1. We consider a $N_{dim} \times N_{dim}$ matrix, where each element is 1 if the corresponding site is occupied by a gold particle (we will describe more precisely the concept of gold particle later), and 0 if the site is empty. We denote by r_0

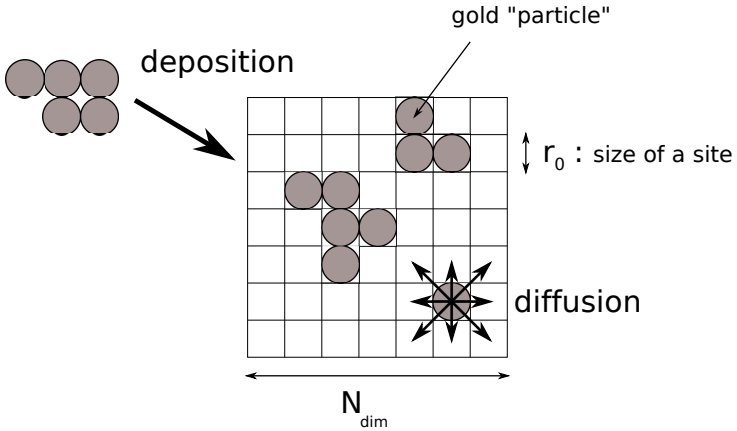


Figure D.1: Geometry of the numerical model.

the lateral size of one site and p the expected filling fraction at the end of the generation. At every iteration of the algorithm, either a new particle is deposited on a free random site or a previously deposited particle diffuses to a more stable neighbour site.

We call *process* a deposition or a diffusion. As a convention, we chose the label $k = 0$ for the deposition of a particle and labels k from 1 to 8 for the 8 possible diffusions to a closest neighbour (see figure D.2)

1	2	3
4		5
6	7	8

Figure D.2: Labels of possible diffusions for a particle from $k = 1$ to 8.

D.1.2 Interaction potential

The physics of the algorithm lies in the interaction between the diffusing gold particles which allows us to compute the probabilities of every process at every iteration. Interactions between transition metal atoms are well described by the interaction potential given by Eq. (D.1), based on a tight-binding second-moment model. The constant r_0 is the lattice constant of the metal, r_{ij} is the distance between atoms i and j, and the constants A, B, p, q are tabulated [81].

$$E_i = A\sum_{j\neq i} e^{-p(r_{ij}/r_0-1)} - B\left[\sum_{j\neq i} e^{-2q(r_{ij}/r_0-1)}\right]^{1/2}, \tag{D.1}$$

We assume that the diffusing particles are clusters of N_{ato} gold atoms interacting which each others. The calculation of the interaction between clusters is a very complicated problem, which leads us to make the assumption of a scaling law between the atomic interaction potential and the interaction potential between particles. Thus, we will use the potential given by Eq. (D.1) for the particles, calling r_0 the lattice constant of the grid and r_{ij} the distance between two particles. In this scaling, there is no reason for the constants A, B, p, q to remain the same as in the atomic potential. We will discuss this later.

Another assumption is to consider only the interactions of a particle with its three kinds of closest neighbours. Figure D.3 shows that there are 12 closest neighbours : 4 at distance r_0 (type A), 4 at distance $r_0\sqrt{2}$ (type B), and 4 at distance $2r_0$ (type C). Denoting by N_A, N_B and N_C respectively the number of neighbours of type A, B and C of a particle placed in site i, the interaction energy reads

$$E_i = A\left[N_A + N_B e^{-p(\sqrt{2}-1)} + N_C e^{-p}\right] - B\left[N_A + N_B e^{-2q(\sqrt{2}-1)} + N_C e^{-2q}\right]^{1/2} \tag{D.2}$$

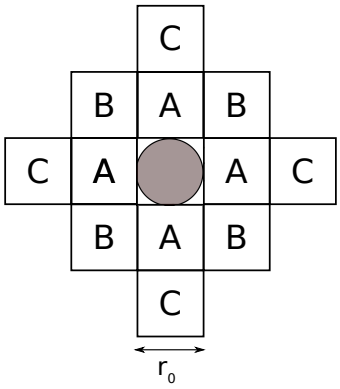


Figure D.3: Closest neighbours of a particle.

D.1.3 Energy barrier for particle diffusion

The diffusion of a particle from a site i to a neighbour site j is a jump allowed by its thermal energy k_BT, where k_B is the Boltzman constant and T the temperature. A major issue in the algorithm is to evaluate the energy barrier corresponding to this jump.

First, we assume that a particle can only diffuse to a more stable site, i.e. to a site of lower energy (figure D.4). In reality, jumping from site i to site j requires some energy even if

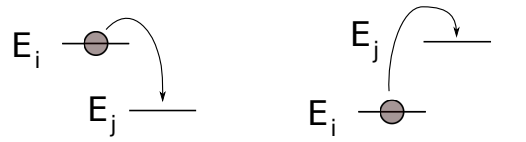


Figure D.4: Diffusion processes.

$E_i \geq E_j$ (see figure D.5). The calculation of the corresponding energy barrier $\Delta E_{i\to j}$ is not a simple problem, even for atoms [79, 159, 80]. We consider that this barrier can be evaluated using Eq. (D.3), where α is a dimensionless constant that accounts for the interaction with the substrate and the rescaling of the potential.

$$\Delta E_{i\to j} = \alpha\,(E_i - E_j) \tag{D.3}$$

D.1.4 Choice of a process

At each iteration of the algorithm, one process is chosen randomly. To do so, one needs to list all available processes, and to define a probability for each of them. Let us define non-normalized

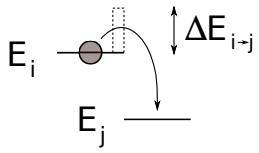


Figure D.5: Diffusion to a more stable site, taking into account the energy barrier $\Delta E_{i\to j}$.

probabilities P'_k for each process. The deposition probability is defined as

$$P'_0 = F.N_{dep}, \tag{D.4}$$

where F is a constant (with dimension s^{-1}) modeling the experimental deposition rate and N_{dep} is the number of particles that remains to be deposited in order to reach the prescribed filling fraction.

The probability for a particle initially located at site i to k-diffuse to site j is given by Eqs. (D.5) and (D.6).

$$p'_{k,i} = 0 \qquad \text{if } E_i < E_j \tag{D.5}$$

$$p'_{k,i} \propto e^{-\Delta E_{i\to j}/k_B T} \qquad \text{if } E_i \geq E_j. \tag{D.6}$$

Hence, the probability to perform a diffusion instead of a deposition is given by

$$P'_k = \sum_{n=1}^{N_{dim}^2} p'_{k,n}. \tag{D.7}$$

Finally, every probability is normalized

$$P_k = \frac{P'_k}{\sum_{k=0}^{8} P'_k}. \tag{D.8}$$

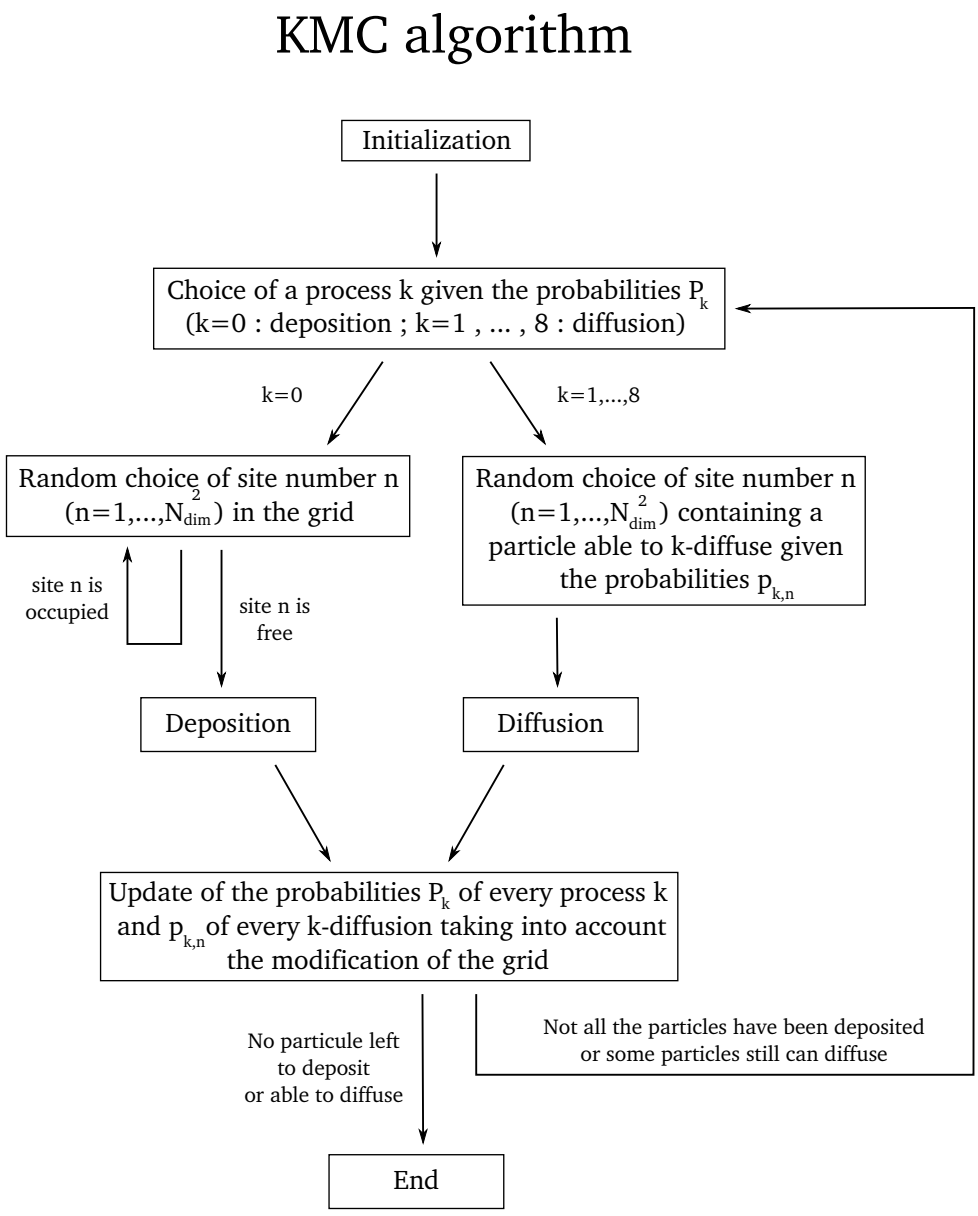


Figure D.6: General description of the algorithm.

Appendix E

Volume Integral method

In this Appendix, we present our numerical method to solve the Maxwell equations on 3D nanostructures. We have developed an exact volume integral method based on the Lippmann-Schwinger equation, that allows us to compute the Green function of nanostructures with no approximation but the discretization of the volume. In particular, we take into account polarization, retardation and near-field effects.

E.1 Weyl expansion of the Green function

Before introducing the volume integral method, we need to present the Weyl expansion of the Green function of a non-absorbing homogeneous medium described by its real dielectric constant ϵ_h. This medium will be referred to as the host medium.

E.1.1 Spatial Fourier transform

Considering monochromatic current sources $\mathbf{j}(\mathbf{r},\omega)$, the propagation equation of the electric field in the host medium reads

$$\boldsymbol{\nabla}\times\boldsymbol{\nabla}\times\mathbf{E}(\mathbf{r},\omega)-\epsilon_h\frac{\omega^2}{c^2}\mathbf{E}(\mathbf{r},\omega)=-i\omega\mu_0\mathbf{j}(\mathbf{r},\omega) \tag{E.1}$$

In the following, we will denote $k=\omega/c$ and $k_h=\sqrt{\epsilon_h}k$. The Green function of the host medium $\mathbf{G}_h$ is defined as the solution of

$$\boldsymbol{\nabla}\times\boldsymbol{\nabla}\times\mathbf{G}_h(\mathbf{r},\mathbf{r}',\omega)-k_h\mathbf{G}_h(\mathbf{r},\mathbf{r}',\omega)=\delta(\mathbf{r}-\mathbf{r}')\mathbf{I}, \tag{E.2}$$

that satisfies an outgoing wave condition. Since the medium is invariant by translation, $\mathbf{G}_h$ only depends on $\mathbf{R}=\mathbf{r}-\mathbf{r}'$ and one can Fourier transform Eq. (E.2). Let us denote $\mathbf{k}$ the conjugate coordinate of $\mathbf{R}$ in Fourier space. Eq. (E.2) transforms into

$$i\mathbf{k}\times i\mathbf{k}\times\mathbf{G}_h(\mathbf{k},\omega)-k_h\mathbf{G}_h(\mathbf{k},\omega)=\mathbf{I}. \tag{E.3}$$

Hence, $\mathbf{G}_h$ reads

$$\mathbf{G}_h(\mathbf{k},\omega) = \left[\left(k^2 - k_h^2\right)\mathbf{I} - \mathbf{k}\otimes\mathbf{k}\right]^{-1} \tag{E.4}$$

The expression of $\mathbf{G}_h$ can be guessed using an integer series expansion.

$$\mathbf{G}_h(\mathbf{k},\omega) = \frac{1}{k^2 - k_h^2}\left[\mathbf{I} - \frac{\mathbf{k}\otimes\mathbf{k}}{k_h^2}\right] \tag{E.5}$$

A matrix multiplication confirms that Eq. (E.5) is the correct inverse required in Eq. (E.4), and hence the correct spatial Fourier transform of $\mathbf{G}_h$.

E.1.2 Weyl expansion

We want to compute $\mathbf{G}_h(k_x,k_y,z,\omega)$ the spatial Fourier transform along x and y (coordinates of $\mathbf{R}$) of the host medium Green function. To do so, we perform the inverse Fourier transform of Eq. (E.5) along the z coordinate. Let us denote k_x, k_y and k_z respectively the conjugate coordinates of x, y and z in the Fourier space.

$$\mathbf{G}_h(k_x,k_y,z,\omega) = \int_{-\infty}^{\infty}\mathbf{G}_h(\mathbf{k},\omega)e^{ik_z z}\frac{\mathrm{d}k_z}{2\pi} \tag{E.6}$$

$$= \int_{-\infty}^{\infty}\frac{1}{k^2 - k_h^2}\left[\mathbf{I} - \frac{\mathbf{k}\otimes\mathbf{k}}{k_h^2}\right]e^{ik_z z}\frac{\mathrm{d}k_z}{2\pi} \tag{E.7}$$

Let us denote k_z^+ the complex that satisfies $(k_z^+)^2 = k_h^2 - k_x^2 - k_y^2$ and $\mathrm{Im}(k_z^+) \geq 0$. The following identities can be computed from the residue method.

$$\int_{-\infty}^{\infty}\frac{e^{ik_z z}}{k_z^2 + k_x^2 + k_y^2 - k_h^2}\frac{\mathrm{d}k_z}{2\pi} = \frac{i}{2k_z^+}e^{ik_z^+|z|} \tag{E.8}$$

$$\int_{-\infty}^{\infty}\frac{k_z e^{ik_z z}}{k_z^2 + k_x^2 + k_y^2 - k_h^2}\frac{\mathrm{d}k_z}{2\pi} = \frac{i\mathrm{sgn}\,(z)}{2}e^{ik_z^+|z|} \tag{E.9}$$

$$\int_{-\infty}^{\infty}\frac{k_z^2 e^{ik_z z}}{k_z^2 + k_x^2 + k_y^2 - k_h^2}\frac{\mathrm{d}k_z}{2\pi} = \frac{ik_z^+}{2}e^{ik_z^+|z|} + \delta(z) \tag{E.10}$$

Using Eqs. (E.8), (E.9) and (E.10), one can transform Eq. (E.6) into

$$\mathbf{G}_h(k_x,k_y,z,\omega) = \mathrm{PV}\left\{\frac{i}{2k_z^+k_h^2}e^{ik_z^+|z|}\mathbf{M}\right\} - \frac{\delta(z)}{k_h^2}\mathbf{e}_z\otimes\mathbf{e}_z. \tag{E.11}$$

where PV denotes the principal value operator and $\mathbf{M}$ the dyadic given by

$$\mathbf{M} = \begin{pmatrix} k_h^2 - k_x^2 & -k_xk_y & -\mathrm{sgn}\,(z)k_z^+k_x \\ -k_xk_y & k_h^2 - k_y^2 & -\mathrm{sgn}\,(z)k_z^+k_y \\ -\mathrm{sgn}\,(z)k_z^+k_x & -\mathrm{sgn}\,(z)k_z^+k_y & k_x^2 + k_y^2 \end{pmatrix}, \tag{E.12}$$

where $\mathrm{sgn}\,(z)$ denotes the sign of a real z. The spatial expansion of the host medium spatial Green function in terms of its Fourier transform coefficients along coordinates x and y is called its Weyl expansion. It reads

$$\mathbf{G}_h(\mathbf{R},\omega) = \frac{i}{2k_h^2}\left\{\int_{-\infty}^{\infty}\int_{-\infty}^{\infty}\mathbf{M}\frac{e^{i\left[k_xX + k_yY + k_z^+|Z|\right]}}{k_z^+}\frac{\mathrm{d}k_x}{2\pi}\frac{\mathrm{d}k_y}{2\pi}\right\} - \frac{\delta(\mathbf{R})}{k_h^2}\mathbf{e}_z\otimes\mathbf{e}_z \tag{E.13}$$

E.2 The Volume Integral method

E.2.1 The Lippmann-Schwinger equation

We consider a volume V filled with a homogeneous material described by a dielectric constant $\epsilon(\omega)$[1]. The system is lying in a homogeneous host medium described by its dielectric constant ϵ_h and its Green function $\mathbf{G}_h$. Considering sources radiating an incident field $\mathbf{E}_0(\mathbf{r},\omega)$, the electric field at any point $\mathbf{r}$ obeys the Lippmann-Schwinger equation (see Appendix A)

$$\mathbf{E}(\mathbf{r},\omega) = \mathbf{E}_0(\mathbf{r},\omega) + k^2[\epsilon(\omega)-\epsilon_h]\int_V \mathbf{G}_h(\mathbf{r},\mathbf{r}',\omega)\mathbf{E}(\mathbf{r}',\omega)\mathrm{d}\mathbf{r}'. \tag{E.14}$$

In order to solve this equation numerically, we discretize V into cells of size Δ, and assume that the electric field is constant in each cell (the volume of cell number j will be denoted by V_j). As far as the Green function is concerned, we define

$$\mathbf{G}_{ij}^{\mathrm{int}} = \int_{V_j} \mathbf{G}_h(\mathbf{r}_i,\mathbf{r}',\omega)\,\mathrm{d}\mathbf{r}'. \tag{E.15}$$

Since the expression of $\mathbf{G}_h$ is analytical, it is possible to consider it constant over the cell, or to integrate it analytically to accelerate convergence. Here, we only present the approach with the analytical integration. Reinserting Eq. (E.15) into Eq. (E.14), one obtains the linear system of N equations satisfied by the values of the electric field inside each cube, denoted $\mathbf{E}_i = \mathbf{E}(\mathbf{r}_i,\omega)$

$$\left\{\mathbf{I} - k^2\left[\epsilon(\omega)-\epsilon_h\right]\mathbf{G}_{ii}^{\mathrm{int}}\right\}\mathbf{E}_i - k^2\left[\epsilon(\omega)-\epsilon_h\right]\sum_{j\neq i}\mathbf{G}_{ij}^{\mathrm{int}}\mathbf{E}_j = \mathbf{E}_0(\mathbf{r}_i,\omega). \tag{E.16}$$

The solution leads to the expression of the three components of the electric field $\mathbf{E}_i$ in cell number i, for all i.

E.2.2 Analytical integration of the Green function over the unit cells

To accelerate convergence, one can analytically integrate the Green function of the homogeneous medium. To do so, one has to perform a Weyl expansion and to work in the Fourier space. The approach detailed here is largely inspired from Ref. [160].

Calculation of $\mathbf{G}_{ij}^{\mathrm{int}}$

When $i \neq j$, no singularity is involved and one can simply integrate the expression of $\mathbf{G}_h(\mathbf{r}_i,\mathbf{r}',\omega)$ [Eq. (E.8)] in direct space over $\mathbf{r}'$.

$$\mathbf{G}_h(\mathbf{r}_i,\mathbf{r}',\omega) = \frac{e^{ik_h|\mathbf{r}_i-\mathbf{r}'|}}{4\pi|\mathbf{r}_i-\mathbf{r}'|}\left\{\mathbf{I} - \left(\mathbf{r}_i-\mathbf{r}'\right)\otimes\left(\mathbf{r}_i-\mathbf{r}'\right) + \left(\frac{ik_h|\mathbf{r}_i-\mathbf{r}'|-1}{(k_h|\mathbf{r}_i-\mathbf{r}'|)^2}\right)\left[\mathbf{I} - 3\left(\mathbf{r}_i-\mathbf{r}'\right)\otimes\left(\mathbf{r}_i-\mathbf{r}'\right)\right]\right\} \tag{E.17}$$

[1]The case of a non-homogeneous dielectric constant is not described here, but our formalism can be trivially generalized to deal with this situation.

Calculation of $\mathbf{G}_{ii}^{\text{int}}$

Let us denote V_j the volume of the unit cell centered at $\mathbf{r}_j$ and Δ the volume of the one centered at $\mathbf{r}=\mathbf{0}$. Using the change of variable $\mathbf{R}=\mathbf{r}_j-\mathbf{r}'$ and knowing that $\mathbf{G}_h(\mathbf{r},\mathbf{r}',\omega)$ only depends on $\mathbf{r}-\mathbf{r}'$ (translational invariance of the host medium), one obtains

$$\begin{aligned}\mathbf{G}_{ii}^{\text{int}} &= \int_{V_i}\mathbf{G}_h(\mathbf{r}_i-\mathbf{r}',\omega)\,\mathrm{d}\mathbf{r}' \\ &= \int_{\Delta}\mathbf{G}_h(\mathbf{R},\omega)\,\mathrm{d}\mathbf{R}\end{aligned} \tag{E.18}$$

To integrate, we use the Weyl expansion of the Green function, that reads (see part E.1)

$$\mathbf{G}_h(\mathbf{r},\omega)=\frac{i}{2k_h^2}\left\{\int_{-\infty}^{\infty}\int_{-\infty}^{\infty}\mathbf{M}\frac{e^{i\left[k_x x+k_y y+k_z^+|z|\right]}}{k_z^+}\frac{\mathrm{d}k_x}{2\pi}\frac{\mathrm{d}k_y}{2\pi}\right\}-\frac{\delta(\mathbf{r})}{k_h^2}\mathbf{e}_z\otimes\mathbf{e}_z, \tag{E.19}$$

where $\mathbf{M}$ is the dyadic defined in Eq. (E.12), and k_z^+ is the complex number that satisfies $(k_z^+)^2=k_h^2-k_x^2-k_y^2$ and $\operatorname{Im}k_z^+\geq 0$. Inserting Eq. (E.19) into Eq. (E.18) and assuming that the unit cell is a cube which lateral size is Δ yields

$$\mathbf{G}_{ii}^{\text{int}}=\frac{i}{8\pi^2k_h^2}\left\{\int\int\int_{-\Delta/2}^{\Delta/2}\mathrm{d}x'\mathrm{d}y'\mathrm{d}z'\int_{k_x,k_y}\frac{\mathrm{d}k_x\mathrm{d}k_y}{k_z^+}\mathbf{M}e^{i\left[k_x x'+k_y y'+k_z^+|z'|\right]}\right\}-\frac{\mathbf{e}_z\otimes\mathbf{e}_z}{k_h^2} \tag{E.20}$$

First, from Eq. (E.18), the diagonal terms of $\mathbf{G}^{\text{int}}$ are equal (every direction plays exactly the same role in the integral). The non-diagonal terms vanish [160]

Let us focus on the component $\mathbf{G}_{zz}^{\text{int}}(\mathbf{r}_i,\mathbf{r}_i)$. We use the following identities

$$\int_{-\Delta/2}^{\Delta/2}e^{ik_x x'}\mathrm{d}x'=\frac{2\sin(k_x\Delta/2)}{k_x}, \tag{E.21}$$

$$\int_{-\Delta/2}^{\Delta/2}e^{ik_z^+|z'|}dz'=\frac{2}{ik_z^+}\left(e^{ik_z^+\Delta/2}-1\right), \tag{E.22}$$

$$\int_{-\infty}^{+\infty}\int_{-\infty}^{+\infty}\frac{\sin(k_x\Delta/2)\sin(k_y\Delta/2)}{k_xk_y}\mathrm{d}k_x\mathrm{d}k_y=\pi^2. \tag{E.23}$$

To perform the spatial integrals in Eq. (E.20), we use Eqs. (E.21) and (E.22). Then we reinject the singularity inside the integral by using Eq. (E.23). Finallly, we obtains the relation

$$\mathbf{G}_{zz}^{\text{int}}(\mathbf{r}_i,\mathbf{r}_i,\omega)=\frac{1}{\pi^2k_h^2}\int_{k_x,k_y}\frac{\sin(k_x\Delta/2)\sin(k_y\Delta/2)}{k_xk_yk_z^{+2}}\left\{\left(k_x^2+k_y^2\right)e^{ik_z^+\Delta/2}-k_h^2\right\}\mathrm{d}k_x\mathrm{d}k_y \tag{E.24}$$

We perform the polar change of variable $k_x=k_{/\!/}\cos\theta$ and $k_y=k_{/\!/}\sin\theta$. This leads to

$$\mathbf{G}_{zz}^{\text{int}}(\mathbf{r}_i,\mathbf{r}_i,\omega)=\frac{1}{\pi^2k_h^2}\int_{k_{/\!/}=0}^{\infty}\frac{\mathrm{d}k_{/\!/}}{k_{/\!/}}\frac{k_{/\!/}^2e^{i\Delta/2\sqrt{k_h^2-k_{/\!/}^2}}-k_h^2}{k_h^2-k_{/\!/}^2}\int_{\theta=0}^{2\pi}\frac{\sin(k_{/\!/}\Delta/2\cos\theta)\sin(k_{/\!/}\Delta/2\sin\theta)}{\cos\theta\sin\theta}\mathrm{d}\theta \tag{E.25}$$

Finally, by making the change of variable $k_z^+ = \sqrt{k_h^2 - k_{/\!/}^2}$, one obtains

$$\mathbf{G}_{zz}^{\text{int}}(\mathbf{r}_i, \mathbf{r}_i, \omega) = \frac{4}{\pi^2 k_h^2}\left[\int_{k_z^+=k_h}^{0} + \int_{k_z^+=i0}^{i\infty}\right] \frac{k_h^2 - k_{/\!/}^2 e^{ik_z^+\Delta/2}}{k_{/\!/}k_z^+} \int_0^{\frac{\pi}{2}} \frac{\sin\left(k_{/\!/}\Delta/2\cos\theta\right)\sin\left(k_{/\!/}\Delta/2\sin\theta\right)}{\cos\theta\sin\theta}\mathrm{d}\theta\mathrm{d}k_z^+ \tag{E.26}$$

E.3 Energy balance

We consider a medium described by its dielectric constant $\epsilon(\mathbf{r})$[2], lying in a host medium described by its real, uniform dielectric constant ϵ_h. The system is illuminated by a source dipole $\mathbf{p}$ located at $\mathbf{r}_s$. The source current associated to the dipolar source is $\mathbf{j}_s(\mathbf{r}, \omega) = -i\omega\delta(\mathbf{r} - \mathbf{r}_s)\mathbf{p}$.

E.3.1 Power transferred to the environment

The average power transferred by the emitter to its environment through the electromagnetic field is

$$P = \frac{\omega}{2}\text{Im}\left[\mathbf{p}^*.\mathbf{E}(\mathbf{r}_s)\right]. \tag{E.27}$$

Note that this power can be either transferred to a radiative mode (emission of a photon in the far field) or a non-radiative mode (the energy stays localized around the emitter and is eventually absorbed by the environment).

When the emitter is embedded in the host medium, this power is deduced from the non-singular imaginary part of the Green function $\text{Im}\,\mathbf{G}_h(\mathbf{0}) \sim k_h/(6\pi)\mathbf{I}$, where $k_h = k\sqrt{\epsilon_h}$. It reads

$$P_e = \frac{\mu_0\omega^3}{12\pi}k_h|\mathbf{p}|^2, \tag{E.28}$$

Finally, when the emitter is embedded in the medium described by $\epsilon(\mathbf{r})$, one can use the Lippmann-Schwinger equation (E.14) and insert it into Eq. (E.27). This yields

$$\frac{P}{P_e} = 1 + \frac{6\pi\epsilon_0}{k_h|\mathbf{p}|^2}\text{Im}\left[\mathbf{p}^*.\int_V \left\{\epsilon(\mathbf{r}) - \epsilon_h\right\}\mathbf{G}_h(\mathbf{r}_s - \mathbf{r}')\mathbf{E}(\mathbf{r}')\,\mathrm{d}^3\mathbf{r}'\right] \tag{E.29}$$

E.3.2 Absorption by the medium (non-radiative channels)

The average power absorbed by the medium reads

$$P_{NR} = \omega\,\text{Im}\left[\int_V \mathbf{j}(\mathbf{r}).\mathbf{E}^*(\mathbf{r})\right]/2 \tag{E.30}$$

Normalizing by the power P_e yields

$$\frac{P_{NR}}{P_e} = \frac{6\pi\epsilon_0^2}{k^2 k_h|\mathbf{p}|^2}\int_V \text{Im}\left\{\epsilon(\mathbf{r}')\right\}|\mathbf{E}(\mathbf{r}')|^2\,\mathrm{d}^3\mathbf{r}' \tag{E.31}$$

[2]The omega dependance is omitted for sake of simplicity. This does not reduce the generality of our discussion.

E.3.3 Radiation to the far field (radiative channels)

We assume that the dipole source is located at the origin ($\mathbf{r}_s = \mathbf{0}$). We consider a point $\mathbf{r}$, and denote $\mathbf{r} = r\mathbf{u}$, where $\mathbf{u}$ is a unit vector. The average power flux at point $\mathbf{r}$, if the latter is located in the far field of the source, reads

$$\mathbf{J}_R(\mathbf{r}) = \frac{\epsilon_0}{2}|\mathbf{E}(\mathbf{r})|^2\mathbf{u}, \tag{E.32}$$

where $\mathbf{E}(\mathbf{r})$ is the field at $\mathbf{r}$ and $\mathbf{u} = \mathbf{r}/|\mathbf{r}|$. The power $P_R(\mathbf{u})$ radiated per unit solid angle $\mathrm{d}\Omega$ in direction $\mathbf{u}$ in the far field reads

$$P_R(\mathbf{u}) = \lim_{r\to\infty} \frac{\epsilon_0}{2} r^2 |\mathbf{E}(\mathbf{r})|^2. \tag{E.33}$$

The field $\mathbf{E}(\mathbf{r})$ is given by the Lippmann-Schwinger equation [Eq. (E.14)]

$$\mathbf{E}(\mathbf{r}) = \mathbf{E}_0(\mathbf{r}) + k^2 \int_V \{\epsilon(\mathbf{r}) - \epsilon_h\}\, \mathbf{G}_h(\mathbf{r}-\mathbf{r}')\mathbf{E}(\mathbf{r}')\, \mathrm{d}^2\mathbf{r}'. \tag{E.34}$$

In the far field limit ($r \gg L$ and $r \gg L^2/\lambda$, where L is the spatial extent of the source), this expression can be simplified using the far field expression $\mathbf{G}_h^R$ of the Green function of the host medium $\mathbf{G}_h$, that reads

$$\mathbf{G}_h^R(\mathbf{r}-\mathbf{r}') = \frac{e^{ik_h r}}{4\pi r}\left[\mathbf{I} - \mathbf{u}\otimes\mathbf{u}\right] e^{-ik_h \mathbf{u}.\mathbf{r}'}. \tag{E.35}$$

The far field expression of the field is

$$\mathbf{E}^R(\mathbf{r}) = \frac{e^{ik_h r}}{4\pi r}\left\{\mu_0\omega^2\left[\mathbf{I} - \mathbf{u}\otimes\mathbf{u}\right]\mathbf{p} + k^2\int_V \{\epsilon(\mathbf{r}) - \epsilon_h\}\, e^{-ik_h\mathbf{u}.\mathbf{r}'}\left[\mathbf{I} - \mathbf{u}\otimes\mathbf{u}\right]\mathbf{E}(\mathbf{r}')\, \mathrm{d}^3\mathbf{r}'\right\} \tag{E.36}$$

Hence, introducing Eq. (E.36) into Eq. (E.33), and normalizing by P_e, the power radiated per unit solid angle in direction $\mathbf{u}$ in the far field is rigorously

$$\frac{P_R(\mathbf{u})}{P_e} = \frac{3}{8\pi}\frac{\epsilon_0^2}{\omega k^2 k_h |\mathbf{p}|^2}\left|\left\{\mu_0\omega^2\left[\mathbf{I} - \mathbf{u}\otimes\mathbf{u}\right]\mathbf{p} + k^2\int_V \{\epsilon(\mathbf{r}) - \epsilon_h\}\, e^{-ik_h\mathbf{u}.\mathbf{r}'}\left[\mathbf{I} - \mathbf{u}\otimes\mathbf{u}\right]\mathbf{E}(\mathbf{r}')\, \mathrm{d}^3\mathbf{r}'\right\}\right|^2 \tag{E.37}$$

The total power radiated by the source in the far field can be computed either by integrating the directional power $P_R(\mathbf{u})$

$$\frac{P_R}{P_e} = \int_{4\pi} \frac{P_R(\mathbf{u})}{P_e}\mathrm{d}\mathbf{u} \tag{E.38}$$

or by using energy conservation, since the energy that is not radiated in the near-field has to be eventually absorbed in the environment

$$\frac{P_R}{P_e} = \frac{P}{P_e} - \frac{P_{NR}}{P_e}. \tag{E.39}$$

Checking the agreement between the results of Eqs. (E.38) and (E.39) is a way to detect errors in the numerical calculations. We have performed this test in all our numerical calculations based on the Lippmann-Schwinger equation.

Appendix F

T-T speckle intensity correlations in the diffusive regime

Contents

F.1 Leading term for the long-range correlation 149
F.2 Useful integrals 150

F.1 Leading term for the long-range correlation

Let us now consider the transmission-transmission geometry, i.e. the correlations between two points located in the output plane $z = z' = d$. In Eq. (5.42), replacing L by its expression and performing the integrals yields

$$F(Kd) = \frac{\pi}{12k^2\ell d}\frac{\sinh^2(K\ell_e)}{K^2}\frac{\sinh(2Kd) - 2Kd}{Kd\sinh^2(Kd)}. \tag{F.1}$$

Eq. (F.1) can be interpreted as the angular correlations between two outgoing plane-wave with a wavevector difference which modulus equals K. Provided that $K\ell_e \ll 1$, i.e. that we focus on the correlation for large distances, it can be approached by

$$F(Kd) = \frac{\pi\ell}{27k^2d}\frac{\sinh(2Kd) - 2Kd}{Kd\sinh^2(Kd)}, \tag{F.2}$$

where we have used $\ell_\epsilon \approx 2\ell/3$. Finally, inserting Eq. (F.2) into Eq. (5.42), and normalizing by the average intensity product $\langle \mathbf{I}(z=d)\rangle^2$ given by Eq. (5.38), one obtains

$$C_2^{T/T}(\Delta r) = \frac{1}{48(k\ell)^2}\frac{\ell}{d}\int_0^\infty J_0(q\Delta r/L_e)\frac{\sinh(2q) - 2q}{\sinh^2(q)}\,\mathrm{d}q, \tag{F.3}$$

where $\Delta r = |\mathbf{R}|$ and J_0 is the Bessel function of first kind and zero order, defined as

$$J_0(x) = \frac{1}{\pi}\int_0^\pi \mathrm{d}\theta\, \exp(ix\cos\theta). \tag{F.4}$$

It can be transformed for the sake of numerical convergence into

$$C_2^{T/T}(\Delta r) = \frac{1}{24(k\ell)^2}\left(\frac{\ell}{d}\right)\left[\frac{1}{2}\int_0^\infty J_0(q\Delta r/L_e)\left\{\frac{\sinh(2q)-2q}{\sinh^2(q)}-2\right\}\,\mathrm{d}q+\frac{d}{\Delta r}\right]. \tag{F.5}$$

Note that this expression diverges for small distances because of the approximation $K\ell_e \ll 1$. This divergence does not have any physical origin, and can be avoided using

$$C_2^{T/T}(\Delta r) = \frac{3}{76(k\ell)^2}\frac{d}{\ell}\int_0^\infty J_0(q\Delta r/d)\frac{\sinh^2(q\ell_e/d)}{q^2}\frac{\sinh(2q)-2q}{\sinh^2(q)}\,\mathrm{d}q. \tag{F.6}$$

F.2 Useful integrals

$$\int_0^\infty e^{-r/\ell}\mathrm{d}r = \ell \tag{F.7}$$

$$\int_0^\infty re^{-r/\ell}\mathrm{d}r = \ell^2 \tag{F.8}$$

$$\int_0^\infty r^2e^{-r/\ell}\mathrm{d}r = 2\ell^3 \tag{F.9}$$

Let $\mathrm{G}(\mathbf{r},\mathbf{r}',\omega)$ the average Green function of the infinite medium, defined by Eq. (5.10).

$$\int \mathrm{d}\mathbf{r}|\langle \mathrm{G}(\mathbf{r},\mathbf{r}',\omega)\rangle|^2 = \frac{\ell}{4\pi} \tag{F.10}$$

$$\int \mathrm{d}\mathbf{r}_1\langle \mathrm{G}(\mathbf{r},\mathbf{r}_1,\omega)\mathrm{G}^*(\mathbf{r}',\mathbf{r}_1)\rangle = \frac{\ell}{4\pi}\frac{\sin(k\Delta r)}{k\Delta r}\exp(-\Delta r/2\ell) \tag{F.11}$$

$$\int_0^d \mathrm{d}z_1(d-z_1)^2\cosh(2Kz_1) = \frac{\sinh(2Kd)-2Kd}{4K^3} \tag{F.12}$$

$$\begin{aligned}\int_0^d \mathrm{d}z_1(d-z_1+\ell_e)^2\cosh[K(d-2z_1)]\\ = \frac{1}{2K^3}\left[K^2(d^2+2d\ell_e+2\ell_e^2)\sinh(Kd)-Kd\cosh(Kd)+\sinh(Kd)\right]\end{aligned} \tag{F.13}$$

Bibliography

[1] A. G. Curto, G. Volpe, T. H. Taminiau, M. P. Kreuzer, R. Quidant, and N. F. van Hulst, "Unidirectional emission of a quantum dot coupled to a nanoantenna," Science **329**, 930 (2010).

[2] R. Sapienza, P. Bondareff, R. Pierrat, B. Habert, R. Carminati, and N. F. van Hulst, "Long-tail statistics of the purcell factor in disordered media driven by near-field interactions," Phys. Rev. Lett. **106**, 163902 (2011).

[3] V. Krachmalnicoff, E. Castanié, Y. De Wilde, and R. Carminati, "Fluctuations of the local density of states probe localized surface plasmons on disordered metal films," Phys. Rev. Lett. **105**, 183901 (2010).

[4] L. Sapienza, H. Thyrrestrup, S. Stobbe, P. D. García, S. Smolka, and P. Lodahl, "Cavity quantum electrodynamics with Anderson-localized modes," Science **327**, 1352 (2010).

[5] J. Gao, S. Combrie, B. Liang, P. Schmitteckert, G. Lehoucq, S. Xavier, X. Xu, K. Busch, D. L. Huffaker, A. De Rossi, and C. W. Wong, "Strongly coupled slow-light polaritons in one-dimensional disordered localized states," Sci. Rep. **3**, 1994 (2013).

[6] L. Allen and J. H. Eberly, *Optical Resonance and Two-Level Atoms* (Dover, New York, USA, 1977).

[7] D. P. Craig and Thirunamachandran, *Molecular Quantum Electrodynamics* (Dover, New York, USA, 1998).

[8] L. Novotny and B. Hecht, *Principles of Nano-Optics* (Cambridge University Press, 2006).

[9] Y. Kaluzny, P. Goy, M. Gross, J. M. Raimond, and S. Haroche, "Observation of self-induced Rabi oscillations in two-level atoms excited inside a resonant cavity: The ringing regime of superradiance," Phys. Rev. Lett. **51**, 1175 (1983).

[10] C. Cohen-Tannoudji, B. Diu, and F. Laloe, *Quantum mechanics* (Hermann, 1997).

[11] L. Novotny, "Strong coupling, energy splitting, and level crossings: A classical perspective," Am. J. Phys. **78**, 1199 (2010).

[12] S. Haroche, *"Cavity Quantum Electrodynamics", in Fundamental Systems in Quantum Optics* (Les Houches Session LIII, 1992).

[13] S. Haroche and J.-M. Raimond, *Exploring the quantum: Atoms, cavities and photons* (Oxford University Press, Oxford, 2006).

[14] P. Berman (ed.), *Cavity Quantum Electrodynamics* (Academic Press, New York, 1994).

[15] T. Yoshie, A. Scherer, H. J., G. Khitrova, H. M. Gibbs, G. Rupper, C. Ell, O. B. Shchekin, and D. G. Deppe, "Vacuum Rabi splitting with a single quantum dot in a photonic crystal nanocavity," Nature **432**, 200 (2004).

[16] V. Krachmalnicoff, D. Cao, A. Cazé, E. Castanié, R. Pierrat, N. Bardou, S. Collin, R. Carminati, and Y. De Wilde, "Towards a full characterization of a plasmonic nanostructure with a fluorescent near-field probe," Opt. Express **21**, 11536 (2013).

[17] R. F. Harrington, *Field Computations by Moment Methods* (IEEE Press, New York, USA, 1992).

[18] A. D. Mirlin, "Statistics of energy levels and eigenfunctions in disordered systems," Phys. Rep. **326**, 259 (2000).

[19] S. Grésillon, L. Aigouy, A. C. Boccara, J. Rivoal, X. Quélin, C. Desmarest, P. Gadenne, V. Shubin, A. Sarychev, and V. Shalaev, "Experimental observation of localized optical excitations in random metal-dielectric films," Phys. Rev. Lett. **82**, 4520 (1999).

[20] V. Shalaev, *Nonlinear optics of random media* (Springer, Berlin, 2000).

[21] J. Aubineau, *Modélision de couches minces métalliques fractales et calculs d'exaltations de champs électromagnétiques.* (Université de Versailles Saint-Quentin, 2005).

[22] T. Förster, "Intermolecular energy migration and fluorescence." Ann. Phys. **437**, 55 (1948).

[23] R. Carminati, R. Pierrat, J. de Rosny, and M. Fink, "Theory of the time reversal cavity for electromagnetic fields," Opt. Lett. **32**, 3107 (2007).

[24] J. W. Goodman, *Statistical Optics* (John Wiley & Sons, New York, 1985).

[25] A. Ishimaru, *Wave Propagation and Scattering in Random Media* (IEEE Press, Oxford, 1997).

[26] P. Sheng, *Introduction to Wave Scattering, Localization, and Mesoscopic Phenomena* (Academic Press, San Diego, 1995).

[27] E. Akkermans and G. Montambaux, *Mesoscopic Physics of Electrons and Photons* (Cambridge University Press, Cambridge, UK, 2007).

[28] B. Shapiro, "New type of intensity correlation in random media," Phys. Rev. Lett. **83**, 4733 (1999).

[29] S. Feng, C. Kane, P. A. Lee, and A. D. Stone, "Correlations and fluctuations ofcoherent wave transmission through disordered media," Phys. Rev. Lett. **61**, 834 (1988).

[30] S. E. Skipetrov and R. Maynard, "Nonuniversal correlations in multiple scattering," Phys. Rev. B **62**, 886 (2000).

[31] B. A. van Tiggelen and S. E. Skipetrov, "Fluctuations of local density of states and C0 speckle correlations are equal," Phys. Rev. E **73**, 045601(R) (2006).

[32] A. Lagendijk, B. A. van Tiggelen, and D. S. Wiersma, "Fifty years of Anderson localization," Phys. Today **62**, 24 (2009).

[33] J. Wang and A. Z. Genack, "Transport through modes in random media," Nature **471**, 345 (2011).

[34] D. Laurent, O. Legrand, P. Sebbah, C. Vanneste, and F. Mortessagne, "Localized modes in a finite-size open disordered microwave cavity," Phys. Rev. Lett. **99**, 253902 (2007).

[35] J. van Bladel, "Some remarks on Green's dyadic for infinite space." IRE Trans. Antennas Propag. **AP-9**, 563 (1961).

[36] A. D. Yaghjian, "Electric dyadic Green's functions in the source region," Proceedings of the IEEE **68**, 248 (1980).

[37] R. J. Glauber and M. Lewenstein, "Quantum optics of dielectric media," Phys. Rev. A **43**, 467 (1991).

[38] C.-A. Guérin, B. Gralak, and A. Tip, "Singularity of the dyadic Green's function for heterogeneous dielectrics," Phys. Rev. E **75**, 056601 (2007).

[39] K. J. Vahala, "Optical micro cavities," Nature **424**, 839 (2003).

[40] R. Carminati, J.-J. Greffet, C. Henkel, and J. M. Vigoureux, "Radiative and non-radiative decay of a single molecule close to a metallic nano particle," Opt. Commun. **261**, 368 (2006).

[41] J. D. Jackson, *Classical Electrodynamics* (John Wiley & Sons, New York, 1998).

[42] C. F. Bohren and D. R. Huffman, *Absorption and scattering of light by small particles* (John Wiley & Sons, New York, 1998).

[43] H. C. van de Hulst, *Light scattering by small particles* (John Wiley & Sons, New York, 1957).

[44] R. Loudon, *The quantum theory of light* (Oxford University Press Inc., New York, 2001).

[45] P. de Vries, D. V. van Coevorden, and A. Lagendijk, "Point scatterers for classical waves," Rev. Mod. Phys. **70**, 447 (1998).

[46] E. Castanié, R. Vincent, R. Pierrat, and R. Carminati, "Absorption by an optical dipole antenna in a structured environment," Int. J. Opt. **2012**, 452047 (2012).

[47] S. Albaladejo, R. Gómez-Medina, L. S. Froufe-Pérez, H. Marinchio, R. Carminati, J. F. Torrado, G. Armelles, A. García-Martín, and J. J. Sáenz, "Radiative corrections to the polarizability tensor of an electrically small anisotropic dielectric particle," Opt. Express **18**, 3556 (2010).

[48] M. Brune, F. Schmidt-Kaler, A. Maali, J. Dreyer, E. Hagley, J. Raimond, and S. Haroche, "Quantum rabi oscillation: A direct test of field quantization in a cavity," Phys. Rev. Lett. **76**, 1800 (1996).

[49] H. J. Kimble, "Strong interactions of single atoms and photons in cavity QED," Physica Scripta **T76**, 127 (1998).

[50] J. M. Wylie and J. E. Sipe, "Quantum electrodynamics near an interface," Phys. Rev. A **30**, 1185 (1984).

[51] C. van Vlack, P. T. Kristensen, and S. Hughes, "Spontaneous emission spectra and quantum light-matter interactions from a strongly coupled quantum dot metal-nanoparticle system," Phys. Rev. B **85**, 075303 (2012).

[52] L. Novotny and N. van Hulst, "Antennas for light," Nat. Photonics **5**, 83 (2011).

[53] K. Vynck, M. Burresi, F. Riboli, and D. S. Wiersma, "Photon management in two-dimensional disordered media," Nat. Mat. **11**, 1017 (2012).

[54] S. Kühn, U. Håkanson, L. Rogobete, and V. Sandoghdar, "Enhancement of single-molecule fluorescence using a gold nanoparticle as an optical nanoantenna," Phys. Rev. Lett. **97**, 017402 (2006).

[55] P. Anger, P. Bharadwaj, and L. Novotny, "Enhancement and quenching of single-molecule fluorescence," Phys. Rev. Lett. **96**, 113002 (2006).

[56] M. P. Busson, B. Rolly, B. Stout, N. Bonod, and S. Bidault, "Accelerated single photon emission from dye molecule-driven nanoantennas assembled on dna," Nat. Comm. **3**, 962 (2012).

[57] E. Castanié, V. Krachmalnicoff, A. Cazé, R. Pierrat, Y. De Wilde, and R. Carminati, "Distance dependance of the local density of states in the near-field of a disordered plasmonic film," Opt. Lett. **37**, 3006 (2012).

[58] J. Michaelis, C. Hettich, J. Mlynek, and V. Sandoghdar, "Optical microscopy using a single-molecule light," Nature **405**, 325 (2000).

[59] S. Kühn, C. Hettich, C. Schmitt, J. P. Poizat, and V. Sandoghdar, "Diamond color centers as a nanoscopic light source for scanning near-field optical microscopy," J. Microsc. **202**, 2 (2001).

[60] Y. De Wilde, F. Formanek, R. Carminati, B. Gralak, P.-A. Lemoine, K. Joulain, J.-P. Mulet, Y. Chen, and J.-J. Greffet, "Thermal radiation scanning tunnelling microscopy," Nature **444**, 740 (2006).

[61] K. Joulain, J.-P. Mulet, F. Marquier, R. Carminati, and J.-J. Greffet, "Surface electromagnetic waves thermally excited: Radiative heat transfer, coherence properties and Casimir forces revisited in the near field," Surf. Sci. Rep. **57**, 59 (2005).

[62] C. Chicanne, T. David, R. Quidant, J. C. Weeber, Y. Lacroute, E. Bourillot, and A. Dereux, "Imaging the local density of states of optical corrals," Phys. Rev. Lett. **88**, 097402 (2002).

[63] R. Sapienza, R. Coenen, J. Renger, M. Kuttge, N. F. van Hulst, and A. Polman, "Deep-subwavelength imaging of the modal dispersion of light," Nat. Mat. **11**, 781 (2012).

[64] M. Frimmer, Y. Chen, and A. F. Koenderink, "Scanning emitter lifetime imaging microscopy for spontaneous emission control," Phys. Rev. Lett. **107**, 123602 (2011).

[65] J. Wenger, D. Gérard, J. Dintinger, O. Mahboub, N. Bonod, E. Popov, T. W. Ebbesen, and H. Rigneault, "Emission and excitation contributions to enhanced single molecule fluorescence by gold nanometric apertures," Opt. Express **16**, 3008 (2008).

[66] E. Castanié, *Émission dipolaire et absorption en champ proche de nanostructures* (Université Pierre et Marie Curie, Paris, 2011).

[67] E. D. Palik, *Handbook of Optical Constants of Solids* (Academic Press, 1998).

[68] P. Bharadwaj, B. Deutsch, and L. Novotny, "Optical antennas," Adv. Opt. Phot. **1**, 438 (2009).

[69] J. Wenger, "Fluorescence enhancement factors on optical antennas: enlarging the experimental values without changing the antenna design," Int. J. Opt. **2012**, 828121 (2011).

[70] C. Awada, G. Barbillon, F. Charra, L. Douillard, and J.-J. Greffet, "Experimental study of hot spots in gold/glass nano composite films by photoemission electron microscopy," Phys. Rev. B **85**, 045438 (2012).

[71] N. J. Borys, E. Shafran, and J. M. Lupton, "Surface plasmon delocalization in silver nanoparticle aggregates revealed by subdiffraction supercontinuum hot spots," Sci. Rep. **3**, 2090 (2013).

[72] P. Gadenne, Y. Yagil, and G. Deutscher, "Transmittance and reflectance *in situ* measurements of semicontinous gold films during deposition," J. Appl. Phys. **66**, 7 (1989).

[73] Z. Shi, G. Piredda, A. C. Liapis, M. A. Nelson, L. Novotny, and R. W. Boyd, "Surface-plasmon polaritons on metal-dielectric nanocomposite films," Opt. Lett. **34**, 3535 (2009).

[74] U. K. Chettiar, P. Nyga, M. D. Thoreson, A. V. Kildishev, V. P. Drachev, and V. M. Shalaev, "FDTD modeling of realistic semicontinuous metal films," Appl. Phys. B **100**, 159 (2010).

[75] X. C. Zeng, D. J. Bergman, P. M. Hui, and D. Stroud, "Effective-medium theory for weakly nonlinear composites," Phys. Rev. B **38**, 10970 (1988).

[76] M. I. Stockman, S. V. Faleev, and D. J. Bergman, "Localization versus delocalization of surface plasmons in nanosystems: can one state gave both characteristics?" Phys. Rev. Lett. **87**, 167401 (2001).

[77] A. K. Sarychev and V. M. Shalaev, "Electromagnetic field fluctuations and optical nonlinearities in metal-dielectric composites," Phys. Rep. **335**, 275 (2000).

[78] A. Cazé, R. Pierrat, and R. Carminati, "Radiative and non-radiative local density of states on disordered plasmonic films," Phot. Nano. Fund. Appl. **10**, 339 (2012).

[79] R. Ferrando and G. Tréglia, "Anisotropy of diffusion along steps on the (111) faces of gold and silver," Science **247**, 59 (1990).

[80] C. Mottet, R. Ferrando, F. Hontinfinde, and A. C. Levi, "A monte-carlo simulation of submonolayer homoepitaxial growth on Ag(110) and Cu(110)," Science **247**, 59 (1998).

[81] F. Cleri and V. Rosato, "Tight-binding potentials for transition metals and alloys," Phys. Rev. B **48**, 22 (1993).

[82] J. Hoshen and R. Kopelman, "Percolation and cluster distribution. i. cluster multiple labeling technique and critical concentration algorithm," Phys. Rev. B **14**, 3438 (1976).

[83] R. F. Voss, R. B. Laibowitz, and E. I. Allessandrini, "Fractal (scaling) clusters in thin gold films near the percolation threshold," Phys. Rev. Lett. **49**, 1441 (1982).

[84] B. Mandelbrot, *The fractal geometry of nature* (Freeman, New-York, USA, 1983).

[85] S. I. Bozhevolnyi, B. Vohnsen, A. V. Zayats, and I. I. Smolyaninov, "Fractal surface characterization: implications for plasmon polariton scattering," Surf. Sc. **356**, 268 (1996).

[86] R. A. Chance, a. Prock, and R. Silbey, "Molecular fluorescence and energy transfer near interfaces," Adv. Chem. Phys. **37**, 1 (1978).

[87] J. Laverdant, S. Buil, B. Bérini, and X. Quélin, "Polarization dependent near-field speckle of random gold films," Phys. Rev. B **77**, 165406 (2008).

[88] E. Fort and S. Grésillon, "Surface enhanced fluorescence," J. Phys. D: Appl. Phys. **41**, 013001 (2008).

[89] P. Andrew and W. L. Barnes, "Energy transfer across a metal film mediated by surface plasmon polaritons," Science **306**, 1002 (2004).

[90] V. K. Komarala, A. L. Bradley, Y. P. Rakovich, S. J. Byrne, Y. K. Gun'ko, and A. L. Rogacj, "Surface plasmon enhanced förster resonance energy transfer between the CdTe quantum dots," Appl. Phys. Lett. **93**, 123102 (2008).

[91] V. N. Pustovit and T. V. Shahbazyan, "Cooperative emission of light by an ensemble of dipoles near a metal nanoparticle: The plasmonic Dicke effect," Phys. Rev. Lett. **102**, 077401 (2009).

[92] S. Aberra Guebrou, C. Symonds, E. Homeyer, J. C. Plenet, Y. N. Gartstein, V. M. Agranovich, and J. Bellessa, "Coherent emission from a disordered organic semiconductor induced by strong coupling with surface plasmons," Phys. Rev. Lett. **108**, 066401 (2012).

[93] M. I. Stockman, "Nanoplasmonics: Past, present, and glimpse into future," Opt. Exp. **19**, 22029 (2011).

[94] M. D. Birowosuto, S. E. Skipetrov, W. L. Vos, and A. P. Mosk, "Observation of spatial fluctuations of the local density of states in random photonic media," Phys. Rev. Lett. **105**, 013904 (2010).

[95] D. E. Chang, Sørensen, E. A. Demler, and M. D. Lukin, "A single-photon transistor using nanoscale surface plasmons," Nat. Phys. **3**, 807 (2007).

[96] P. A. Huidobro, A. Y. Nikitin, C. González-Ballestero, L. Martín-Moreno, and F. J. García-Vidal, "Superradiance mediated by graphene surface plasmons," Phys. Rev. B **85**, 155438 (2012).

[97] G. Lerosey, J. de Rosny, A. Tourin, and M. Fink, "Focusing beyond the diffraction limit with far-field time reversal," Science **315**, 1120 (2007).

[98] X. Li and M. I. Stockman, "Highly efficient spatiotemporal coherent control in nanoplasmonics on a nanometer-femtosecond scale by time reversal," Phys. Rev. B **77**, 195109 (2008).

[99] A. Sentenac and P. C. Chaumet, "Subdiffraction light focusing on a grating substrate," Phys. Rev. Lett. **101**, 013901 (2008).

[100] A. Cazé, R. Pierrat, and R. Carminati, "Spatial coherence in complex photonic and plasmonic systems," Phys. Rev. Lett. **110**, 063903 (2013).

[101] R. L. Weaver and O. I. Lobkis, "Ultrasonics without a source: Thermal fluctuation correlations at MHz frequencies," Phys. Rev. Lett. **87**, 134301 (2001).

[102] E. Larose, L. Margerin, A. Derode, B. van Tiggelen, M. Campillo, N. Shapiro, A. Paul, L. Stehly, and M. Tanter, "Correlation of random wavefields: An interdisciplinary review," Geophysics **71**, SI11 (2006).

[103] T. Setälä, K. Blomstedt, M. Kaivola, and A. T. Friberg, "Universality of electromagnetic-field correlations within homogeneous and isotropic sources," Phys. Rev. E **67**, 026613 (2003).

[104] J. de Rosny and M. Fink, "Overcoming the diffraction limit in wave physics using a time-reversal mirror and a novel acoustic sink," Phys. Rev. Lett. **89**, 124301 (2002).

[105] P. M. Morse and H. Feshbach, *Methods of theoretical physics* (McGraw-Hill, New York, 1953).

[106] S. Mazzucco, N. Geuquet, J. Ye, O. Stéphan, W. Van Roy, P. Van Dorpe, L. Henrard, and M. Kociak, "Ultralocal modification of surface plasmons properties in silver nanocubes," Nanolett. **12**, 1288 (2012).

[107] V. A. Markel, "Anderson localization of polar eigenmodes in random planar composites," J. Phys. Condens. Matter **18**, 11149 (2006).

[108] C. Sauvan, J. P. Hugonin, I. S. Maksymov, and P. Lalanne, "Theory of the spontaneous optical emission of nanosize photonic and plasmon resonators," Phys. Rev. Lett. **110**, 237401 (2013).

[109] A. K. Sarychev, V. A. Shubin, and V. M. Shalaev, "Anderson localization of surface plasmons and nonlinear optics of metal-dielectric composites," Phys. Rev. B **60**, 16389 (1999).

[110] C. M. Soukoulis, Q. Li, and G. S. Grest, "Quantum percolation in three-dimensional systems," Phys. Rev. B **45**, 7724 (1992).

[111] I. Chang, Z. Lev, A. B. Harris, J. Adler, and A. Aharony, "Localization length exponent in quantum percolation," Phys. Rev. Lett. **74**, 2094 (1995).

[112] D. A. Genov, A. K. Sarychev, and V. M. Shalaev, "Plasmon localization and local field distribution in metal-dielectric films," Phys. Rev. E **67**, 056611 (2003).

[113] K. Seal, D. A. Genov, A. K. Sarychev, H. Noh, V. M. Shalaev, Z. C. Ying, X. Zhang, and H. Cao, "Coexistence of localized and delocalized surface plasmon modes in percolating metal films," Phys. Rev. Lett. **97**, 206103 (2006).

[114] B. Shapiro, "Large intensity fluctuations for wave propagation in random media," Phys. Rev. Lett. **57**, 2168 (1986).

[115] M. J. Stephen and G. Cwilich, "Intensity correlation functions and fluctuations in light scattered from a random medium," Phys. Rev. Lett. **59**, 285 (1987).

[116] F. Scheffold and G. Maret, "Universal conductance fluctuations of light," Phys. Rev. Lett. **81**, 5800 (1998).

[117] L. Tsang and J. A. Kong, *Scattering of Electromagnetic waves: Advanced Topics* (John Wiley & Sons, New York, 2001).

[118] M. Born and E. Wolf, *Principles of Optics* (Cambridge University Press, Cambridge, UK, 1999).

[119] K. Vynck, R. Pierrat, and R. Carminati, "Polarization and coherence of electromagnetic waves in uncorrelated disordered media," to be published (2013).

[120] S. Hikami, "Anderson localization in the nonlinear-σ-model representation," Phys. Rev. B **24**, 2671 (1981).

[121] J. F. de Boer, M. P. van Albada, and A. Lagendijk, "Transmission and intensity correlations in wave propagation through random media," Phys. Rev. B **45**, 658 (1992).

[122] R. Pnini and B. Shapiro, "Fluctuations in transmission of waves through disordered slabs," Phys. Rev. B **39**, 6986 (1989).

[123] R. Pierrat, *Propagation et émission du rayonnement en milieu diffusant. Application à l'imagerie des milieux complexes.* (École Centrale Paris, Paris, 2007).

[124] R. Pierrat, N. Ben Braham, L. F. Rojas-Ochoa, R. Carminati, and F. Scheffold, "The influence of the scattering anisotropy parameter on diffuse reflection of light," Opt. Commun. **281**, 18 (2007).

[125] L. S. Froufe Pérez, *Estadísfica de la dispersión de ondas en medios desordenados* (Universidad Autónoma de Madrid, 2006).

[126] A. P. Mosk, A. Lagendijk, G. Lerosey, and M. Fink, "Controlling waves in space and time for imaging and focusing in complex media," Nature Photon. **6**, 283 (2013).

[127] J. Bertolotti, E. G. van Putten, C. Blum, A. Lagendijk, W. L. Vos, and A. P. Mosk, "Non-invasive imaging through opaque scattering layers," Nature **491**, 232 (2012).

[128] P. Sebbah (ed.), *Waves and Imaging through Complex Media* (Kluwer Academic, Dordrecht, 2001).

[129] A. Cazé, R. Pierrat, and R. Carminati, "Near-field interactions and nonuniversality in speckle patterns produced by a point source in a disordered medium," Phys. Rev. A **82**, 043823 (2010).

[130] W. K. Hildebrand, A. Strybulevych, S. E. Skipetrov, B. A. van Tiggelen, and J. H. Page, "Observation of infinite-range intensity correlations near the 3D Anderson localization transition," Arxiv p. 1303.7042 (2013).

[131] L. S. Froufe-Pérez, R. Carminati, and J. J. Sáenz, "Fluorescence decay rate statistics of a single molecule in a disordered cluster of nanoparticles," Phys. Rev. A **76**, 013835 (2007).

[132] L. S. Froufe-Pérez and R. Carminati, "Lifetime fluctuations of a single emitter in a disordered nanoscopic system: The influence of the transition dipole orientation," Phys. Stat. Sol. (a) **205**, 1258 (2008).

[133] R. Pierrat and R. Carminati, "Spontaneous decay rate of a dipole emitter in a strongly scattering disordered environment," Phys. Rev. A **81**, 063802 (2010).

[134] P. V. Ruijgrok, R. Wüest, A. A. Rebane, A. Renn, and V. Sandoghdar, "Spontaneous emission of a nanoscopic emitter in a strongly scattering disordered medium," Opt. Express **18**, 6360 (2010).

[135] S. Faez, A. Strybulevych, J. H. Page, A. Lagendijk, and B. van Tiggelen, "Observation of multifractality in Anderson localization of ultrasound," Phys. Rev. Lett. **103**, 155703 (2009).

[136] A. Rodriguez, L. J. Vasquez, K. Slevin, and R. A. Römer, "Multifractal finite-size scaling and universality at the Anderson transition," Phys. Rev. B **84**, 134209 (2011).

[137] S. E. Skipetrov and I. M. Sokolov, "Absence of Anderson localization of light in a random ensemble of point scatterers," Arxiv p. 1303.4655 (2013).

[138] E. Purcell, "Spontaneous emission probabilities at radio frequencies," Phys. Rev. **69**, 681 (1946).

[139] K. Drexhage, "Influence of a dielectric interface on fluorescence decay time," J. Lumin. **1**, 693 (1970).

[140] G. Rempe, H. Walther, and N. Klein, "Observation of quantum collapse and revival in a one-atom maser," Phys. Rev. Lett. **58**, 353 (1987).

[141] C. Weisbuch, M. Nishioka, A. Ishikawa, and Y. Arakawa, "Observation of the coupled exciton-photon mode splitting in a semiconductor quantum microcavity," Phys. Rev. Lett. **69**, 3314 (1992).

[142] E. Peter, P. Senellart, D. Martrou, A. Lemaître, J. Hours, J. M. Gérard, and J. Bloch, "Exciton-photon strong-coupling regime for a single quantum dot embedded in a microcavity," Phys. Rev. Lett. **95**, 067401 (2005).

[143] A. Trügler and U. Hohenester, "Strong coupling between a metallic nanoparticle and a single molecule," Phys. Rev. B **77**, 115403 (2008).

[144] P. Vasa, W. Wang, R. Pomraenke, M. Lammers, M. Maiuri, C. Manzoni, G. Cerullo, and C. Lienau, "Real-time observation of ultrafast rabi oscillations between excitons and plasmons in metal nanostructures with J-aggregates," Nature Phot. **7**, 128 (2013).

[145] S. John, "Electromagnetic absorption in a disordered medium near a photon mobility edge," Phys. Rev. Lett. **53**, 2169 (1984).

[146] S. John, "Strong localization of photons in certain disordered dielectric superlattices," Phys. Rev. Lett. **58**, 2486 (1987).

[147] S. Mazoyer, J. P. Hugonin, and P. Lalanne, "Disorder-induced multiple scattering in photonic-crystal waveguides," Phys. Rev. Lett. **103**, 063903 (2009).

[148] M. Spasenovic, D. M. Beggs, P. Lalanne, T. F. Krauss, and L. Kuipers, "Measuring the spatial extent of individual localized photonic states," Phys. Rev. B **86**, 155153 (2012).

[149] H. Thyrrestrup, S. Smolka, L. Sapienza, and P. Lodahl, "Statistical theory of a quantum emitter strongly coupled to Anderson-localized modes," Phys. Rev. Lett. **108**, 113901 (2012).

[150] A. Cazé, R. Pierrat, and R. Carminati, "Strong coupling to 2D Anderson localized modes," Phys. Rev. Lett. **111**, 053901 (2013).

[151] B. C. Gupta and Z. Ye, "Localization of classical waves in two-dimensional random media: A comparison between the analytic theory and exact numerical simulation," Phys. Rev. E **67**, 036606 (2003).

[152] D. J. Thouless, "Electrons in disordered systems and the theory of localization," Phys. Rep. **13**, 93 (1974).

[153] A. Yamilov and H. Cao, "Highest-quality modes in disordered photonic crystals," Phys. Rev. A **69**, 031803(R) (2004).

[154] G. M. Conley, M. Burresi, F. Pratesi, K. Vynck, and D. S. Wiersma, "Light transport and localization in two-dimensional correlated disorder," Arxiv p. 1307.1899 (2013).

[155] F. Lemoult, M. Fink, and G. Lerosey, "Acoustic resonators for far-field control of sound on a subwavelength scale," Phys. Rev. Lett. **107**, 064301 (2011).

[156] I. M. Vellekoop and A. P. Mosk, "Focusing coherent light through opaque strongly scattering media," Opt. Lett. **32**, 2309 (2007).

[157] C. H. Wilcox, "Debye potentials." J. Math. and Mech. **6**, 167 (1957).

[158] M. Wubs, L. G. Suttorp, and A. Lagendijk, "Multiple-scattering approach to interatomic interactions and superradiance in inhomogeneous dielectrics," Phys. Rev. A **70**, 053823 (2004).

[159] F. Hontinfinde, R. Ferrando, and A. C. Levi, "Diffusion processes relevant to the epitaxial growth of Ag on Ag(110)," Surf. Sc. **336**, 306 (1996).

[160] P. C. Chaumet, A. Sentenac, and A. Rahmani, "Coupled dipole method for scatterers with large permittivity," Phys. Rev. E **70**, 036606 (2004).